

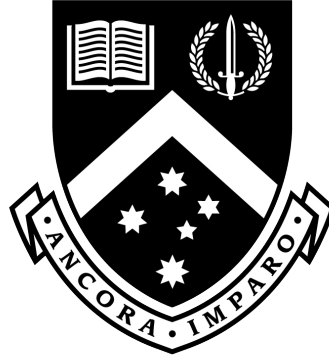


MONASH University

*On Long Timescale Recurrent Active Region Coronal Jets:
The Coronal Geyser Structure*

Alin Răzvan Paraschiv

A thesis submitted for the degree of Doctor of Philosophy at Monash University in 2018
School of Mathematical Sciences



**On Long timescale Recurrent Active Region Coronal Jets:
The Coronal Geyser Structure**

by

ALIN RĂZVAN PARASCHIV
B.Sc. M.Sc.

Thesis submitted to **Monash University**,
in fulfilment of the requirements for the degree of
Doctor of Philosophy

Main Supervisor: Dr. Alina Cătălina Donea
Associate Supervisor: Prof. Paul Stuart Cally

August 2018
Melbourne, Australia

Copyright notice

© Alin Răzvan Paraschiv 2018

I certify that I have made all reasonable efforts to secure copyright permissions for third-party content included in this thesis and have not knowingly added copyright content to my work without the owner's permission.

"The nitrogen in our DNA, the calcium in our teeth, the iron in our blood, the carbon in our apple pies were made in the interiors of collapsing stars. We are made of star stuff."

Carl Sagan

Abstract

The peculiarities of our Sun and its visible atmosphere have produced awe in humankind since times immemorial. Huge efforts have been made in the last one hundred fifty years into understanding the rich variety of discovered solar phenomena. Some initial questions are still unanswered today! Nowadays with the advance of technology, the properties of small eruptive solar features became a puzzling curiosity. During its solar disk transit in September 2011 the solar active region 11302 showcased a vast display of solar jets. Here, we observe multiple co-temporal jet phenomenology, study the lower atmosphere magnetic topology, reconstruct magnetic structures, and analyze the emission mechanisms responsible for ten jet events occurring at the active region's periphery.

The identified jet events were detected in extreme-ultraviolet filter images and were correlated with low lying magnetic features and particle acceleration events. The jets gave rise to intense lower atmosphere heating and interplanetary electron beams that even reached the earth's magnetosphere. The impact that jets have across different layers of the solar atmosphere and their interaction with local features of solar activity is discussed emphasizing the associated magnetic field reconfiguration sites in the lower corona.

We report the identification of base-arch structures in the lower solar atmosphere which undergo multiple magnetic field reconfigurations and are the main trigger of solar jets. These sites are classified as "Coronal Geysers". The intrinsic studied structure had emitted jets quasi-periodically for the entire time the active region was visible on the solar disk. Almost all jets exhibit a strand-like morphology undergoing untwisting motions which suggest torsional waves may propagate along the so-called 'open' magnetic fields during eruptions.

The nature of the underlying magnetic field reconfiguration is discussed, focusing on the comprehensive interpretation of lower atmosphere hot brightpoints and ribbons, and on deciphering the relation between jets, brightpoints, and interplanetary radio bursts. To our knowledge, the long term jet recurrence and its association with a persistent magnetic configuration, identified as the 'geyser structure', was not previously discussed. The data analysis of this phenomenon provides new information for theoretical modeling of jets and allows for a better assessment of a new hypothesis that base-arch heating and jet emission are triggered by recurring small-scale filament eruptions.

Subject Headings: Sun: jets; Sun: corona, photosphere; Sun: UV radiation, X-rays; Sun: activity; Sun: radio radiation; Sun: heliosphere; Sun: atmospheric motions; Sun: magnetic reconnection; Sun: magnetic fields;

Declaration

I hereby declare that this thesis contains no material which has been accepted for the award of any other degree or diploma at any university or equivalent institution and that, to the best of my knowledge and belief, this thesis contains no material previously published or written by another person, except where due reference is made in the text of the thesis.

This thesis includes 1 original paper published in peer reviewed journals and 3 manuscripts in preparation or submitted status. The core theme of the thesis is Recurrent Solar Active Region Coronal Jets. The ideas, development and rewriting up of all the papers in the thesis were the principal responsibility of myself, the student, working within the School of Mathematical Sciences, Monash University, under the supervision of Dr. Alina Donea and Prof. Paul Cally.

The inclusion of co-authors reflects the fact that the work came from active collaboration between researchers and acknowledges input into team-based research.

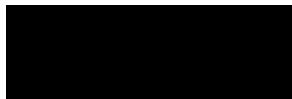
My contribution to the work involved the following:

(1)	(2)	(3)	(4)	(5)	(6)
1	Are All Flare Ribbons Simply Connected to the Corona?	<i>Astrophys. J.</i> Published	45%, draft input; key ideas; Coronal EUV, Magnetic, and radio data analysis; observations co-alignment; revisions input.	EJudge 25% Concept, key ideas, and analytical calculations, Draft writing and review. D.Lacatus, 25% draft review and IRIS interpretation. A.Donea, & C.Lindsey, 5% discussions.	yes
2	Long timescale Recurrent/Homologous Coronal Jets: Coronal Geyser Structures as sources of electron beams and interplanetary Type-III radio bursts	In prep. Prospective <i>Astrophys. J.</i>	95%, key ideas; draft writing; data analysis; study concept	Alina Donea, 5% Draft revision and discussions	no
3	On the Physical Parameters and Energy Budget of Active Region Recurrent Coronal Jets	In prep. Prospective <i>Astrophys. J.</i>	95%, key ideas, draft writing, data analysis and conceptual framework	Alina Donea, 5% Draft revision and discussions	no
4	The Magnetic Topology of a Geyser Site and Trigger Mechanism for Recurrent Active Region Jets	In prep. Prospective <i>Solar Phys.</i>	95%, key ideas, draft writing, data analysis and conceptual framework	Alina Donea, 5% Draft revision and discussions	no

*(1) Thesis Chapter; (2) Publication Title; (3) Publication Status; (4) Student's nature and % of contribution; Co-authors nature and % of contribution; (6) Monash student co-author.

I have rewritten, reordered, and renumbered sections of submitted or published papers in order to generate a consistent presentation within the thesis.

Student signature:



Date: 18.08.2017

The undersigned hereby certify that the above declaration correctly reflects the nature and extent of the student's and co-authors' contributions to this work. In instances where I am not the responsible author I have consulted with the responsible author to agree on the respective contributions of the authors.

Main Supervisor signature:



Date: 18.08.2017

Contents

Abstract	V
Declaration	VII
Abbreviations and Nomenclature	XI
Outline	XII
Introduction	1
1 On Small-scale Flare Ribbons, Recurrent Coronal Jets, and the AR11302 Geyser Structure	13
1.1 Morphology of Recurrent Active Region Jets	13
1.1.1 Multiwavelength analysis of Active Region Jets	15
1.1.2 A Timeseries of Active Region Jets	18
1.1.3 Geyser Jets Morphological Parameters and Helical Motions	20
1.2 Flare Ribbon Corona Connectivity	23
1.2.1 Interpreting EUV and Magnetic Data	24
1.2.2 Discussion	26
1.2.3 Conclusions	30
2 Coronal Geyser Structures as Sources of Electron Beams and Interplanetary Type-III Radio Bursts	31
2.1 Observations, Datasets, and Instrumentation	31
2.2 Coronal Geysers and Type-III Bursts	33
2.2.1 Timeseries Correlation of Coronal Jets and Type-III Radio Bursts	35
2.2.2 Modeling the Heliospheric Travel of Upward Electron Beams	37
2.3 Summary and Discussion	40
3 Thermal and Non-Thermal Properties of Active Region Recurrent Coronal Jets	45
3.1 Differential Emission Measure of Thermal Plasma	45
3.2 On Differential Emission Measure Inversions	47
3.2.1 Background and Methodology	47
3.2.2 The Filter Ratio Technique	48
3.2.3 Single Gaussian Chi-square Minimization	49
3.2.4 Regularized Chi-square Minimization	51
3.2.5 Sparse Inversion and Minimization	52
3.3 Geyser EUV Thermal Emission	54
3.3.1 The Footpoint Emission Measure of the J2, J3, and J6 Eruptions	54
3.3.2 Jet Outflow Emission Measure Profiles of the J2, J3, and J6 Eruptions	61
3.4 Geyser X-Ray Energetics	67
3.5 Discussion	72
4 The Magnetic Topology and Extrapolated Field Configuration of a Lower Atmosphere Geyser Site	81
4.1 Solar Vector Magnetic Fields	81
4.1.1 The SDO-HMI Instrumentation	82
4.1.2 Interpreting Vector Magnetic Field Observations	83
4.1.3 Custom Vector Magnetic Field Disambiguation	87

4.2	Tracking Magnetic Moving Features at the Periphery of AR11302	90
4.2.1	Geyser Site Magnetic Ingredients	90
4.2.2	Jets Generated by Magnetic Grain Flux Cancellation	91
4.2.3	Jets Generated by Small Scale Flux Emergence	93
4.2.4	Non-Erupting Geyser Footpoint Events	94
4.3	Geyser Structure Magnetic Field Extrapolations	95
4.3.1	A Potential Field Approximation	96
4.3.2	A Non-Idealized Geyser Interpretation	97
4.4	Discussion	101
Outlook		XVII
Appendix		XXIII
A	The multiwavelength view of the AR11302 geyser site jets	XXIII
B	The AR11302 geyser jets slit-jaw perspective	XXIX
C	Magnetic moving features interacting with the AR11302 site	XXXIX
Acknowledgements		LI
List of Figures		LIII
List of Tables		LVIII
Bibliography		LIX

Abbreviations and Nomenclature

AIA	Atmospheric Imaging Assembly onboard SDO [Lemen et al., 2012]
AR	Active Region
AU	Astronomical Unit
BP	Bright Point
CH	Coronal Hole
COR1	Inner Heliospheric Coronagraph onboard STEREO [Thompson et al., 2003]
EUV	Extreme UltraViolet
EIS	EUV Imaging Spectrometer onboard HINODE [Young et al., 2007]
EIT	EUV Imaging Telescope onboard SOHO [Delaboudinière et al., 1995]
EUVI	Extreme UV Imager onboard STEREO [Wuelser et al., 2004]
FOV	Field of View
HINODE	Japanese Solar-B Mission [Kosugi et al., 2007]
HMI	Helioseismic and Magnetic Imager onboard SDO [Scherrer et al., 2012]
HXR	Hard X-ray
IRIS	Interface Region Imaging Spectrometer [De Pontieu et al., 2014]
JET	Collimated ejection of solar plasma
L_{\odot}	Solar Visible Spectrum Luminosity
L_{Cor}	Solar Corona Luminosity
LFF	Linear Force-Free approximation
LASCO	Large Angle Spectrometer Coronagraph onboard SOHO [Brueckner et al., 1995]
LOS	Line of Sight
MHD	Magnetohydrodynamics
NLFF	Non-Linear Force-Free approximation
PFF	Potential Force-Free approximation
RHESSI	Reuven Ramaty High Energy Solar Spectroscopic Imager [Lin et al., 2002]
SDO	Solar Dynamics Observatory [Pesnell et al., 2012]
SECCHI	Sun Earth Connection Coronal and Heliospheric Investigation [Howard et al., 2008]
SOHO	Solar and Heliospheric Observatory [Domingo et al., 1995]
STEREO	Solar Terrestrial Relations Observatory [Kaiser et al., 2008]
SWAVES	The Radio and Plasma Wave investigation onboard STEREO [Bougeret et al., 2008]
SXR	Soft X-ray
SXT	Soft X-ray Telescope onboard YOHKOH [Tsuneta et al., 1991]
UV	Ultraviolet
WAVES	The Radio and Plasma Wave investigation onboard WIND [Bougeret et al., 1995]
XRT	X-ray Telescope onboard HINODE [Golub et al., 2007]
YOHKOH	Japanese Solar-A mission [Ogawara et al., 1991]

Outline of the Thesis

Solar jets are small-scale collimated ejections of hot plasma that are typically released in the outer corona. Jets have recently become a hot study topic in the solar community. Jet-like events appear in many forms and sizes, e.g. coronal polar and active region jets, chromospheric jets and Type-II spicules. Recent studies seem to converge on the same set of fundamental processes responsible for generating jet eruptions at different scales. The jet dynamics, properties and intrinsic implications are widely debated in the field. This work aims to shed light on active region coronal jets, addressing their contribution and involvement in the larger solar processes. However, the detailed physical processes that govern such small-scale eruptive processes are not fully understood. Are recurrent or homologous jets the result of a series of self-similar reconnection events involving a base arched structure (micro-filament) that is subjected to energy storage and release mechanisms? Alternatively, do recurrent jets result from a chaotic behavior of lower atmosphere features that interact with a local twisted filament to give rise to jet eruptions?

Due to the long timescale of our studied recurring jet eruptions we have assumed the existence of quasi-stable base structures which were entitled “Coronal Geysers”. These structures are described herein. The Geyser’s characteristics are examined by means of timeseries analysis, EUV and X-Ray energetic budget estimation, lower atmosphere manifestations, and the study of chromospheric reconnecting footpoints. We propose these long lived, quasi-stable, EUV/X-Ray jet Geyser reconnection sites are good proxies of coronal sources for Type-III radio bursts. The correlations are remarkable as EUV involves thermal emission whereas radio bursts are generated by non-thermal processes. The energetics of a significant dataset of active region jets are presented. The results are used to infer and compare the physical properties of jet plasma simultaneously at the base geyser site and along the jet spire. To this extent, physical plasma parameters are obtained via differential emission measurements using multiple inversion techniques and X-Ray source reconstruction.

The nature of the underlying magnetic reconnection is discussed, stressing the prudent interpretation of lower atmosphere magnetic structures. Aiming to understand the base reconnective processes that govern small scale flaring sites, we scrutinized the belief that flare ribbons in the chromosphere result from energy transport from the overlying corona by studying ribbons of modest flares. While most ribbons appear connected to the corona, we conclude that at least two mechanisms should be considered when addressing heating processes that lead to flare ribbon emission.

An overview of solar observations is presented in the **Introduction**. The corona, essential to our scope, is briefly illustrated. The conceptual evolution of the two important questions of solar research is discussed, namely the coronal heating problem and slow solar wind acceleration, emphasizing the role that solar jets may play in the intricate processes that govern the solar atmosphere.

Chapter 1 describes active region jet morphology revealing typical parameters: lifetime, scale, outflow speed, torsional motions, outflow orientation, etc. by employing current jet emission models and image-data analysis techniques. Cooler plasma eruptions were detected in very close temporal proximity of the main jet eruptions. The physical nature of modest lower atmosphere flares is investigated by debating their assumed linkage to the corona.

Chapter 2 debates the relation between active region jets and other phenomena. Type-III radio beams propagating upwards and signs of downwards propagating beams have previously been associated with coronal jet emission sites. A new statistical correlation between coronal jets and non-thermal electron beams propagating in the inner heliosphere is presented.

Chapter 3 examines the energetics of active region jets. Physical plasma parameters: temperature, density, flux contributions, etc. are obtained via the inversion of the six narrow-band SDO-AIA filtergrams and RHESSI X-Ray source reconstruction. The results are used to infer and compare the physical properties of jet plasma simultaneously at the base geyser site and along the jet spire. When compared to the more studied polar coronal hole jets, the energy release is quite substantial, more powerful than was theoretically expected.

Chapter 4 illustrates the base photospheric and/or chromospheric magnetic structure that emits the multiple recurrent jets. The magnetic reconnection topology involved in jet emission is studied through the analysis of magnetic moving features. The photospheric magnetic fields correlated to the geyser location and involved in generating active region jets are used to derive the force-free field extrapolations, and the higher magnetic structures are reconstructed revealing the configuration and dynamics of our jet inducing geyser region.

Introduction

About five billion years ago in a spiral arm of our galaxy, the Milky Way, a small cloud comprised of gas and dust started to accrete. The cloud developed a core, which under its own weight condensed gradually increasing its inner temperature and density, up to the point of igniting nuclear fusion. A battle between the pressure gradients of exothermic nuclear processes and compressing gravitational forces began. In the course of time, a stalemate was achieved and a balance between the two opposing forces initiated our life-giving star, the Sun.

Some billions of years have passed, the solar system evolved and stabilized into the current configuration. The evolution of the most beautiful and endless forms of biological life have been tremendously influenced by solar luminosity and energy bombardment. Eventually, civilizations arose and, from the dawn of humanity, chronicles narrate the fascination and awe that our star imprinted in our ancestors' consciousness. Humanity worshiped our star and deities who represent the Sun creating many beliefs and legends. The Sun was often adored as god of truth, honesty, virtue, prophecy, intellect, vitality, and fertility. That is why when the solar eclipses occurred, humanity was deeply affected. The events were naively associated with omens or catastrophes. Finally, with the advent of modern science and technology, new curiosity has motivated mankind to study the Sun and its atmosphere's features, this time as natural phenomena.

The solar corona is the outer extended part of the solar atmosphere. From a spatial perspective, the corona is considered to extend from a height of ~ 2000 km above the solar photosphere (visible surface) to millions of kilometers into the inner heliosphere. Coronal structures have varying morphologies and heights. These structures are usually anchored in the photosphere and extend outwards giving the corona an inhomogeneous aspect. Compared to the visible surface, the corona is extremely faint ($L_{Cor}/L_{\odot} = 10^{-6}$). The only way of observing the solar corona is when the solar disk is occulted, and historically one could only observe the corona when this condition occurred naturally during a total solar eclipse. Reports describing coronal structures derived from eclipse observations are scarce especially before the 17th century. Most historical observations report only a glow around the Sun, which later-on was presumed to be the scattering of the photospheric light in our atmosphere, which in turn proved to be partly false. One of the first observations of the corona, though this information is contested, dates back to 1063BCE and it is tied to Babylonian eclipse observations, see Fotheringham [1920], Newton [1970] for additional information:

“On the twenty-six day of the month Sivan in the seventh year the day was turned to night, and fire in the midst of the heaven.”

The first physical interpretations of coronal structures revolved around the belief that observed structures were optical illusions or a phenomenon originating in the atmosphere of the Earth or of the Moon. The corona was recognized as a distinct component of

the solar atmosphere in the first part of the 20th century. In the middle of the 19th century astronomical observations reported that the Moon had no atmosphere, but more importantly, spectroscopic analysis had begun to be applied to solar observations, by bringing the newly devised spectroscopes on eclipse expeditions. Menzel [1931] was one of the first to obtain solar spectroscopic images, naming them ‘flash spectrum’. Some strong emission lines such as $H\alpha$ and Ca II H&K lines, not fully understood even today, were first observed in the totality phase of the eclipses. Spectroscopy was in its incipient form and not all emission lines visible in the corona could be clearly associated with distinct elements. The first ‘coronium’ lines were discovered by C.A. Young and W. Harkness in the 1869 eclipse. No known ion at the time emitted near those wavelengths. They assumed that a new element, coronium, was responsible for these peculiar emissions. The brightest coronal ‘green’ line (5303Å) and ‘red’ line (6374Å) were first observed. Other important fainter lines were subsequently detected by Hiei and Hirayama [1970].

The discovery of coronal emission lines was at the time the most outstanding problem in astrophysics. From eclipse observations it is known that the corona changes its structure throughout the sunspot cycle. At minimum solar activity, the corona is mainly elongated along the solar equatorial direction. In contrast, the coronal structures are uniformly distributed at all latitudes at maximum solar activity. The predictions at that time assumed a very low temperature (~ 6000 K) of the coronal plasma. The first correct temperature assumptions were made at the beginning of the 20th century, by Lyot and Marshall [1933] with a newly invented device called a coronagraph. They found that the coronal green line is very broad due to thermal broadening, but could not associate a temperature, because they did not know the mass of the ion that was emitting the line. The first correct estimate of the coronal temperature was inferred indirectly by Grotrian [1933]. The eclipse observations in the Ca II H&K lines revealed an electron velocity of 109 cm s^{-1} which could not be consistent with an expected hot gas emitting at 6000 K. The above mentioned electron velocity could only be associated with gas temperatures in the order of $10^6 - 10^7$ K. The coronal plasma is composed mainly of ionized H, ($> 90\%$), partially and fully ionized He ($\sim 9\%$) and highly ionized heavier elements ($\leq 1\%$). The first correct interpretation was reported by Edlén and Tyrén [1939] and Edlén and Swings [1942] who proved that the previously observed coronium lines were actually emitted by Fe and Ca in high stages of ionization ($Fe\ x$, $Fe\ xiv$, $Ca\ ii$, etc.). In order for the elements to reach such high levels of ionization, a plasma temperature of at least 10^6 K is required, proving that coronal gas is indeed very hot. Edlén identified 19 of the total of 24 emission lines of the corona which were observed at the time and, as a consequence, explained the large physical scale of the corona.

In conclusion, the corona is best portrayed using emission line observations. The basic coronal emission lines are placed in the far ultraviolet spectrum and have been photographed regularly from space starting in the 1970s. The S-082 instrument aboard Skylab was very important in this regard. So many emission lines were recorded that most of them overlapped, creating ‘line blending’ problems, some still unsolved. Subsequent efforts have demonstrated the value of such observations and numerous missions were designed to study the corona. The Spartan Package [Kohl et al., 1994] aboard the Space Shuttle and Ultraviolet Coronagraph/Spectrograph [UVCS] on the dedicated Solar and Heliospheric Observatory [SOHO; Domingo et al., 1995] mission. The ‘emission-line’ (E) corona represents the only component that arises out of thermal emission of actual coronal gas, consisting of emission in spectral lines formed by the high temperature coronal ions [Golub and Pasachoff, 2009]. The corona emits widely across the entire radiation spectrum, from radio waves to ultraviolet and X-Rays, although preferentially the emission

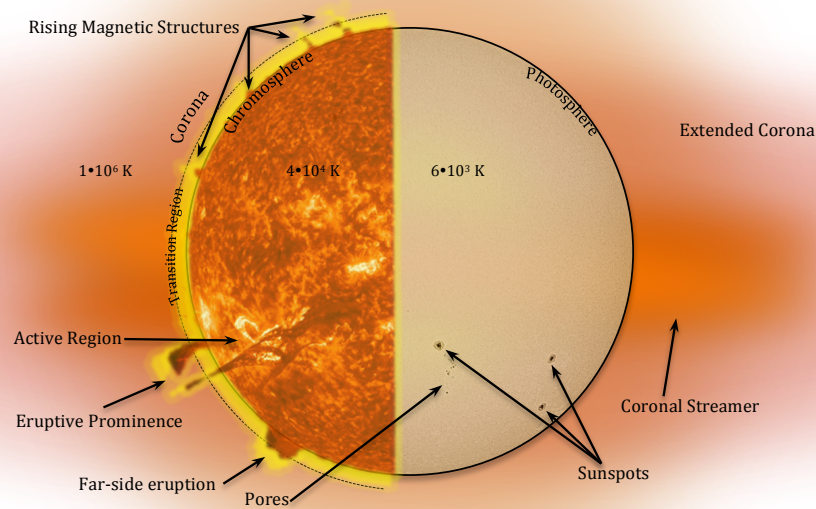


Figure i.1: Schematic depiction of the observational features of the solar atmosphere. The principal solar atmospheric layers, the Photosphere, Chromosphere, Transition Region, and Corona are illustrated along with their associated main plasma temperatures and solar atmospheric structures.

is concentrated in isolated emission lines, making it easy to observe independent plasma using narrow-band filters. The E corona was discovered at visible light wavelengths, but due to the high temperature of emitting plasma, the ultraviolet and soft X-Ray region of the spectrum dominate. The line coronal emission is the driving observable interpreted in our analysis performed on coronal jets.

The works of Bengt Edlén and Walter Grotrian on coronal emission lines were fundamental for the advance of astrophysics, and fields like atomic theory and spectroscopy. For the first time, temperatures in the order of 10^6 K were assumed for coronal plasma. A profound consequence stems: the coronal emission implies high and fully ionized plasma. Comparing these temperatures to the recorded solar surface temperatures of ~ 6000 K we are confronted with the problem of coronal heating. How can a temperature of a factor 200 higher than the surface temperature be maintained? If we assume that coronal heating can be explained by radial thermal conduction, then the solar atmospheric temperature should increase in height up to the chromosphere and then, slowly decrease outwards. Additionally, if UV and X-Ray emission losses are included, the corona should cool itself in a matter of hours.

A more physical approach is to consider the temperature as the fundamental physical parameter used to describe the solar corona. Energy transport by radiation, conduction, and convection leads us to conclude that the plasma temperature should decrease from the photosphere into the solar atmosphere. In reality the corona reaches very high temperatures on the order of 10^6 K. Skylab data revealed that the corona is highly structured by the surface magnetic fields that extend upwards. The standard view of coronal heating is that free magnetic energy is either built up in the corona or transported to the corona, due to re-arranging of the magnetic field lines in the photosphere. Figure i.1 sketches the main layers of the solar atmosphere. A very steep increase in temperature from chromospheric 10^4 K to coronal 10^6 K temperatures occurs within a transition region which is only ~ 500

km wide. Taking this into account the corona can be roughly defined as being the portion of the solar atmosphere where the temperature is higher than 10^5 K.

Coronal heating still stimulated intense discussion, although the issue has been known for about a century. Figure i.2 presents the Fontenla et al. [2011] model index 1003 and 1013 analytical approximations of temperature and density distributions along the main solar atmospheric layers corresponding to an active network region. The physical explanation of this phenomenon is currently missing. Different theoretical models have tried to explain the phenomenon, among them some that employ ubiquitous eruptive spicules and coronal jets have been recognized as a manifestation of upward propagating energy. Two mechanisms, wave heating and nanoflare heating, that have been commonly adopted by the solar community are currently being refined. Progress in the last few decades has been incremental, although none of the current endeavors can be currently seen as a full ‘solution’. One of the most popular heating mechanism is the wave heating model [see review, Nakariakov and Verwichte, 2005]. The wave model proposes either pure Alfvén or more general fast/alfvénic waves as a possible transport mechanism which heats the solar corona to the observed temperatures of the order of 10^6 K by transporting convective energy from the lower layers of the solar atmosphere. A fast/alfvénic wave is a low-frequency traveling oscillation of ions which if trapped in a wave guide (e.g. flux tube) propagates in the direction of the magnetic field as a kink or sausage wave.

Progress in theoretical models has mainly been made using 3D MHD simulations that include gravitational effects, more realistic models of the transition region etc., but controversies about the nature of the waves exist. Historically, it was presumed that pure Alfvén waves were dominant in the transition region and corona. Recent results appear to tip the scale in favor of fast/Alfvénic kink waves, though the topic is still actively being debated [e.g. Cally, 2017]. Some theoretical models of coronal heating mechanisms involve, as a primary energy source, chromospheric or coronal footpoints that ‘generate’ upward propagating fast kink waves. Observationally, Tomczyk et al. [2007] found signatures of Alfvén wave presence in intensity, line-of-sight velocity, and linear polarization images of the solar corona. Ubiquitous upward propagating wave movement consistent with the direction of the magnetic field was reported. The authors estimate of the energy carried yielded inconclusive results.

Other peculiar phenomenology was reported. Judge et al. [1998] provided evidence of dominant downflowing slow/compressional waves in quiet sun regions if one takes into account only wave coronal heating, noting that other scenarios and mechanisms can also explain their observed data. The authors argue in favor of an alternative scenario which describes coronal heating in terms of the “Parker” nanoflare coronal model [see review, Parnell and De Moortel, 2012]. This envisions a multistage mechanism with various underlying components. The initial energy comes from an electromagnetic mechanical driver, which has a coupling with a magnetic energy storage point, usually a chromospheric/coronal footpoint. Under specific conditions, magnetized fluid or plasma instabilities can occur, resulting in a loss of equilibrium. This can be done with or without mechanical energy transport, the first implying a local plasma heating process while the second connotes eruptions and mass release into the heliosphere. Regardless of the mechanical driver, the resulting pressure forces plasma to flow, becoming trapped in coronal structures.

On the observational side, De Pontieu et al. [2011] used novel observations from the Solar Dynamics Observatory, [SDO; Pesnell et al., 2012] and the Solar-B [Hinode; Kosugi et al., 2007] mission to reveal a ubiquitous coronal mass supply in chromospheric plasma in

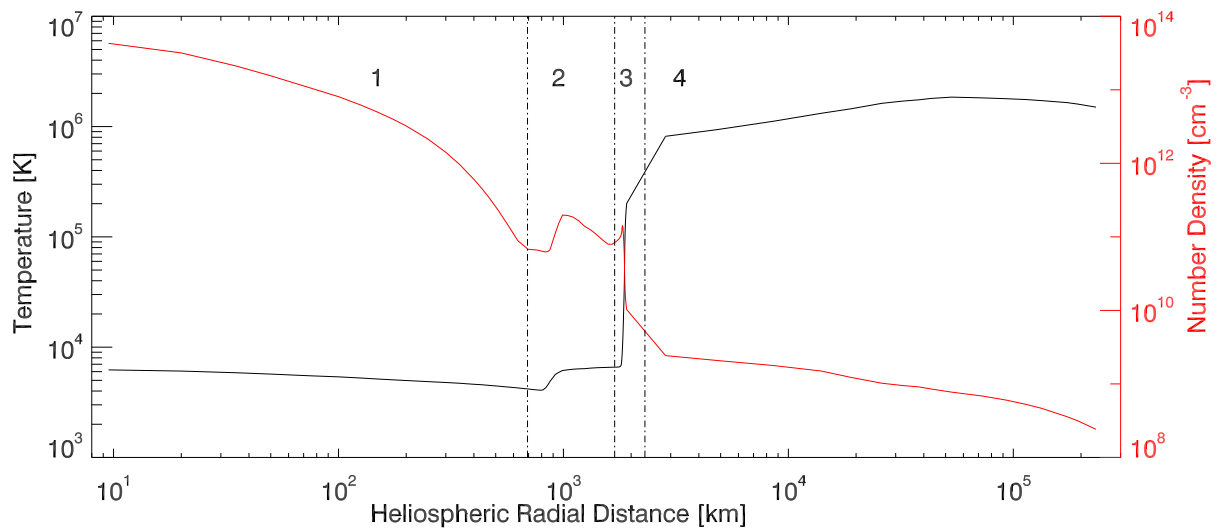


Figure i.2: Solar atmospheric density and temperature distributions plotted against radial heliospheric height. The main heliospheric layers are: The Photosphere(1); Chromosphere(2); Transition Region(3); Corona and inner heliosphere(4). A very sharp increase in temperature can be observed manifesting in the very narrow (~ 500 km) Transition Region. This manifestation constitutes the coronal heating problem. The graphs correspond to an enhanced network atmosphere, e.g. above a small scale pore, obtained via the Fontenla et al. [2011] models, using chromospheric (Model Index 1003) and coronal (Model Index 1013) boundary values.

the form of fountain like jets or spicules which are reportedly accelerated upward into the corona where plasma is somehow heated to temperatures above 10^6 K. These observations provided constraints on the nanoflare mechanism and highlight the importance of the transition region. Very optimistic reports have been presented as support of the nanoflare scenario, [see, Tian et al., 2014, Hansteen et al., 2014]. The variance of small scale eruptive phenomena is high, and their physical parameters are dependent on many external constraints. Singular cases are far from representing a general picture. More thorough and larger sample analyses are required in order to present a compelling argument.

Existing coronal heating models usually cover only a simplified and incomplete subset of these stages due to restrictions. Efforts concentrate on merging such models in order to lead to a more realistic and physically quantifiable picture which in turn can be fitted to observations. The nature of the nanoflare process also proves elusive. A weak consensus revolves around including small-scale EUV and Soft X-Ray phenomena, e.g. microflares and nanoflares that produce jet-like eruptions, within the standard flare model [see review, Shibata and Magara, 2011]. Small-scale phenomena provide a basis to allow estimation of their energy budget that can be utilized in coronal heating discussions. Simulated data sets of microflares and nanoflares in EUV and soft X-Rays have proved that these transient phenomena are, energetically, on the same order of magnitude with the radiative loss of the average quiet Sun corona, proving that the associated small-scale magnetic reconnection processes, occurring in the low atmosphere, can be a primary heating source of the corona [Aschwanden, 2005, chapter 9].

The purpose of this work is to provide new observationally driven insights on the physics of solar coronal jets by examining their base structures, e.g. footpoints (coronal brightpoints), reconnection sites, and the local magnetic field configuration responsible for recurrent (self repeating) and homologous (self similar) jet eruptions. Coronal jets were first described as strongly collimated ejections of plasma observed by ultraviolet and X-Ray imagers and in coronagraphs [St. Cyr et al., 1997] and hypothesized as a possible mass

supply to the solar wind flux. Traditionally, coronal jets are defined as reconnection driven ubiquitous small-scale collimated eruptions that are ejected towards the outer corona, presumably into the interplanetary medium. Two distinct jet categories arose: polar jets occurring inside large scale polar coronal holes mostly observed around the solar minimum activity period, and active region jets commonly located in boundaries of active regions, observed closer to the maximum of the solar cycle.

Kinematics of polar jets were first studied during the solar minimum activity period by Wang et al. [1998] using images from the Large Angle and Spectrometric Coronagraph [LASCO; Brueckner et al., 1995] and the Extreme ultraviolet Imaging Telescope [EIT; Delaboudinière et al., 1995] onboard SOHO. The authors derived bulk outflow speeds of $\sim 250 \text{ km s}^{-1}$ hinting that these velocities may reflect the actual outflow speeds of the slow background polar wind. The jets have been observed traveling outwards into the inner heliosphere, could be detected at heights up to $3.7R_{\odot}$, and typically have angular widths of around $3^{\circ} - 7^{\circ}$ as measured from the Sun's center. By first correlating EUV with white-light coronagraph observations the authors postulated a trigger mechanism by field line magnetic reconnection between emerging dipoles and neighboring 'vertical' fields. See for example fig. i.4. These jet events were observed to be ubiquitous and described as having a beam-like structure (collimated) morphology as they were more easily distinguishable against the less active polar region background. Cirtain et al. [2007] predicted that jets are transient phenomena that may occur at much higher rates than large-scale events. The study of Savcheva et al. [2007], based on observations from the X-Ray telescope [XRT; Golub et al., 2007] onboard Hinode was fundamental in understanding coronal jets. The authors measured the apparent outward velocity, the height, width and lifetime of a significant sample of jets. The authors presented one of the first statistical studies of jet transverse motions, obtaining velocities of $< 35 \text{ km s}^{-1}$, which indirectly hinted at the existence of Alfvénic waves that propagate along the newly reconnected fieldlines. The observational manifestation of this feature is the so-called 'untwisting motions', which were detected as instrumentation improved over the last decade. Independent results by Kim et al. [2007] closely followed, confirming the hypothesis via line spectroscopy interpretation, detecting non-thermal line broadenings and Doppler velocities in jet outflows that are associated with traveling Alfvénic waves.

The connections between jets and other events related to solar activity were studied using data from the Solar Terrestrial Relations Observatory [STEREO; Kaiser et al., 2008] twin coronagraphs [COR1; Thompson et al., 2003], and the Extreme Ultraviolet Imagers [EUVI; Wuelser et al., 2004] by Raouafi et al. [2008]. They showed that the onsets of polar plumes are associated with jet eruptions. The work was extended [Raouafi and Stenborg, 2014], the authors suggesting a tendency for plumes to be dependent on the occurrence of transients like small-scale jets allegedly resulting from low-rate (slow) magnetic reconnection. This result is important in the context of Sweet-Parker reconnective regimes becoming less popular in recent times. The decay phase of plumes was found to be characterized by gradual fainting as a result of flux cancellations, explained by either closely repeated events or low reconnection rate. Nisticò et al. [2009, 2011] provided observational evidence to argue that ubiquitous small-scale reconnection is an intrinsic feature of the solar corona. Typical plasma physical characteristics of polar jets was first described and an electron temperature determination for the erupting jet plasma of $0.8 - 1.3 \cdot 10^6 \text{ K}$ was realistically estimated via the inversion of EUVI data. Currently we would assume this result as a lower bound, expecting ejected plasma in the $2 - 4 \cdot 10^6 \text{ K}$ range, subject to local conditions and reconnection strength. Enhanced results of polar jets were subsequently

obtained using better quality data or improved inversion schemes [see Pucci et al., 2013, Young and Muglach, 2014, Paraschiv et al., 2015]. Figure i.3 presents a quick emission measure inversion solution of a coronal jet. The topic is herein extended and debated in Chapter 3.

Following the work of Nisticò et al. [2009], Paraschiv et al. [2010] identified and studied white-light jets observed by STEREO COR1 white light coronagraphs. More than ten thousand white-light jets observed at the minimum of solar activity between 2007 and 2008 were identified. Events were cross correlated with EUVI-195Å bright points on the solar disk. The association was done based on the changes (morphological, brightening, disappearing etc.) of the bright points located in regions close to the solar limb. This work suggested that the number of jets with high outflow speeds needs to be reasonably large to contribute significantly to the solar wind. Solar jets can have different morphologies and kinematic properties. The speed estimated for a subset of COR1 jets was $100\text{--}560\text{ km s}^{-1}$, though it may be that events seen in COR1 are only the most prominent and long lived jets. A recent eclipse white light jet study performed by Hanaoka et al. [2018] showed that faint X-Ray polar jets may actually extend to COR1 heights, contributing to a small extent to the solar wind outflow.

A morphological dichotomy of coronal jets was proposed by Moore et al. [2011] based on different observational features and their associated emission mechanisms. The authors showed that about half of their sampled events fit the standard reconnection picture for coronal jets (emerging flux model), whereas the rest correspond to another type. The non-standard jets are described as being hotter, having a higher outflow speed and were correlated with a jet-base magnetic arch which undergoes blowout eruptions, similar to a full-size CME eruption. Expanding the study [Moore et al., 2013], the authors showed many more similarities between Standard and Blowout jets like lateral expansion, and axial rotation exist, also implying that erupting type-II spicules are miniature counterparts X-Ray jets that are generated by granule-size emerging dipoles.

Pucci et al. [2013] observationally analyzed the difference between X-Ray standard and blowout jets. They aimed at inferring differences in physical parameters corresponding to the two categories. They analyzed the morphological profiles, speeds, temperatures, and densities for two case events and concluded that the blowout jet had a superior outflow speed, higher plasma temperature, and is rooted in a stronger magnetic field region when compared with the standard event. An estimate of the released energy for both events is also presented. As the discussion alluded to, no clear boundaries exist in discerning or labeling coronal eruptive phenomena.

It is debated whether events ranging from very small type-II spicules up to large scale CME eruptions may be explained using a common physical frameset. Over such an enormous range of energies, individual independent case measurements would only contribute as a baseline, but do not offer us the possibility of extracting larger contextual information. To this extent, Paraschiv et al. [2015] measured the amount of energy contribution and mass flux that significant sets of X-Ray jets supply towards the mass outflow and heating polar coronal holes. They found that although the contributions were not negligible, they were also not sufficient to explain either of the phenomena. Note that no major jet event occurred during the selected periods of observations. The authors also hinted that an anti-correlation may exist between the plasma number density and peak temperature in jet eruptions. The technique that is currently used, namely spectroscopic filtergram imaging, makes us visualize the corona using ‘horse blinders’, and today’s standard estimations provide only parameters inside a very narrow energetic range.

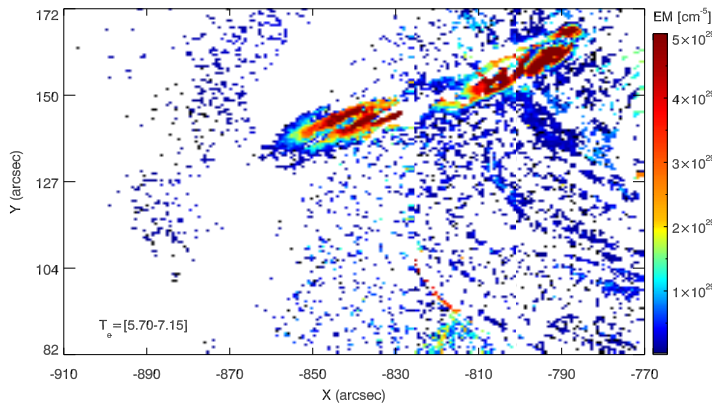


Figure i.3: Running-difference map of the emission measure recovered via the Hannah and Kontar [2012] regularized inversion. The emission is integrated across the $\log(T_e) = [5.70, 7.14]$ portraying a coronal jet eruption (13:08UT), associated to the AR11302 recurrent jet ‘geyser-like’ site. Multiple such sites were discovered in the literature, see table 2.1). Simultaneous ‘strand’ eruption components are observed along the jet’s body.

Hence it is possible that the total contribution by polar jets to the ‘larger picture’ is still being underestimated.

The jet contribution to the mass and heating flux of the high corona has been recently explored via numerical modeling. Török et al. [2016] and Lionello et al. [2016] performed numerical simulations of a large scale coronal grid, where the solar wind flux was implemented. The authors estimated the total contribution of simulated coronal jets to the mass and energy budgets of the solar wind to be less than 3% and 1.0%, respectively. Although the measurement uncertainties were found to be rather large, their results closely matched observations reported by Pucci et al. [2013], Paraschiv et al. [2015]. The authors hint that parametric analyses of coronal jet parameters are required in order to properly constrain these contributions. Most probably, such contributions will have only a momentary contribution to the solar wind flux due to scarcity, manifesting as microstream peaks in the outflow [Neugebauer, 2012]. Current knowledge suggests that flows driven along pseudo-streamer structures may be associated with the solar wind outflow, though there is still debate, and the detailed processes are still elusive [Cranmer et al., 2017].

New results by Sterling et al. [2015] suggest that the blowout scenario may be responsible for both previously classified event types and no fundamental physical difference exists. Chandra et al. [2015] and Li et al. [2015] qualitatively correlated different observations and decided in favor of the emerging flux model. The observational evidence presented by Sterling et al. [2015] and backed up by simulations [Lee et al., 2015] suggests that this scenario could be incorrect. Cheung et al. [2015b] analyzed 4 jets originating from a pore embedded in the interior of a supergranule to obtain data-driven simulations that show that the emergence of magnetic field structures in the vicinity of the pore supplies the magnetic twist needed for recurrent helical jet formation. This assumption is backed up by recent observational evidence; e.g. the magnetic moving features analysis performed by Chen et al. [2015] and lower atmosphere magnetic field configurations responsible for recurrent jet eruptions highlighted by Mulay et al. [2016]. Although the Sterling et al. [2015] jet emission model is observationally confirmed, it is currently premature to assume it as the standard jet emission mechanism [see Raouafi et al., 2016].

Active Region jets have only recently become a very active research topic due to the improvement in imaging and cadence of the available instrumentation. The magnetic topology associated with these events tends to usually be more complex, making AR jets hotter and larger when compared to polar jets [Moore et al., 2010, Sako et al., 2013]. Current day studies do not necessarily restrict possible ‘jets’ to the complete ‘traditional’ definition as the term became loosely interpreted. For the purpose of our study, we have framed our jet events in the traditional definition, emphasizing their presumed local microflaring footpoints and their escape into the inner heliosphere. Short time recurrent active region (AR) jet emission has been discussed in the past. Shimojo et al. [1996],

Shimojo and Shibata [2000] studied X-Ray jets originating in active regions, quiet sun, and coronal holes, finding that $\sim 68\%$ of the jets appear in or near active regions, also proposing an associations between coronal jets and micro or nano class flares.

Active region jets were first simulated in 3D by Moreno-Insertis et al. [2008] who introduced a sheared flux rope in a tilted magnetic field configuration. The system initially formed a current sheet, which in turn reconnected releasing jet-like emission. It is interesting that the emission reached temperatures in the range of $\log(T_e) \sim 7$. The magnetic topology revealed a spire configuration, similar to observations [e.g. Nisticò et al., 2009]. Thermal conduction effects were implemented in similar jet eruption scenaria by Fang et al. [2014], producing jets comprised of untwisting spires of mixed hot and cool plasma. These simulations were found to accurately match X-Ray observations.

Three dimensional simulations of a small active region field were performed by Archontis et al. [2010] framing the eruptions inside the emerging flux scenario. Simulated AR jets were found to take place in short successive recurrent phases. An important question arose; would such magnetic configurations evolve towards equilibrium? Further input was provided by Pariat et al. [2009, 2010] who found two distinct regimes of reconnection in simulations of penumbral AR jets: an impulsive 3D mode involving a helical rotating current sheet that generates the jet and a quasi-steady mode that occurs in a 2D-like current sheet located along the fan between the sheared spines, arguing that these different regimes can explain the observed link between jets and plumes. The reconnection is generated via impulsive energy release in the form of a kink instability, releasing a helical jet.

Analyzing jets originating in solar coronal holes, Moreno-Insertis and Galsgaard [2013] modeled a set of recurring jet ejections that resemble mini-CMEs suggesting that their physical properties may resemble blowout jets. The authors found that the eruptions were not in fact homologous, the first jets exhibiting signs of tether-cutting reconnection as observationally described by Moore et al. [2010] while the subsequent events appeared to be triggered by kink instabilities. Alternate similar results were reported by Archontis and Hood [2013] who managed to reproduce distinct standard versus blowout erupting topology, with the latter being similar to the Moreno-Insertis and Galsgaard [2013] determination. In a series of recent modeling works, Pariat et al. [2015, 2016] further constrained the driving processes that can generate straight or helical jets by means of a parametric study on the magnetic field configuration and plasma beta range. The modeling effort led the authors to propose a ‘breakout’ model of solar jet eruptions, involving an erupting unstable microfilament embedded in an open field. This model was proposed to be analogous to the Sterling et al. [2015] observational hypothesis.

With the continuous advances to higher resolution and faster timescales, the study of recurrence in jets gained momentum. The current generation SDO spacecraft, provides high spatial and temporal resolution and the ability to perform multiwavelength analysis of coronal jets. The SDO instruments gave us new answers pertaining to jet emission and excitation mechanisms. This research addresses ‘recurrence’ by discussing the flaring site (also known as the jet’s brightpoint or in more general terms as a flaring footpoint) that generates multiple jets. The homologous aspect of multiple recurrent jets is a consequence of the local conditions and the repeated nature of the reconnections in the flaring site. Current literature describes fast recurring jets, usually from one site during a very short period of time typically 2-6 hours. The behavior of such sites on longer timescales and detailed emission mechanisms still remain vastly unexplored. Using the Atmospheric Imaging Assembly [AIA; Lemen et al., 2012] and the Helioseismic and Magnetic Imager [HMI; Scherrer et al., 2012] data, Guo et al. [2013], Schmieder et al. [2013] discussed three

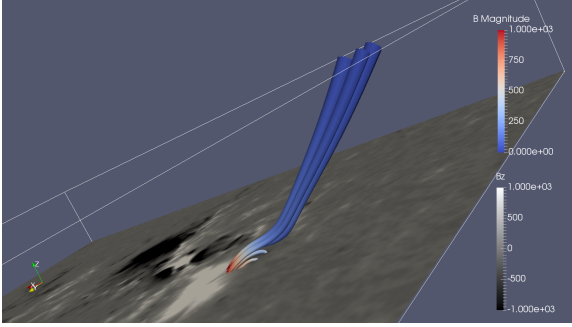


Figure i.4: Model of the coronal magnetic field extrapolated under the force-free potential field assumption (see eq. (4.7)). Base layer represents the vertical B_z component of the magnetic field, scaled in the $[-1000 \text{ G}, 1000 \text{ G}]$ interval and computed at 01:36UT on 25 September 2011. Two low lying loops are conspicuous under a penumbral canopy field of the active region, that is extending to the outer heliosphere.

fast recurring active region coronal jets aiming to understand their morphology, reporting twisting motions, and issues that may occur by comparing their observations with existent models.

Fast recurring jet observations were first discussed by Chifor et al. [2008a]. They found a correlation between recurring magnetic flux cancellation close to a pore and the X-Ray jet emission. The study associated chromospheric ribbon brightenings with jet eruptions. Nowadays this is treated as an implicit assumption [Testa et al., 2014]. The connection is not explained by a single scenario, and individual events should not be readily associated without careful consideration of alternative explanations. It is important to continuously address the elementary assumptions implied in treating complex (and usually non-linear) systems. To this extent Judge et al. [2017] emphasized that chromospheric ribbons can be disconnected from the corona showing that part of the Testa et al. [2014] studied events are indeed detached, and can be reasonably described employing a low altitude (chromospheric) flaring scenario. The discussion is elaborated in section 1.2.

Detailed SDO-AIA filtergram and Hinode [EIS; Young et al., 2007] spectroscopic properties of fast recurring AR jet sets are presented by Mulay et al. [2016, 2017a]. Detailed parameter estimations were presented and arguments in favor of flux cancellation were provided. The bulk outflow of erupting material has $T_e \sim 2 \cdot 10^6 \text{ K}$ and plasma number density has been estimated to be $n_e \sim 1 \cdot 10^{10} \text{ cm}^{-3}$. The energy input appears substantially higher when compared to polar jet estimations. The authors differentiated a secondary temperature peak, $T_e \sim 4 - 5 \cdot 10^6 \text{ K}$, and have attributed it to the flaring footpoint. Any emission measure estimation should be ‘taken with a grain of salt’, as inversion techniques represent (in a best case scenario) tolerable approximations, added on top of known assumptions which, in turn, may not hold true in some cases. Our case is not divergent. The main assumptions and problems arising when inverting solar observations are described in section 3.1.

Panesar et al. [2016] analyzed a set of very energetic (strong footpoint flaring) recurrent jets (alternatively labeled as homologous) that are tied to CMEs, offering an interesting comparison between the CME triggering jets and the non-CME events. All jets originated from the same base-arched structure, which the authors identified as a microfilament footpoint. In a series of papers, Sterling et al. [2016, 2017] analyzed sets of recurring AR jets and discussed potential trigger and emission mechanisms, concluding that magnetic flux cancellation should be considered as a fundamental process for AR jet production. On the other side, Sakaue et al. [2017, 2018] presented a case study where flux emergence plays a significant role in producing an AR jet. A spectral analysis of the hot and cool components corresponding to their analyzed jet is reported. This work favors the model where a magnetic flux cancellation scenario is the most probable mechanism, but does not agree with excluding alternate views. As previously mentioned, caution should be used when

addressing such issues, as the most probable particular explanation may not necessarily be the unique solution. Chapter 4 discusses the lower photospheric manifestations that may be responsible for triggering coronal jets.

In case studies of short timescale recurrent EUV and X-Ray jet eruptions, detectable microflaring activity at the jet footpoint was reported alongside co-temporal Type-III radio bursts [Kundu et al., 1995]. Solar radio bursts are classified based on radio dynamic spectra morphology and sometimes are associated with emission sources on the solar surface. One important characteristic is their drift rate. Type-III radio bursts are a subclass representing fast drifting enhancements in the radio dynamic spectra manifesting electron beams that escape towards the interplanetary medium. Krucker et al. [2011] suggested that non-thermal electron events are released by magnetic reconnection events between open and closed magnetic field lines in a spire (quasi-separatrix) configuration. Innes et al. [2011] showed that a small number of recurrent jets originating in an AR penumbra correlate well with detected Type-III radio bursts. This has been extended by Mulay et al. [2016], who claimed correlations of different AR jets with radio bursts. We stress that there the possibility of accidental overlapping of EUV and SWAVES [Bougeret et al., 2008] signals exist. McCauley et al. [2017] and Cairns et al. [2018] use state of the art observations and probed into the reconnection processes that generated both the coronal jets and the observed Type-III bursts. A comprehensive review on Type-III emission is presented in Reid and Ratcliffe [2014]. Currently, Type-III burst generation is linked to flaring (or microflaring) events in the lower corona [see Reid and Ratcliffe, 2014, chap. 2.5.2], and they are associated with either CME's or jets in a number of case studies [see Raouafi et al., 2016, chap. 7.1]. Aspects like a broader definitive correlation between coronal sources and Type-III bursts, SEP production from microflare sites, and jet vs. CME source type are still elusive and worthy of further discussion. Our efforts are presented in Chapter 2. We aim to push this discussion further, by proposing long lived, quasi-stable, EUV and X-Ray jet reconnection sites, labeled herein as coronal Geysers, as 'trustworthy' coronal sources for Type-III bursts.

Important questions are now waiting for answers: Are recurrent or homologous jets the result of a series of self-similar reconnection events involving a base arched structure (microfilament) subjected to energy storage and release mechanisms? Alternatively, are recurrent jets resulting from a 'chaotic' behavior of lower atmosphere features that via their interaction with a local twisted filament give rise to jet eruptions? What is the relation between the thermal and non-thermal processes arising from reconnection occurring in small scale erupting sites? Due to the vastness of topics, the observations, mathematical modeling, data, and instrumentation that are used will be described in each section. The observed coronal geyser structure is described subsequently. The Geyser characteristics are examined by means of timeseries analysis and correlated EUV and X-Ray energetic budget estimation is generated. Intrinsic limitations are considered. The lower atmosphere manifestations such as magnetic moving features analysis and magnetic field modeling are discussed. The nature of chromospheric reconnecting footpoints is debated. Due to the long timescale of our studied structure and high number of recurring jet eruptions we have assumed the presence of a quasi-stable base structure which we entitle as 'Coronal Geyser'. Geysers will be discussed extensively in ensuing chapters.

CHAPTER 1

On Small-scale Flare Ribbons, Recurrent Coronal Jets, and the AR11302 Geyser Structure

Foreword: We present observations of active region coronal jets. The generally expected and particular jet morphologies and characteristics are compared. Physical properties such as the lifetimes, scales, outflow speeds, torsional movements, and outflow orientation, are all estimated via dedicated data and image analysis techniques. An unexpectedly high number of recurring jet eruptions were traced back to one unique intermittent reconnection site, leading us to assume the presence of a quasi-stable base magnetic structure, named ‘Coronal Geyser’. A meticulous slit-jaw analysis revealed signs of substantial helical energy release along the jet spire. Jet emission models are discussed in the context of our observed emitting footpoint. Cooler plasma eruptions were detected in very close temporal proximity of the main jet eruptions. The physical nature of lower atmosphere flaring brightpoints or ribbon regions is examined and their universally presumed link to the corona is explored.

1.1 Morphology of Recurrent Active Region Jets

Coronal jets are small-scale solar phenomena that have been actively debated in the last few decades. These events have photospheric magnetic footpoint sites of size <20 Mm, are highly collimated outflows and are energetically at least one order of magnitude smaller when compared to standard B class flares. Jet ejecta have become more puzzling as new data revealed complex physical mechanisms. The simulations and theory first showcased idealized configurations, like small-scale Sweet-Parker [Sweet, 1958, Parker, 1957] or Petscheck [Petschek, 1964] models, that applied to an x-type reconnecting footpoint could perfectly match their current time observations both morphologically or energetically [e.g. Sheeley et al., 1975, Rust et al., 1977]. Theory focused on fast reconnection, such as suggested by Petschek, above the far slower Sweet-Parker case. Models such as these were so robust that even today, with some revisions, represent a good approximation provided they are properly utilized and constrained. Today’s jet eruption numerical experiments have evolved tremendously, where we envision complicated flux-rope filamentary structures that are embedded in uncombed magnetic field topologies [see Wyper et al., 2018, Moreno-Insertis and Galsgaard, 2013].

The advance in data analysis was also significant. Rust et al. [1977] used SKYLAB data to perform one of the first studies of X-Ray enhancements that are associated to $H\alpha$ surges. These phenomena will be named active region jets. Coronal jets are hypothesized to be CME-like manifestations that occur at small scales. The current jet assumptions involve helically tensioned microfilaments, that are subjected to destabilization mechanisms, releasing plasma ejections [Sterling et al., 2015, Moore et al., 2013, Raouafi et al., 2016].

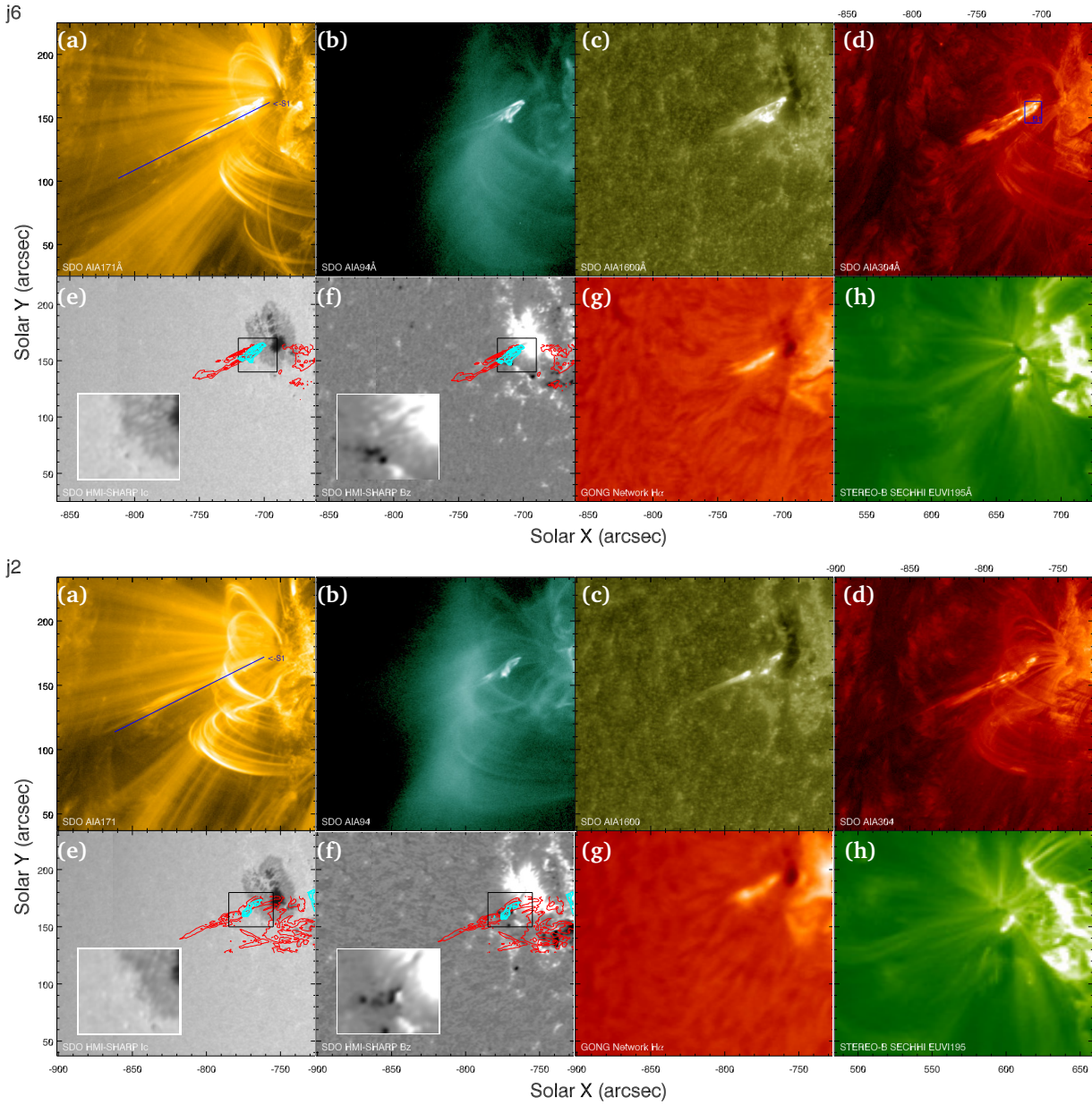


Figure 1.1: Coronal jets (*Upper panel: J6, 13:09UT 25.09.2011, Bottom panel: J2, 01:13:09UT 25.09.2011*) as revealed by multiple observations. The individual multiwavelength portrayals of all J1 to J10 jets are presented in appendix A. The figure sub-panels represent different correlated manifestations of jet activity: (a) SDO AIA-171Å ($T \sim 0.8 - 1$ MK) and timeseries tracked slit (S1) position; (b) AIA-94Å ($T \sim 5 - 8$ MK); (c) AIA-1600Å ($T \sim 0.4$ MK + continuum); (d) AIA-304Å ($T \sim 0.5$ MK) and timeseries tracked region (B1) position; (e) SDO HMI intensity continuum with added AIA-304Å (red) and AIA-94Å (blue) contours, (f) HMI SHARP (active region patch) vertical B_z magnetogram with added AIA-304Å (red) and AIA-94Å (blue) contours; (g) BBSO H α ; (h) STEREO-B EUVI-195Å ($T \sim 1 - 2$ MK) different viewpoint observation. Filtergram temperatures are provided here for comparison and are only approximate. A full DEM analysis is required in order to recover plasma physical temperatures. An emission measure estimation is available in chapter 3.

Coronal jets are identified with reconnection driven small-scale collimated eruptions directed towards the outer corona. Very few cases of material falling back after such eruptions are reported [Chandrasekhar et al., 2014]. It is commonly assumed that the ejected material is captured by the solar wind outflow and directed towards the interplanetary medium. Based on the described morphologies, two distinct jet categories arose. Intensively studied are the polar jets occurring inside large scale polar coronal holes. These events are mostly observed around the solar minimum activity period. On the other hand, active region jets are commonly located in boundaries of active regions and are naturally observed closer to the maximum of the solar cycle. As described in the introduction, AR jets are roughly a factor 3-6 larger than polar jets and more than one order of magnitude more energetic. Several topics regarding these eruptions are still being actively debated. A few morphological considerations are needed in order to advance active region jet understanding.

The active region AR11302 emerged from the east limb on September 23, 2011. The general solar activity was very high during the lifetime of the AR. It generated more than eighty C-class and M-class flares, also releasing two X-class flares. Most flaring events were accompanied by large scale CMEs, some of which were geoeffective. The region had initially a beta-gamma-delta complexity with three large sunspots, but it was already on the decaying phase when it emerged from the solar limb. The solar activity during 25 September 2011 was also monitored by other observatories and it is chosen as our preferred date of study. During this day the AR11302 has produced six M-class and two C-class large scale flares. The active region was positioned near the eastern solar limb, (X,Y)~(600,100) at 14:00UT. A small penumbral region situated in the south-eastern side of AR11302 drew our attention as it appeared to persistently emit coronal jets.

1.1.1 Multiwavelength analysis of Active Region Jets

Figure 1.1 shows AR jets multiwavelength observations in the coronal and chromospheric extreme ultraviolet (EUV) and ultraviolet (UV) channels of SDO-AIA along with SDO-HMI magnetograms. SDO-AIA provides full-disk solar images, observing the sun in 7 EUV, 2 UV, and 1 WL channels, with a spatial platescale resolution of $\sim 0''.6 \text{ pix}^{-1}$ and temporal cadence of 12 seconds. The SDO data was obtained using the JSOC pipeline¹ and processed to level 1.5 using custom implementations of the standard calibration procedures (e.g. coalignment, respiking, aia_prep corrections, exposure normalization etc.). All data was pre-processed using the Solarsoft (SSWIDL) package².

We have re-spiked all the SDO-AIA data in order to prepare for the spectroscopic interpretation discussed in chapter 3. The standard JSOC procedures for creating the primary data products automatically corrects for cosmic ray bombardment of SDO's detectors, as they tend to produce localized saturated signal in small clumps or individual pixels. This procedure is considered reliable when scales similar to the size of flares, etc. Re-spiking the data is a controversial procedure. By visual inspection, we noticed a smoothing of some very small scale ($< 4''$) flaring patches of SDO-AIA data. Since the small jet footpoints ($\sim 10''$) and other small scale flaring ribbons ($\sim 7'' - 8''$), like the event discussed in section 1.2, may be totally or partly affected, we chose to reintroduce the filtered out signal in the analyzed data.

The SDO-AIA sub-panels (fig. 1.1 a-d) present individual EUV jet multiwavelength

¹<http://jsoc.stanford.edu/ajax/exportdata.html>

²<http://www.lmsal.com/solarsoft/>

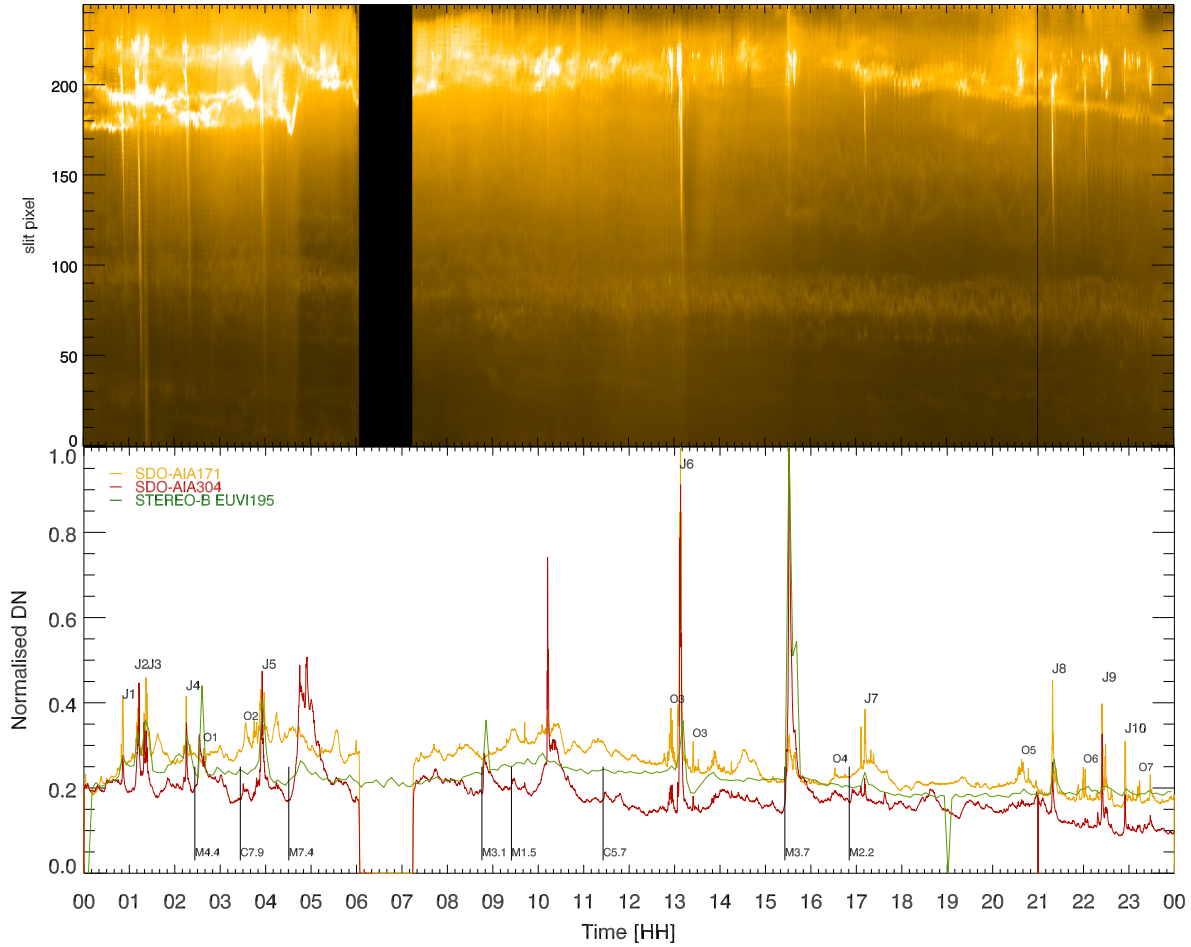


Figure 1.2: Geyser structure full-day region tracking: **Upper panel:** S1 slit (fig. 1.1 a) based tracking along the jet eruptions direction as applied to the AIA-171Å data. **Bottom panel:** The B1 (fig. 1.1 d) 13'' × 17'' region centered around the Geyser flaring footpoint (jet bright-point) using SDO's AIA-171Å, AIA-304Å, and STEREO-B EUVI-195Å filters. Two datagaps are present in the AIA series at 06:03-07:12 and 21:00-21:02, and in the STEREO-B series at 19:00-19:10. Individual jet events are labeled J1-J10 and other peculiar geyser flaring, that do not exhibit any distinguishable jet emission are labeled O1-O7. Major AR11302 flaring events that can potentially interact with the B1 integrating region are illustrated.

observational aspects. We have selected two events during their erupting phase in order to highlight their individuality. The multiwavelength plots corresponding to all jet events can be found in appendix A. Sub-panels a-d represent in order, AIA-171Å and AIA-94Å coronal filters along with the AIA-1600Å and AIA-304Å lower transition region and chromospheric filters. The filters cover a wide range of plasma that is seen to be emitting simultaneously. Clear morphological differences can be observed. The AIA-94Å shows consistent emission at the region of the jet footpoint, where almost no sign of the jet outflow material can be observed. The AIA-171Å and AIA-304Å filters, although sensible to different temperatures, complement the observations. The jet's ejecta are well identified, whilst the footpoint emission is weaker and less uniform. We used these two filters to derive the jet's outflow speed and morphological parameters (table 1.1). We note that the AIA instrument records the filtergram data in succession, thus a temporal difference between the 'simultaneous' AIA images exists, although it is smaller than 12 s.

When comparing the SDO-AIA images, it apparently appears that the jet ejecta are heated to a different temperature than their footpoints. One can readily approximate emitting temperatures to the SDO-AIA filtergrams based on the temperature of the main

filter emission line. Specifically the jet ejecta can be associated to temperatures of 0.4, 0.5, and 0.8 MK, while its footpoint appears in a hotter range, at $T_e > 5$ MK. Such an analysis would be erroneous. The SDO-AIA filter temporal responses are actually scattered across approximately two orders of magnitude and recovering emission from filtergrams is not straightforward. The AIA-94Å filtergram has a notably uncertain interpretation as the atomic data comprising the emission is not fully understood. More advanced techniques that will be described in section 3.2 are needed in order to assess this aspect.

The SDO-HMI SHARP data (described in section 4.1.1) help to reveal the lower atmosphere structures involved in jet production (fig. 1.1e-f). Contours of hot AIA-94Å (blue) and cool AIA-304Å (red) emission are over-plotted in order to further correlate the individual jet emission pinpointing the jets location. Magnetic field data are very important in context of assessing the jet's origin in the lower atmosphere. We can for the moment observe a correlation of the hot footpoints to a modest pore in the intensity white-light continuum (sub-panel e); a small-scale flux dipole, with a potential inversion line rooted at the edge of the sunspot's penumbra (sub-panel f). A careful interpretation of this data (see section 4.1.3) is required due to the small magnetic fluxes that are close to detection limits.

Most jets are correlated with Type-III radio burst emission detected by the STEREO-B radio instrument (chapter 2). Data from the EUVI-195Å imager aboard the STEREO-B observatory show (fig. 1.1h) a different vantage point of the jet emitting geyser structure. The jets seem to propagate along apparent open field lines heading to the high corona. Only footpoint flaring can be observed. The main bodies of the jets remained mostly undetectable in the EUVI-195Å emission due to projection effects combined with the lower $\sim 1''.1 \text{ pix}^{-1}$ spatial and ~ 5 min temporal resolutions. Additionally, AR11302 was outside the FOV of the second STEREO-A spacecraft, thus negating any possibility of multiple vantage point analysis for EUV data. The orbital positions of the three observatories (sketched in fig. 2.2) proved to be useful for our work. A correlation analysis that also includes inverse correlations is performed in context of radio data interpretation. See further on section 2.2.1.

The connection between 'jet-like' eruptions at different temperatures has been studied since the Skylab era. Rust et al. [1977] may have offered the first association between jets, in the form of 'X-Ray enhancements' and H α surges. H α emission occurs in a different temperature regime that is not directly correspondent to SDO-AIA EUV observations. We have utilized the synoptic ground based GONG network H α observations to investigate H α surges (fig. 1.1 g) that may be occurring in close temporal correlation with the EUV jets eruptions. Mulay et al. [2016] qualitatively correlated all their discussed events using ground based H α data, attributing their emission to chromospheric temperatures. We report similar results, where we identified correspondent lower atmosphere H α surges for all our identified jets. The two manifestations occurred co-temporally taking into account the 1 min temporal cadence of utilized GONG data. We could not find a longer eruption onset delay as hypothesized by Chae et al. [1999] for any intrinsic event. Such delay may be constrained by non-apparent factors. Also, We emphasize the fact that these surges are morphologically different from the UV and EUV eruptions.

It has been debated whether to consider these eruptions as a cooler component of the main eruption or as a separate eruption along adjacent fluxtubes. We advocate in favor of the second case. To our knowledge, this was first thoroughly discussed by Canfield et al. [1996] who interpreted spectroscopic observations of H α surges, proposing a model of adjacent eruptions based on correlated X-Ray and H α observations. Chae et al. [1999] pursued this idea hypothesizing that the two manifestations are different, but dynamically

intertwined. Both studies also discussed helical energies that may be stored and released in the form of reconnection jets. Jiang et al. [2007] discussed possible time delays between jet and surge onset, in the case of both magnetic flux emergence and cancellation scenarios.

A very interesting proposal came from the theoretical results. Nishizuka et al. [2008], Nóbrega-Siverio et al. [2016], and Moreno-Insertis and Galsgaard [2013] interpreted the cool eruption as possibly occurring due to a whip-like ouster of local chromospheric plasma due to the impulsive nature of the reconnection event. The authors also discussed alternative scenarios involving plasma asymmetries, arguing that better observation-simulation comparison is needed in order to form a better understanding.

Overall, cool and hot eruptions are found in both observations and numerical experiments. This suggests that cooler, possibly filamentary material, is widely implicated in jet eruptions. No spectroscopic H α data could be found for our observational interval hindering the possibility of quantitatively assessing the topic via H α approach. We detected untwisting motions along the main body of the jet eruptions. We recovered correspondent information via magnetic field analysis (chapter 4).

1.1.2 A Timeseries of Active Region Jets

Having reviewed the main observational features of two examples from the AR11302 coronal jet dataset, we focus now on portraying the recurrent and homologous behavior of these events. Firstly, by recurrent one understands that a set of events appear to be produced at the same location. In the case of jets this hints at a quasi stable structure that generates the eruptions. By homologous one understands that the recurrent jet events also appear to be geometrically self-similar. The available literature uses the terms interchangeably. This is to be understood as the two terminologies do merge in a significant number of cases. We stress that counter examples exist, including our present case. Our imaging revealed that significant differences appear between analyzing larger datasets with high resolution, see appendix A. This aspect was also constrained in the past by available instrumentation, as finer imaging has only recently become available. We can observe for example the difference between the fig. 1.1 panel a vs. panel d which theoretically record the same emission. The two EUV instruments launch dates are only spaced by four years! Due to historic and referencing reasons, we chose to use both recurrent and homologous across this present work in the hope of unifying the two terminologies.

Ten individual recurrent jets could be observed erupting from the same site. We point to the reader that the site emitted jets on previous and subsequent days. We chose the observing day due to the high output of events. The individual jets, J1 to J10, were detected by performing a tracking procedure, calculating a narrow, 1 pixel wide, ‘slit’ that is depicted in fig. 1.1 a. All SDO-AIA filters recovered at least in part all ten events. The slit was aligned parallel direction of the first jet eruption (J1) and also passes through the reconnection footpoint. Accounting for the solar rotation, we shifted the slit’s position for twenty four hours. The results are presented in fig. 1.2 (upper panel). All the subsequent jet events followed the same propagation direction, erupting along an apparent open magnetic flux and, at least at larger scales, appeared homologous to J1. These characteristics are similar to other sets recurrent events [Jiang et al., 2007, Chifor et al., 2008a].

We did not detect any jet events originating from the observed unique footpoint and guided along a different direction. The J1 to J8 events can be seen propagating along the length of the slit while the J9-10 events are modest, exhibiting short spatially constrained flaring and next to none jet emission. The average plane-of-sky velocity of the 10 jets is

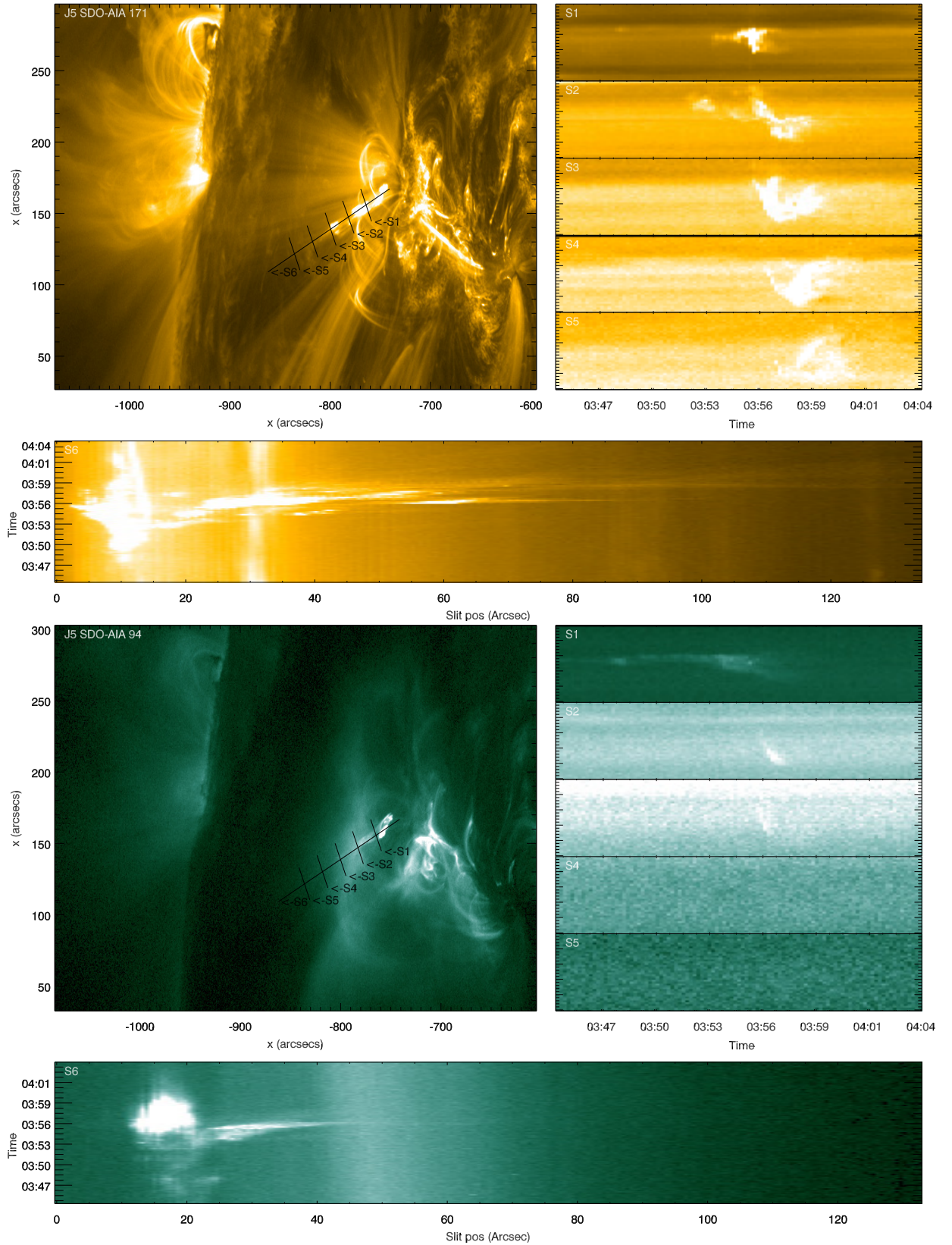


Figure 1.3: The Geyser coronal jet J5 eruption is interpreted via a slit-jaw method. A slit system comprising six slits was developed and utilized. A narrow parallel slit (S6) together with five, also narrow, perpendicular slits (S1 to S5) were calculated manually and fitted over the AIA-171Å (upper panel) and AIA-94Å (bottom panel) filtergrams (AIA-304Å in appendix B). The S6 slit is traced along the jet's axis and is stretched to depict both the jet's erupting outflow and the footpoint flaring. The S1-S5 evenly spaced slits are positioned perpendicular to the jet's outflow direction. The S1 slit is close to the geyser site, crossing over the lower flaring footpoint. All jets outflow speeds and eruption morphologies presented in table 1.1 were deduced from analyzing the plasma traversing the slit system. The individual slit based determinations of all J1 to J10 jets are presented in appendix B.

found to be $\sim 230 \text{ km s}^{-1}$. Once jet reconnection occurs, the magnetic field lines snap and untwisting motions act simultaneously with plasma flow. Most jets present a degree of untwist, depending upon the pre-erupting magnetic geometry of the twisted filament.

To our knowledge, other works that addressed recurrent jets did so mostly on small timescales and few events. We have labeled the structure as a coronal geyser due to its stability and quasi-periodical generation of jets. More information and features of this structure can be found in section 2.2. To test the uniqueness of the footpoint, the geyser site (flaring footpoint) was identified by performing a twenty four hour full cadence tracking procedure of the AIA-171Å and AIA-304Å emission on a $13'' \times 17''$ region represented by box B1 (fig. 1.1 b) that is centered around the geyser footpoint. The footpoint DN flux is presented in fig. 1.2 (bottom). We used a similar size integrating box on EUVI-195Å imager data to investigate the three-dimensional structure of jets and spatially correlate the geyser location. Though the temporal cadence is much lower (5 minute) cadence, we recovered the flaring correspondent to most SDO-AIA jets. Due to the separation in between the SDO and STEREO-B space crafts ($\sim 97^\circ$) the AR appears on the western side of the visible disk. Two features could be initially distinguished: A penumbral flaring loop similar to the SDO-AIA data and a pore-like footpoint rooted in the immediate southward direction, see fig. 1.1h and extended discussion in section 4.3.

In fig. 1.2 (bottom), we have also observed minor flaring activities labeled O1 to O7 that are originating from the geyser location. The flaring events can appear individually or in groups, but do not exhibit any visible signs of jet emission in any of the SDO-AIA EUV channels. Other noticeable spikes in the timeseries data could only be correlated to local heating, diffraction grating artifacts or local plasma downflows occurring in the B1 integration region (fig. 1.1 d) that resulted from large flares developing in AR11302.

1.1.3 Geyser Jets Morphological Parameters and Helical Motions

Following the idea of Schmieder et al. [2013], we have tried to reveal the complex behavior of the eruptions by extracting six ‘slits’ which were utilized to analyze the geyser’s ten detected jet eruptions. We have reused the initial narrow slit, now renamed to S6, as following the direction of all jet events and crossing all jets eruption bodies. The location was chosen as best to pass through the cylindrical center of all jet eruptions. Along S6, we have chosen five evenly paced slits, S1 to S5, that are perpendicular to the initial S6, and in turn to the jet eruptions. The S1 slit is chosen to cross one of the geyser’s footpoints while the S2 to S5 only cover the jets ejects. The whole system was tracked to account for solar rotation, with the exception of main jet eruption times. This was chosen in order to accurately recover the main scaling parameters of the ten eruptions.

The slit-based results corresponding to J5 are represented in fig. 1.3. The slit system position is portrayed, and the crossing of the J5 jet eruption in all six slits is presented in the case of AIA-171Å, AIA-304Å, and AIA-94Å. We immediately observe that the same eruption, in between the same observing times exhibits different morphologies in the three renditions. As discussed earlier, the three filters, in general are sensitive to different plasma emission. We observe a wider eruption from the cooler AIA-304Å viewpoint. Intriguing is the almost lack of any discernible emission as viewed from the AIA-94Å filter. Almost only localized brightening in the geyser footpoint was detected. A faint jet is seen erupting though it appears to dissipate very fast to non-detectable levels. The filter has response over a wide range of temperatures, but a lack of the main emission so clearly recorded by the AIA-171Å leads us to hypothesize that we may indeed witness high temperature emission.

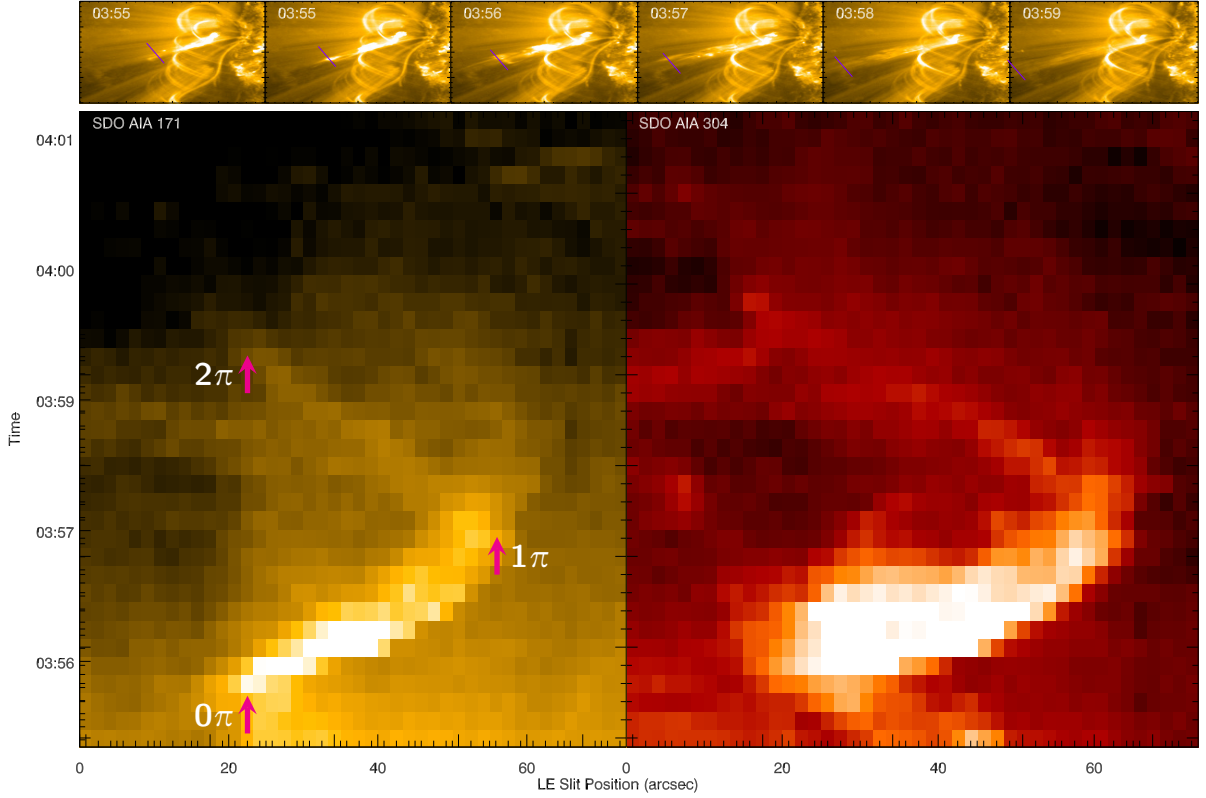


Figure 1.4: The geysers coronal jet J5 subjected to a slit based feature tracking procedure. **Upper Panel:** A perpendicular narrow slit is temporally tracking the movement of one of the jet’s leading edge strands. **Bottom Panel:** The selected strand propagation in time as revealed by the AIA-171Å and AIA-304Å filtergrams. A clear helical movement of $\sim 2\pi$ is observed before the jet dissipated in the fluxtube.

For now, we draw the reader’s attention to the flaring footpoint as seen from the S6 perspective at $\sim 20''$ on the slit position. Whereas the AIA-304Å and AIA-171Å microflaring emission starts well before the jet ejection is released, in the AIA-94Å filter, the stronger emission occurs only after the main jet is released. If we would not observe such clear eruption in the other filters, we might be led to conclude that maybe the site lost its connection to the overlying corona. We will show in section 1.2 that a chromospheric-coronal connection of small-scale loops is not a universal fact. The delayed AIA-94Å emission manifests across multiple events. The slit-based renders of all jet eruptions are found in appendix B We will explain this peculiar AIA-94Å behavior as a manifestation of a post-microflare chromospheric evaporation heating (section 3.4).

Using the slits timeseries (fig. 1.3), the lateral sizes of all eruptions were calculated using the perpendicular slits S1 to S5. The longitudinal size was estimated from both a transit time from S2-S5 but also from the extend in S6. These parameters are needed in order to recover volume information. We have utilized both the AIA-171Å and AIA-304Å filters due to the different scales recovered. A summary is presented in table 1.1.

The jet outflow speeds were determined. We assume that the jet ejecta are escaping along a direction close to being perpendicular to the line of sight. All ten jet outflow speeds were determined using three independent measurements, obtaining similar determinations. We have linearly fitted the profiles depicted in the S6 plots, have computed transit times for the S2 to S5 slits (where available), and linearly the difference in arrival time across the S2-S5 slits. Due to the high uncertainty ($\sim 10 - 20\%$) inherent to such measurements, we decided to record (table 1.1) the average across the different measurements of the outflow

Table 1.1: Basic morphological estimates of the observed geyser jets. Individual jet scale lengths and outflow propagation speeds are derived from the slit-jaw analysis of the SDO AIA-304Å and AIA-171Å filtergrams. The eruptions are assumed to be perpendicular to the line of sight. The length of the jets was estimated as the maximum outward extent of the jet spire during the eruptive phase. The estimated flow speed is projected along the line of sight, thus it is assumed to be an underestimate of the natural outflow speed. The n/a positions denote events for which the respective measurement could not be applied.

No.	Time [hh : mm UT]	AIA filter	Width [km]	Length [km]	Proj. Speed [km s ⁻¹]
J1	00:51 UT	171	4145	22314	251
		304	2997	21512	258
J2	01:13 UT	171	2532	66528	252
		304	2616	93600	195
J3	01:22 UT	171	3488	n/a	177
		304	3924	n/a	207
J4	02:17 UT	171	1625	25937	189
		304	2403	15920	183
J5	03:55 UT	171	2616	28700	251
		304	3052	28069	231
J6	13:09 UT	171	4890	66135	305
		304	4011	n/a	285
J7	17:11 UT	171	1744	17178	151
		304	1458	20160	168
J8	21:19 UT	171	1980	32504	323
		304	2668	40867	308
J9	22:25 UT	171	950	9735	177
		304	1308	12744	177
J10	22:55 UT	171	950	n/a	n/a
		304	1308	n/a	n/a

speed. The individual speed variations between the three measurement were $< 15\%$. We repeated the measurements for different filtergrams obtaining more than reasonable comparisons, with the exception of the J2 event where the AIA-171Å speed was significantly higher than the AIA-304Å, suggesting a possible decoupling between two bulks of plasma. These derived outflow speeds are generally consistent, where expected values are in the range of $100 - 600 \text{ km s}^{-1}$. See Paraschiv et al. [2010], Savcheva et al. [2007] for a general jet velocity distribution and Guo et al. [2013], Schmieder et al. [2013], Mulay et al. [2016] for corresponding results of active region jets.

A large fraction of our studied events were observed to exhibit helical untwisting motions as they propagate. This aspect can be observed in the fig. 1.3 S6 slit figure, where the individual jet strands are seen unraveling. Additionally, in the S2-S5 slits it can be observed that the eruption is seen propagating in an oscillatory manner, and not straight as we would expect. This is occurring due to the sideways drift followed by a direction reversal of the jet eruptions. We draw attention to fig. 1.4 (upper panel) where we combined our previous procedures and developed a slit that is traced perpendicular to a jet's (J5) leading edge following the deduced jet's outflow speed. We have managed to reasonably time-track the bright leading edge of the jet eruption in time. The timeseries slit is presented in fig. 1.4 (bottom panel) for both the AIA-171Å and AIA-304Å filtergrams. Before the jet dissipated, we clearly distinguished a 2π axial rotation.

The untwisting motions for the intrinsic geyser site were found to be in the range of $1.6 - 2.2\pi$. We consider these estimations as lower range values as we are limited by the observations. Using a feature tracking analysis, Chen et al. [2012] found jet untwisting movements in the order of $\sim 1.7\pi$. The theoretical efforts in understanding jet helical motions provided additional input into this still unresolved topic. Moore et al. [2013] analysed a larger sample of events and found untwisting motions of $< 2.5\pi$ with the bulk of events around $0.25 - 0.5\pi$. Untwisting jet models have been produced by multiple groups Pariat et al. [2009, 2010], Moreno-Insertis and Galsgaard [2013], Lee et al. [2015], etc. Main conclusions point to a helical energy storage, that subsequently develops into

a kink-like instability, which in turn is observed indirectly as a helical jet. The nature of untwisting motions can not be easily inferred via EUV filtergrams. An investigation of the underlying structures involved in the geyser's jet production is presented in section 4.2.

1.2 Flare Ribbon Corona Connectivity

We consider the observational basis for the belief that flare ribbons in the chromosphere result from energy transport from the overlying corona. We study ribbons of modest flares using magnetic as well as intensity data from the Hinode, SDO and IRIS missions. While most ribbons appear connected to the corona, we find one ribbon with no evidence for such a connection. Evolving horizontal magnetic fields suggest that reconnection with pre-existing fields can explain the data. We conclude that at least two mechanisms are responsible for the heating that leads to flare ribbon emission.

The purpose of the Judge et al. [2017] paper and collaboration was to test the hypothesis that flare ribbons are invariably linked with downward transport of energy released in the corona. In the standard [CSHKP; see Carmichael, 1964, Sturrock, 1966, Hirayama, 1974, Kopp and Pneuman, 1976, and the review by Shibata and Magara [2011]] model, energy propagates to lower atmospheric layers [Gold and Hoyle, 1960], eventually being dissipated. Brightpoints and flaring ribbons are observed. The standard flare model is backed up by a vast amount of observational evidence, and the connection between energetic electron precipitation and flare ribbons has become generally accepted Judge et al. [2015], Sadykov et al. [2016]. The review by Fletcher et al. [2011] described the morphological differences between HXR sources and flare ribbons, revealing a tendency for the first to be concentrated on the outer edges of UV flaring ribbons but co-spatial with H α brightpoints. Is the standard flare model universal? The relationship between beams of particles, and more generally, energy transport, from the corona to the flare ribbons is not fully understood and energy may be stored and released in regions other than the corona.

Testa et al. [2014, henceforth "T2014"] inferred the presence of non-thermal particles by combining data from IRIS[De Pontieu et al., 2014] with non-thermal beam model synthetic data. The synthetic data are required because an instrument like IRIS cannot by itself be used to infer non-thermal particles. T2014 interpreted Si IV Doppler signatures to discuss differences between beam transport and local energy conduction models. We note that the post-impulsive dynamics as reflected in Si IV as well as most UV emission is weakly linked to energy transport mechanisms. We decided to re-examine the data examined by T2014. For most of their ribbons, magnetic data (and 'moss' emission) support the idea that a coronal magnetic connection exists prior to the ribbon emission. However we also find a ribbon that is not obviously connected to the overlying corona, and that appears to be incompatible with the standard model.

This particular ribbon drew our attention first because it has no discernible 'moss' emission prior to the flare. This is illustrated in fig. 1.5 using data from the SDO-AIA instrument. Moss emission is one of the observational hints of coronal connections to the lower atmosphere. We show (section 1.2.1) that the ribbon is centered over a region where no longitudinal magnetic field structures exist. These properties single out this ribbon as being different from the rest in the study of T2014. The absence of moss is also observed in our fig. 1.5 AIA-1400Å panel and in the AIA-193Å panel from T2014, Fig. 1. The ribbon in question may be part of a subclass of flares. Both power law distributions [Nishizuka et al., 2009] and arguments concerning the universal nature of reconnection support the notion

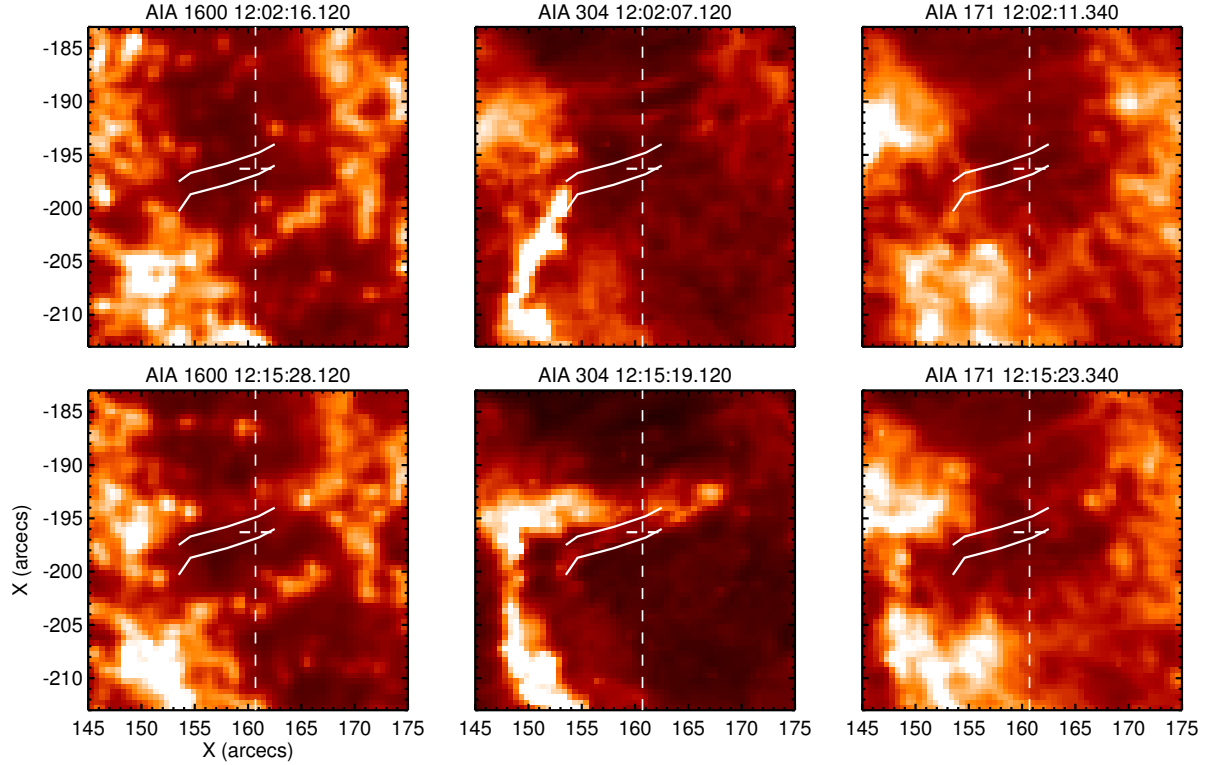


Figure 1.5: Intensity data from the SDO-AIA instrument on the SDO spacecraft are shown as a function of heliographic solar X and solar Y coordinates. The field of view spans part of active region 11890 on 2013 November 9th. The data highlight the chromospheric and coronal environment surrounding the flare ribbon under examination. Upper/lower panels show data prior to/during ribbon brightening, respectively. In SDO-AIA data, the ribbon is seen most clearly in the 304 Å band (predominantly He II), and marginally in the 1600 Å band (a mix of transition region lines and chromospheric continuum emission). Our study is originally prompted by the absence of ‘moss’ emission in AIA-171 Å overlying the ribbon, which is outlined by the two white lines. Typical moss emission is seen all around the ribbon in the bright patches of network plage emission, for example at $(X, Y) = (170, 190)$, associated with strong LOS magnetic fields. (see fig. 1.7).

that the physics might be independent of scale. See extended discussion in the [Introduction](#).

1.2.1 Interpreting EUV and Magnetic Data

We refer to T2014 for the circumstances of the IRIS and other observations of active region 11890 on 2013 November 9th. Figure 1.6 shows images from the IRIS and the SDO-AIA instruments close to peak emission of the ribbon of central interest located 252'' SW of Sun center. The azimuth (angle between the projected and local solar vertical direction) is $\vartheta = 15^\circ$ from the line-of sight, with $\mu = \cos \vartheta = 0.96$. We will refer to this ribbon as the ‘ribbon D’ following the annotations of T2014. During the IRIS observations the chromospheric ribbon brightened twice, of which only the first, weaker, event was discussed by T2014. Here we concentrate on the second brightening which is similar in morphology. The bright ribbon is clearly seen at its brightest phase (12:15:41 UT) in the lower left panel of fig. 1.6. This ribbon’s locus is traced in figs. 1.6 and 1.7 using black lines, while the T2014 event is traced with a white loci. This makes no difference to our conclusions because we examine the magnetic connectivity between the corona and ribbon prior to both brightenings.

The ribbon is not manifesting in the AIA-1600 Å UV bandpass, that samples the UV

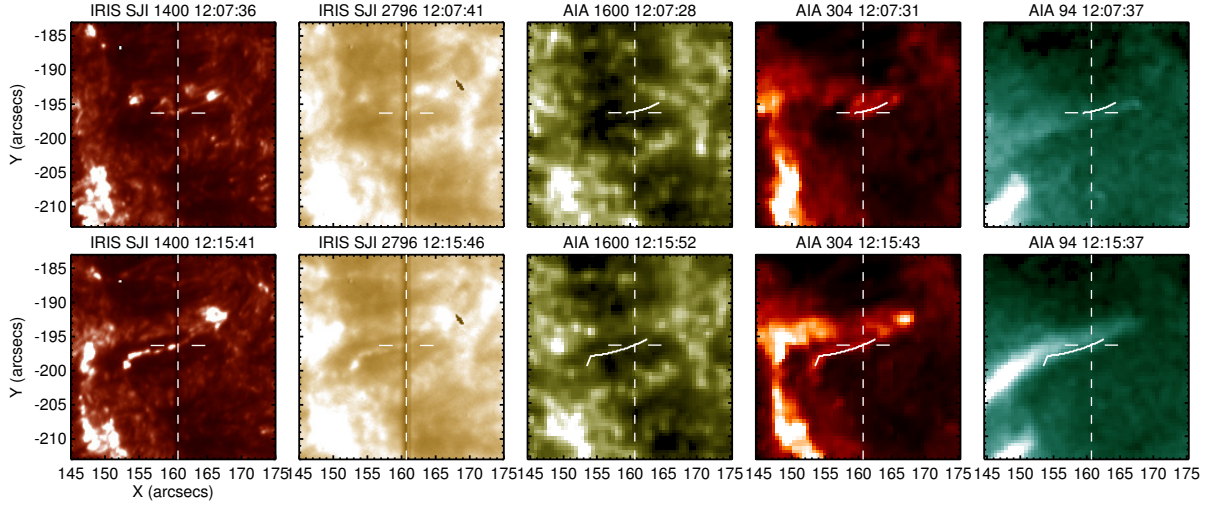


Figure 1.6: Intensity data are shown for active region 11890 on 2013 November 9th, corresponding to two modest flaring events associated to ribbon D. Upper panels show the weaker 12:07 flare ribbon analysed by Testa et al. [2014]. Lower panels show the stronger flaring peaking at 12:15. All panels have been co-aligned by eye to approximately $0''.3$. The solar coordinates are referred to the coordinate system specified in the headers. Only a $30'' \times 35''$ field of view is shown, to highlight the precise position of the flare ribbon traced in all panels except for the slit-jaw IRIS panels.

continuum emission along with a set of intense emission lines, e.g. C IV, He II (1640 \AA), etc. On the other side, the ribbon D manifests in the IRIS Mg II slit-jaw image (fig. 1.6) which can form anywhere across the entire chromosphere. The AIA-94Å appears superficially to overlap with the ribbon. However in movies S1 and S2 provided by T2014, the AIA-94Å emission clearly originates from closer to the larger 150 G UV flaring patch seen near $(X, Y) = (167, -192)$, and just accidentally overlaps the ribbon due to LOS effects. We have examined all other channels from the AIA instrument between 12:15 and 12:16 UT. The clearest indicator of the D ribbon seen is the AIA-304Å channel which samples mostly He II. Emission is not detected in the AIA-1700Å UV continuum channel, but during the ribbon's brightening there are hints of weak emission in all EUV coronal channels. Hence, the near-absence of AIA-1600 Å ribbon emission and its presence in lines from Mg II to He II roughly places that the ribbon D emission in the upper chromosphere or transition layers.

Figure 1.7 depicts the magnetic components obtained from raster scans with the Hinode spectro-polarimeter [SP Tsuneta et al., 2008]. We utilized data from the CSAC at HAO, and prepared using the MERLIN inversion code. The coordinates are all rotated to a reference frame close in time to the two ribbon flaring events obtained using HMI. Given the small size of the ribbons, we chose to base our further analysis on the Hinode raster scans due to the higher spatial resolution and magnetic sensitivity. The Hinode SP data have been carefully co-aligned to those of HMI to an accuracy of $\approx \pm 0''.3$. The results are peculiar! There is essentially just noise in the line-of-sight (longitudinal) component of the field B_L near the ribbon D. The Hinode data give a mean value of $11 \pm 10 \text{ G}$ for the longitudinal field calculated from areas extending $2''$ around the ribbon loci shown. The noise in longitudinal field acquired with the SP corresponds to just $3 \text{ Mx cm}^{-2} \cdot \text{pix}^{-1}$. The average Hinode tangential (near-horizontal) field component B_T is $73 \pm 24 \text{ G}$. If connections existed from ribbon D to AIA-94Å or other EUV filtergrams, there would be several such origins distributed along the ribbon D loci.

The raster scans from Hinode SP shown in fig. 1.7 were recorded about one hour before and six hours after the ribbon D emission. An intermediate scan was started but failed during the flaring period, containing no useful data. But from the data shown, three characteristics

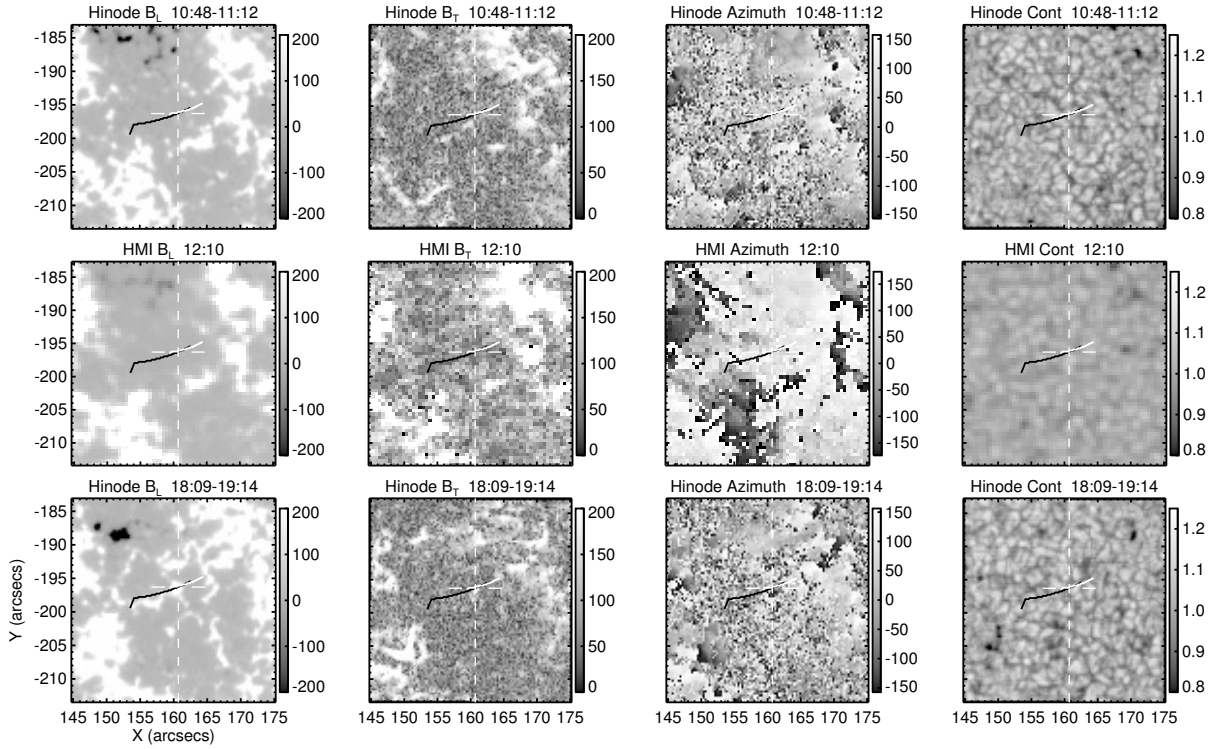


Figure 1.7: Magnetic data are shown for active region 11890, before, during, and after the two flares at 12:07 (ribbon extent traced with a white line) and 12:15 (black line) shown in fig. 1.6. Each row shows longitudinal, tangential fields, un-dissambiguated field azimuth, and the continuum intensity. The upper panels show the Hinode scan obtained before the flares, the middle panels show HMI data closest to the flaring events, and the lower panels show Hinode data from the next complete scan some six hours later. Six hours is a considerable fraction of the lifetimes of supergranules, so surface field evolution has occurred between the two Hinode scans.

caught our attention. Firstly, the 200 G horizontal flux seen near ribbon D before the flaring is replaced by 200 G vertical field components hours after the flare. Secondly, the azimuth of the field in the neighborhood of the ribbon before the flare has significant spatial coherence, with a mean value close to 44^{+31}_{-27} relative to the N-S direction. This aspect suggests, albeit weakly, the presence of an emerging magnetic field roughly along the same direction as the long axis of the ribbon. SDO-HMI unfortunately does not have the sensitivity to reveal these small-scale horizontal fields in the upper photosphere during this period.

1.2.2 Discussion

T2014 acknowledged chromospheric reconnection as an alternative scenario for their flaring ribbons but readily dismissed any discussion on the topic. Chromospheric reconnection could in principle provide an alternative explanation for the observed chromospheric and TR variability: “The moss brightenings clearly occur at conjugate footpoints of hot loops undergoing heating, and there is a clear correlation between the coronal and chromospheric/TR emission, naturally explained by beam heating.” The above statement seems contradicted by our finding from section 1.2.1 in the case of Ribbon D. We acknowledge that all other bright ribbons and kernels discussed in T2014 lie above or unresolvable close to regions with discernible vertical fields. The absence of a longitudinal field above about 10 G in the photosphere near Ribbon D suggests that there is little or no magnetic flux emerging through this region into the corona.

The ribbon D pre-flare magnetic field

Small flaring ribbons do not generate detectable changes outside the immediate proximity of the loci. The chromospheric magnetic field is significantly different than the photospheric footpoint. Assuming the detected low strength photospheric fields, difficulties appear when tracing the origin of chromospheric fields. The entire stratified chromosphere spans about 1500 km, which corresponds to $\approx 2''$. In fig. 1.7 the ribbon is surrounded by no fields with values < 10 G extending at least $2''$ all around the ribbon.

The presence of any longitudinal (vertical) field would prove a coronal connection along the ribbon. The Hinode panel B_L in the top left of fig. 1.7 shows 30–40 G fields are rooted to the south of both ends of Ribbon D, extending along few square arcseconds. These fields are not visible in HMI by the time of the flare, 1 h 22 m later (second row, fig. 1.7). These small concentrations are some $5''$ from the center of Ribbon D. Could longitudinal fields been moved in the time-gap to the location of Ribbon D by photospheric surface motions? Berger et al. [1998] calculated a coefficient of $\kappa \approx 80 \text{ km}^2 \text{ s}^{-1}$ for surface diffusion rates around active regions, corresponding to a timeframe of tens of minutes of observations. In our $t \sim 100$ time-gap, elements would diffuse a distance $\frac{1}{3}\sqrt{\kappa t} = \frac{1}{3}\sqrt{80 \times 6000} \approx 200 \text{ km } 0.3''$ using this coefficient. Supergranular diffusion in regions far from strong fields is larger, with $\kappa < 800 \text{ km}^2 \text{ s}^{-1}$. This case is presumed improbable given the uncertainties and stochastic assumptions provided by Berger et al. [1998]. Even with such a high rate of diffusion, the surface diffusion would have to accumulate from within a distance of $\sim 1''$ of the Ribbon D.

The Ribbon D post-flare magnetic field

In the six hours between the flare and the second Hinode scan) relatively strong post-flare longitudinal network fields appear in the lowest panel of fig. 1.7. It is seen meandering underneath the position of Ribbon D, with a length $\ell \approx 10''$. Either emergence and/or surface diffusion of field must be responsible for this new network flux. The new network flux amounts to $\Phi \approx 200$ G times the apparent area of the network, $\approx 1'' \times \ell'' \equiv 5 \times 10^{16} \text{ cm}^2$, so that $\Phi \approx 10^{19} \text{ Mx}$. To build this flux from the mean pre-ribbon longitudinal field strength of 10 G, this flux would have to have collected, merged and strengthened from an area of about 200 square arcseconds, about 100 Mm^2 . This area is far larger than the area available for diffusion in the time available, which we write as $L\ell \approx \frac{1}{3}\kappa 21600 \approx 6 \text{ Mm}^2$, even using $\kappa \approx 800 \text{ km}^2 \text{ s}^{-1}$.

It seems that some flux emergence into the chromosphere occurred between the first and second Hinode scans. Such flux emergence is below the detection limit for HMI (row 2, column 2 of fig. 1.7) but is hinted at by the coherent horizontal field seen in the first Hinode scan (row 1, column 2 of fig. 1.7). We suggest that this flux emergence might help explain the presence of Ribbon D, in particular the horizontal fields that appear somewhat close to the ribbon in the pre-ribbon Hinode scan strongly indicate horizontal flux. Any horizontal fields are too noisy to be seen as any coherent structure rising through the photosphere. Beginning close to 18:00 UT, the longitudinal field patch close to (-165,-201) migrated quickly towards the position of the clump of flux seen underlying Ribbon D in the last Hinode (18:09-19:14 UT) scan.

Even if we cannot conclusively detect horizontal emerging flux, we can conclude that the magnetic conditions around Ribbon D are qualitatively different to the other ribbons discussed by T2014.

Coronal Energy requirements

Can a coronal origin for our ribbon be ruled out? Let us consider the energy requirements, for this we can use figure 3 of T2014. From this figure we see that the Mg II k line has excess emission averaging 400 DN/second/spatial pixel for a period of 200 seconds. Using calibration factors SolarSoft routine `iris_get_response.pro`, we find the intensity of Mg II k is $I_k = 1.5 \times 10^5 \text{ erg cm}^{-2} \text{ s}^{-1}$. The k line contributes $\approx 10\%$ of the total chromospheric radiative losses known in 1981 [Table 29 of Vernazza et al., 1981], and allowing for a doubling of the losses due to the inclusion of Fe II lines, we find that the excess emission is $\approx 20 \times 4\pi I_k \approx 4 \times 10^7 \text{ erg cm}^{-2} \text{ s}^{-1}$. The same calculation for the Si IV 1403 Å line gives an excess intensity of $6 \times 10^3 \text{ erg cm}^{-2} \text{ s}^{-1}$, 25 times smaller than seen in the k line.

We assume that we have a field strength of 10 G, corresponding to the 3σ upper limit, emerging from the region of Ribbon D into the corona. (Below we relax this assumption). The total energy per unit area in a straight tube of length L is $LB^2/8\pi$, which for $L \approx 10^{10} \text{ cm}$ (100 Mm, as used by T2014) and $B < 10 \text{ G}$ gives $< 4 \times 10^{10} \text{ erg cm}^{-2}$. The AIA-304Å frame in movie ‘S2’ of T2014 shows that the heating of Ribbon D continues beyond the time span of the IRIS sequence which ends at 12:17:16UT. Thus we can set a time $> 10^2$ seconds for the duration of the heating. Therefore the overlying corona can supply $< 4 \times 10^8 \text{ erg cm}^{-2} \text{ s}^{-1}$ of magnetic power per unit area into the chromosphere below. If, optimistically, we assume that 10% of the magnetic energy along this tube is free energy available, then just $< 4 \times 10^7 \text{ erg cm}^{-2} \text{ s}^{-1}$ is available. This is close to the energy requirements of the quiet Sun chromosphere [Anderson and Athay, 1989] and our excess estimate above. An alternative limit can be derived using the Alfvén crossing time for the tube is L/V_A . With a pre-flare coronal gas pressure $p \approx 0.1 \text{ dyne cm}^{-2}$, $T = 10^6 \text{ K}$, we have a density $\rho \approx 2 \times 10^{-15} \text{ g cm}^{-3}$ and $V_A < 700 \text{ km} \cdot \text{s}^{-1}$. Then $L/V_A > 140 \text{ km s}^{-1}$.

The energy available in a coronal tube is formally enough to account for the radiation losses from the chromosphere below. But our estimate is a strict upper limit because: 1. We have used the 3σ “detection” of longitudinal field from the Hinode scan 1 hour before the flare, the energy is $\propto B_L^2$. The field strength in the overlying corona is surely lower than the 10 G upper limit in the photosphere; 2. The energy is $\propto L$, and L has been taken from neighboring coronal structures seen clearly in the AIA-94Å channel that are rooted in far stronger concentrations; 3. We have assumed that 10% of all the magnetic energy is available for release within the tube, and 4. We have assumed that sufficient time exists for this energy to be released. Reconnection typically takes place at $0.1V_A$, through complex dynamical mechanisms such as the plasmoid instability [e.g. Bhattacharjee et al., 2009]. Thus the dynamical time for energy release becomes too long $L/0.1V_A \approx 1400 \text{ s}$.

It appears that Ribbon D cannot be reconciled by heating from the above corona. Either the dynamical time is too long ($L = 100 \text{ Mm}$) or, if L is small enough to account for the dynamical time, then the free energy $\propto L$ is insufficient to account for the observed losses.

Now let us permit the coronal connection to include the transverse component of the field as well as the longitudinal component. Then we expect the connection to the corona to be highly oblique to the line of sight, as is seen in the AIA-94Å image (fig. 1.6). In this case, the observations are reconciled with a beam heating picture: the energy release rate from the corona is $< 2 \times 10^9 \text{ erg cm}^{-2} \text{ s}^{-1}$ and the dynamical time is about 200 s, compared with about $2 \times 10^7 \text{ erg cm}^{-2} \text{ s}^{-1}$ and 100 s respectively. The energy available is approximately fifty times bigger, and the Alfvén speeds seven times larger. But is this scenario credible? The morphology of the horizontal field and the absence of moss coronal emission simply does not support the idea that the fields detected are connected to the corona.

Local heating

We are forced to consider *local* sources of heating for Ribbon D. The tangential field in the Hinode scan is around 75 G. Let us consider the emergence of a near-horizontal tube of flux through the chromosphere in a quasi-steady state prior to some energy release process. It emerges into pre-existing field in the upper chromosphere in the active region where a pre-existing canopy field exists, fields rooted elsewhere in stronger concentrations which have turned horizontal to ensure pressure balance as the chromospheric gas pressure drops well below the magnetic pressure. The total energy density available in an emerging tube with this field strength is $B_T^2/8\pi \approx 220 \text{ erg cm}^{-3}$. The Alfvén speed is roughly $B_T/\sqrt{4\pi\rho_u} \approx 200 \text{ km s}^{-1}$ where $\rho_u \approx 10^{-12} \text{ g cm}^{-3}$ is the density in the upper chromosphere. Let us assume that the tube emerges into canopy fields, rooted in more distant network patches, of a lower strength. To estimate the strength we note that in the neighborhood of the ribbon the longitudinal flux is all of the same sign, average longitudinal flux density over a region centered at the ribbon is about $55 - 80 \text{ Mx cm}^{-2}$, depending on the local area chosen. For the surrounding $20'' \times 20''$ area (of order one supergranule in size) the average is 80 Mx cm^{-2} . We envisage that the locally emerging flux begins to reconnect with the canopy field and generate the extra emission in Ribbon D. To account for the ribbon, we require, as above, $4 \times 10^7 \text{ erg cm}^{-2} \text{ s}^{-1}$ for about 200 seconds. Once the reconnection starts, it will proceed at a rate close to $0.1V'_A$, where V'_A is the Alfvén speed in the reconnecting component of the field [Bhattacharjee et al., 2009, Comisso and Bhattacharjee, 2016]. If the angle between the emerging tube and the canopy fields is ϑ , then $V'_A = V_A \sin \vartheta$. Thus the reconnection will convert magnetic into thermal energy at the rate

$$F < 0.1 \sin^3 \vartheta \frac{B_T}{\sqrt{4\pi\rho_u}} \frac{B_T^2}{8\pi} < 5 \times 10^7 \quad [\text{erg cm}^{-2} \text{ s}^{-1}], \quad (1.1)$$

where we have used $\sin \vartheta = 0.5$ as a rough estimate of the mismatch in directions of the horizontal and canopy fields. It seems that there is power available from chromospheric reconnection to drive the radiation losses seen in ribbon D. With a (vertical) inflow speed into the reconnection layer of $0.1 \sin \vartheta V_A \approx 25 \text{ km s}^{-1}$, lasting for ≈ 200 seconds, the reconnection advects a total mass per unit area of $m_R = 2.5 \times 10^6 \times 200 \rho_u = 5 \times 10^{-4} \text{ g cm}^{-2}$ from the chromosphere into the reconnection layer. If this partially ionized plasma is heated via dynamical instabilities (e.g., the plasmoid instability, [Bhattacharjee et al., 2009]) or kinetic processes (ion-neutral collisions, for instance), then this emerging flux effectively leads to heating in the upper chromosphere for column masses above $m_R = 5 \times 10^{-4} \text{ g cm}^{-2}$. Interestingly, this corresponds roughly to the range of heights between which the proposed beam dissipation arises in the models of T2014 (Fig. S4). Therefore, we would expect similar dynamical signatures from this type of heating as beam heating when the reconnected field has access to the overlying corona.

Ribbon D chromospheric reconnection?

One might argue that the chromosphere remains “closed” not open to the overlying corona, and therefore that lines formed are trapped in closed field lines under a low- β regime in which significant line shifts observed in Si IV cannot be observed. However, in this picture we envisage plasma mass advected into the canopy fields which are themselves open to the overlying corona, a process commonly called “interchange reconnection”. In this scenario, dynamics is expected along the canopy field lines resulting from deposition of

energy in plasma of similar column masses, analogous to the beam heating scenario. This ambiguity reminds us that lines such as Si IV are susceptible to significant effects resulting from either or both the corona and chromosphere. Also, it must be remembered that Si IV intensities are a factor of 25 weaker than the Mg II lines. Thus, these lines reflect only a small fraction of the energy release and its properties in the evolving atmosphere.

A common reason for discounting chromospheric reconnection is that the ribbons “light up” between observations separated by tens of seconds, and that there is nothing that can communicate one part of the chromosphere to reconnect on these time scales. But this is not correct near active regions with transverse fields of order 70 G. Ribbon D has a horizontal extend of about 7 Mm (fig. 1.6), so it would take just 14 seconds for magnetic perturbations, such as a tearing mode, to propagate horizontally across the surface. Further, an emerging flux rope defines a ribbon-line morphology as it interacts with the overlying fields. Therefore we respectfully disagree with the dismissal of chromospheric reconnection discussed in section S3 of T2014, in the case of Ribbon D.

Finally, a widely held belief that the chromosphere is highly dynamic has arisen from studies seeking dynamical phenomena associated with the chromosphere [e.g. De Pontieu et al., 2007]. The question would then arise if the upper chromosphere would shred a rope of horizontal flux before it could interact with pre-existing fibrils extending across supergranular cells. But this is a non-issue since simple estimates of such things as spicules and related phenomena show them to cover no more than 0.1% of the solar surface area, and to originate at supergranular vertices. Spectral observations of the solar disk with HRTS by Dere et al. [1983] show both line-widths and shifts very rarely approach those of the dynamic type II spicules reported by de Pontieu and colleagues. It is also clear from narrow-band imaging observations of spectral lines formed in the upper chromosphere, such as the Ca II infrared triplet lines, that fibril structures are stable on time scales of hours or more [e.g. Cauzzi et al., 2008].

1.2.3 Conclusions

Evidence that one of the low-energy flare ribbons analyzed by T2014 is most probably magnetically disconnected from the corona is provided. Calculations show that sufficient energy exists in the emerging magnetic field for local dissipation in the upper chromosphere to account for the observed behavior. Our analysis therefore refutes the T2014 conclusion: “Our analysis provides tight constraints on the properties of such electron beams and new diagnostics for their presence in the non-flaring corona.” The interpretation of data from spectrograph instruments like IRIS is non-unique. The recorded spectra represent the result of a set of non-linear effects including the elusive heating terms in the energy transport function, recognized as the coronal heating problem discussed in the **Introduction**. Concluding, two mechanisms that can produce modest flaring ribbons, one of them is based on energy transport from the overlying corona, as T2014 showed, while the other assumes local energy storage. Observationally, the lack of vertical magnetic fields (decoupling) during ribbon D’s flaring led to the conclusion that a beam scenario is not applicable in this particular case. The other ribbons discussed by T2014 did not appear clearly decoupled from the corona and this hypothesis can not be applied for those events. We remind the reader that these ribbons act on a very different energy scale when compared with large flares. To our knowledge, evidence for coronal disconnection in the case of standard flares has not been found. A generalization of this scenario would be premature.

CHAPTER 2

Coronal Geyser Structures as Sources of Electron Beams and Interplanetary Type-III Radio Bursts

Foreword: The link between the active region thermal EUV jets and non-thermal solar phenomena is debated. The AR11302 jet eruptions produce significant perturbations on the ambient solar atmosphere. We emphasize the non-thermal electron beams that produce Type-III radio bursts which are presumed to originate via magnetic reconnection. The coronal sources of Type-III radio bursts remain unresolved, although flaring sites of varied scales have been proposed. Individual Type-III radio bursts have been observationally associated with jet eruptions. We report that upwards-propagating electron beams and signs of downwards-propagating beams are generated by the geyser reconnection events. Our Geyser site, along with five additional datasets from literature are carefully correlated temporal-wise with interplanetary Type-III radio bursts detected by the STEREO-SWAVES and WIND-WAVES instruments. We propose the six identified coronal geysers as potential coronal sources for Type-III radio bursts and implicitly upwards accelerated electron beams. The consequences and implications are debated within.

2.1 Observations, Datasets, and Instrumentation

AR11302 was the source of a variety of eruptive events: X-class and M-class flaring, complex CME eruptions, small-scale events, etc. By small-scale we understand eruptions and flaring footpoints which are roughly at least one order of magnitude smaller in scale and power when compared to the standard ($>B$ class) eruptive coronal manifestations. A typical microflare event dissipates energies in the order of $\leq 10^{-5}$ erg cm $^{-2}$ s $^{-1}$, as observed in 1-8Å X-Ray flux measurements. Section 1.1 briefly described the active region in terms of its eruptive manifestations. The AR11302 main standard and small-scale flaring events are portrayed in fig. 1.2.

Multiwavelength observations in the coronal EUV channels from SDO [Pesnell et al., 2012] are used. The SDO-AIA imager [Lemen et al., 2012] provides the highest resolution full-disk solar images, observing the sun in ten UV and EUV channels, with a spatial platescale resolution of $\sim 0.6'' \cdot \text{pix}^{-1}$ and a temporal cadence of 12 s. The data were processed using the Solarsoft (SSWIDL) package. The raw data were extracted via the JSOC pipeline and processed to level 1.5 using the standard calibration procedure (e.g. co-alignment, respiking, aia_prep corrections, etc.).

The jet activity is linked to the host active region [private communication; Donea and Cairns, 2013]. A case study of jet generated Type-III radio bursts was presented by Cairns et al. [2018] using high quality ground-based radio observations. The authors studied radio manifestations of ‘jet’ activity in between 01:11UT and 01:24UT. These events are

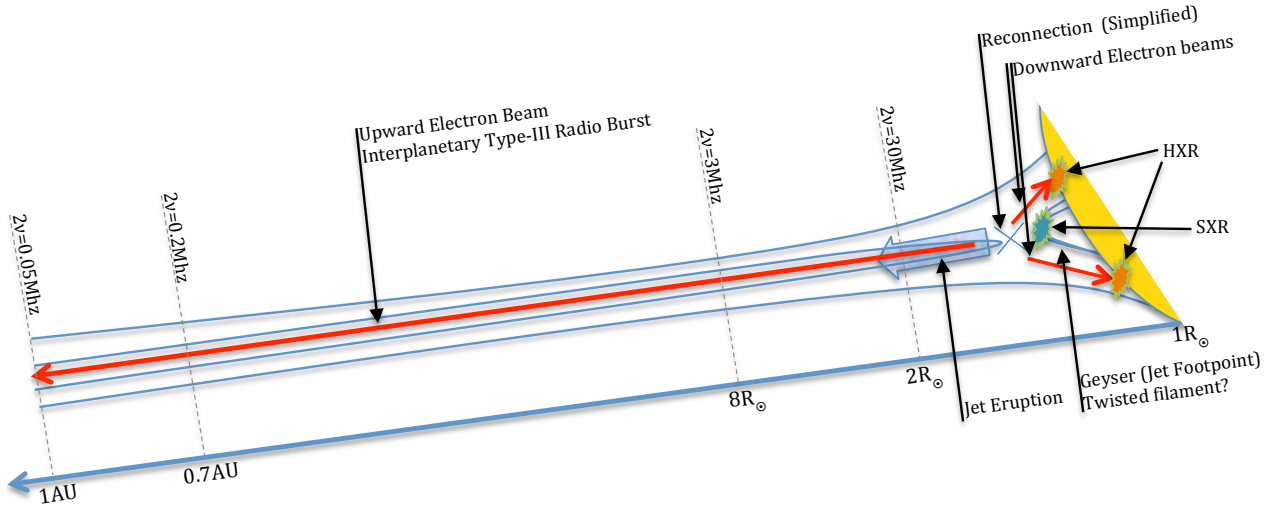


Figure 2.1: Schematic illustration of observational jet eruption features along with the associated upwards and downwards electron beams. The upwards beam propagation into the heliosphere is characterized using the observational properties of generated Type-III radio bursts. The cartoon is consistent with the widely accepted flare scenario based on magnetic reconnection, referred to as the CSHKP[Carmichael, 1964, Sturrock, 1966, Hirayama, 1974, Kopp and Pneuman, 1976] standard flare model that now also includes potential particle acceleration mechanisms [see review; Shibata and Magara, 2011].

also covered by our analysis. We have disentangled the flaring episodes, and separated two distinct jets, labeled as J2 and J3 in our EUV recurrent jet list. Our ten geyser EUV jets were detected using timeseries tracking of the geyser footpoint (see section 1.1.2). The unique jet footpoint is located at the south-eastern periphery of AR11302. EUV Jet events associated with the same footpoint were detected in multiple days during the AR11302's visible lifetime. We limited our observations to a time span of 24 hours, selecting the date of 25.09.2011, as this day was most prolific in generating jets. More than ten distinct coronal jet events were observed. Additionally, a few microflares were observed as non-erupting coronal Bright Points (BP) without displaying distinguishable signs of EUV jet eruptions.

Images from the EUVI-195Å instrument [Wuelser et al., 2004] aboard STEREO-B [Kaiser et al., 2008] observatory show a different vantage point of the jets, compared to SDO-AIA (appendix A e.g. panels a vs. d). The EUVI-195Å viewpoint suggests that the eruptions may be propagating along apparent open field lines toward the high corona. The STEREO-B EUVI-195Å observed only the flaring of the jets footpoint (geyser). The main outflow jet emissions remained hardly detectable due to projection effects combined with the lower sensitivity, spatial ($1.1'' \text{ pix}^{-1}$) and temporal (300 s) resolution of EUVI-195Å. Additionally, AR11302 was outside the FOV of the STEREO-A spacecraft, thus negating the possibility of additional vantage point analysis.

The WIND [WAVES; Bougeret et al., 1995] and STEREO [SWAVES; Bougeret et al., 2008] radio data were used to investigate the relationship between the interplanetary Type-III radio bursts and the jet geyser eruptions. Our focus, the solar upward propagating Type-III radio bursts, are also ubiquitous events present in synoptic radio dynamic spectra (fig. 2.2). They represent observational signatures of coherent electron beams that stream through 'open' magnetic fields in the high solar corona and inner heliosphere ([see reviews; Reid and Ratcliffe, 2014, Shibata and Magara, 2011, and references therein]. A schematic of the processes is presented in fig. 2.1. The electron beams become bump-on-tail unstable [Sarkar et al., 2015] and interact with the local plasma via a set of non-linear processes

as they pass through the medium. As a result, plasma oscillations at the local plasma frequency and its harmonics are generated. The oscillations are sensitive to the plasma density (eq. (2.1)) and manifest observationally as radio bursts.

$$\nu_{pe} = \sqrt{\frac{e^2 \cdot n_e}{\pi \cdot m_e}} = 8978.47 \cdot \sqrt{n_e}, \quad \text{for } n_e \text{ in units of cm}^{-3}. \quad (2.1)$$

The upward Type-III bursts are an observational subclass of low frequency radio emission. They are characterized by a fast frequency drift in the radio spectra maps occurring due to the mildly relativistic propagation speed ($\beta = v/c \sim 0.1 - 0.3$) of the indirectly-recognized electron beams. See Reid and Ratcliffe [2014] review for a detailed description of the topic.

Assuming a coronal and inner heliospheric density distribution one can theoretically reproduce the travel of upwards electron beams propagating into the corona that are detected as Type-III radio bursts. For this, we use a starting $\nu_{pe} \approx 300 - 500$ MHz (chromosphere) and an end $\nu_{pe} \approx 0.02 - 0.2$ MHz (1AU) frequencies of the generated bursts. In practice, such a determination is limited by the observing constraints. The STEREO and WIND instruments cover a frequency range from 16 MHz to 0.01 MHz and have a temporal cadence of 60 s. In fig. 2.3 the radio timeseries were interpolated in order to reproduce the SDO-AIA temporal cadence, but discussed uncertainties remain set to 1 datapoint per minute.

We describe the small-scale jet eruptions using the [CSHKP; see Carmichael, 1964, Sturrock, 1966, Hirayama, 1974, Kopp and Pneuman, 1976] standard flare frameset with included particle acceleration mechanisms [see review; Shibata and Magara, 2011]. We chose to understand that particle acceleration mechanisms are a product of the magnetic reconnection processes. Shibata and Magara [2011] predicts also the existence of downwards beams. They stream towards the flare footpoints along the newly reconnected field lines. In the present case, the hard X-Ray emission observed during footpoint flaring events is a clear evidence of the existence of high energy tails which are consistent beams. The most accepted model for X-Ray emission is the thick-target bremsstrahlung. This is extensively discussed in section 3.4. The Figure 2.1 sketch shows a generalized schematic view of a small-scale reconnection-driven jet. The observational features are emphasized under the assumption that the magnetic reconnection is involved generating unstable electron beams. This may not always be the case.

2.2 Coronal Geysers and Type-III Bursts

The geyser site, (labelled G1) was identified by performing a 24 hour full cadence tracking procedure, applied to the AIA-171Å and AIA-304Å data. We focused our attention on a 13''x17'' region centered around the geyser flaring loops. Individual jets, J1 to J10, were detected as originating from the structure. To complement our work, we searched the available literature and selected five more additional recurrent jet sites that manifested similarly to our region (see table 2.1. These sites have similar sizes, with the exception of the G5 site (34''x30'') which is also associated with more energetic flaring.

One G1 jet eruption (J6) is briefly described with respect to the emission measure recorded by the SDO-AIA filters, in order to recover important additional information regarding the geyser footpoint. We recovered the Differential Emission Measure (*DEM*) peak emitting temperatures using the regularized inversion method developed by Hannah and Kontar [2012] applied to the SDO-AIA 171Å 193Å 211Å 94Å 131Å and 335Å filter

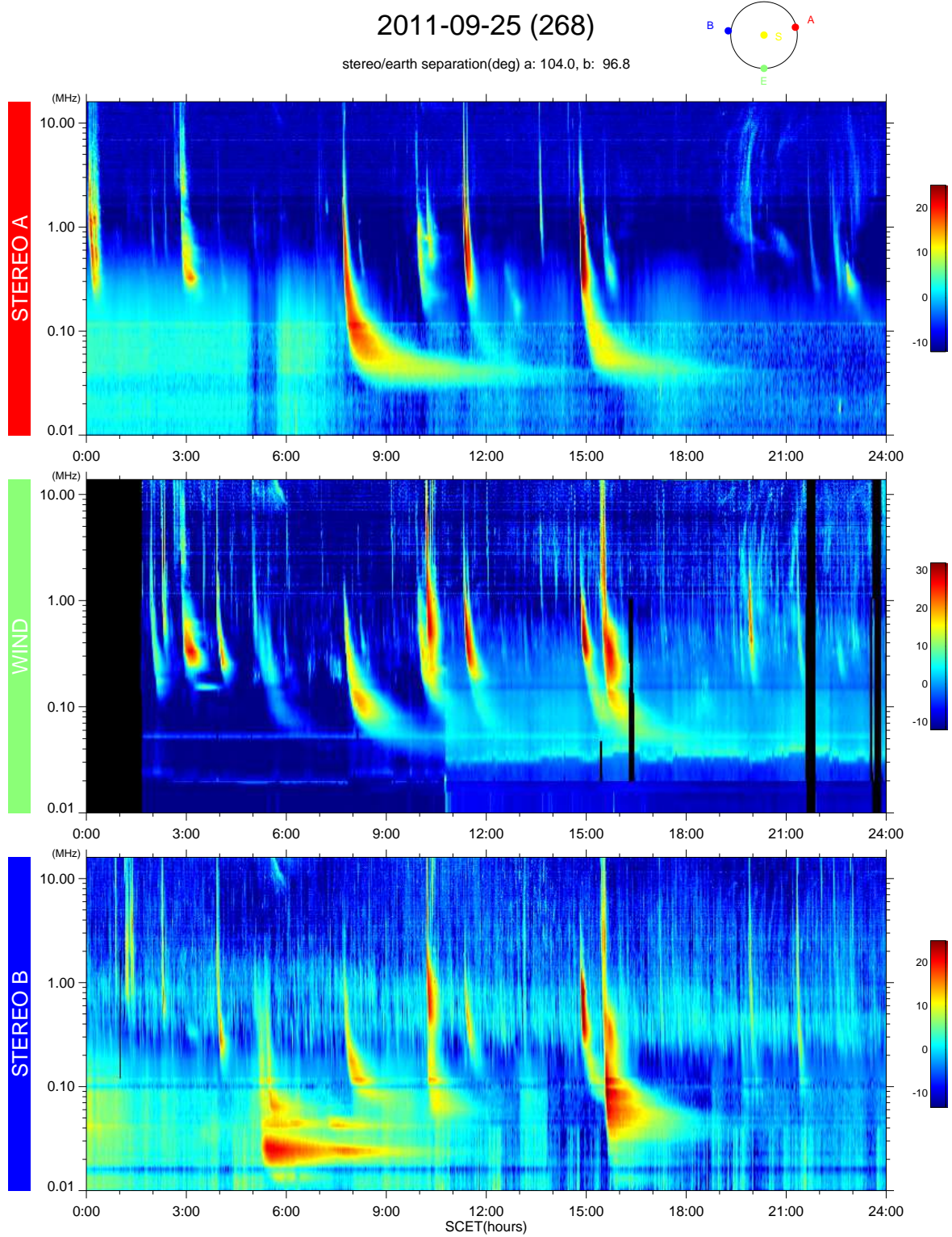


Figure 2.2: Dynamic spectra of the solar radio emission as viewed from the STEREO-B SWAVES, STEREO-A SWAVES, and WIND WAVES perspectives. The relative satellite positions are shown in the upper right corner. The E (earth) position corresponds to the position of WIND and SDO. The active region appears on the western side of STEREO-B's visible disk and were detected by EUVI's SWAVES instrument. The jet events were temporally positively correlated with both the WIND and STEREO-B data, although a fraction of the jets were missed by WIND. The site was not visible from the STEREO-A viewpoint. Plots are reproduced from the NASA-GSFC swaves service.

set. It is worth mentioning that this is a particularly impulsive jet and hard X-Ray emission was observed at the geyser location during the eruption. The analysis revealed two distinct temperature peaks: first at $\log T_e \sim 6.3 \pm 0.1$ K corresponding to the main jet eruption; the second peak is more pronounced and associated to the flare of the geyser, centered around $\log T_e \sim 6.9 \pm 0.12$ K and co-spatial to the HXR flaring footpoints. The lower value agrees with the interpretation provided by Mulay et al. [2016] and along with its correspondent $n_e \sim 0.5 - 1 \cdot 10^{10} \text{ cm}^{-3}$ are used as limits for further computations (table 3.2). A detailed DEM analysis is treated separately in chapter 3.

In the EUV, all G1 jet events followed the same propagation direction, erupting along an apparent ‘open’ magnetic field; they were homologous, exhibiting a behavior similar to the recurrent events studied by Sterling et al. [2016], Chen et al. [2015], Yu-kun et al. [2016], Panesar et al. [2016], Liu et al. [2016] which we incorporated in our analysis (see table 2.1). Importantly, these studies do not address the EUV to radio burst associations. The dataset selection is not exhaustive but our goal is understanding recurrent (or homologous) jets that span across longer timeframes, hinting at the existence of the quasi-stable, possibly twisted, geyser structures. The G1 dataset was temporally tracked inside an arbitrarily chosen time interval although events originating from the structure could be detected in previous and subsequent days. This behavior is found in all included datasets. We chose to limit the tracking to the (recurrent) jet events discussed in each cited original study in order to emphasize the existence of the geyser structures and keep clear referencing.

Using the same procedures as for our G1 site, the G2, G3, G4, and G6 geysers are tracked on shorter time intervals between 7 h - 11 h. The G5 dataset tracking is 22 h similar in lifetime to the G1 site. A total of 50 out of claimed 54 geyser jet events could be reproduced (fig. 2.3) analogous to the original studies. At the site G1, the EUV J1 - J6, and J8 events can clearly be distinguished, whereas the events J7, J9, and J10 are weaker, exhibiting short timescales, smaller intensity flaring, and modest jet emission. Most of G4 and G5 events are correspondingly also modest in size. We also observed additional minor flaring activities, spatially correlated with the geyser locations. These events manifested individually or in groups, but do not trigger any visible signs of jet emission in any of the SDO-AIA channels.

2.2.1 Timeseries Correlation of Coronal Jets and Type-III Radio Bursts

We put to test the claimed association (see discussion in [Introduction](#)) between the EUV jets and interplanetary Type-III radio bursts by superposing the EUV Geyser structure timeseries with STEREO SWAVES and WIND WAVES dynamic spectrum radio data for all discussed individual jet eruptions. In table 2.1 we present the main observed correlations and uncertainties and fig. 2.3 depicts the superposed timeseries data for all sites. A significant set of underlying assumptions and uncertainties involved are considered: Jet events for sites G2-G6 were recorded based on the identifications provided by their respective studies. Some ‘expected’ events in the G4 and G6 Geyser sites could not be separated or differentiated in our SDO-AIA timeseries or by visual inspection.

The temporal correlations are influenced by the low data cadence of the radio signal. Additionally, radio data may be unreliable as the signal is sometimes saturated by multiple overlapping events. The Signal to Noise Ratio (SNR) corresponding to positively associated radio bursts is calculated. To this extent, the correlations were always performed by identifying a radio burst that immediately follows the main SDO-AIA EUV site flaring.

The associations were calculated based on the time difference between the peak emission in the AIA-171Å and the subsequent associated radio burst. When that was not

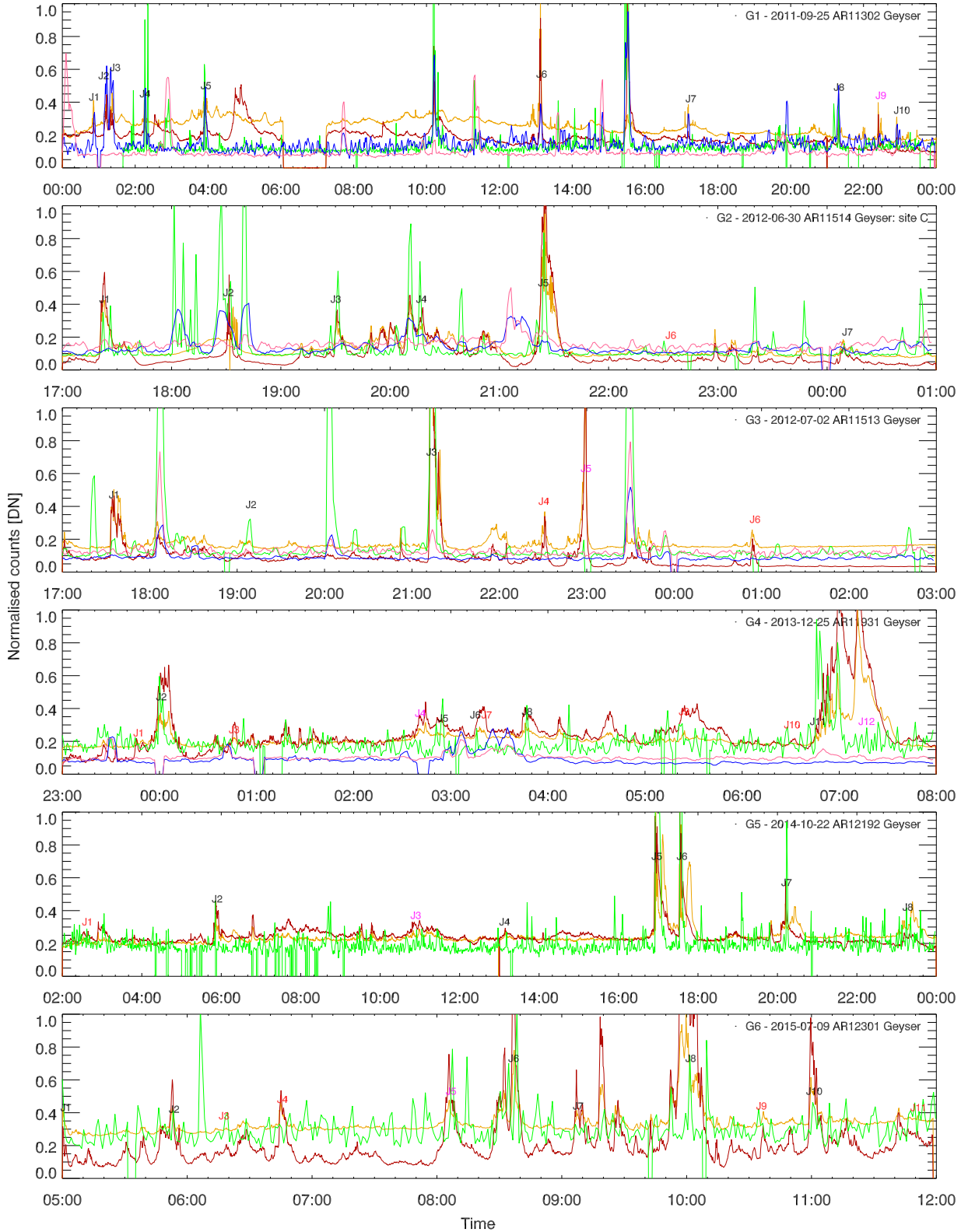


Figure 2.3: Temporal tracking of the regions centered on the studied geyser structures using SDO's AIA-171Å (yellow), AIA-304Å (red), STEREO-B SWAVES (blue), STEREO-A SWAVES (pink) and WIND WAVES (green) data. The individual jets are labelled incrementally for each referenced dataset. The x-axis (time) is not normalised across the dataset. The temporal range for each site is arbitrarily set to be analogous to the original studies. Uncorrelated events labels along with very faint or expected events which we could identify are marked (red). Uncertain events are also highlighted (purple). The radio data is slightly moved up on the y-axis in order to increase plot readability. Additional information on the six datasets can be found in Table 2.1.

possible, the time difference at the onset of the two signal peaks was used. Also, the AIA-304Å signal is sometimes time-delayed when compared to the AIA-171Å making it unsuitable for this task. For particular events, there may be multiple bursts generated corresponding to multiple SDO-AIA flaring peaks occurring in short timescales of < 180 s (e.g. G1 site, J2 and J3). The ‘expected’ non-separable events along with jets that were not followed shortly by a radio bursts were deemed uncorrelated and marked as red in fig. 2.3. Purple colored events were classified as weakly correlated, due to either uncertain radio burst SNR, unreliable time delay between the SDO-AIA and burst peak times, or unclear SDO-AIA signal.

The flaring Geyser sites were usually observed by multiple satellites, each providing a unique vantage point for radio burst interpretation. The recorded STEREO and WIND radio signal is integrated over the entire solar disk. SDO and WIND share co-spatial viewpoints, while the two STEREO satellites share unique different viewpoints. This opens the possibility of positive correlations described above, but also negative correlations based on viewpoints that do not observe the flaring site. Since SDO is the main instrument currently used for EUV observations, all sites, G1-G6 are visible from its viewpoint that is also associable to the WIND signal. The G2, G4, G5, and G6 sites are observed close to a disk central location. The G1 and G3 sites had a lateral disk position. The G1 site appears the eastern side of AR11302. Due to the separation between the SDO and STEREO-B spacecrafts ($\sim 97^\circ$), the AR also appears on the western side of STEREO-B’s visible disk. Events were positively correlated for both the WIND and STEREO-B data, although a portion of the jets were missed by WIND due to datagaps. The site was not visible from the STEREO-A viewpoint, and no coincidental association could be made. In other words, all 10 events were negatively correlated using the STEREO-A viewpoint.

Geyser site G3 had a similar configuration. AR11513 was situated to the western side of the solar disk. Due to the separation between the SDO and STEREO-A spacecraft ($\sim 119^\circ$) the AR also appears on the eastern side of STEREO-A’s visible disk, and the jet to Type-III burst association could also be established. No coincidental association was established using STEREO-B, which does not observe the site. We can report that this negative correlation holds for all events spanning across G1-G4 datasets, and no coincidental and/or falsely associated events was possible, strengthening our assumptions regarding the positive correlations. The G5 and G6 sites have no STEREO data associated due to the STEREO satellites being out of contact during their far-side crossing. Table 2.1 contains summaries regarding both positive and negative correlations.

2.2.2 Modeling the Heliospheric Travel of Upward Electron Beams

All three radio data sources, namely STEREO-A, STEREO-B, and WIND that were utilized to obtain the fig. 2.3 correlation depict the radio emission matching an oscillating plasma frequency harmonic of $2\nu_{pe} = 3$ MHz, corresponding to an approximate heliospheric height, $R \sim 8.10R_\odot$. As the figure reveals, this choice was deemed as the optimal compromise as lower frequencies usually involve more unrelated emitting features or noise, impeding detection. Also, the correspondent heliospheric height is smaller than $\sim 10 R_\odot$ where solar wind becomes supersonic.

In fig. 2.4 (left) histogram, the time delay between SDO-AIA flaring and radio Type-III burst detection times is presented. The time delay is *always positive*, meaning that the radio burst is subsequent to the EUV emission ($T_{EUV} - T_{burst} > 0$), as expected by assuming that the $2\nu_{pe} = 3$ MHz burst signal corresponds to considerable heights. The time delay was

Geyser Dataset	No. Jets	Type-III Radio Bursts 1. 2.	Correlated (1.) Events SNR	Study Reference
G1 AR11302 25.09.2011T00:00-23:59	10	S-B: 9(+1)/10 W: 5(+1)/7	S-A: 0/10 $9/10 > 3\sigma$ $2\sigma < 1/10 < 3\sigma$	This work Paraschiv et al. [2018]
G2 AR11514 30.06.2012T17:00-01:00	7 site C	W: 6/7	S-B+S-A: 0/7 $5/7 > 3\sigma$ $2\sigma < 1/7 < 3\sigma$	Sterling et al. [2016]
G3 AR11513 02.07.2012T17:00-03:00	6	W: 3(+1)/6 S-A: 3/6	S-B: 0/6 $4/6 > 3\sigma$	Chen et al. [2015]
G4 AR11931 25.12.2013T23:00-08:00	10/12	W: 5(+2)/10	S-B+S-A: 0/10 $2/10 > 3\sigma$ $2\sigma < 6/10 < 3\sigma$	Yu-kun et al. [2016]
G5 AR12192 22.10.2014T02:00-00:00	8	W: 6(+1)/8	x $5/8 > 3\sigma$ $2\sigma < 2/8 < 3\sigma$	Panesar et al. [2016]
G6 AR12301 09.07.2015T05:00-12:00	9/11	W: 6(+1)/9	x $5/9 > 3\sigma$ $2\sigma < 2/9 < 3\sigma$	Liu et al. [2016]

Table 2.1: Jet datasets collected from different literature studies. Radio data sources are STEREO-A (S-A), STEREO-B (S-B), and Wind (W). The detected jets column lists the events that were observed by the corresponding studies. All correlated events were checked for statistical relevance against background radio counts. Not all events described in the G4 and G6 datasets could be distinctively separated from the SDO-AIA background. The established temporal correlations are described in section 2.2. Uncertain events are listed inside brackets. The three data sources occupy unique positions for each dataset, enabling both positive (1) and negative (2) correlations to be discussed via individual source position.

measured at either the maximum peaks or the onset times of the two signals based on the individual measurement particularities of the 50 jets. When both methods could be utilized, they yielded identical results. The data cadence for the six SDO-AIA datasets is 12 s. The radio data is averaged every 60 s and interpolated to a 12 s interval to match the SDO-AIA rate. A Gaussian fit over the time delay distribution histogram revealed an average for the time delay of 72 s, constrained by a $\sigma = 27$ s width.

We ask the following: Does the observed time delay reflect a physical property pertaining to the correlation or is just the result of a stochastic process? The analytical approximation of Mann et al. [1999] was used to answer this question. The approximation describes an heliospheric radial density model that can be used to characterize a electron beam (observed radio burst) traveling in the inner heliosphere via eq. (2.1) by converting the observed emitting plasma harmonic to a local plasma density value, which in turn corresponds to a radial upwards distance from a source surface, particularly, our chromospheric site. The average burst drift rate between STEREO's starting frequency of 16 MHz and our chosen 3 MHz was estimated at $1.3 \text{ pix} = 78 \text{ s}$. This should not be confused with the time delay discussed previously!

$$\frac{\partial \rho}{\partial t} + \nabla \cdot \rho \mathbf{v} = 0. \quad (2.2)$$

$$\rho \left[\frac{\partial \mathbf{v}}{\partial t} + (\mathbf{v} \cdot \nabla) \mathbf{v} \right] = -\nabla p + \mathbf{J} \times \mathbf{B} + \mathbf{g} \rho = -\nabla p + \frac{1}{\mu_0} \mathbf{B} \times (\nabla \times \mathbf{B}) + \mathbf{g} \rho. \quad (2.3)$$

$$\frac{\partial \mathbf{B}}{\partial t} = -\nabla \times \mathbf{E} = \nabla \times (\mathbf{v} \times \mathbf{B}). \quad (2.4)$$

The Mann et al. [1999] approach solves the continuity, momentum and Faraday magnetohydrodynamic equations (eqs. (2.2) to (2.4)) assuming radial scalar functions for the magnetic field $\mathbf{B}=\mathbf{B}(r)$ and plasma outflow velocity $\mathbf{v}=\mathbf{v}(r)$. The initial conditions of the equations are constrained by observations. The $\mathbf{v}(r)$ term can be found by integrating the continuity equation where the mass flux is a function of the source temperature. The Parker [1958] solar wind equation eq. (2.5) is obtained.

$$v(r)^2 = v_c^2 \cdot \left[4 \ln\left(\frac{r}{r_c}\right) + \ln\left(\frac{v(r)^2}{v_c^2}\right) + \frac{4r_c}{r} - 3 \right]. \quad (2.5)$$

Then $v(r)^2$ can be substituted back in the integrated form of continuity equation, which can be solved analytically for lower heliospheric heights by assuming a non-supersonic wind speed, $v < v_c$. A barometric height formula valid for a hydrostatic subsonic regimes can be displayed as a dependence on the local plasma density

$$n_e(r) = n_s \cdot e^{\frac{A}{R_\odot} \cdot \left(\frac{R_\odot}{r} - 1\right)}, \quad (2.6)$$

or on the harmonic plasma oscillating frequency

$$\nu_{pe}(r) = \nu_s \cdot e^{\frac{A}{2R_\odot} \cdot \left(\frac{R_\odot}{r} - 1\right)}. \quad (2.7)$$

It is worth mentioning that the Mann et al. [1999] model provides reasonable observational cross-validations under the assumption that the globally averaged electrons distribution do not depend strongly on coronal structures. The observations of Koutchmy [1994] showed a difference of up to three orders of magnitude in plasma density between coronal streamers, quiet equatorial regions and polar regions at $1.3R_\odot$. Thus, we emphasize that the radial density model offers a general picture of the outer corona only if carefully utilized inside sensible hypotheses and custom tailored boundary value assumptions.

To this extent, fig. 2.4 (right) shows the approximate dependence of the heliospheric electron density on the radial distance (in solar radii) as obtained from the eq. (2.1). Following the Mann et al. [1999] recommendations and discussed DEM limits (section 2.2), we set the constant $A/R_\odot = 13.83$ where A is a ratio of gravitational and thermal components. The starting parameters $n_s = 5.14 \cdot 10^9 \text{ cm}^{-3}$ and $\nu_s = 644 \text{ MHz}$ are corresponding to a $\sim 1 - 2 \cdot 10^6 \text{ K}$ coronal site rooted $\sim 2 \text{ Mm}$ ($1.01R_\odot$) above the photosphere. The above measured 78 s drift rate corresponds to an harmonic oscillating frequency drop $16 \rightarrow 3 \text{ MHz}$ or a $7.93 \rightarrow 0.28 \cdot 10^5 \text{ cm}^{-3}$ density decrease. This is fitted to a heliospheric travel distance of $8.10 - 2.73 = 5.37R_\odot$, where the $8.10R_\odot$ start correspond to the subsonic approximation. This results in an averaged beam propagation speed of $v/c \sim 0.16$. This places the detected beam in the lower end of the mild relativistic regime.

We assume that a beam (observed as a radio burst) is initiated co-temporally with the SDO-AIA flaring. We observed the phenomena as traveling in $16 \rightarrow 3 \text{ MHz}$ frequency region, (constrained by the instrumentation), corresponding to a traveled distance between $1.01 \rightarrow 8.10R_\odot$. We fit the resultant beam propagation speed to the traveled distance according to the density model and estimate an analytically driven time delay of $\sim 90 \text{ s}$ between the EUV flaring and radio burst. The estimation corroborates the observed $72 \pm 27 \text{ s}$ time delay at least at a qualitative and order of magnitude estimation.

We emphasize that a more rigorous uncertainty estimation is not needed as the resulting estimations are close to detection limits, and models have limited applicability. Modeling the travel to a larger heliospheric distance is improper as the analytic approximation holds true only for a non-supersonic solar wind. Observationally, the radio dynamic spectra cadence, even when partially mitigated by oversampling to the SDO-AIA 12 s cadence, influences the observed time delay estimation as it is close to the 60 s data sampling. To our knowledge, no further constraints can be applied to the design of this experiment, as uncertainties are instrumental in nature. Radio observations in higher frequency ranges and data sampling are required in order to increase the precision of this established correlation.

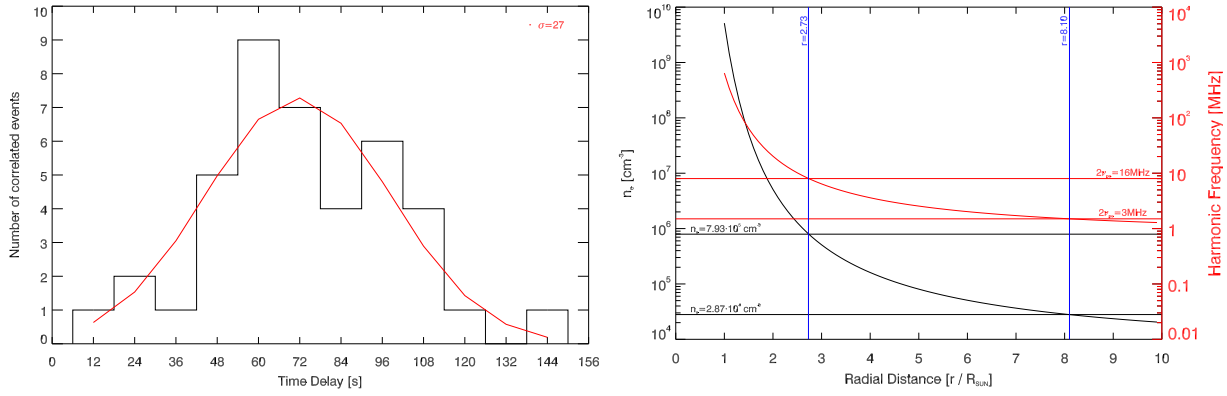


Figure 2.4: Observational and analytical interpretation of the recorded time delay between the SDO-AIA microflaring jet onset events and the correlated interplanetary Type-III radio bursts.

Left Panel: Time delay between the peak/onset SDO-AIA 171Å flaring of the Geyser structure versus the associated subsequent Type-III bursts. The distribution is Gaussian fitted with its peak corresponding to the 72 s delay and a $\sigma = 27$ uncertainty. Events ≤ 24 s and ≥ 120 s are marked as uncertain in fig. 2.3.

Right Panel: Type-III Burst drift parameters as depicted from a number density viewpoint (black) and first harmonic frequency (red) as a function of the radial distance from the chromosphere via eq. (2.6) or eq. (2.7). Units are normed solar radii. The 16 MHz or $7.93 \cdot 10^5 \text{ cm}^{-3}$ start corresponds to a heliospheric height of $2.73 R_{\odot}$ and the low boundary 3 MHz or $2.87 \cdot 10^4 \text{ cm}^{-3}$ signal corresponds to radial distance of $8.10 R_{\odot}$.

2.3 Summary and Discussion

We revealed unique coronal sources, labeled herein as Coronal Geysers, that produced sets of recurrent EUV jets and multiple interplanetary Type-III radio bursts. The geysers generated multiple small-scale recurrent coronal jets that escaped along ‘open’ magnetic fields into the outer corona. The Geyser structures are described as identifiable EUV footpoints, rooted in the penumbral regions of the complex AR11302, that are subjected to recurring microflaring episodes (see chapter 3). These quasi-stable structures interact via reconnection with the magnetic canopy of the active region, and topologically could be classified as twisted microfilaments, similar to the one described by Sterling et al. [2015], although the dichotomy predicament is still under debate [see Raouafi et al., 2016].

Multiple EUV/X-Ray jet inducing Coronal Geysers, are observed by the SDO-AIA instrument. The individual temporal association between the EUV/X-Ray jets and Type-III radio bursts escaping into the inner heliosphere is presented following the standard flare model assumption that both emissions are released concurrently via magnetic reconnection.

Six separate Coronal Geysers are analyzed. The G1 structure represents the reference dataset analyzed throughout this work. The G2-G6 coronal Geysers are collected from the currently available literature by selecting sites that released multiple homologous/recurrent jets over a significant time period (>6 h), complying to our geyser structure frame-set.

We have identified 50 jets generated by the six Geyser sites. From this total, 35 plus 6 uncertain jet events were positively associated (82%) to propagating Type-III interplanetary radio bursts. A negative correlation analysis yielded no false correlation, although coincidences may exist outside our discussed events. 9 EUV events could not be correlated to Type-III radio bursts. 4 events claimed in the literature sourced could not be detected by us in the EUV timeseries flux (see fig. 2.3 and Liu et al. [2016], Yu-kun et al. [2016]). These missing jets were not counted towards the total.

This work aims to generalize the results of Chifor et al. [2008a] and Innes et al. [2011] which studied recurrent AR jets and their associated Type-III for short time intervals.

Recurrent jets from multiple sites were readily associated to Type-III emission by Mulay et al. [2016]. All recurrent jet datasets, long or short lived, are selected with a degree of subjectivity. The G1 geyser had a lifetime of at least one day. In our case, the tracking of G1 was limited to 24h due to data constraints, although the structure had a considerably longer lifetime. In the case of the G2-G6 Geyser structures, jet eruptions outside the discussed time intervals were detected by us. A longer timeseries analysis on the G2, G3, G4, and G6 geyser sites may reveal longer lifetime scales, analogous to the G1 and G5 sites.

The utilized source literature discussed EUV recurrent jets [Sterling et al., 2016, Chen et al., 2015, Yu-kun et al., 2016, Panesar et al., 2016, Liu et al., 2016]. The studies reported similar morphological jet and footpoint properties to G1. Due to the apparent topological variations between small-scale coronal sources, we did not assess whether the coronal geyser frameset can further be extended to encompass a common magnetic topological configuration. We reconstructed the topology of the G1 site using meticulous interpretation of the low atmosphere magnetic field structures (section 4.3).

We have reconstructed the time delay between the onset of SDO-AIA flaring and interplanetary Type-III radio bursts: An analytically derived time delay of ~ 90 s (see fig. 2.4, right) is comparable to the observational results, where the centroid of the Gaussian fit applied to the SDO-AIA171Å vs Type-III radio bursts, revealed a average time delay of 72 s (fig. 2.4, left). Given the finite number of studied jets, we acknowledge the limitations of our statistics, and present the results as a order of magnitude estimation.

Geyser sites G2 and G5 are linked [Sterling et al., 2015, Panesar et al., 2016] in part to flares of magnitudes *B* and sometimes *C*, although most eruptive events that are classified as microflares (X-Ray flux $\leq 10^{-5}$ erg cm $^{-2}$ s $^{-1}$). The other sites, namely G1, G3, G4, and G6, are identified as typical microflare sites, with only very few events exhibiting stronger eruptions. As expected, the electron beam generation is ubiquitous across the different scales of coronal jet events.

The Sterling et al. [2015] microfilament eruption model assumes the existence of multiple reconnection events that constitute an observed blowout [See also the blowout eruption cartoon of Moore et al., 2010] jet eruption. In our study, the observed EUV jet's threaded morphological features (section 1.1 and appendix A) are compatible with an eruptive filamentary structure. The G1: J2, J3, J5 and J6 jets were highly dynamic and exhibited multiple Type-III bursts manifesting due to electron beams generated co-temporally with the multiple SDO-AIA EUV flaring peaks. The multiple flaring peaks and correlated bursts are plotted in fig. 2.3 while more EUV detail is presented in the fig. 3.1 footpoint flaring timeseries plot. This aspect suggests that multiple individual reconnection events are occurring in very short timescales. From a radio viewpoint, multiple short (<2-3 min) timed 'electron injections' (electron beam generation) are reported by McCauley et al. [2017] in their high resolution Murchison Widefield Array [MWA; Tingay et al., 2013] Type-III bursts study. Assuming the standard flare model, we hypothesize that 'short electron injections' may be produced in the flaring stages of a microfilament eruptions.

The study of Cairns et al. [2018] is observing the in-depth X-Ray, EUV and higher frequency manifestations of a flaring episode covering a ~ 15 minute period. In our analysis, we separated the episode into the G1 J2 and G1 J3 events. The authors argued in favor of the standard flare model implying that electron beams are accelerated in or near the reconnection sites but also acknowledged that more evidence is needed to validate the hypothesis. Our analysis adds more weight to the argument by analyzing a statistically large set of events, where 50 distinct coronal jets are manifesting in six independent geyser structures. The authors acknowledge that special conditions are required to observe radio

manifestations for reconnection sites. Our results are optimistic in this regard, where our determination, performed on multiple independent datasets, resulted in correlations for 82% events, although 9 non-correlated events remain. A possible explanation of the special conditions required for generating upwards propagating electron beams may lie in the fact that a homologous flaring site may not always reconnect with an ambient magnetic field that is tied to the outer corona [Judge et al., 2017]. Even when a coronal connection exists, if the reconnection would occur in denser chromospheric regions, we hypothesize that enhanced collisions might suppress the generation of high energy particles. We are not aware of any report of this happening at the scales discussed here.

Our estimation based on DEM limits on the local plasma and on the extrapolated magnetic fields places the geyser’s flaring site at a height of maximum 2.3 Mm. This result suggests that the geyser is located at smaller than previously quoted heights, e.g. Cairns et al. [2018] who placed the source at 5-10 Mm. Their lower limit can be considered an upper approximation, but the higher limit is not compatible with a low atmosphere site, and the “Heights < 10 Mm correspond to the nominal chromosphere.” [Cairns et al., 2018] does not represent an accurate approximation. We attributed the 2.3 Mm heights to correspond to a region in between the high-chromosphere and low corona based on the local conditions. The chromosphere is depicted in hydrostatic numerical experiments (e.g. Fontenla et al. [2011] models, fig. i.2) to be at heights lower than 2 Mm. Chromospheric structures have been seen extending to heights of ~ 4 Mm in non polar regions [Johannesson and Zirin, 1996].

A very interesting discussion that spans in the Cairns et al. [2018] study is the discrepancy between higher frequency (MWA, Learmonth, etc.) and low frequency (STEREO and WIND) observations. The higher frequency Type-III radio bursts matched with their interplanetary counterparts for the G1 J3 event. This did not occur for the G1 J2 event which does not exhibit any higher frequency signatures (see, Cairns et al. [2018], fig. 4). Our timeseries analysis (fig. 2.3) showed that three SDO-AIA flaring peaks existed for the three interplanetary Type-III bursts associated to J2 and two SDO-AIA flaring peaks existed for the J3 event. This can also be observed in the zoomed-in Cairns et al. [2018], fig. 7. The radio data had a consistent travel time based on our analysis, being almost identical for the two eruptive events leading to our assertion that both EUV jet events correlate with the interplanetary bursts. Now, the X-Ray energy that is dissipated towards the lower atmosphere differs substantially between the two jets. Detailed RHESSI spectral fitting results are provided in section 3.4. Could this be an indicator that the physical properties of the two events are very dissimilar? We hint that DEM solutions and X-Ray energetic budgets for the two events are of particular interest. A full DEM analysis of the footpoint is provided in section 3.3.1.

Recent work based on the groundbreaking higher frequency MWA data [McCauley et al., 2017] probes into the finer structure of the processes that govern the reconnection site and discuss how a complex magnetic topology can give rise to high frequency beam splitting near or at the coronal source. They derived average beam travel speeds of $0.2c$ using a technique that is independent from the frequency drift rates used in our estimation. Their result is consistent with our $0.16c$ estimation, where we estimated a relatively small uncertainty ($\sigma = 0.06$) in the beam propagation speed, though this may be skewed by the limited data cadence and event sample. The propagation speed may be related to the flaring strength, magnetic field strength or topology and should be evaluated on an case by case basis.

This study presents data analysis and analytic modeling of a statistically significant sample of recurrent jet microflaring footpoints, designated as Coronal Geysers, that act as

sources of upwards accelerated electron beams and interplanetary Type-III radio bursts. A comprehensive database of EUV recurrent jets is presented and temporally correlated with the interplanetary Type-III radio bursts observed by the STEREO-SWAVES and WIND-WAVES instruments. The temporal correlations revealed a systematic time delay (72 ± 27 s) between the detection of thermal EUV plasma and the non-thermal generated Type-III radio bursts. We hypothesize that under a standard flare scenario, the electron beams are accelerated at the same time as the EUV jets by recurrent reconnection events at the location of each identified coronal geysers. Using a heliospheric density model adapted to our observations, we computed the electron beam propagation times in the inner heliosphere, constrained the averaged time delay factor to be in the order of 90 s, closely confirming the observations. These results confirmed the scaling of standard flare properties to micro-class flaring, found that recurrent jet-inducing microflare sites are sources of electron acceleration, and demonstrated that ‘geysers’ are reliable coronal sources of ubiquitous interplanetary Type-III radio bursts.

To summarize, our results represent a global approximation, as they are based on a statistically significant event sample from several different geyser sites, all rooted near active regions. The accuracy of the EUV-burst correlation is limited by the instrumental capabilities and constraints in the analytic solution. Better quality radio data with higher temporal cadence and higher frequency range are needed to probe into the intricate flaring processes of our star. Our future work will focus on closing the gap between higher frequency radio imaging at the source locations and the interplanetary electron beams. As solar energetic events exhibit a high morphological and energetic variability, we believe that the assumed theoretical physical mechanisms can only be scrutinized in solar conditions by utilizing significant datasets. The study of solar (small-scale) flares is an intrinsic topic of solar research due to the close proximity and consequently higher quality observations. As seen, current observational and theoretical results on electron beam generation and propagation show that although a general phenomenological understanding holds true, a unifying mechanism still proves elusive. Further input on particle acceleration, transport and escape into the inner heliosphere in the context of Sun-Earth interconnections is a key aspect that can be extended to more general astrophysics applications.

CHAPTER 3

Thermal and Non-Thermal Properties of Active Region Recurrent Coronal Jets

Foreword: The thermal and non-thermal properties of jets from a comprehensive dataset are presented. The results are used to infer and compare the physical properties of the plasma in recurrent jets simultaneously at the base geyser footpoint and along the jets outflow. The jets were observed in EUV and X-Ray emission, by the SDO-AIA and RHESSI instruments. To our knowledge the long lasting recurrent behavior of a unique jet generating footpoint (the geyser) has not been discussed comprehensively in the literature. We present details about the main plasma physical parameters: temperature, density, energy flux contributions, etc. via differential emission measures of the six SDO-AIA narrow-band filtergrams using multiple inversion techniques. Furthermore, we perform the source reconstruction and the spectrographic analysis of higher energy X-Ray data using RHESSI observations. Active region jets are found to be energetically stronger than the largely studied polar jets. The data analysis of this phenomena will provide new information for theoretical modeling of jets and possibly allow for a better assessment of the microflare driven eruption scenaria.

3.1 Differential Emission Measure of Thermal Plasma

The Solar EUV spectra contains emission lines of ions formed over a wide range of temperature and density regimes. Therefore line ratios and emission measure techniques are an essential tool for the determination of the physical conditions of hot plasma. These techniques have been extensively refined in the last decades where relative intensity ratios of density sensitive emission line or filtergram pairs have become a familiar sight in recent times. The applicability of this technique is dependent on the atomic interpretation of the ion transitions.

Differential emission measures (DEMs) are the solution to an inverse problem resulting from emission line intensities of a partially or fully ionized optically thin astrophysical plasma of constant abundances and in local thermal equilibrium. Following the work of Craig and Brown [1986] we describe the physical and mathematical interpretation of the ill-posed inversion problem.

The total line intensity of a two level atom for a given transition i occurring from a upper level u to a lower level l is given by

$$I_i = \frac{h\nu_i}{4\pi} \int_z n_u^i(z) A_{ul} dz \quad [W m^{-2} sr^{-1}], \quad (3.1)$$

where h is the Plank constant, ν_i is the integrated frequency of an emission line, A_{ul} is the

Einstein coefficient for spontaneous de-excitation and $n_u^i(z)$ is the population density of the upper level of the i transition. The intensity is assumed to be integrated along the whole width of the line. For a coronal gas in a collisionless approximation, the rate of spontaneous de-excitation (A_{ul}) dominates over the collisional de-excitation rate (C_{ul}), where $A_{ul} \gg C_{ul}$.

The population density n_u can be approximated to the square of the local electron density n_e^2 multiplied with a function of temperature. See Craig and Brown [1986] for full details. The common observable quantity, the ‘Intensity’, (I) is derived from the spectroscopic or filtergram total integrated signal in an area cross-section ($[cm^2]$). The observed signal is interpreted as

$$I_i = \int_{-z}^z n_e^2 G_i(T_e) dz \quad [W m^{-2} sr^{-1}], \quad (3.2)$$

where $G(T_e)$ represents a response function comprised by the atomic and physical constraints. Note that in practice this is a function of a pre-determined temperature. Integrating in depth (z) we can recover a volume (usually in cm^3), thus enabling us to estimate the average plasma density contained within the volume. A plasma filling factor quantity needs to be assumed. The filling factor is subsequently addressed in context of our jet observations, see section 3.2.1.

Equation (3.2) can be rewritten in terms of temperature space by considering:

$$n_e^2 dz \leftrightarrow DEM(T_e) dT_e, \quad \rightarrow DEM(T_e) = \frac{n_e^2 dz}{dT_e} \quad [cm^{-5} \cdot K^{-1}]. \quad (3.3)$$

The studied plasma is fitted in $[T_e, T_e + dT_e]$ intervals, and is presumed of constant n_e density inside the temperature space [Craig and Brown, 1986]. In a formal case, the response function can be reduced by revealing that the differential emission measure represents the distribution of emitting material at a given temperature and placed inside a volume

$$I_i = G_i(T_e) \int_{T_e} DEM(T_e) dT_e. \quad (3.4)$$

The total emission measure represents the total emission of a number of emitting particles from the LOS volume bounded by the cross-sectional area or from the particles emitting inside a temperature range. In practice, (eq. (3.5)) the integrated emission measure can be obtained from the physical observable intensity I and the response function $G_i(T_e)$ using either the eq. (3.2) or eq. (3.4) formalisms.

$$EM = \int_{-z}^z n_e^2 dz = \int_{T_e} DEM(T_e) dT_e \quad [cm^{-5}]. \quad (3.5)$$

The I term ideally represents the total intensity of a narrowband emission line or filtergram observation. The SDO-AIA EUV filters, which record optically thin coronal plasma in narrowband wavelengths can not be used to directly infer plasma densities due to the multithermal response. Practically, one potential filter ratio will manifest for multiple temperatures across the observed plasma, which has very wide temperature response in the range of $\log T_e = [5.5, 7.5]$ K.

$$\begin{bmatrix} I_1 \\ I_2 \\ \dots \\ I_n \end{bmatrix} = \begin{bmatrix} G_{11} & G_{12} & \dots & G_{1m} \\ G_{21} & G_{22} & \dots & G_{2m} \\ \dots & \dots & \dots & \dots \\ G_{n1} & G_{n2} & \dots & G_{nm} \end{bmatrix} \begin{bmatrix} DEM_1 \\ DEM_2 \\ \dots \\ DEM_m \end{bmatrix}. \quad (3.6)$$

Multiple filtergram observations, with individual temperature sensitivities are coupled inside a system (eq. (3.6)), and compared to sets of theoretical responses, with the aim of calculating the best theoretical response solutions that match the observed intensities. Mathematically, this represents an inverse problem. First, a set of small temperature bins under which the theoretical DEM can be calculated are generated. The theoretical temperature range can be divided into uniform logarithmic temperature intervals $T_{bin} = \log T_e$. Equation (3.7) can be used to calculate the total EM inside such one temperature bin from the differential emission measures following eqs. (3.3) to (3.5). The inversion problem is solvable using either statistical minimization, iterative schemes or matrix reduction schemes.

$$EM(T_{bin}) = n_e^2 \frac{dl}{d \log T_e} = \frac{T_e \cdot DEM(T_e)}{\ln(10)}. \quad (3.7)$$

3.2 On Differential Emission Measure Inversions

3.2.1 Background and Methodology

The thermal geyser structure is recorded using the SDO-AIA EUV imager. The filtergrams representing emission line image data are characterized by a multithermal emission line contributions over a broad temperature range. Six SDO-AIA filter centered on EUV bandpasses [94Å, 131Å, 171Å, 193Å, 211Å, 335Å] are used in our determination. These filtergrams are centered on emission lines of Fe [XVIII, VIII, IX, XII, XIV, XVI], theoretically spanning plasma in the $T_e = [0.4, 30]$ MK range. Higher temperature observations (e.g. Hinode XRT) can be used to add information from plasma in the higher temperature range. No such suitable observations exist for our geyser observation. The AIA-304Å data is neglected due to the broad non-isothermal response and the optical thick He II plasma sampled by the filter [Warren, 2005].

The J2, J3, and J6 jets are analyzed. The three events were selected due to the fact that they were detected in the high energy RHESSI observations, and the unique geyser footpoint was reconstructed with the RHESSI source modeling. The other jet events were not observed by RHESSI. The RHESSI analysis results are presented in section 3.4. The DEM inversion was attempted using multiple inversion models. The simplest DEM interpretation, namely the filter ratio technique (section 3.2.2) was initially applied. More complex inversion methods are subsequently utilized and their output emission measured are cross-validated.

The Aschwanden [2013] (section 3.2.3, henceforth ‘A2013’) method is a simple and straightforward implementation of a single Gaussian fitting solution optimized using a χ^2 minimization. The Hannah and Kontar [2012] (henceforth ‘H2012’) approach optimizes an initial ‘guessed’ solution obtained by a similar χ^2 minimization, but this time solved in a matrix form of possible filtergram ratios fitted inside bins spaced along an empirical temperature range. The Cheung et al. [2015a] inversion (henceforth ‘C2015’) uses the Simplex algorithm to reduce a under-determined linear system, where the two independent variables are evenly spaced temperatures bins and the number of available filtergram intensities. Comparing the individual attempts should theoretically yield similar emission

measures, though differences will exist based on the assumptions implicit to each method. Section 3.3 presents the results of the three inversion methods.

We have developed scripts, pre-calibrations, and custom implementations of the methods described in the Aschwanden [2013], Hannah and Kontar [2012] and Cheung et al. [2015a] papers and public inversion codes. Additionally, the SDO-AIA response curves were customized to our observational parameters. We applied the temporal orbital degradation factor (via the *timedepend_date* keyword), normalize I using the SDO-EVE full disk measurements, an up-to date version of the CHIANTI [V8.0x; Del Zanna et al., 2015] atomic database, and the higher temperature and energy corrections that are not accounted by default in the CHIANTI database (*chiantifix* keyword). The H2012 and A2013 inversions do not account for the above corrections. By default, the schemes were using the response curves as simulated by the pre-flight and initial conditions as of May 2010. These corrections substantially alter the output results when compared to the outputs of the default inversion codes.

The energetic nature of jets still proves elusive when discussing plasma parameters in fine details. The literature results are quite divergent. Whether this is a result of individual interpretation and considered assumptions, or the energetic variance of individual small scale eruptions is quite high remains an open topic worth discussing. To our optimistic interpretation, the considered corrections will generate results that better approximate the observed plasma properties.

3.2.2 The Filter Ratio Technique

The most straightforward approach and interpretation of plasma emission measure and density determinations is a implementation of the ‘filter ratio technique’ used on Hinode XRT filter inversions [see Parashiv et al., 2015, Pucci et al., 2013]. This method requires prior knowledge of the temperature of the emitting plasma and assumes that the analyzed emitting volume is isothermal along the line of sight. As previously discussed, eq. (3.8) presents the general physical interpretation of a filtergram intensity signal. In practice the plasma’s emitting temperature (T_e) was assumed following the results of the T_e calculation done using the H2012 and C2015 methods. The local plasma density can be inferred via any two EM measurements in filters that have comparable response for a given temperature.

$$I_{fil} = F_{fil}(T_e) \cdot \int n_e^2 dz = F_{fil}(T_e) \cdot \int DEM(T_e) dT_e \quad [DN \cdot s^{-1} \cdot pixel^{-1}]. \quad (3.8)$$

When analyzing a particular observation the background emission can be subtracted. The remaining counts (Pixel Datanumbers, DN) correspond to to the quantity $I_{loop} - I_{bkg}$, where I_{loop} represents the emission of the studied hot structure and I_{bkg} represents the emission of the background corona. Usually plasma emission is attributed to both local background coronal and hot flaring components, e.g. $n_{e(obs)} = n_{e(bkg)} + n_{e(loop)}$. Rewriting eq. (3.8) the two emission components have the following form;

$$\begin{aligned} I_{cor} &= F_{fil}(T_e) \cdot \int_{-\infty}^{\infty} n_{e(bkg)}^2 dz, \\ I_{loop} &= F_{fil}(T_e) \cdot \left[\int_{-\infty}^{-z/2} n_{e(bkg)}^2 dz + \int_{-z/2}^{z/2} (n_{e(bkg)} + n_{e(loop)})^2 dz + \int_{z/2}^{\infty} n_{e(bkg)}^2 dz \right], \end{aligned} \quad (3.9)$$

where z is the width of the structure along the line of sight.

We can write down the equation for different individual AIA filter pairs, thus obtaining a 2^{nd} order linear system for any filter combination pair (eq. (3.10)) where $F_{fil}(T_e)$ is known because the temperature is assumed known. By cross-checking different filter combinations, similar results should theoretically be obtained. The method proved to be unsuited and unreliable output was produced when applied in practice in the case of our hot AIA footprint dataset. See section 3.3.1 for discussion.

$$\begin{aligned} (I_{loop} - I_{bkg})_{fil1} &= F_{fil1}(T_e) \cdot z \cdot (n_{e(loop)}^2 + 2 \cdot n_{e(loop)} \cdot n_{e(bkg)}), \\ (I_{loop} - I_{bkg})_{fil2} &= F_{fil2}(T_e) \cdot z \cdot (n_{e(loop)}^2 + 2 \cdot n_{e(loop)} \cdot n_{e(bkg)}). \end{aligned} \quad (3.10)$$

3.2.3 Single Gaussian Chi-square Minimization

Current inversion scheme solutions employ more robust mathematical methods in order to recover thermal structure from AIA filtergrams. The Chi-Square minimization [Pearson, 1900, Cochran, 1952] represents the backbone of most of the standard inversion procedures. Although both the H2012 and A2013 codes rely on the same mathematical method for inverting the six AIA channels, they exhibit a set of different implementations, physical and methodological assumptions, and outputs. The C2015 inversion uses a different scheme.

In the context of the A2013 [Aschwanden, 2013]¹ model, the χ^2 test can be computed pixelwise for a set of the above mentioned six observable AIA filtergrams intensities (I_{fil}) and their correspondent instrument temperature response functions (F_{fil}), see eq. (3.11).

$$\chi^2 = \sum_{i=1}^k \frac{(O_i - E_i)^2}{E_i} \implies \chi^2 = \frac{1}{3} \sum_{i=1}^6 \frac{(I_{fil[i]} - F_{fil[i]})^2}{\sigma_{I[i]}^2}. \quad (3.11)$$

The σ_I quantity represents the standard uncertainty in the individual AIA filter flux counts. This is the equivalent to the E_i term present in the standard definition of the χ^2 test representing a set of expected values. Equation (3.12) assumes that the fluxes are normalized both spatially and in the temporal domain. The flux was read pixelwise, and the exposures are normalized to $DN \cdot s^{-1}$ during the prep procedure. σ_I should not be confused with σ_{T_e} discussed below. The $1/(i - i_{free}) = 1/3$ factor comes from the third order degree of freedom of the parameters of the Gaussian fitted response functions.

$$\sigma_{I[i]} = \sqrt{I_{fil[i]}}, \quad \text{for } i \in [1, 6]. \quad (3.12)$$

The optimal (lowest χ^2) solution is selected from the total combinations of DEM solution space for the EM, T_e , and σ_{T_e} quantities. The T_e range was restricted to the $0.5 \leq T_e \leq 15$ MK, due to the problems arising in unreliable (low counts) in the bottom-low range and from ‘flat’ response function behavior at the end part of the sensitivity interval. A2013 recommends an even more constrained temperature range compared to our above mentioned T_e range but due to the fact that our events exhibit generally hot loops for which $T_e \geq 10$ MK we adopted a more relaxed restriction on the upper T_e limit while still obtaining reasonable uncertainties. The sampled temperature range was binned in equally spaced logarithmic intervals, which along with the multithermal plasma components affecting the temperature widths, will severely increase the χ^2 fit error estimates!

¹http://www.lmsal.com/aschwand/software/aia/aia_dem.html

The recovered plasma parameters should ideally represent an isothermal emission along the FOV of each pixel cross-section. This is the most important assumption that arises from such a determination, mainly due to the fact that it does not necessarily hold true for a generic examined coronal plasma. To get out of this predicament we need to introduce the σ_{T_e} parameter which represents a set of Gaussian temperature widths set to be equally spaced in the logarithmic T_e range that is taken into account when attributing the theoretical filter responses F_{fil} to the bins in the T_e range. Following the A2013 implementation we have used the $\sigma_{T_e} = [0.1, 0.2, \dots, 1.0]$ range.

The T_e quantity can thus be interpreted as an ‘emission measure weighted temperature’ [Aschwanden, 2013] where the dominant component of the emitting plasma is the base of the determination for a pixel FOV cross-section. The caveat of this estimation is the loss of information on potential secondary (non-dominant) emitting plasma at a different T_e bin that is outside the σ_{T_e} uncertainty of the dominating plasma. This aspect needs to be accounted for in our analysis as in multiple pixel location and time instances the emission of the jet material leaving the reconnection site is superimposed over the base flaring loops. In our determination, σ_{T_e} maps denote the selected temperature width from a set of iterable quantities) which is interpreted from a physical point of view as the temperature uncertainty in the EM (total flux) determination resulted from the minimum obtained χ^2 .

The recovered DEM,

$$DEM = \frac{1}{\Delta T} \sum_{i=1}^6 \frac{I_{fil[i]}}{F_{fil[i]}} \quad [\text{cm}^{-5} \cdot \text{K}^{-1}], \quad (3.13)$$

suffers from the same limitations discussed for T_e . The emission measure is correspondent to the best fit between the Gaussian modeled theoretical response functions and actual detected flux data. This means that we detect only the EM correspondent to plasma at a relative temperature T_e constrained by the σ_{T_e} width. As discussed above, the A2013 inversion returns only the DEM quantity correspondent to the peak T_e that was deduced. In order to recover the entire EM of the region (pixel) we have adopted the eq. (3.14) approximation. This is a simplification of the standard formulation used in literature (e.g. see eq. (5) from Aschwanden [2013]), but it is a sufficient determination given the large uncertainties involved.

$$EM = DEM \cdot \Delta T = DEM \cdot [(T_e + \sigma_{T_e}) - (T_e - \sigma_{T_e})] = DEM \cdot 2\sigma_{T_e} \quad [\text{cm}^{-5}]. \quad (3.14)$$

A simple but well established geometrical approximation [Susino et al., 2013, Aschwanden et al., 2013] was adopted,

$$n_{e-loop} = \phi \cdot \sqrt{\frac{EM}{z}} \quad [\text{cm}^{-3}]. \quad (3.15)$$

The z quantity represents the depth of the emitting region. Assuming a cylindrical geometry the quantity is approximated in practice to the width of the structure. The width (σ) can be measured by Gauss fitting the transversal edges of the structure then taking the FWHM parameter of the fit: $z = 2\sqrt{2\ln(2)} \cdot \sigma$ or measured pixelwise. Afterwards, the quantity is usually averaged across the length of the emitting structure. The loop filling factor ϕ represents a fractional amount of volume that is occupied by the emitting plasma. Naturally, this factor has a huge impact in the plasma density n_e determination. The observations that we employ do not permit us to get an estimate of this quantity, and thus we had used the

widely accepted assumption: $\phi = 1$, meaning that the entire deduced volume is completely filled with plasma.

3.2.4 Regularized Chi-square Minimization

The H2012 [Hannah and Kontar, 2012]² implementation relies on the same ‘ χ^2 test’ as a base, but uses a alternative approach. The authors present a regularization method based on resolving the AIA filter flux I_{fil} information as a linear system of six equations, one for each suitable AIA filter, as a function of the theoretical filter response functions F_{fil} as factors for twelve (unknown) $DEM(T_e)$ quantities of selected temperature intervals/bins.

We obtain an under-determined system which requires a set of external bounds/conditions for extracting any meaningful solutions. This system is transferred to matrix form and solved using a Singular Value Decomposition (SVD) scheme. This type of approach, although under different assumptions and conditions has been applied to a number of solar observing instruments and data (e.g. RHESSI: Lin et al. [2002], X-Ray spectra fitting: Kontar et al. [2004]). The regularized inversion methods became popular for solar observations. The main quoted strong points are:

- (i) The matrix formulation and subsequent SVD solver is operation-wise linear, making implementations fast.
- (ii) These methods produce faster and provide comparative results to more complex methods, e.g. second order SVD and maximum entropy regularizations. Judge et al. [1997] offers a comparison between these different methods and a broad discussion over the limitations on inverting emission line spectra.
- (iii) Linear error propagation also limits the uncertainty of the solutions producing, in theory, ‘smoother’ results (see Craig [1977], Craig and Brown [1986], and H2012 for detailed discussions).

Now, following the work of H2012 we can use the differential emission form of eq. (3.8) and introduce the unknown desired quantity $DEM(T_e)$. The term can be inserted into the minimization criterion from eq. (3.11) and solved as a linear system for the six filters along bins in the selected temperature range,

$$\chi^2 = \left[\frac{(I_{fil} - F_{fil} \cdot DEM(T_e))^2}{\sigma_I^2} \right] \rightarrow \min, \quad \text{where :} \quad \begin{array}{l} fil = [1, 6] \\ \log T_e = [5.7, 7.3] \end{array} \quad (3.16)$$

We can solve this linear system by imposing an additional condition in the form of Lagrangian multipliers,

$$\chi^2 = \left[\frac{(I_{fil} - F_{fil} \cdot DEM(T_e))^2}{\sigma_I^2} + \lambda (L \cdot (DEM(T_e) - DEM_0(T_e)))^2 \right] \rightarrow \min, \quad (3.17)$$

where L represents a constraint matrix, λ is the ‘regularization parameter’, and $DEM_0(T_e)$ represents an initial guess solution resulting from solving eq. (3.16). The optimal solution $DEM(T_e)$ with its correspondent regularization parameter λ can be obtained analytically following the results from the Hansen [1992] generalized SVD solution, see Hannah and

²<http://www.astro.gla.ac.uk/iain/demreg/>

Kontar [2012, eq. 6]. It is worth noting that due to background subtraction procedures or large uncertainties that may be present in the I_{fil} or $F_{fil}(T_e)$ quantities, a positive (physical!) solution for DEM_{T_e} can not be guaranteed mathematically. Due to this a λ regularization parameter is selected only if $DEM_{T_e} > 0$, i.e the minimum regularized solution which returns a positive emission measure.

The implementation runs the optimization two times: an initial guess followed by a more refined/constrained solution. For the initial guess, eq. (3.17) is minimized considering $DEM_0(T_e) = 0$. The solution ($DEM_{guess}(T_e)$) obtained is usually ‘weakly regularized’, $\chi^2 > 10$. The constraint matrix is set to $L = I$. From a physical point of view, this represents a zero-order constraint, i.e. the smallest amount of plasma that can model the observed fluxes.

The second minimization run takes $DEM_0(T_e) = DEM_{guess}(T_e)$ expecting a goodness of fit $\chi^2 < 2$. The result $DEM(T_e)$ is analytically the result of an unknown differential equation encompassing: heating, cooling, radiative, heat transport, etc. terms. It is normally a differentiable quantity itself and we have set-up and $d DEM(T_e) = L$ as its first derivative following Kontar et al. [2004] and Hannah and Kontar [2012]. Depending on case by case conditions a $DEM(T_e)$ solution can be obtained using higher order L derivatives constraints. This would also shift the weight from the input data in favor of the guesstimate constraints. H2012 state that such a further constraint may be useful in cases of uncertain data measurements, but ultimately it is left to the observer to judge the applicability of each of these discussed adjustments.

Our Geyser footprint average n_e was also derived via the recovered emission distribution resulting from the H2012 regularization method discussed above, taking into account the eq. (3.15) and the previously stated assumptions. The implementation is used to invert the six filter response F_{fil} into the emission measure and via further manipulations, the electron temperature(T_e) quantity can be obtained. This operation is done on a per pixel basis and results are presented as total EM distribution across temperature bins for one time instance over a selected jet region. The H2012 solution for our geyser is depicted in fig. 3.1.

The H2012 method does not resolve only the peak EM measured around the dominant T_e as the A2013 approximation does, but fits the total recovered EM into temperature bins inside the selected temperature region. Loop and jet plasma T_e determination is done after background corona subtraction via $I - I_0 \leftrightarrow EM - EM_0$ leaving only the EM of geyser loop plotted versus plasma temperature. We have fit the EM distribution peaks with a Gaussian function, helping us obtain a average emitting plasma temperature.

3.2.5 Sparse Inversion and Minimization

Suppose we arrange the SDO-AIA inversion problem as an under-determined 2^{nd} order linear system. The temperature response range can be divided into equally spaced logarithmic intervals $T_j + \Delta T_j$. Thus eqs. (3.4) and (3.5) become

$$I_i = \sum_{j=0}^{20} \int_{T_j}^{T_j+\Delta T_j} G_i(T_j) \cdot DEM(T_j) dT_j \rightarrow I_i = \sum_{j=0}^{20} G_{ij} \cdot EM_j. \quad (3.18)$$

assuming that $G(T)$ is averaged across one temperature interval. I is a vector of six observed SDO-AIA intensities and EM represents a yet unknown solution vector. Theoretically, $m = 6$; $0 \leq i \leq 5$ accounting for the available SDO-AIA filter observations, and $n = 21$; $0 \leq j \leq 20$ to account for equally spaced bins along the $\log T_e = [5.7, 7.7]$ range. In practice

the temperature is constrained to a smaller domain due to the uncertainty in the SDO-AIA response data. Nonetheless, in the case of SDO-AIA observations $m < n$ will hold true. The equation system $I_i = G_{ij} \cdot EM_j$ is severely under-determined in temperature, giving a space of potential EM solutions.

The C2015 [Cheung et al., 2015a]³ solution addresses the inversion using an alternative minimization scheme, not based on the χ^2 principle. The main goal is to converge on a particular solution from the solution set of the above defined system. As expected, that solution must also best model the underlying physical conditions and assumptions. Sparse solutions have been shown by Candes and Tao [2006, 2007] to better reproduce under-determined signal data when compared with χ^2 , minimum energy, and least squares minimizations. Formally we can state the approach as

$$G_{ij} \cdot EM = I_i, \quad \text{where:} \quad EM = \sum_{j=0}^{20} EM_j \text{ and } EM \rightarrow \min. \quad (3.19)$$

C2015 acknowledge that the solution is not a physically constrained procedure in terms of plasma physical properties. Additional constraints need to be enforced in the minimization of eq. (3.19) in order to converge on a physically plausible solution.

$$\sum_{j=0}^{20} EM_j \rightarrow \min, \quad \text{constrained by:} \quad \begin{array}{l} EM \geq 0 \\ I - \sigma \leq G \cdot EM \leq I + \sigma \quad \text{if } I > \sigma \end{array} \quad (3.20)$$

In practice the $\sum_{j=0}^{20} EM_j$ is minimized taking into account that the EM_j solutions need to be positively defined. Also, due to uncertainties in the filtergram intensities I_i , the solution space is allowed to slightly deviate from the rigid interpretations given by eqs. (3.5) and (3.18). This deviation can just be modeled using a simple Gaussian like sigma, similar to eq. (3.12). C2015 employ a more physically constrained model, by setting the deviation value equal to the more complex SDO-AIA computed uncertainty obtained via Solarsoft's *aia_bp_estimate_error.pro*. The routine returns statistical errors along with uncertainties resulting from instrumental errors.

Lower count filters such as AIA-94Å may not always record datanumbers higher than the σ error estimation for regions that are characterized by lower temperature coronal plasma. In such cases the left side of the double inequality constraint from eq. (3.20) is set to '0' in order to force the positivity of recovered EM solutions. The inversion method is relying on L1 norms, which can be solved by very fast computational schemes (in this case, the simplex algorithm is utilized). The solution is characterized by a low number of initial constraints, does not overfit the data by adding additional assumptions, e.g. regularization or parametrization, and naturally forces positive (physically relevant) EM. Under these arguments, C2015 convincingly argue that the method is consistent with the Ockham's Razor aphorism.

³<http://tinyurl.com/aiadem>

3.3 Geyser EUV Thermal Emission

3.3.1 The Footpoint Emission Measure of the J2, J3, and J6 Eruptions

In order to estimate the EM and energetic partition using our selected inversion methods, we need to first discuss the geometric underpinning of the three footpoint structures presented in fig. 3.1. The footpoint's rough physical dimensions are estimated using the AIA-131Å and AIA-94Å filtergrams. The two filters are adequate in representing hot loop morphologies due to their high temperature sensitivity, while the other four are not satisfactory as they manifest in lower temperature regimes and all filters seem to exhibit localized intensity saturated pixels. Fully saturated pixels were excluded from measurements. This aspect will induce uncertainties in the EM determinations that will be discussed herein.

The filtergram background and flaring intensities I are calculated. Figure 3.1 depicts the temporal evolution of the recorded AIA counts correspondent to our jet events. The intensity is averaged across the footpoint region. Summarily, one could start discussing the emission evolution from such plots. We select the AIA-171Å filter and isolate one data subset without footpoint activity to sample the background coronal intensity. The same interval can be chosen for both J2 and J3 events. This corresponds to observations between 01:00-01:08 where no footpoint emission could be detected. The total background average is $I_{171} = 1334$ DN.

Analogously, we can choose the background conditions corresponding to J6. In this case three data subsets without footpoint activity were chosen to sample the background

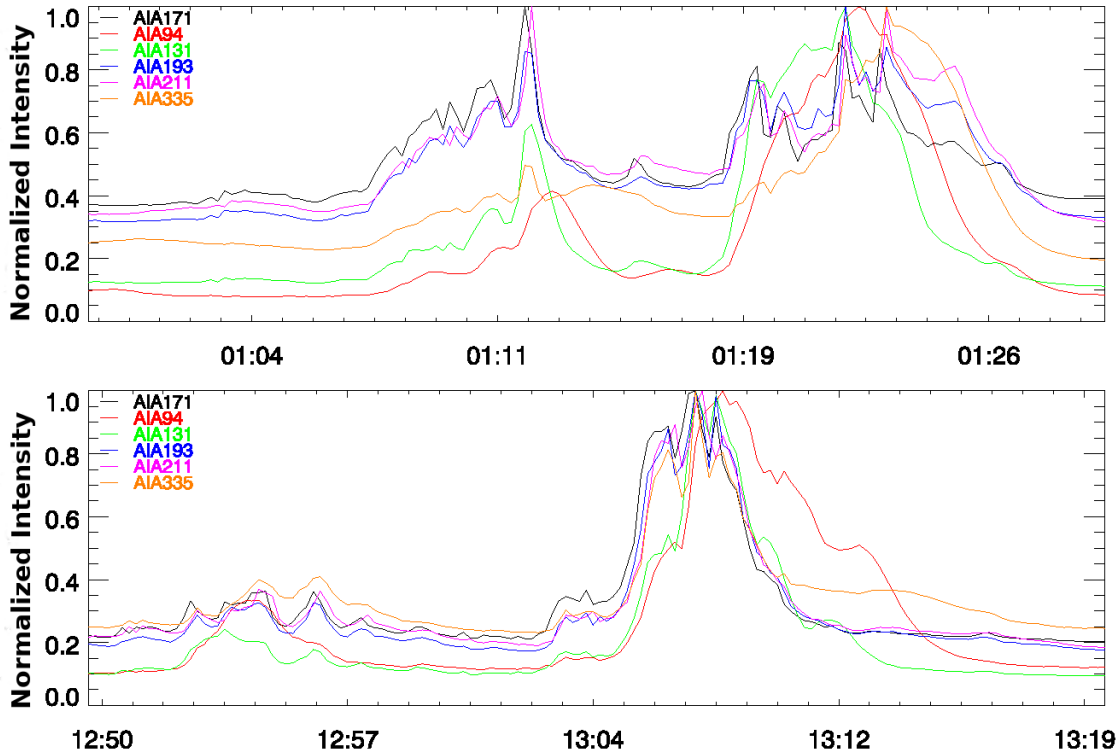


Figure 3.1: Total Intensity timeseries of the six utilized SDO-AIA filters, temporally centered around the three eruptions. Pixel intensity was averaged inside the individual footpoint borders, illustrated by the contour of the AIA-131Å sub-panel of fig. 3.2. The upper panel corresponds to the temporally close J2 and J3 events while the bottom panel corresponds to the J6 jet event.

intensity. Two of them before the jet eruptions and one after the flaring event. These are: 12:50-12:52 where $I_{171} = 1040$ DN, 12:57:00-13:03 where $I_{171} = 1066$ DN, and 13:11-13:19 with $I_{171} = 1070$ DN. Total background average counts are $I_{171} = 1059$ DN. As can be seen, the two sets of measurements are comparable, although separated temporally by 12 hours. Would this status hold true during the main eruption times?

The J2 flaring $I_{171} = 2175$ DN (01:09:01:13) and J3 flaring $I_{171} = 2141$ DN (01:19-01:24) are next to identical. The J6 counts, $I_{171} = 4887$ DN (13:06-13:10) are substantially higher. One could associate the AIA-171Å to its main emission component and state that in this case, we are looking at plasma around $1 \cdot 10^6$ K and that there is a significant difference in density between events in the order of 2. Note that these results are correspondent to just the AIA-171Å filter. We will discover that in the case of the J2 and J3 similar counts, the actual *DEMs* are not that similar as they currently appear. This reasoning can be extended to multiple filters, leading eventually to inconclusive analyses, some which do not even attempt to produce filtergram inversions. As described in section 3.1, these discussions are ill-suited to filtergram coronal observations. We do take note of the obtained background versus flaring conditions separation into temporal subsets. The background and flare condition DEM derived further-on rely on the above determination as five out of the six SDO-AIA filters exhibit nearly identical temporal response. The AIA-94Å filter reveals a consistent small time delay of perceivable 12 – 24 s (constrained by the 12 s data cadence) at each eruption onset, followed by a slower cooling phase towards background emission when compared with the other filtergrams.

In order to accurately recover the footpoint EM, some geometrical approximations of the studied structure are required. The geometry of the three footpoints is revealed by the AIA-94Å and AIA-131Å filters in which two main loops can be distinguished. Due to projection effects these flaring loops are not easily separated. Notably, the loops have a typical diameter of $5.65 \pm 1 \text{ pix} = 2467 \pm 436 \text{ km}$, irrespective of the individual jets. Assuming a cylindrical geometry, the loop width can be used in order to approximate the depth of the emitting region. Additionally, the width (W) and height (H) of the emitting structure can be recovered. The total width of the emitting structure does not represent the sum of the individual widths as the features are intertwined, but is obtained as an average width across the length, including the areas where the two loops appear separated. The separation area, although rather large in appearance, exhibits systematic stronger emission than the background along all SDO-AIA filters thus being included in the width estimation.

J2 width: $W = 11 \pm 2 \text{ pix} \rightarrow 4798 \pm 872 \text{ Km}$.

Height of both J2 loops: $H = 41 \pm 3 \text{ pix} \rightarrow 17889 \pm 1308 \text{ Km}$.

J3 width: $W = 9 \pm 2 \text{ pix} \rightarrow 3926 \pm 872 \text{ Km}$.

Height of both J3 loops: $H = 48 \pm 3 \text{ pix} \rightarrow 20972 \pm 1308 \text{ Km}$.

J6 width: $W = 14.1 \pm 3 \text{ pix} \rightarrow 6150 \pm 1308 \text{ Km}$.

Height of the J6 loops: $H_a = 39.5 \pm 3 \text{ pix} \rightarrow 17220 \pm 1308 \text{ Km}$.

$H_b = 28.2 \pm 3 \text{ pix} \rightarrow 12300 \pm 1308 \text{ Km}$.

The measurements influenced by projection effects. In the case of J6, we chose H_a as being the footpoint height. The total contour area is represented by the contours of fig. 3.2, AIA-131Å sub-figures. Comparative physical dimensions are summarized in table 3.2.

The J2, J3, and J6 plasma n_e can be possibly obtained via careful selection of filter ratio measurements assuming isothermal plasma, prior knowledge of the T_e quantities, and taking into account expected n_e values. Filter ratio based estimations were previously used in the context of solar jets [Pucci et al., 2013, Paraschiv et al., 2015], although applied to

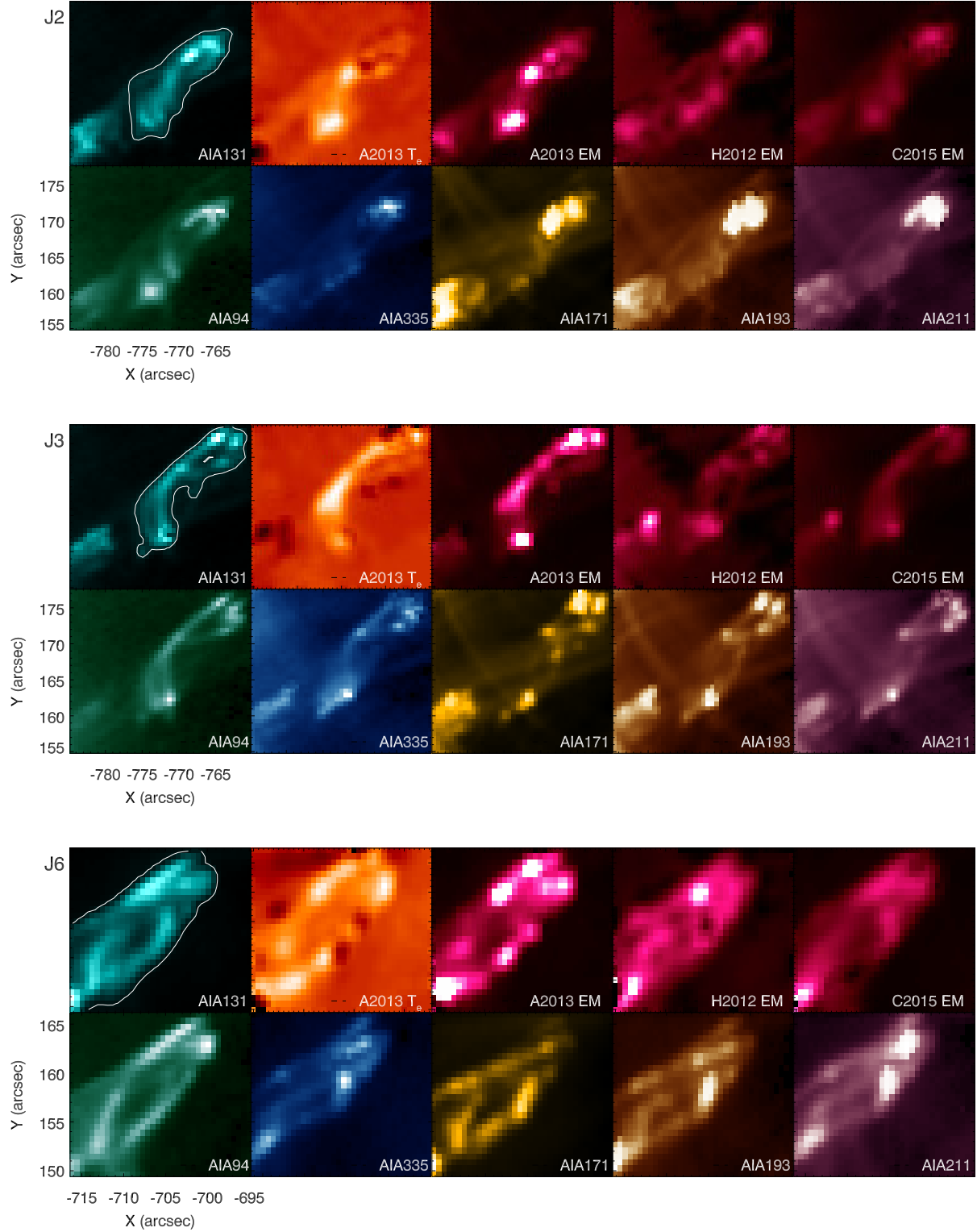


Figure 3.2: Observational features of the footpoint structures during the main phase corresponding to the J2, J3, and J6 events. The Coronal Geyser is revealed in each SDO filtergram, DEM inversion, and peak temperature maps around maximum flaring times: 01:13:00UT for J2 (Upper), 01:19:00UT for J3 (Middle), and 13:08:24UT for J6 (Bottom) respectively. Each of the depicted AIA filters exhibits a unique morphology, where the AIA-131Å and AIA-94Å filters are the closest to resembling the DEM emission maps. The contours correspondent to the AIA-131Å sub-panels represent the distinct borders of the observed flaring footpoints, at peak emission time and corresponding to each event. The total EM maps are plotted inside the $[5 \cdot 10^{27}, 5 \cdot 10^{28}]$ interval and the A2013 T_e map is plotted inside the $\log T_e = [5.7, 7.0]$ K interval

different types of observations. The method keynotes are described in section 3.2.2. For the set of AIA filter pairs, assuming an emission depth of $z \sim 2400$ km, we postulate that the footpoint is multithermal in nature and has two emitting plasma components at dominant temperatures of $\log T_e = 6.3$ and $\log T_e = 7.0$. The footpoint's EM peaks are quantitatively estimated via the more advanced A2013, H2012, and C2015 inversion methods. We thus obtain averaged 'filter ratio' DEM estimations.

$$J2 \rightarrow n_{e(loop)} = 0.45 \cdot 10^{11} \text{ cm}^{-3} \text{ and } n_{e(bkg)} = 0.24 \cdot 10^{11} \text{ cm}^{-3} \text{ obtained for } \log T_e \sim 7.0 K.$$

$$n_{e(loop)} = 1.64 \cdot 10^{11} \text{ cm}^{-3} \text{ and } n_{e(bkg)} = 1.10 \cdot 10^{11} \text{ cm}^{-3} \text{ obtained for } \log T_e \sim 6.3 K.$$

$$J3 \rightarrow n_{e(loop)} = 0.48 \cdot 10^{11} \text{ cm}^{-3} \text{ and } n_{e(bkg)} = 0.23 \cdot 10^{11} \text{ cm}^{-3} \text{ obtained for } \log T_e \sim 7.0 K.$$

$$n_{e(loop)} = 2.17 \cdot 10^{11} \text{ cm}^{-3} \text{ and } n_{e(bkg)} = 1.87 \cdot 10^{11} \text{ cm}^{-3} \text{ obtained for } \log T_e \sim 6.3 K.$$

$$J6 \rightarrow n_{e(loop)} = 0.97 \cdot 10^{11} \text{ cm}^{-3} \text{ and } n_{e(bkg)} = 0.44 \cdot 10^{11} \text{ cm}^{-3} \text{ obtained for } \log T_e \sim 7.0 K.$$

$$n_{e(loop)} = 0.25 \cdot 10^{11} \text{ cm}^{-3} \text{ and } n_{e(bkg)} = 0.17 \cdot 10^{11} \text{ cm}^{-3} \text{ obtained for } \log T_e \sim 6.3 K.$$

Although the hot temperature values are relatively correspondent to the other inversion attempts described below, the EM correlated to the lower temperature bin is at least one order of magnitude higher. This may be explained by multiple reasons. For example, one cause may be the saturated pixels, of most of the 'low temperature' filters which would contribute towards miscalculating ratios, thus giving erroneous assessments of the local plasma conditions. This can possibly also explain why the hotter temperature estimations are close to the other determinations: part of the AIA filters are not very responsive to hot temperatures and usually do not saturate when exposed to hotter emission. A filter ratio methodology is generally not suitable in the case of SDO-AIA observations. Our initial hypothesis was to evaluate if under certain special conditions (e.g. assuming an expected near-isothermal temperature), specific filtergram ratios may prove to reflect credible plasma parameters, (e.g. AIA-94Å vs AIA-131Å for $\log T_e \sim 7.0$ or AIA-171Å vs AIA-193Å for $\log T_e \sim 6.3$). We could not identify any reliable filter combination. The main filter ratio results are summarized in table 3.1.

Table 3.1: *J2, J3, and J6 footpoint plasma density [$n_e \cdot 10^{11} \text{ cm}^{-3}$] for all possible SDO-AIA filter pair combinations derived via the filter ratio formulations described in section 3.2.2. The determinations are performed for the two distinct emitting temperature regimes of $\log T_e \sim 7.0$ and $\log T_e \sim 6.3$. The method proved invalid as the filter ratio results are inconsistent across the SDO-AIA filtergram ratios.*

AIA Ratio	$J2_{loop}$		$J2_{bkg}$		$J3_{loop}$		$J3_{bkg}$		$J6_{loop}$		$J6_{bkg}$	
	6.3	7.0	6.3	7.0	6.3	7.0	6.3	7.0	6.3	7.0	6.3	7.0
94/131	1.13	0.09	1.67	0.05	2.25	0.16	3.70	0.13	0.37	0.14	0.03	0.13
94/171	2.11	0.89	0.89	0.01	2.34	0.75	3.56	0.03	0.15	1.62	0.09	0.01
94/193	1.79	0.44	1.13	0.01	2.87	0.57	4.06	0.05	0.09	0.78	0.15	0.02
94/211	1.47	0.58	1.28	0.01	2.25	0.60	3.69	0.04	0.09	1.14	0.16	0.01
94/335	1.46	0.18	1.29	0.02	2.63	0.29	3.16	0.07	0.11	0.28	0.12	0.06
131/171	2.29	0.89	0.23	0.01	1.81	0.76	0.86	0.02	0.21	1.62	0.35	0.01
131/193	1.95	0.44	0.27	0.01	2.05	0.49	0.76	0.03	0.19	0.88	0.38	0.01
131/211	1.54	0.57	0.34	0.01	1.54	0.60	1.01	0.03	0.19	1.14	0.39	0.01
131/335	1.52	0.18	0.35	0.03	2.54	0.30	0.61	0.05	0.21	0.29	0.37	0.04
171/193	1.81	0.51	1.58	0.78	2.01	0.49	1.06	0.61	0.09	0.92	0.16	1.43
171/211	1.57	0.56	1.83	0.71	1.56	0.55	1.37	0.54	0.09	1.07	0.16	1.23
171/335	1.56	0.45	1.84	0.87	2.48	0.42	0.86	0.70	0.12	0.83	0.13	1.60
193/211	1.49	0.51	1.43	0.20	1.61	0.54	1.66	0.23	0.05	1.04	0.03	0.30
193/335	1.48	0.25	1.44	0.43	2.45	0.31	1.09	0.41	0.11	0.43	0.01	0.73
211/335	1.44	0.31	0.98	0.55	2.54	0.36	0.62	0.53	0.11	0.59	0.01	1.11

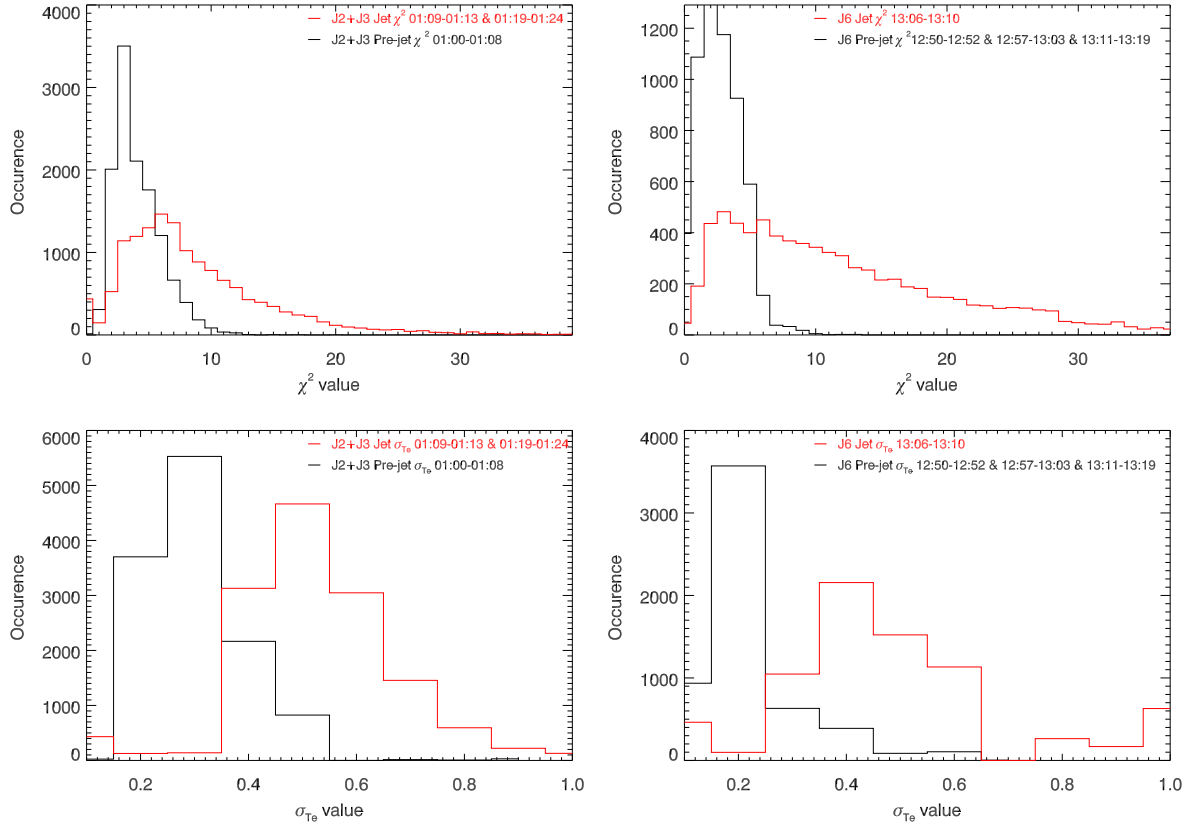


Figure 3.3: SDO-AIA A2013 χ^2 inversion uncertainty distributions inside the selected jet emitting region. **Upper Panel:** Histograms of χ^2 fit goodness for quiet (background) conditions as compared to peak flaring time. **Bottom Panel:** Histograms of the temperature widths σ_{T_e} comparing quiet sun and peak flaring conditions. The distributions are comprised from the individual fitting results of the pixels corresponding to the footpoint area and across the temporal domain corresponding to flaring and quiet sun conditions. The H2012 χ^2 results exhibit an analogous behavior.

A practical consideration on the validity of inversion methods is provided by the estimations presented in fig. 3.3. The errors corresponding to the A2013 method are presented, representing a standardized picture of inversions, especially χ^2 based methods. For a generic coronal plasma, the fitting residuals are small (< 4) indicating a well constrained solution. This behavior follows the standard (and rather optimistic!) estimates of the literature [Aschwanden and Boerner, 2011]. Analyzing the same fitting results we find that accuracy is lost during peak flaring times. This effect occurs due to the saturation of some filters which generates non-physical ratios. It is worth noting that our events exhibit only very few saturated pixels in small localized patches, under 10% of the total region. Any result should be only evaluated as an order of magnitude estimate. Additionally, the uncertainty given by the maximum temperature width σ_{T_e} detected pixel-wise inside the flaring time interval is also severely increasing when compared to quiet sun conditions. The J2 and J3 errors, even in quiet conditions are higher than the ones depicted for J6. The issue most probably originates from projection effects and hot loops from above the emission site that are not easily removed by background subtraction due to their dynamics.

The A2013 methodology described in section 3.2.3 allows us to estimate a total emission of plasma from a volume along with an emission measure weighted average temperature. No further splitting of the EM in temperature bins is possible. The temporal evolution of the emission measure is presented fig. 3.4 (upper panel). The Gaussian is fitted inside a

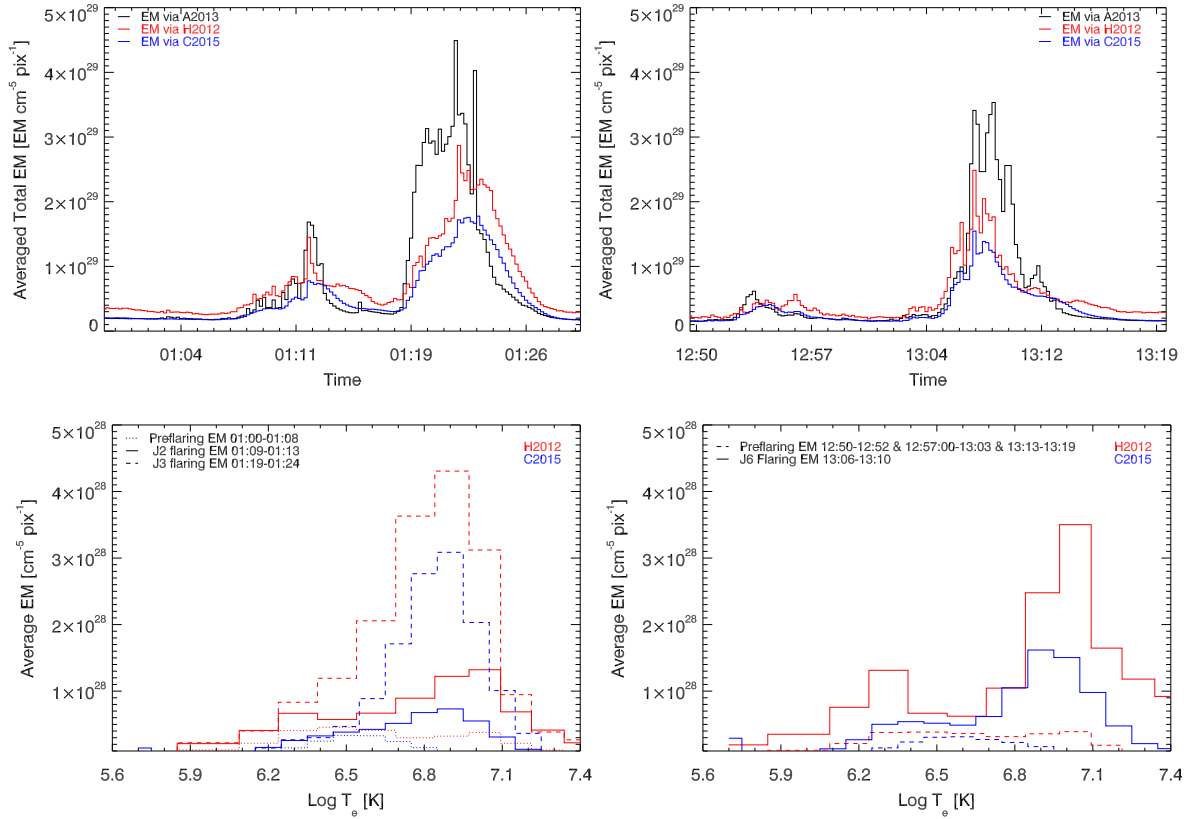


Figure 3.4: SDO-AIA EM results corresponding to the three analyzed flaring events of the geyser footpoints recovered via the three alternative inversion approaches. Values are averaged across the footpoint areas. **Upper Panel:** Total average emission measure over the dominant $T_e \pm \sigma_{T_e}$ range for A2013, and across the $\log T_e \sim [5.7, 7.3]$ temperature space recovered from the H2012 and C2015 inversion methods. A general agreement occurs between the different approaches, though small systematic differences can be seen manifesting. **Bottom Panel:** Temporally averaged emission measure plotted against the electron T_e bins for the selected temporal subsets of quiet and flaring plasma conditions via H2012 and C2015 inversions. The different events exhibit their unique emission temperature distributions.

temperature space in the range of $\log T_e = [5.7, 7.3]$. As previously discussed, the A2013 method will fit in a region that may well be multithermal due to the projection of the main jet emitting material above the flaring site. The temperature estimation depends on the actual emission measure distribution along the temperature space, a property which is not recovered directly by using this simplified type of modeling. Nonetheless, all three recorded events are reasonably well constrained emission measure wise.

The main A2013 results are summarized below (see section 3.2.3).

$$Bkg_{J2} \rightarrow EM_0 = 0.19 \pm 0.04 \cdot 10^{29} \text{ cm}^{-5} \text{ for } \log T_e = 6.43 \pm 0.18K \rightarrow n_e = 0.09 \cdot 10^{11} \text{ cm}^{-3}.$$

$$J2 \rightarrow EM = 0.76 \pm 0.18 \cdot 10^{29} \text{ cm}^{-5} \text{ for } \log T_e = 6.58 \pm 0.22K \rightarrow n_e = 0.18 \cdot 10^{11} \text{ cm}^{-3}.$$

$$J3 \rightarrow EM = 2.52 \pm 0.34 \cdot 10^{29} \text{ cm}^{-5} \text{ for } \log T_e = 6.80 \pm 0.24K \rightarrow n_e = 0.32 \cdot 10^{11} \text{ cm}^{-3}.$$

$$Bkg_{J6} \rightarrow EM_0 = 0.16 \pm 0.03 \cdot 10^{29} \text{ cm}^{-5} \text{ for } \log T_e = 6.41 \pm 0.16K \rightarrow n_e = 0.08 \cdot 10^{11} \text{ cm}^{-3}.$$

$$J6 \rightarrow EM = 1.96 \pm 0.10 \cdot 10^{29} \text{ cm}^{-5} \text{ for } \log T_e = 6.63 \pm 0.25K \rightarrow n_e = 0.28 \cdot 10^{11} \text{ cm}^{-3}.$$

The global EM recovered using the H2012 and C2015 methods are assessed below. Both inversions give solutions for higher temperature bins. However, we choose to limit the above sums to $\log T_e < 7.30$ due to the uncertain solutions given that the temperature response is mostly flat for high temperatures. This further emphasizes that our DEM results are likely under-determined. Using the same temporal slots we derived averaged background and jet total EM along the full temperature range for all events.

Average footpoint results recovered via the H2012 regularization inversion (see section 3.2.4):

$$Bkg_{J2} \rightarrow EM_0 = 0.19 \pm 0.14 \cdot 10^{29} \text{cm}^{-5} \text{ for } \log T_e = [5.7, 7.3] \rightarrow n_e = 0.09 \cdot 10^{11} \text{cm}^{-3}.$$

$$J2 \rightarrow EM = 0.73 \pm 0.21 \cdot 10^{29} \text{cm}^{-5} \text{ for } \log T_e = [5.7, 7.3] \rightarrow n_e = 0.17 \cdot 10^{11} \text{cm}^{-3}.$$

$$J3 \rightarrow EM = 1.74 \pm 0.22 \cdot 10^{29} \text{cm}^{-5} \text{ for } \log T_e = [5.7, 7.3] \rightarrow n_e = 0.26 \cdot 10^{11} \text{cm}^{-3}.$$

$$Bkg_{J6} \rightarrow EM_0 = 0.21 \pm 0.16 \cdot 10^{29} \text{cm}^{-5} \text{ for } \log T_e = [5.7, 7.3] \rightarrow n_e = 0.09 \cdot 10^{11} \text{cm}^{-3}.$$

$$J6 \rightarrow EM = 1.46 \pm 0.24 \cdot 10^{29} \text{cm}^{-5} \text{ for } \log T_e = [5.7, 7.3] \rightarrow n_e = 0.24 \cdot 10^{11} \text{cm}^{-3}.$$

Average footpoint results recovered via the C2015 sparse inversion (see section 3.2.5):

$$Bkg_{J2} \rightarrow EM_0 = 0.16 \pm 0.12 \cdot 10^{29} \text{cm}^{-5} \text{ for } \log T_e = [5.7, 7.3] \rightarrow n_e = 0.08 \cdot 10^{11} \text{cm}^{-3}.$$

$$J2 \rightarrow EM = 0.48 \pm 0.18 \cdot 10^{29} \text{cm}^{-5} \text{ for } \log T_e = [5.7, 7.3] \rightarrow n_e = 0.14 \cdot 10^{11} \text{cm}^{-3}.$$

$$J3 \rightarrow EM = 1.33 \pm 0.22 \cdot 10^{29} \text{cm}^{-5} \text{ for } \log T_e = [5.7, 7.3] \rightarrow n_e = 0.23 \cdot 10^{11} \text{cm}^{-3}.$$

$$Bkg_{J6} \rightarrow EM_0 = 0.15 \pm 0.12 \cdot 10^{29} \text{cm}^{-5} \text{ for } \log T_e = [5.7, 7.3] \rightarrow n_e = 0.08 \cdot 10^{11} \text{cm}^{-3}.$$

$$J6 \rightarrow EM = 0.98 \pm 0.19 \cdot 10^{29} \text{cm}^{-5} \text{ for } \log T_e = [5.7, 7.3] \rightarrow n_e = 0.19 \cdot 10^{11} \text{cm}^{-3}.$$

As can be seen, the three measurements are compatible, noting that the C2015 emission measure is lower. The background quiet coronal emission also appears negligible when compared to flaring periods. The total EM plotted in fig. 3.4 (upper panel) can be further refined on a case by case basis by assessing the temperature distribution of the emission. In fig. 3.4 (bottom panel), the H2012 and C2015 inversion results are depicted for the time-frame of maximum emission. Both distributions exhibit the same EM curve with a small non-agreement in the low temperature bins ($\log T_e < 6.0$) and a strong disagreement at very high temperatures ($\log T_e > 7.3$) that is excluded by omitting the respective bins. A subset of T_e intervals are selected as peak emission temperatures with ΔT_e widths for each flaring event.

Figure 3.4 (bottom left) depicts the J2 and J3 geyser footpoint emission measures. The J2 footpoint emits in two distinct temperature spaces. Gaussian fitting over each of the two observed temperature peaks reveals centers at $\log T_e \sim 6.40 \pm 0.20$ K and $\log T_e \sim 7.00 \pm 0.19$ K. A one Gaussian fit over the two temperature sub ranges revealed the J2 region averaged temperature $\log T_e = 6.70 \pm 0.22$ K comparable to the result of the A2013 method. Although the emission is probably separated, the hot temperature component is dominating and it almost completely blends with the lower EM peak.

J3 manifests a higher temperature regime. A Gaussian fit over the one detected temperature peak reveals the center at $\log T_e \sim 6.75 \pm 0.45$ K. Notice the very wide temperature width. The value is very close to the A2013 determination, since in this case, the fitting parameters coincide and the more meticulous H2012 and C2015 inversions can be approximated with the A2013 method.

The J6 footpoint presents a consistent double peak flaring, see fig. 3.4 (bottom right). Gaussian fitting over each temperature peak reveals peak emission measures centered at $\log T_e \sim 6.30 \pm 0.15$ K and $\log T_e \sim 7.00 \pm 0.20$ K. The region averaged $\log T_e = 6.67 \pm 0.28$ K, as expected from the A2013 determination.

In order to refine our determination we have utilized the H2012 and C2015 temperature distributions to limit the emission measure over the above defined dominant temperature ranges. Using the same temporal slots as in the case of A2013 we calculated the geyser footpoint region averaged total emission measure using H2012:

$$\begin{aligned}
J2 \rightarrow & EM = 0.23 \pm 0.09 \cdot 10^{29} \text{ cm}^{-5} \text{ for } \log T_e = [6.17, 6.60] \rightarrow n_e = 0.09 \cdot 10^{11} \text{ cm}^{-3}. \\
& EM = 0.41 \pm 0.12 \cdot 10^{29} \text{ cm}^{-5} \text{ for } \log T_e = [6.77, 7.14] \rightarrow n_e = 0.13 \cdot 10^{11} \text{ cm}^{-3}. \\
J3 \rightarrow & EM = 1.60 \pm 0.22 \cdot 10^{29} \text{ cm}^{-5} \text{ for } \log T_e = [6.30, 7.14] \rightarrow n_e = 0.26 \cdot 10^{11} \text{ cm}^{-3}. \\
J6 \rightarrow & EM = 0.27 \pm 0.10 \cdot 10^{29} \text{ cm}^{-5} \text{ for } \log T_e = [6.17, 6.47] \rightarrow n_e = 0.10 \cdot 10^{11} \text{ cm}^{-3}. \\
& EM = 0.87 \pm 0.42 \cdot 10^{29} \text{ cm}^{-5} \text{ for } \log T_e = [6.77, 7.14] \rightarrow n_e = 0.19 \cdot 10^{11} \text{ cm}^{-3}.
\end{aligned}$$

The Geyser's footpoint average EM measurements using the C2015 inversion:

$$\begin{aligned}
J2 \rightarrow & EM = 0.16 \pm 0.09 \cdot 10^{29} \text{ cm}^{-5} \text{ for } \log T_e = [6.10, 6.60] \rightarrow n_e = 0.08 \cdot 10^{11} \text{ cm}^{-3}. \\
& EM = 0.23 \pm 0.12 \cdot 10^{29} \text{ cm}^{-5} \text{ for } \log T_e = [6.80, 7.20] \rightarrow n_e = 0.10 \cdot 10^{11} \text{ cm}^{-3}. \\
J3 \rightarrow & EM = 1.20 \pm 0.22 \cdot 10^{29} \text{ cm}^{-5} \text{ for } \log T_e = [6.30, 7.20] \rightarrow n_e = 0.23 \cdot 10^{11} \text{ cm}^{-3}. \\
J6 \rightarrow & EM = 0.18 \pm 0.10 \cdot 10^{29} \text{ cm}^{-5} \text{ for } \log T_e = [6.20, 6.50] \rightarrow n_e = 0.09 \cdot 10^{11} \text{ cm}^{-3}. \\
& EM = 0.56 \pm 0.42 \cdot 10^{29} \text{ cm}^{-5} \text{ for } \log T_e = [6.80, 7.20] \rightarrow n_e = 0.15 \cdot 10^{11} \text{ cm}^{-3}.
\end{aligned}$$

3.3.2 Jet Outflow Emission Measure Profiles of the J2, J3, and J6 Eruptions

A few methodological differences exist between the main jet and footpoint DEM analysis. In the case of the three jet structures we aim at revealing the untwisting strands that comprise the observed events. Any temporal data average would smooth out these details. Additionally, when compared to the footpoint emission measure, the jet body emission is fainter resulting in no filtergram intensity saturation, leading to better constrained results comparable with the Aschwanden and Boerner [2011] estimation and the background condition uncertainties discussed in section 3.3.1.

We have selected one time instance in which the jets bodies can be seen as separated from the footpoint and each event was enveloped in a distinct region of interest. The jets were then analyzed in the background subtracted regions. For comparison, this procedure was repeated for two additional frames, situated ± 12 s before and after the main selected frames, revealing no substantial differences in the temperature distributions of inverted emission measures. The standard lifetimes of jet eruptions is > 2 min. Following these suppositions, a timeseries evolution of the three jet eruptions is depicted in fig. 3.5. The detailed EM distributions are presented in fig. 3.6. Figures 3.7 and 3.8 portrays the temperature constrained emission measure maps correspondent to the three jets via the H2012 and C2015 methods.

The temporal behavior of the jet eruptions is presented in fig. 3.5 as resulting from all inversion methods. The background coronal contribution is not subtracted in this case as will return non-physical results outside the jets main eruption times. The A2013 inversion returns by default the averaged DEM due the method's assumptions (see section 3.2.3). In order to recover an integral EM for comparison to the C2015 and H2012 results we employ the approximation given by eq. (3.14). Our application of the H2012 method utilizes eq. (3.7) in order to convert from DEM to EM values. We obtain systematic slightly lower emission measure via the C2015 method as analogous to the footpoint analysis results. Nonetheless, the quantities are in general agreement. The Gaussian average emitting temperature was obtained via the A2013 inversion.

The J2 eruption exhibits a very peculiar temporal profile as the average temperature in the selected region actually decreases while the EM slightly increases. The 'high' background pre-jet temperature can be linked to hot plasma rain atop the neighboring hot field lines along the line of sight. These structures are triggered by a subsequent large scale flare and

are no longer present near the time of the J6 eruption, hence the more straightforward profile, where a modest heating of the jet region manifests. We note that the T_e variations are less than the computed uncertainties, although they are temporally matching the more substantial density variations. Based on the assumption that our uncertainties are a result of a systematic stochastic process, these T_e variations can only be speculated by association with the more trustworthy EM evolution. We hypothesize that the decrease in temperature is possibly explained by just an increase in the local density as the jet passes with no steep temperature increase.

The EM distributions of the erupting material are presented for all events in fig. 3.6. We see that the pre-flare (background) conditions are similar for all three events. We would expect this to happen in the case of J2 and J3 which are temporally separated by about 10 minutes, while the J6 is occurring 12 hours later than J3 and surprisingly exhibiting almost the same background profile. Both the C2015 and H2012 background results depict an expected quasi-uniform distribution of coronal plasma in the $\log T_e = [6.0, 7.0]$ range with a slight prevalence of hotter plasma. This is a property of the selected region, and such distributions are unique based on region selections that are constructed. These profiles thus show that even with individual region selections, the geyser footpoint was tracked accurately in the long timescales involved in order to depict the same area and the erupting plasma is propagating along the same general direction.

The above fact becomes very important when discussing the individual jet eruptions. Using the basic parameters summarized in table 3.2 we see that individual eruptions are geometrically unique. The physical parameter estimations are also unique, counter to

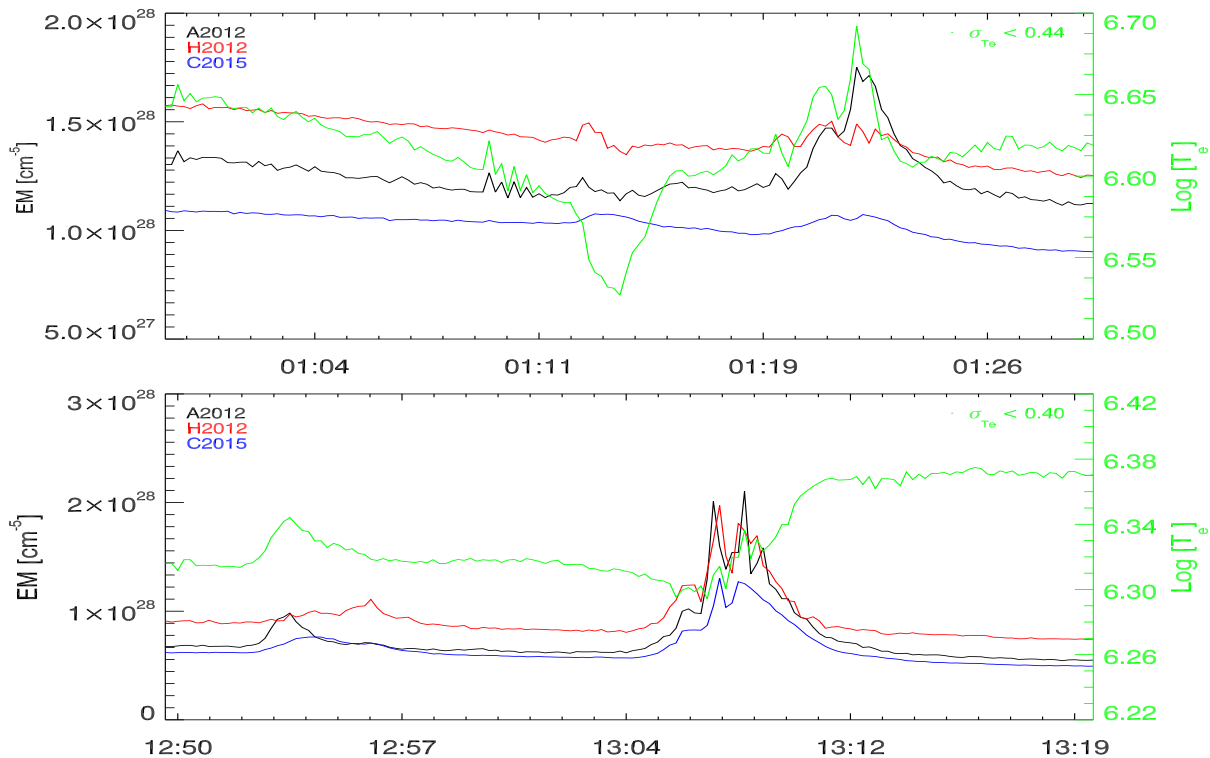


Figure 3.5: Timeseries set depicting the A2013, H2012, and C2015 inversions of the main jet emission in selected regions. Both the region averaged EM and A2013 T_e estimations are depicted for the two datasets containing the three events. The plotted temperature range is constrained in order to depict the co-temporal variation of the two quantities, although the absolute temperature variations are modest. No T_e averages have been provided for the C2015 and H2012 inversions as no unique temperature was found at one timeframe.

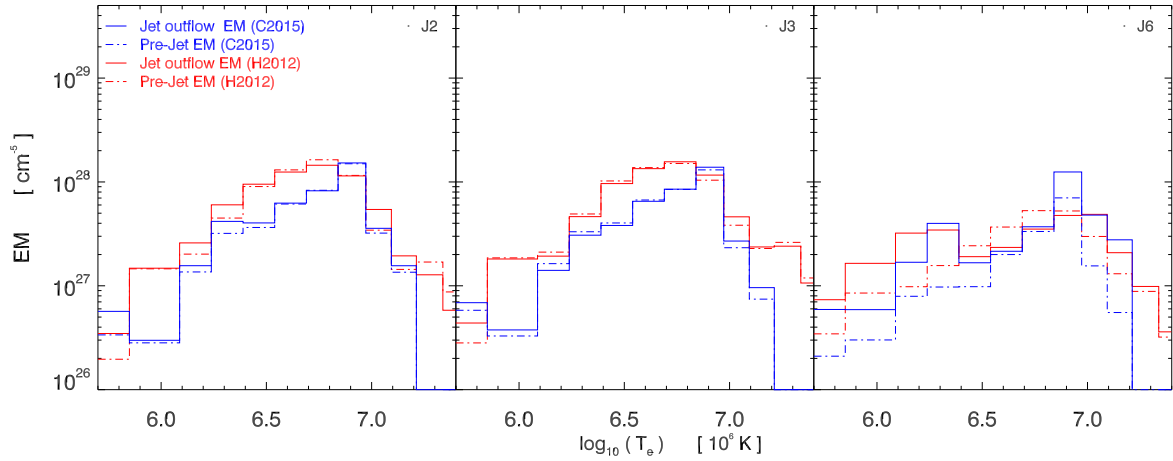


Figure 3.6: The J2, J3, and J6 EM profiles across the temperature space as derived from the H2012 and C2015 inversions. Erupting material is plotted against the quieter background selected for each individual event. Data was re-binned in the same intervals in order to better compare the EM profiles.

what a homologous self-repeating eruption scenario would predict. In our sample, all three events show particular EM distributions along the temperature spaces. The emitting plasma correspondent to the J2 event can be characterized by three distinct temperature regions: a small but significant emission in the lower coronal range $\log T_e \sim [5.9, 6.4]$, no significant change from background EM in the $\log T_e \sim [6.6, 6.8]$, and a distinct EM was recovered in the $\log T_e \sim [6.9, 7.2]$ range. The J3 jet is revealed to have no significant increase in EM, or sometimes even a discernible decrease, in the $\log T_e \sim [5.9, 6.7]$ range while manifesting in the $\log T_e \sim [6.8, 7.2]$ hotter emission. These two events, although different in particularities can still be globally estimated by Gaussian fitting. On the other hand, the J6 event clearly presented two distinct and significant emitting structures, one lower temperature component $\log T_e \sim [6.1, 6.5]$, and one hot emission component, $\log T_e \sim [6.9, 7.1]$. A one Gaussian fitting around this event, will produce non-physical results, and this eruption clearly exhibits multitemperature components. We assumed emission measures $\log T_e > 7.3$ are uncertain in both determinations, and do not discuss the respective quantities.

The jets main physical parameters as recovered by the A2013 inversion:

$$J2 \rightarrow EM = 6.34 \pm 0.25 \cdot 10^{28} \text{ cm}^{-5} \text{ for } \log T_e = 6.58 \pm 0.20K \rightarrow n_e = 0.16 \cdot 10^{11} \text{ cm}^{-3}.$$

$$J3 \rightarrow EM = 6.28 \pm 0.24 \cdot 10^{28} \text{ cm}^{-5} \text{ for } \log T_e = 6.83 \pm 0.28K \rightarrow n_e = 0.13 \cdot 10^{11} \text{ cm}^{-3}.$$

$$J6 \rightarrow EM = 3.66 \pm 0.14 \cdot 10^{28} \text{ cm}^{-5} \text{ for } \log T_e = 6.54 \pm 0.33K \rightarrow n_e = 0.09 \cdot 10^{11} \text{ cm}^{-3}.$$

The A2013 results can not be directly compared and presented in the fig. 3.6 EM distributions. The general agreement between the three methods in the case of the main jet bodies is presented qualitatively in fig. 3.5.

We set J3 as an example, assuming the eruption to be best described by a single Gaussian profile. We interpret the A2013 inversion as an ‘emission measure weighted average temperature’ and assume that $6.28 \cdot 10^{28} \text{ cm}^{-5}$ represents the total of emitting material in supposed bins that sit inside a hypothetical Gaussian function with fitting parameters, $a = 6.28 \cdot 10^{28}$, $b = 6.83$, and $c = 0.28$ resulted from the A2013 inversion. We then fit the Gaussian function over the two other EM distributions. The A2013 EM can thus be compared with the total emission measures, under the Gaussian and corresponding to each C2015 and H2012 inversion. A total of $2.81 \cdot 10^{28} \text{ cm}^{-5}$ resulting from the C2015 inversion along with $2.89 \cdot 10^{28} \text{ cm}^{-5}$ resulting from the H2012 output were calculated. Thus, the A2013 EM is overestimated by a factor of 2 in the case of the J3 eruption.

The A2013 flux presented in fig. 3.5 is thus quantifiable to a comparable recovered EM. As stated previously, the three different events will exhibit their individual interpretation. J2 corresponds to a similar explanation. The J6 profiles agree very well between the three inversion results if we use the above A2013 interpretation. The main physical parameters are summarized below.

The jet eruption EM as recovered by the H2012 inversion:

$$\begin{aligned}
 J2 \rightarrow EM &= 0.54 \pm 0.09 \cdot 10^{28} \text{ cm}^{-5} \text{ for } \log T_e = [6.00, 6.18] \rightarrow n_e = 0.05 \cdot 10^{11} \text{ cm}^{-3}. \\
 EM &= 1.08 \pm 0.12 \cdot 10^{28} \text{ cm}^{-5} \text{ for } \log T_e = [7.04, 7.17] \rightarrow n_e = 0.06 \cdot 10^{11} \text{ cm}^{-3}. \\
 J3 \rightarrow EM &= 2.81 \pm 0.14 \cdot 10^{28} \text{ cm}^{-5} \text{ for } \log T_e = [6.60, 7.14] \rightarrow n_e = 0.09 \cdot 10^{11} \text{ cm}^{-3}. \\
 J6 \rightarrow EM &= 0.83 \pm 0.10 \cdot 10^{28} \text{ cm}^{-5} \text{ for } \log T_e = [6.00, 6.30] \rightarrow n_e = 0.04 \cdot 10^{11} \text{ cm}^{-3}. \\
 EM &= 1.16 \pm 0.16 \cdot 10^{28} \text{ cm}^{-5} \text{ for } \log T_e = [6.77, 7.14] \rightarrow n_e = 0.05 \cdot 10^{11} \text{ cm}^{-3}.
 \end{aligned}$$

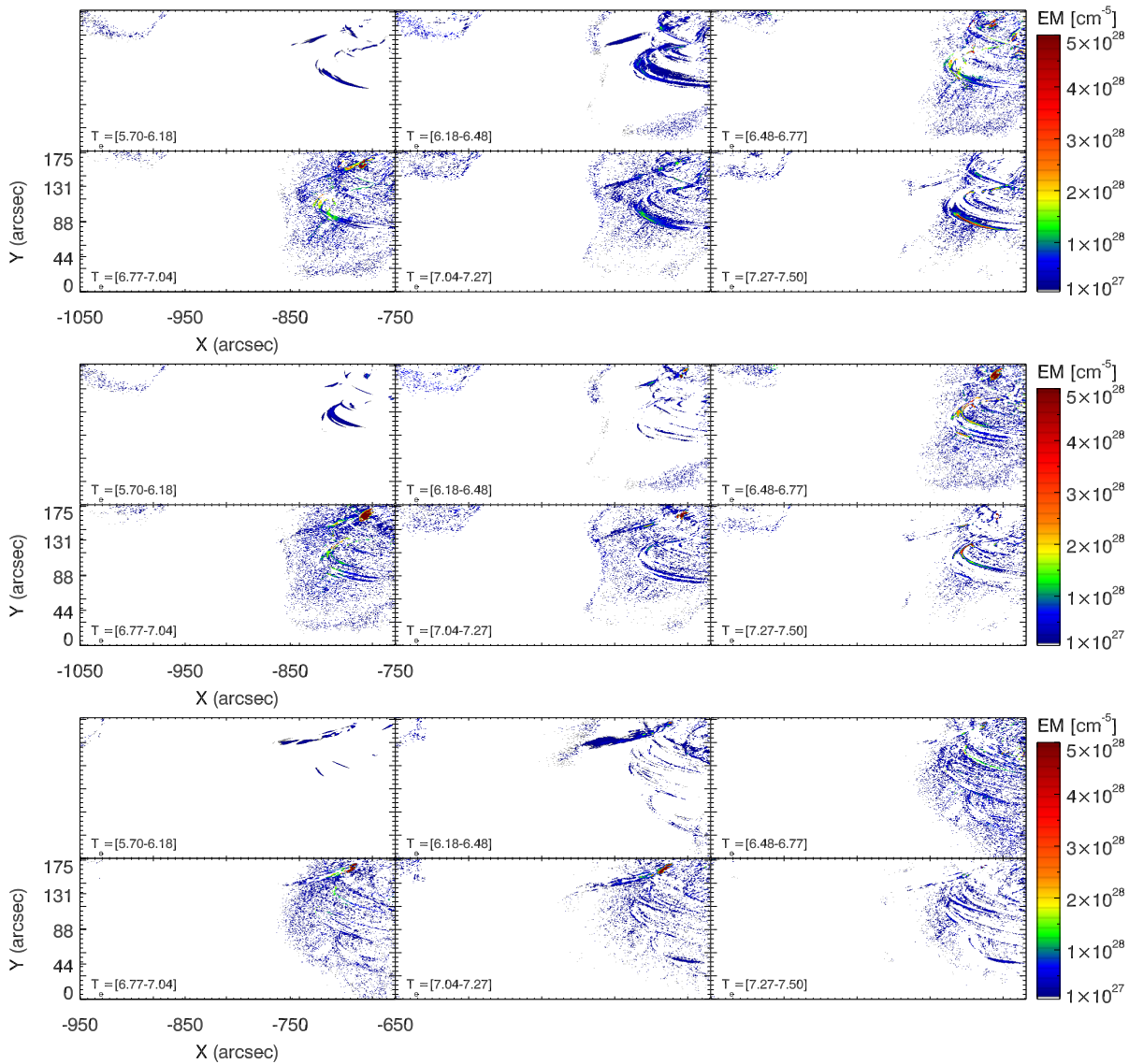


Figure 3.7: The H2012 inversion emission measure maps correspondent to the erupting jets material and unique geyser footpoint presented for the J2 (upper), J3 (middle), and J6 (bottom) events. The EM profiles are mapped across the selected T_e bins of approximately 0.3 in logarithmic size revealing different strands (spires) manifesting in different temperature ranges and spatial locations in all three cases.

The jet eruption EM resulting from the C2015 inversion:

$$J2 \rightarrow EM = 0.30 \pm 0.09 \cdot 10^{28} \text{ cm}^{-5} \text{ for } \log T_e = [5.70, 6.30] \rightarrow n_e = 0.03 \cdot 10^{11} \text{ cm}^{-3}.$$

$$EM = 1.36 \pm 0.12 \cdot 10^{28} \text{ cm}^{-5} \text{ for } \log T_e = [6.90, 7.20] \rightarrow n_e = 0.07 \cdot 10^{11} \text{ cm}^{-3}.$$

$$J3 \rightarrow EM = 2.89 \pm 0.22 \cdot 10^{28} \text{ cm}^{-5} \text{ for } \log T_e = [6.60, 7.20] \rightarrow n_e = 0.09 \cdot 10^{11} \text{ cm}^{-3}.$$

$$J6 \rightarrow EM = 0.41 \pm 0.10 \cdot 10^{28} \text{ cm}^{-5} \text{ for } \log T_e = [6.00, 6.30] \rightarrow n_e = 0.03 \cdot 10^{11} \text{ cm}^{-3}.$$

$$EM = 1.21 \pm 0.12 \cdot 10^{28} \text{ cm}^{-5} \text{ for } \log T_e = [6.90, 7.20] \rightarrow n_e = 0.05 \cdot 10^{11} \text{ cm}^{-3}.$$

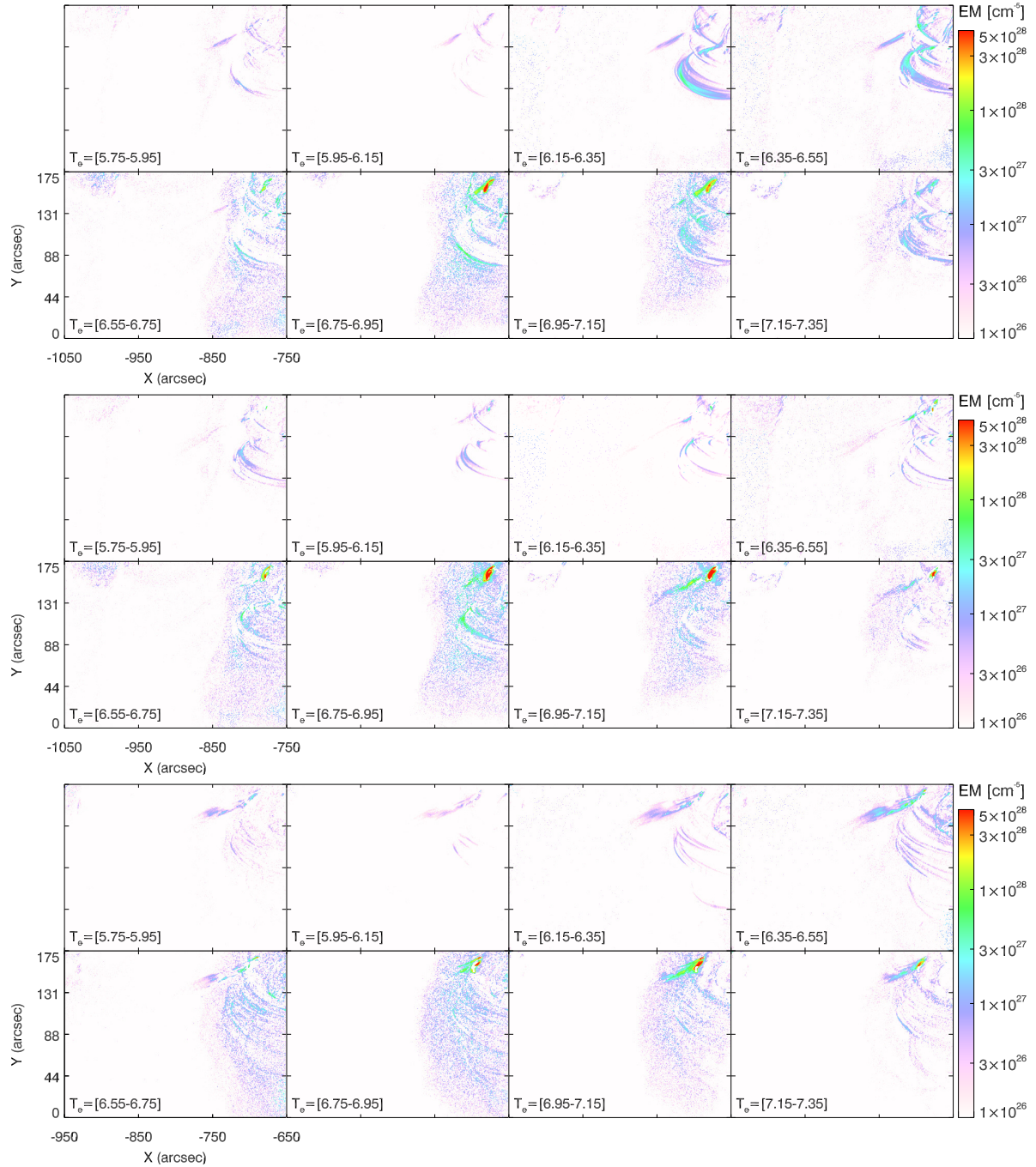


Figure 3.8: The C2015 inversion emission measure maps correspondent to the erupting jets material and unique geyser footpoint presented for the J2 (upper), J3 (middle), and J6 (bottom) events. The EM profiles are mapped across the selected T_e bins revealing different strands (spires) manifesting in different temperature ranges and spatial locations in all three cases.

The jet eruption EM can be compared with their footpoint counterparts. In section 3.3.1, we speculated that the two emission peaks observed in fig. 3.4 (bottom) may correspond to a superposition of plasma resulting from the geyser footpoint and jet erupted material. Consequentially, since the jet body is tracked inside a region that does not contain the footpoint, the temperature distribution represented in fig. 3.6 should be dominated by the lower temperature plasma. This assumption proved to be erroneous for all three jet eruptions. A distribution of higher and lower temperature emission could be established along all jet bodies analogous to the footpoint estimation. The distributions can be alternatively explained by multiple strands, heated to different temperatures that are erupting simultaneously. The hypothesis is supported by the available data.

The multiple EM spikes presented in the timeseries plots fig. 3.5 and fig. 3.4 (upper panel) are possibly generated by successive fast reconnection events inside a blow-out type eruption mechanisms as described by Moore et al. [2013] and Sterling et al. [2015, 2016]. Further evidence is provided by the emission measure maps recovered via the H2012 (fig. 3.7) and C2015 (fig. 3.8) inversion results. The recovered EM were summed across multiple ensuing temperature bins in order to increase readability. The number of summed bins were chosen to not be perfectly overlapping between the two inversions. The independently created maps reveal that two main strands exist for all events; one manifesting in the low temperature intervals and one in the higher temperature range. These visible strands are morphologically unique and are separated spatially. We note that this result is still most probably a simplified picture of the actual eruption configuration due to the spatial resolution of the filtergram observations and limitations in the ill posed EM inversion procedures. In the SDO-AIA filtergrams, more than two strands can be visually observed, but such details are not accurately recovered in the inverted EM maps due to mostly high thermal widths characteristic of the solutions but also because of low counts characteristic of small bin sizes. Individual strand morphology could for example be recovered in fig. i.3 by summing over a large temperature $\log T_e \sim [5.7, 7.15]$ range EM maps. Obviously the individual strand temperature information is lost in this case.

Table 3.2: Jet and Geyser footpoint morphological parameters as derived from the SDO AIA-304Å, SDO AIA-171Å, SDO AIA-94Å, and AIA-131Å filters. The plasma physical and energetic parameters are derived via the Aschwanden [2013], Hannah and Kontar [2012] and Cheung et al. [2015a] inversion approaches, taking into account the morphological parameters, geometrical approximations, and the particular assumptions and limitations of the models.

No.	Time [hh : mm]	AIA filter	Width [km]	Height [km]	v_{proj} [km s ⁻¹]	log T_e [K]			n_e [10 ¹¹ cm ⁻³]; $\phi = 1$		
						C2015	A2013	H2012	C2015	A2013	H2012
Jet Plasma											
J2	01:14:00	171 304	2532 2616	66528 93600	252 195	6.00 ± 0.30 7.05 ± 0.15	6.58 ± 0.20	6.10 ± 0.08 7.10 ± 0.06	0.03 0.07	0.16	0.05 0.06
J3	01:22:24	171 304	3488 3924	94323 n/a	177 207	6.90 ± 0.30	6.83 ± 0.28	6.89 ± 0.29	0.09	0.13	0.09
J6	13:10:24	171 304	4890 4011	66135 n/a	305 285	6.15 ± 0.15 7.05 ± 0.15	6.54 ± 0.33	6.17 ± 0.13 7.00 ± 0.22	0.03 0.05	0.09	0.04 0.05
Footpoint Plasma											
J2	01:13:00	131 94	4978 D:2467	17889	n/a	6.40 ± 0.20 7.00 ± 0.20	6.58 ± 0.22	6.38 ± 0.21 6.96 ± 0.18	0.08 0.10	0.18	0.09 0.13
J3	01:19:00	131 94	3926 D:2467	20972	n/a	6.75 ± 0.45	6.80 ± 0.34	6.75 ± 0.41	0.23	0.32	0.26
J6	13:08:24	171 94	6150 D:2467	17220	n/a	6.35 ± 0.15 7.00 ± 0.20	6.63 ± 0.25	6.29 ± 0.08 6.96 ± 0.12	0.09 0.15	0.28	0.10 0.19

3.4 Geyser X-Ray Energetics

In the standard flare picture, beams of non-thermal particles are generated alongside EUV and X-Ray thermal emission. Outward beam propagation is correlated with a larger set of geyser sites in chapter 2, showing that these sites generate upwards electron beams. A qualitative schematic of observable flare signature is offered in fig. 2.1. The detailed thermal EUV emission of our geyser site (recurrent flaring footpoint) is explored in section 3.3.1. The nature of the reconnection processes involved is further investigated by means of higher energy spectroscopic analysis, pursuing the currently elusive down-streaming electron beams that are hypothesized as part of the standard flare scenario.

The Reuven Ramaty High-Energy Solar Spectroscopic Imager [RHESSI; Lin et al., 2002] is a NASA small explorer mission, in operation since 2002. The instrument was devised to investigate the emission measure, energetics, and particle acceleration in solar flares, operating in X and γ ray energies. RHESSI records spectroscopic data using nine rotating collimator grids, in front of a spectrograph, covering the entire visible sun with a $\sim 2''$ spatial resolution. Energy emissions between 3 KeV and 17 MeV can be detected. Additionally, the instrument can perform high energy imaging of hot solar features. At X-Ray energy levels, optical design telescopes (e.g. EUV; SDO-AIA, X-Ray; Hinode-XRT) can not easily achieve adequate spatial resolution due to physical and technical limitations (e.g. diffraction grazing incidence optics, incomplete spectral line theory, etc.) and instrument size constraints. RHESSI uses its rotating collimators to produce imaging by means of Fourier transform analysis. A source will be visible by a certain set of detectors at a fixed time. As the instrument rotates, the difference in arrival time between the detectors can be used for generally precise reconstruction of the solar source morphology and to pinpoint its location. The timeseries is formally inverted to yield an emission map, assuming that the sources do not change during integration.

A general overview of the RHESSI imaging is provided by Hurford et al. [2002]. Different source reconstruction techniques are available as part of the RHESSI data analysis SolarSoft package, SSW/HESSI. The main reconstruction algorithms are the Back-Projection [Hurford et al., 2002], Clean [Dennis and Pernak, 2009], Maximum Entropy [Schmahl et al., 2007], visibility forward fit [Hannah et al., 2008], and Pixon [Metcalf et al., 1996]. We have utilized the Pixon method in order to perform the X-Ray source reconstruction of our footpoints. A pixon represents the abstraction of a pixel-like cell structure, where the information (e.g. number, size, width, etc.) in such a cell would depend on a measured global quantity. A set of such pixons is minimized with respect to the information content of a pseudo-image. In this particular case the pixons are assumed circular, in order to restrict the number of degrees of freedom of the ill-posed problem. The minimum pixon quantity that can reproduce the maximum of available information is the reconstructed source image. The pixon solution is quoted to be the most accurate in terms of spatial domain and photon distribution [Hurford et al., 2002], but suffers from a major limitation in computational speed due to the non-linearity posed, generally being two orders of magnitude slower when compared to the other algorithms.

Our case dataset requires just a few reconstructions where the best accuracy possible is desired, making pixon the best candidate model for source reconstruction. The results of the high energy emission source reconstruction, corresponding to the individual J2, J3 and J6 recurrent jet eruptions, part of the AR11302 geyser structure are presented here. The RHESSI X-Ray source location could be extrapolated for just the three eruptions corresponding to our geyser site. We draw attention to the fact that the other seven jets

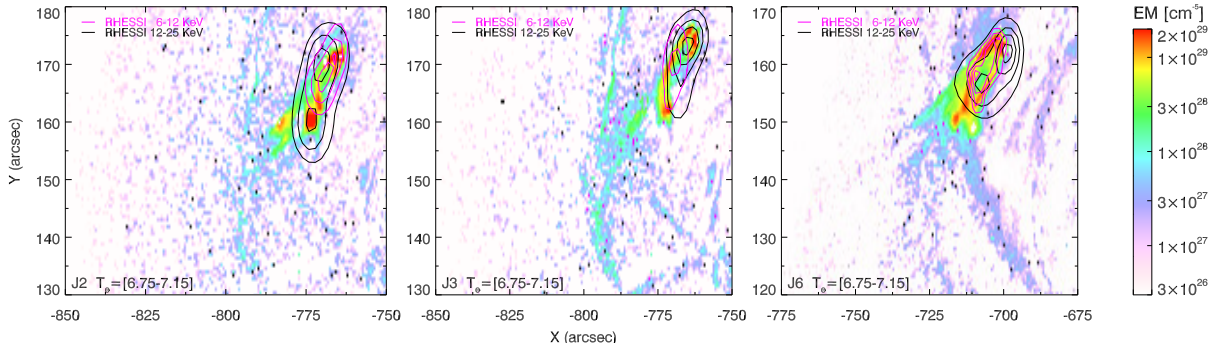


Figure 3.9: RHESSI X-Ray emission over-plotted on three of the jet eruptions (the J2-01:13UT, J3-01:19UT, and J6-13:08UT events). Contours represent the soft (magenta) 6 – 12 KeV and hard (black) 12 – 25 KeV energy channels. The contours represent the normalized $[0.3, 0.5, 0.7, 0.9]$ levels. The EM maps were recovered via the C2015 method, and depict the onset times of the jet eruptions which are closest to maximum peaks in the RHESSI flux data.

were unmeasurable by RHESSI! There is an important distinction between this situation and, for example not obtaining a reconstruction solution. In our data set, all three of the measurable events had their respective coronal source recovered. In the complementary set of seven, two distinct issues hindered analysis:

- (i) RHESSI integrates the entire visible disk of the Sun. The lightcurves corresponding to a subset of geyser jets were being masked by stronger flaring, occurring in close temporal proximity.
- (ii) Events occurred during RHESSI spectrum data gaps, as the instrument has not offered full day synoptic coverage.

This behavior can also be checked in the GOES daily X-Ray flux product which suffers from the same limitations. The SDO-AIA thermal analysis follows this data limitation, and thus only the three events were subjected to DEM estimates.

Figure 3.9 presents the pixon X-Ray source reconstruction. The locations are overplotted on the EM maps recovered at the times of peak flaring emission using the C2015 inversion summed over the higher SDO-AIA DEM range, 6–10 MK, showed in section 3.3.1 to be most responsive to the jet eruptions. The three eruptions manifested in the 6–12 KeV and 12–25 KeV RHESSI energy bands, with almost no detectable emission compared to background counts in the higher energy channels (> 25 KeV). Very close to background counts were detected in the 3 – 6 KeV channel. We chose to not include these in our analysis due to the high uncertainty. We also note that five out of the nine collimator filters were in use during the geyser observation times.

The formal textbook delimitation between hard and soft X-Rays varies due to particularities in measurement and processes involved. Usually ~ 10 KeV is quoted. From a solar plasma physical perspective, we attribute soft X-Ray emission to thermal radiation of hot loops assumed in at least quasi equilibrium states and hard X-Ray emission to a thick-target bremsstrahlung process of non-thermal electrons, that are supposedly accelerated by reconnection events. The potential presence of non-thermal emission is a clear indicator of impulsive flaring events. In all our three particular cases distinct 12 – 25 KeV vs. 6 – 12 KeV X-Ray source morphologies were reconstructed. It can be observed that the contoured sources do not perfectly overlap the SDO-AIA EM map footprints. This can be attributed to multiple effects:

- (i) The RHESSI sources were recovered with a $4''$ resolution binning because of the relatively low counts of the discussed microflares. RHESSI is primarily designed to study standard flares, which can be several orders of magnitude more powerful.
- (ii) The position of the geyser site makes it prone to geometrical effects that limit the accuracy of the reconstruction. The size of the solar disk slightly varies between the EUV and X-Ray wavelengths. Additionally, the proximity of the geyser structure to the solar limb creates projection distortions.
- (iii) Only five out of the nine RHESSI detectors were in use, limiting the input data and thus the accuracy of the pixon determination.

The 12–25 KeV X-Ray source locations are wide and elongated exhibiting two distinct emission locations in the case of J2 and J6, and one strong source along with a very elongated lower intensity contour, oriented towards the bottom flaring footpoint of J3. These indeed seem to qualitatively correspond to the footpoints of the flaring loops involved in the jet generation, as visualized via the C2015 EM maps. In the case of the 6–12 KeV emission, the sources appear smaller in size and seem to consistently sit between the two 12–25 KeV and EUV loop footpoints, for all three jet events. This visual interpretation may lead us to attribute a hard X-Ray label to the 12–25 KeV emission and soft X-Ray association for the 6–12 KeV channel.

It is possible to associate the 12–25 KeV separated footpoints emission to impact sites of downstreaming non-thermal electron beams, that are ‘braked’ by the lower (and collisional!) atmosphere. The 6–12 KeV emission can be in turn interpreted as a thermal emission from the heated loop top, after the reconnection onset. Can we safely assume that this hypothesis holds true and emission splits into thermal and non-thermal components along our available energy ranges at least for our three test cases? In section 1.2, we analyzed a presumably non-thermal small-scale flaring site [‘ribbon D’; Testa et al., 2014, Judge et al., 2017] of a similar scale to our geyser structure. We showed that such assumptions, although intuitive, may not always reflect the local emission conditions, as high energy emission was found to be caused by the heating of a chromospheric flare. Although compelling, when considering the geyser jets, the X-Ray source reconstruction is not an sufficient argument by itself.

Thermal emission is predominant in the low energy bands, while non-thermal emission becomes dominating at energies over 20 KeV. In part this is because of the $1/\epsilon^2$ dependence of the $e^- - e^-$ collision time, of electrons with energy ϵ . In practice, the energy cutoff needs to be addressed on an individual basis as eruption power scaling and local conditions can significantly skew interpretation. The imaging reconstruction capabilities are not the only strong-point of the RHESSI instrument. The satellite’s primary data product is represented by the X-Ray spectrometric flux. A specific feature’s energy spectrum can be extracted, calibrated, and fitted against a vast repository of thermal and non-thermal energy distribution analytical functions. This analysis can be performed using either the command line SSW/SPEX or the more modern GUI SSW/OSPEX module.

The total RHESSI count temporal evolution is depicted in fig. 3.10, (left panel). The resulting lightcurves are modest when compared to standard flare manifestations. The 25–50 KeV channel does not record emission above background levels. Such a behavior is expected when resolving events that are less energetic in order of magnitude scales. The photon flux spectra were obtained for the three eruptions (fig. 3.10, right panel), at times correspondent to the main flaring phase recovered in the EUV determination (section 3.3.1). The recommended RHESSI spectrum integration time is ~ 4 s. In the present case we integrated the spectra on slightly longer periods of about 15–30 s in order to create

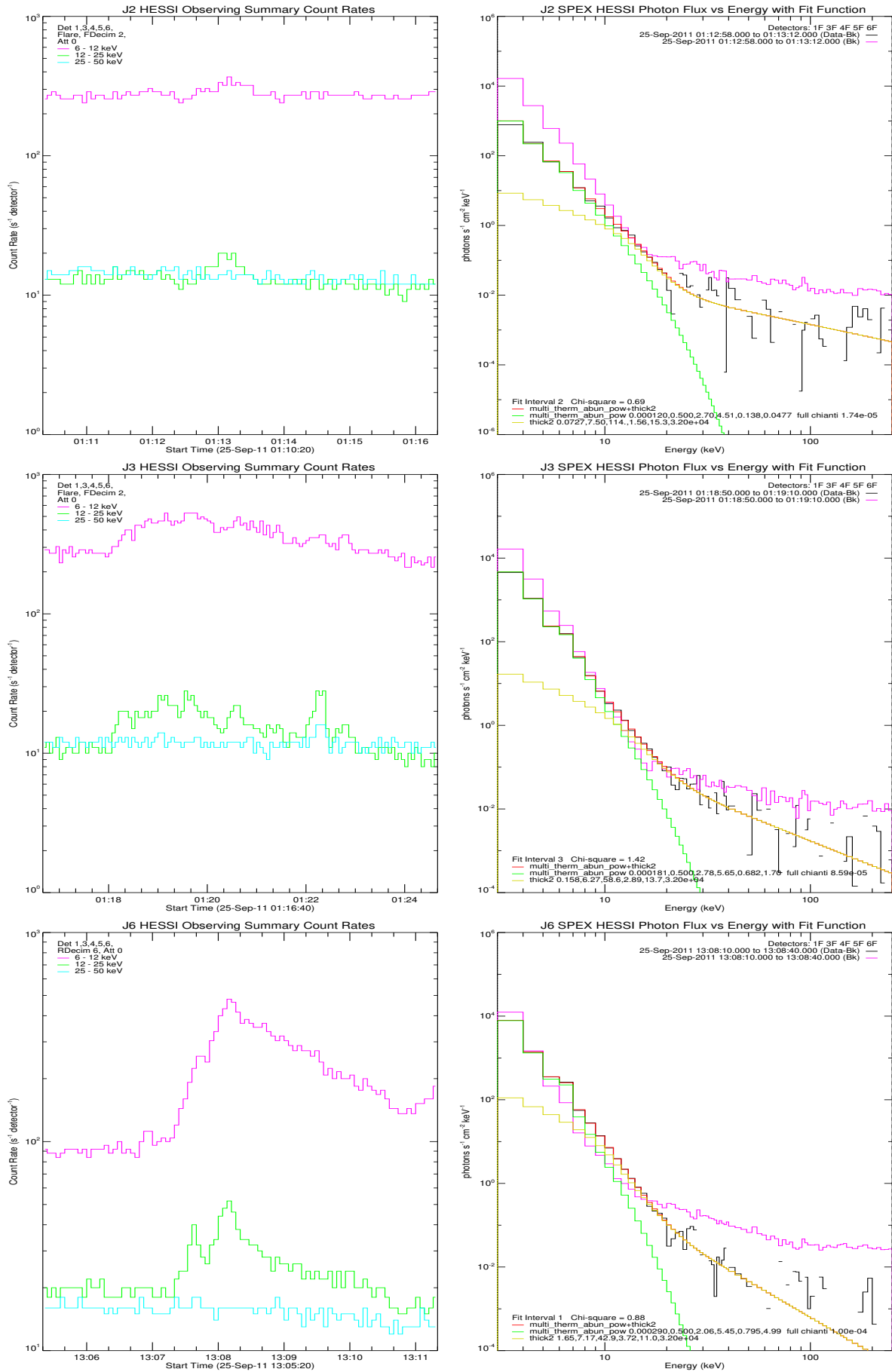


Figure 3.10: RHESSI X-Ray emission spectrum correspondent to the J2, J3, and J6 jet eruptions. **Left Panels:** Timeseries plots of the total X-Ray count rates for the 6 – 12 KeV, 12 – 25 KeV, and 25 – 50 KeV channels. **Right Panels:** Thermal and non-thermal plasma emission models fitted on the spectral distribution in the 1 KeV to 250 KeV range. No discernible emission could be recovered in the 25 – 50 KeV and higher channels. We focus on the results at energies < 30 KeV. The spectra was averaged over short timescales correspondent to peaks in the photon flux timeseries of the 12 – 25 KeV band.

statistically significant spectra. It can be observed that on the very high energy domain, no significant counts over the background levels were recorded.

The reconstructed X-Ray energy spectra were fitted with a series of thermal and non-thermal plasma emission models that are relevant in the 1 – 250 KeV energy range. The background and the difference between flaring and background counts were plotted. It is worth noting that the flaring time photon flux, is in general few factors higher than the background. In a larger context, it appears that although the footpoints of jets, are of modest size and energy, they do significantly manifest in a full disk signal integration. It is worth investigating how many individual microflares studied by Hannah et al. [2008] have initiated jets? We believe that important implications arise if whole or part of these events have injected mass to the slow solar wind flux! This is left for future work.

We attempted to best reproduce the observational spectra with one or a combination of multiple models, at least in the < 30 KeV range where significant counts above the background levels exist. This by itself is an indicator that multiple processes are manifesting during one eruption. Most larger flare X-Ray emission is reliably recovered by a *vth+b_pow* model that assumes a combination of optically thin isothermal emission and a non-thermal double power law function that models thick-target bremsstrahlung emission. Significantly, no single model was able to accurately reproduce any of the three jet spectra. Models based on exponential function distributions (e.g. *multi_therm_exp*) proved particularly unsuited in our particular cases. A set of two emission models was found to reliably reproduce all the observed spectra. We have utilized the multithermal power function (*multi_therm_abun_pow*) to reproduce the lower energy in combination with a double power law thick-target bremsstrahlung (*fthick2*) to model the higher energy part of the spectra. We note that this model combination yielded the best fit under decent residual constraints, $\chi^2 < 1.5$.

When quantifying the three individual jet footpoints, we observe that the intersection between the two fitting function differs. This corresponds to the emission measure of each event. The cutoff energies are: 8.5 KeV for J2, 10.5 KeV for J3, and 10.2 KeV for J6. Note that this correlates with the EUV DEM profiles of the footpoints. The individual fit parameters correspond to physical quantities. The counts in the higher energy range allow for an estimation of the downward beam electron flux. A DEM measure is recovered for each event. We compute the DEM of the RHESSI sources corresponding to a peak emitting temperature $T_e = 2$ KeV (or $\log T_e = 7.36$) assuming a volume approximation by utilizing

$$V = \pi \cdot \frac{D^2}{4} \cdot H, \quad (3.21)$$

where D is the footpoint loop diameter and H is the loop arc length. The two parameters are available in table 3.2.

We have obtained local plasma densities and DEM resulting from RHESSI thermal fitting (*multi_therm_abun_pow*) as follows:

$$J2 \rightarrow \text{DEM} = 0.000120 \cdot 10^{49} \text{ cm}^{-3} \text{KeV}^{-1} \text{ for } \log T_e = 7.36 \rightarrow n_e = 0.04 \cdot 10^{11} \text{ cm}^{-3}.$$

$$J3 \rightarrow \text{DEM} = 0.000181 \cdot 10^{49} \text{ cm}^{-3} \text{KeV}^{-1} \text{ for } \log T_e = 7.36 \rightarrow n_e = 0.04 \cdot 10^{11} \text{ cm}^{-3}.$$

$$J6 \rightarrow \text{DEM} = 0.000290 \cdot 10^{49} \text{ cm}^{-3} \text{KeV}^{-1} \text{ for } \log T_e = 7.36 \rightarrow n_e = 0.06 \cdot 10^{11} \text{ cm}^{-3}.$$

The X-Ray emission measures can be compared to the emission measures recovered using the EUV techniques. The determinations correspond to hot plasma in a range which was determined to be unreliable in our EUV determinations. The absolute n_e quantities are significant in context, at least to a qualitative level. Suppose we bypass the high temperature

safeguard and interpret the EUV EM profiles from fig. 3.4 (bottom panel) to follow a similar power law decrease at higher temperatures. We hypothesize that the EUV $\log T_e = 7.36$ results are significant and measure the n_e for all three jets to be in the order of $0.02 - 0.06 \cdot 10^{11} \text{ cm}^{-3}$. The two independent estimations therefore appear to be compatible.

3.5 Discussion

The differential emission measures of recurrent active region jets

The jet eruptions have been described in terms of the emission measure recorded by the SDO-AIA filters. The SDO-AIA filter intensity can be expressed as the integral along the line of sight of the total emitting ionized plasma times the temperature response function computed using the CHIANTI database, as depicted in eq. (3.8). We have recovered the Differential Emission Measure using four different inversion schemes applied to the AIA [171Å, 193Å, 211Å, 94Å, 131Å, and 335Å] filter set. With the noted exception of the filter ratio technique, we have found a good agreement between the inversion results following the described assumptions (section 3.1), methods (section 3.2), and observational constraints (section 3.3).

The case of possible plasma parameter determination via relative filter ratios, as described in section 3.2.2, is assessed. We have determined all possible SDO-AIA filter ratio values assuming a multithermal emission centered at two peaks assumed to be $\log T_e = 6.30$ K and $\log T_e = 7.00$ K. These peaks were shown to be fairly accurate using the other inversion methods (fig. 3.4). The goal was to assess if any SDO-AIA ratio may prove suitable for diagnostics, in an assumed near isothermal temperature range. Our determination (table 3.1) showed that there does not appear to exist a set of reasonable ratio combinations for any event, at the deduced peak temperatures. This method proved to not be suitable for SDO-AIA filtergram data.

We stress that even when employing the utmost care, plasma inversion methods are fundamentally limited, representing mathematical models that contain significant subjectivity when addressing the ill-posed problem [see discussions in Craig and Brown, 1986, Judge et al., 1997, Aschwanden et al., 2015], and [Cheung et al., 2015b]. Even in the best particular conditions, EM inversions should be considered just approximations of plasma physical conditions and need to be corroborated with independent complementary observations and modeling. On the other hand, we advise against initiating vague discussions on ‘multiwavelength’ or ‘multitemperature’ SDO-AIA analyses that do not attempt to produce filtergram inversions, relying on an unfounded association of filters to unique temperatures or on relative filter ratios. As described in section 3.1, such discussions are ill-suited in the context of coronal filtergram observations.

Multiple studies [Cheung et al., 2015b, Hanneman and Reeves, 2014] performed joint inversions of EUV and X-Ray observations. The works demonstrated that adding X-Ray imaging data to the EUV filtergram sets can greatly improve the accuracy of coronal plasma determinations, especially in the high temperature plasma domains. Unluckily, our geyser site was not imaged by X-Ray instruments like Hinode XRT.

Testa et al. [2011] found that, in the case of microflares and nanoflares, the DEM emission is characterized by multithermal plasma; an expected $\log T_e = 6.30$ K component and a second significant hot plasma $\log T_e \sim 7.00$ contribution. The authors argue that this property is compatible with existing nanoflare models. We have herein observed this characteristic for both footpoint (fig. 3.4) and jet eruption (fig. 3.6) emission. We have

found two distinct peaks during flaring and subsequent jet eruption timeframes. One peak was situated at $\sim 2 - 3$ MK while the other stronger peak is centered around $6.9 - 7.1$ MK.

Our lower temperature range estimations are consistent with the ones recently obtained in the jet study of Mulay et al. [2016]. The authors did not address higher temperature emission where $\log T_e > 7$ due to concerns that existed at the time with the accuracy of the solution. Based on the consistent results from our coupled SDO-AIA and RHESSI observations, we argue that the recent improvements in the CHIANTI database allow to constrain higher temperatures SDO-AIA observations. The high temperature emission peaks are also compatible with the Moreno-Insertis et al. [2008] and Moreno-Insertis and Galsgaard [2013] MHD results which predict hot $\log T_e \sim 7$ emission. We note that the $\log T_e > 7.3$ data is still highly unreliable. When discussing recovered EM and correspondent n_e determinations our typical $n_e = 3 - 9 \cdot 10^9 \text{ cm}^{-3}$ is comparable to the Mulay et al. [2016] determinations of $n_e = 2 - 11 \cdot 10^9 \text{ cm}^{-3}$ where we have compared only our low temperature emission. The Mulay et al. [2016] study selected 20 jets from multiple sites that span across multiple years of solar activity. On the simulation side, Moreno-Insertis and Galsgaard [2013] also reported plasma density estimates of $n_e \sim 10^9 \text{ cm}^{-3}$, noting that in this case, the authors were modeling a blowout coronal hole jet.

Our estimation and Mulay et al. [2016] arbitrarily selected a ‘safe’ filling factor $\phi = 1$ which is always an overestimation as EUV observations can not be used for ϕ calculations. The erupting material density may be a unique property of each jet footpoint. In a subsequent comprehensive spectroscopic study, Mulay et al. [2017a] brought together SDO-AIA, Hinode XRT, and Hinode EIS observations in order to analyze the DEM of one large coronal jet. One important result is the $\phi = 0.005$ estimation correspondent to the density sensible Fe XII ratio forming at $\log T_e = 6.30$. Other works on small scale features have reported similar estimations [e.g. Chifor et al., 2008b]. In a subsequent work Mulay et al. [2017b] used IRIS observations to calculate a $\phi = 0.1$ in chromospheric regions. Judge [2000] addressed spectroscopic filling factors of the transition region for both homogeneous and non-homogeneous plasma conditions finding $\phi = 0.12 - 1$ to match observations. Moreno-Insertis and Galsgaard [2013] found $\phi = 0.2$ as a result of their simulations. As can be seen, any measurement is dependent on the observation and its limitations. The filling factor conundrum is still an actively debated issue.

Could there be even more than the two erupting components associated to jet eruptions? The ‘hot’ and ‘cool’ eruption definitions are loosely employed in the literature. We have adopted the nomenclature as the standard coronal DEM emission temperatures of $\log T_e \sim 6.3$ K and $\log T_e \sim 7.0$ K. The different studies adopt the terminologies, not in any way wrong, based on the discriminant observations. For example, Mulay et al. [2017b] refer to cooler eruptions as being in the $\log T_e \sim 5$ K range, while other works may refer to H α eruptions manifesting in the $\log T_e \sim 3 - 4$ K range [Canfield et al., 1996]. Similar particularities affect the ‘hot’ attribute.

Mulay et al. [2017a] proved the existence of multithermal plasma components in a jet eruption using a techniques involving emission line isolation from the AIA filtergrams finding consistent Fe XVIII emission. A noteworthy problem that may arise when interpreting DEM observations is the uncertainty in the inversion of the AIA-94Å filter that has complex multitemperature plasma components [Del Zanna, 2013]. A solution may consist in isolating the Fe XVIII emission in the AIA-94Å channel as proposed by Warren et al. [2012]. Mulay et al. [2017b] used lower height IRIS observations in order to further constrain a lower emission component. Although they recovered hot flaring ions, Mulay et al. [2017b] concluded that hot > 8 MK emission is unlikely for jet eruptions, at least in their case.

Microflare sites have been shown to exhibit > 8 MK thermal emission [Hannah et al., 2008]. RHESSI hot thermal emission of the same type was recovered for our geyser case. We have to note that the high variability of such events may allow both interpretations to coexist in a hypothetical event space. If in the case of the jets footpoints studied by Mulay et al. [2016, 2017b] there is no discernible hot emission, one can interpret that there is no sign of impulsive reconnection occurring for these events. Another class of jets can maybe be found by exploring this facet.

Hot flaring > 8 MK loop emission has been extensively observed and modeled [see review; Reale, 2014] at both large and small scales. All three inversion codes used herein were subjected to validation tests for hot flaring emission. As stressed herein, DEM techniques are not dependent on the studied physical system and suffer from fundamental limitations. The Hinode-XRT inversion method, *xrt_dem_iterative2* that is transformed and used for AIA observations by Mulay et al. [2017b] has been shown by multiple works to underestimate DEMs in the case of synthetic data [Aschwanden et al., 2015, Hannah and Kontar, 2012], possibly corroborating their discovery of only lower temperature SDO-AIA emission. We have shown herein, hopefully to a sufficient degree of confidence, that our events, and recurrent jet inducing sites in general, exhibit high temperature emission with a substantial EM. Additionally, the magnetic field configuration prior to the jets plays a crucial role in the energetics of jet events.

Our observations require a multithermal hypothesis involving multiple strands, heated to different temperatures that are erupting almost simultaneously. SDO-AIA resolution can distinguish multiple strands, that are erupting co-temporally. Both the C2015 and H2012 inversion EM maps (figs. 3.7 and 3.8) of the three jets revealed at least two main morphologically different strands that are spatially separated. Radially, they appear at slightly different heights in one time-instance. We draw attention to the SDO-AIA fluxes presented in fig. 3.1 where, for all three analyzed eruptions, multiple short successive flaring peaks could be detected. This behavior can also be observed, although smoothed out, in the total computed EM timeseries flux in both the case of the jet eruptions (fig. 3.5) and footpoint (fig. 3.4, upper panel) analyses.

The erupting strands can be interpreted as multiple short succession flaring events. We can interpret the subsequent flaring peaks in terms of current jet emission models. A blowout microfilament eruptions involving subsequent reconnection events that seemingly give rise to a unitary jet eruption was hypothesized in a series of papers [Sterling et al., 2015, 2016, 2017, Panesar et al., 2016]. The authors proposed magnetic cancellation across a neutral line to be the fundamental process that drives jet eruptions. This is analogous to the now common large scale flare scenaria. Our DEM detection of subsequent flaring events indirectly support the microfilament eruption supposition and theory.

One interpretation of quasi periodic pulsations (QPP) observed in large scale flares and even stellar flares may also explain our observations. Hayes et al. [2016] studied the bursty nature of the reconnection from multiwavelength QPPs occurring during the impulsive phase of an X class flares. Their AIA signal timeseries [Hayes et al., 2016, fig.1] is qualitatively correspondent to our fig. 3.1 if we disregard the substantial difference in power and time scaling. The authors interpreted the observed X flare QPP as episodic particle acceleration and plasma heating in the reconnecting flux tubes. On the other hand, such an association is at the moment speculative, and can only be viewed as in interesting prospect. QPP events are not fully understood, and multiple alternative interpretations have been offered [see review; Nakariakov and Melnikov, 2009]. Nakariakov et al. [2018] interpreted QPPs in radio data of a microflare site as a superposition of multiple harmonics

of oscillations, acknowledging that the interpretation is not unique. In our case, the X-Ray emission (section 3.4) manifests close to instrumental detection limits along with the short lifetimes of microflares hinders the possibility of multiple time analysis of hot thermal and non-thermal emission needed for quantitative interpretation of this aspect.

Jet energetics in a coronal context

The coronal implications of jet and jet like eruptions have been debated extensively. The contribution that jet like eruptions may have to the slow solar wind flux, or the influence in coronal heating remain open questions in the community. Two types of microflare generated solar jets exist: polar jets, originating usually open magnetic field regions of the polar coronal holes and active region jets can be found at the periphery of dynamic active regions, around complex magnetic field topologies. The main differences between polar jets and their active region counterparts is summarized in the [Introduction](#). The DEM analysis of the jet structure (body) was a necessary step in order to evaluate the energy output of active region jets. The energy budget can be estimated as a sum of separate energy fluxes,

$$F = F_{kin} + F_{pot} + F_{th}. \quad (3.22)$$

where the three components represent the kinetic, potential, and internal energy flux estimations [Pucci et al., 2013, Paraschiv et al., 2015]. Additional terms like a radiative loss or an Alfvénic wave flux can potentially be added to our determination. In practice we chose to neglect them as they can not be computed directly from our observations. Thermal conduction timescales are incompatible with the cadence of AIA observations.

The energy output of our three analyzed events was estimated. The energy release will vary across the different individual events, although at the global scale the eruptions appear as homologous. The approximation of the three flux quantities are described below.

$$F_{kin} = \frac{1}{2} \cdot n_e \cdot m_H \cdot v^3 \quad [erg \cdot cm^{-2} \cdot s^{-1}]. \quad (3.23)$$

$$F_{pot} = n_e \cdot m_H \cdot g \cdot H \cdot v \quad [erg \cdot cm^{-2} \cdot s^{-1}]. \quad (3.24)$$

$$F_{th} = \frac{\gamma}{\gamma - 1} \cdot n_e \cdot k_B \cdot T_e \cdot v \quad [erg \cdot cm^{-2} \cdot s^{-1}]. \quad (3.25)$$

The n_e quantity represents the erupting material's density, v is the outflow speed of the erupting plasma. This should not be confused with the emitting volume V that is utilized in eq. (3.26). H is the height of the jet and g represents the gravitational acceleration of the sun ($g = 274.13 m \cdot s^{-2}$) at $1R_\odot$. γ represents the ratio of the specific heats. Since the coronal plasma can be approximated to a monoatomic gas, we assumed $\gamma = \frac{5}{3}$. We have used the A2013 inversion results due to the simpler interpretation, where the EM is the peak of a temperature weighted Gaussian distribution. The following results with units in $erg \cdot cm^{-2} \cdot s^{-1}$ are obtained and visualized against the polar jet estimation of Pucci et al. [2013] and Paraschiv et al. [2015]. Note that the coronal losses are $\sim 10^7 erg \cdot cm^{-2} \cdot s^{-1}$.

$$\begin{aligned} J2 \rightarrow & F_{kin} = 2.14 \cdot 10^8 \quad F_{pot} = 1.23 \cdot 10^8 \quad F_{th} = 4.82 \cdot 10^8 \rightarrow F \approx 8 \cdot 10^8. \\ J3 \rightarrow & F_{kin} = 0.60 \cdot 10^8 \quad F_{pot} = 0.99 \cdot 10^8 \quad F_{th} = 5.37 \cdot 10^8 \rightarrow F \approx 7 \cdot 10^8. \\ J6 \rightarrow & F_{kin} = 2.13 \cdot 10^8 \quad F_{pot} = 0.83 \cdot 10^8 \quad F_{th} = 3.28 \cdot 10^8 \rightarrow F \approx 7 \cdot 10^8. \\ \text{Paraschiv et al. [2015]} \rightarrow & F_{kin} = 0.01 \cdot 10^8 \quad F_{pot} = 0.01 \cdot 10^8 \quad F_{th} = 0.07 \cdot 10^8 \rightarrow F \approx 0.1 \cdot 10^8. \\ \text{Pucci et al. [2013]} \rightarrow & F_{kin} = 0.30 \cdot 10^8 \quad F_{pot} = 0.03 \cdot 10^8 \quad F_{th} = 0.17 \cdot 10^8 \rightarrow F \approx 0.5 \cdot 10^8. \end{aligned}$$

Careful consideration when computing energetic estimations needs to be employed. Inside our homologous self recurrent jet dataset all three eruptions were unique from the point of EM determinations. The flux values are individually obtained for the J2, J3, J6, and Pucci et al. [2013], while the Paraschiv et al. [2015] determination represents a 18 event average. Across all five examples, the F_{pot} appears to be mildly significant. With the noted exception of the Pucci et al. [2013] jet, the F_{th} appears to be dominating the emission, displaying a factor 2-5 more power allocated to fluxtube heating in disfavor of F_{kin} . We find that the jet EM profiles depicted in fig. 3.6, where a substantial quantity of hot coronal plasma is being ejected, agree with the flux ratio.

Another possible caveat may lie in the fact that the J2, J3 and J6 estimations are obtained using the EUV DEM alone, while the Pucci et al. [2013], Paraschiv et al. [2015] results are obtained using Hinode XRT inversions. This is relevant in the context of a comparison. Multiple works [Su et al., 2018, Schmelz et al., 2015, Wright et al., 2017] claim a calibration issue leads to a difference of factor ~ 2 between SDO-AIA and Hinode XRT instruments and propose a scaling of the X-Ray data. Concurrently, works as C2015 (synthetic data) and Hanneman and Reeves [2014] and Mulay et al. [2017a] (observational measurements) show that adding XRT to AIA generated DEM measurements contributes in a positive way to the solution. Such problems are not necessarily related to a calibration issue as DEM estimations are in general more subjected to limitations in the inversion scheme or observations. In this work we chose to not use SDO-AIA DEM responses for $\log T_e > 7.3$, that being already an optimistic assumption given the flat nature of the SDO-AIA response in that range. This is a necessary global precaution, where the standard coronal plasma is better constrained on a global scale due to the lower degrees of freedom in the imposed inversion matrix. We also note our particular case in which we allow $\log T_e < 7.4$ emission in the C2015 inversion, we obtain identical counts to the thermal X-Ray DEM fit.

On a related but different note, Testa et al. [2011] found that a possible discrepancy existed where Hinode's EIS counts were underestimated when compared to XRT, suggesting that, at least at the respective time, an abundance problem may exist. Del Zanna [2013], Mulay et al. [2017a] found an excellent agreement between SDO-AIA counts and EIS data. The CHIANTI database has also significantly improved in recent years. In the current case, the flux determinations scale linear with respect to computed plasma densities, a cross-calibration factor of 2 – 3 cannot possibly account for a difference of 1-2 orders of magnitude in between the XRT vs. SDO-AIA computed fluxes.

Active region jets, at least in the case of the AR11302 geyser structure, appear to be stronger, in order of magnitude scales, than their polar coronal hole counterparts. As revealed in section 2.2, the intrinsic geyser site is of medium size when compared to other flaring footpoints. The polar jet contribution to coronal hole heating was shown by Paraschiv et al. [2015] to be significant, but more than one order of magnitude insufficient. Although the net flux estimations are intriguing, the formation region is substantially different in the case of active penumbral topology and a correspondent computation is not valid.

Studies such as this are utilized to find and visualize the detailed and intricate mechanisms that govern coronal processes. Contrariwise, prudence is required when addressing the larger context as the main coronal drivers (e.g. reconnection flares) are manifesting in a very wide energy range (nanoflare-microflare-flare), with non-linear power scalings. Our geyser flares proved to be weak when measured against the Hannah et al. [2008] microflare distribution, although the ejecta are overwhelmingly stronger when compared to the polar counterparts that are also attributed to microflaring reconnection. The nanoflare scale is usually reserved for more modest events, manifesting

at chromospheric heights, scales, and temperatures [Judge et al., 1998, Tian et al., 2014, Bharti et al., 2017, Tian et al., 2018]. Only by employing statistically valuable studies, we can gather meaningful coronal context data. The ‘coronal geyser’ nomenclature aims to be a first step towards a pursuit of a wider sample automated survey of active region jets. The main parameters resulted from the Paraschiv et al. [2015] were cross-checked using MHD simulations by Török et al. [2016], Lionello et al. [2016] and taken into account in models of mass and energy injection to the solar wind outflow.

In more recent work, Török et al. [2016] and Cranmer et al. [2017] debate the heliospheric influence of the modest polar coronal hole jets. Could the difference in scale between polar and active region jets fill the missing energy and mass release? Active region jets are hard to fit in the same picture, making comparisons very troublesome. Shimojo et al. [1996] and Shimojo and Shibata [2000] show that most Yohkoh-SXT jets occur near or in active regions. On the other hand, statistics of a very large number of events [Paraschiv et al., 2010] recorded at heliospheric heights by the twin STEREO-COR1 coronagraphs showed that a overwhelming proportion of white-light jets were associated with the two polar coronal holes. The Paraschiv et al. [2010] study is centered around the solar minimum between the 23 and 24 cycles, while the Shimojo and Shibata [2000] study is performed on an ascending phase of activity. Similarly, the Paraschiv et al. [2015] XRT jets were recorded in polar coronal holes during the extended minimum period. Thus, any determination of ejected flux and mass outflow needs to be addressed in the context of the global solar activity, as there are huge differences in interpretation.

Nonetheless, AR jet eruptions are a relatively scarce phenomena, and probably can only offer momentary inputs to the solar wind in the form of transients. The solar wind stream is currently discontinuous e.g. the sources are not fully resolved, in regions close to the solar surface. Neugebauer [2012] showed that microstreams in the solar wind were property-wise correlated to polar coronal hole jets. It is much more challenging to prove such a connection for active region jets and geyser footpoints as the heliospheric connectivity should not be taken for granted as in the case of polar jets. Our geyser dataset viewed in the context of the heliospheric travel of electron beams along ‘open’ fluxtubes as described by fig. 2.1 may provide valuable information for constraining solar wind parameters. A tracking of such geyser ejecta up to in-situ particle flux detectors as WIND and ACE may prove extremely fruitful. In conclusion, we speculate that although very energetic, active region jets lack the ubiquitousness that their polar counterparts exhibit, limiting their potential influence on heliospheric energetics and dynamics.

Microflares and downwards acceleration of particles

The three analyzed recurrent coronal jets were subjected to high energy analysis using RHESSI observations. When compared to typical microflare pictures where jet emission is not always detected, the geyser site’s flaring episodes appear to be more impulsive. The analysis of the footpoint flaring revealed that the energy release is quite substantial. An analogy to standard flares may exist. As flaring events can be eruptive or confined based on local conditions, it can be speculated that microflare jets may be compared to ribbon heating generated by lower atmosphere microflare events. Can our geyser be considered a typical microflare site?

From a thermal perspective, X-Ray spectral analysis is performed during peak X-Ray emission and EUV flaring (fig. 3.10). We were not able to reproduce the observed RHESSI spectra, using exponential (Gaussian) based thermal emission models. The EUV DEM

profiles recovered in fig. 3.4 (bottom) also appear to sharply decrease towards the high temperature regions. The issue is reported in microflare studies [Inglis and Christe, 2014, Kirichenko and Bogachev, 2017]. Inglis and Christe [2014] deduce that a Gaussian DEM can not jointly fit a combined SDO-AIA and RHESSI emission measures and propose a simple uniform DEM that has a high cutoff frequency. Although this determination seems to solve the punctual issue of ‘fusing’ the data, important information on the microflare source will be lost via the intrinsic smoothing. We advocate in favor of meticulous interpretation of recovered DEM profiles as, at least in the case for our geyser site, the EM distributions are multithermal, and Gaussian methods were shown to be misleading.

Hannah et al. [2008] offer a comprehensive statistical study of automatically detected RHESSI microflares, processing over 25000 events. The authors found DEM in the order of $10^{45} - 10^{47} \text{ cm}^{-3}$, in volumes of about $10^{25} - 10^{27} \text{ cm}^3$ with dissipated thermal energies E_{th} of $10^{26} - 10^{30} \text{ erg}$. Our geyser footpoint events had RHESSI DEMs of 10^{45} cm^{-3} in a volume of $\sim 10^{25} \text{ cm}^3$ and computed thermal energies of $J2 = 2.5 \cdot 10^{27} \text{ erg}$, $J3 = 3.4 \cdot 10^{27} \text{ erg}$, and $J6 = 3.85 \cdot 10^{27} \text{ erg}$. Furthermore, we mention the study of Wright et al. [2017] who analyzed the thermal characteristics of an impulsive microflare using the new generation [*NuSTAR*; Harrison et al., 2013] observations. Our results agree to the Wright et al. [2017] estimated energies of $E_{th} = 9 \cdot 10^{27} \text{ erg}$. We have assumed the filling factor $\phi = 1$ (see eq. (3.15)) and utilized

$$E_{th} = \frac{\gamma}{\gamma - 1} \cdot n_e \cdot k_B \cdot T_e \cdot V, \quad (3.26)$$

where the coronal plasma was approximated to a monoatomic gas, $\gamma = 1.66$, V represents the emitting volume, and n_e is the volume reconstructed local plasma density. We note that our employed specific heat factor of 2.5 is slightly different from the 3 factor used generally in the literature [Hannah et al., 2008, Wright et al., 2017, de Jager et al., 1986].

The geyser site is energetically near the lower limits of thermal microflare power. The thermal energy remain roughly the same even when considering the EUV EM $\log T_e \sim 7$ results and acknowledging that the RHESSI soft X-Ray thermal component may reflect just a small portion of the total emitting plasma. For both intrinsic data and Hannah et al. [2008] the emission measures and footpoint thermal energetics need to be considered as upper limits, due to the unity filling factor assumed.

The standard flare picture now assumes downward particle acceleration, where non-thermal electron beams stream towards the newly reconnected flare footpoints resulting in chromospheric evaporation which in turn heats the entire loop structure. X-Ray emission source morphologies of the three jets were reconstructed using RHESSI’s imaging capabilities (fig. 3.9). Two distinct morphologies are reproduced in hard and soft X-Ray energy bands, whereas the hard emission is spatially separated into two sources corresponding to the geyser footpoint. The soft X-Ray emission presented in a more compact source, that corresponds to the loop top. The distinct source morphology along with the hard X-Ray footpoint separation is a first indicator that we are indeed observing particle acceleration.

Microflare non-thermal spectral fitting was also performed. The power P_N of the non-thermal electrons that manifest at energies higher than the non-thermal cutoff E_c was determined using the eq. (3.27) formula (see Brown [1971], Hannah et al. [2008], Wright et al. [2017]). The F_e term represents the total non-thermal electron flux in units of 10^{35} e s^{-1} and δ represents the power law spectral index. We have extracted the function parameters from the fitting of the *fthick2* thick-target model (fig. 3.10). Not all parameters are derived in all determinations as the different studies used their respective assumptions

and analytical approximations when computing P_N . Particularly, the non-thermal cutoff E_c is shown by Hannah et al. [2008] to be problematic as the expected range is affected by thermal emission. The authors chose an analytical alternative in their evaluation,

$$P_N(> E_c) = 1.6 \cdot 10^{-9} \cdot E_c \cdot F_e \cdot \frac{\delta - 1}{\delta - 2}. \quad (3.27)$$

The nanoflare non-thermal heating results as revealed by the T2014 [Testa et al., 2014] paper discussed in section 1.2 are also presented as a scale comparison. We emphasize the fact that it was shown in section 1.2 [Judge et al., 2017] that both a low atmosphere flare or non-thermal beam heating can explain the respective nanoflare observational data. Just one case of the T2014 event set was revealed to be disconnected from the corona. The T2014 study presents model driven constraints on non-thermal beam scenarios applicable to nanoflares. The main results along with the literature values are presented below:

$J2 \rightarrow$	$\delta \sim 7.50$	$E_c \sim 15.3 \text{ KeV}$	$F_e = 0.07$	\rightarrow	$P_N = 2.10 \cdot 10^{26} \text{ erg s}^{-1}$.
$J3 \rightarrow$	$\delta \sim 6.27$	$E_c \sim 13.7 \text{ KeV}$	$F_e = 0.16$	\rightarrow	$P_N = 4.32 \cdot 10^{26} \text{ erg s}^{-1}$.
$J6 \rightarrow$	$\delta \sim 7.17$	$E_c \sim 11.0 \text{ KeV}$	$F_e = 1.65$	\rightarrow	$P_N = 3.46 \cdot 10^{27} \text{ erg s}^{-1}$.
Hannah et al. [2008] \rightarrow	$\delta \sim 4 - 10$	$E_c \sim 9 - 16 \text{ KeV}$		\rightarrow	$P_N \sim 10^{25} - 10^{28} \text{ erg s}^{-1}$.
Inglis et al. [2014] \rightarrow		$E_c \sim 9 - 14 \text{ KeV}$		\rightarrow	$P_N \sim 10^{25} - 10^{26} \text{ erg s}^{-1}$.
Wright et al. [2017] \rightarrow	$\delta > 7$	$E_c = 7 \text{ KeV}$		\rightarrow	$P_N \sim 10^{25} - 10^{26} \text{ erg s}^{-1}$.
Testa et al. [2014] \rightarrow		$E_c = 10 \text{ KeV}$		\rightarrow	$P_N \sim 10^{24} \text{ erg s}^{-1}$.

The geyser footpoint does fit in the general non-thermally emitting microflare picture, but issues with the RHESSI sensitivity are apparent. Hannah et al. [2008] document issues in the quantitative estimation of non-thermal properties of the less intense microflares, only 15% of their events were associated with identifiable non-thermal emission, of importance being the fact that the lack of quantitative non-thermal emission fitting was probably not occurring due to a lack particle acceleration, but more probably due to the high uncertainties in fitting a non-thermal component. In our geyser case, the *thick2* fit residuals were significant ($\sim 35\%$) in all three eruptions. We consider the non-thermal fitting as trustworthy.

Our data can not distinguish if chromospheric evaporation is the main process that drives electron thermalization as envisioned by the standard flare model. Similar conclusions are found by Inglis and Christe [2014] who offer alternative scenarios that may explain their microflare dataset. The author's events appear less impulsive than the geyser footpoint analyzed herein. In order to evaluate the chromospheric evaporation hypothesis a comparison of the power ratio between the resulting thermal heating and presumably prior energy injection via thick-target bremsstrahlung is required. Inglis and Christe [2014] found that the computed thermal energies are substantially higher than their non-thermal counterparts, analogous to the Hannah et al. [2008] results. Based on the fact that the thick-target model fitting coefficients are uncertain and have a dependence on the observed photon flux, we assumed that the RHESSI instrumentation is not accurate enough to resolve such fine details.

The geyser observational data at peak flaring time is fitted by both thermal and non-thermal emission models, showing evidence of downwards particle acceleration in the case of jet-inducing microflare events. Jet eruption reconnection is thus brought closer to the standard flare model. Prior to the flare phase a thermal solution could be found to fit background counts, but, as expected, no non-thermal function was able to reproduce the data. RHESSI is one of the most successful solar missions up to date, massively helping us

advance our knowledge of flare energetics and particle acceleration for the last two decades. A new mission focused on high energy spectroscopy and imaging is highly desired. An increase in energy resolution along with lower instrumental noise, will help settle the main problems of small scale flaring properties.

CHAPTER 4

The Magnetic Topology and Extrapolated Field Configuration of a Lower Atmosphere Geyser Site

Foreword: Aiming to understand the base reconnection processes that govern small-scale flaring sites, we analyzed the configuration and dynamics of the the base photospheric and chromospheric magnetic structures that emits the multiple geyser recurrent jets. Taking into account the current solar magnetic field observation capabilities, careful consideration needs to be employed when discussing the small-scale magnetic field evolution around the penumbral jets formation area. We discuss the nature of the geyser’s underlying magnetic reconnection focusing on two complementary approaches: The magnetic reconnection topology involved in the jet eruptions is described via analysis of magnetic moving features aiming to understand if a unique self repeating process is responsible for driving the apparently homologous jet eruptions; The photospheric magnetic fields correlated to the geyser location and involved in generating active region jets are derived under the force-free assumption. The chromospheric and transition region magnetic structures are reconstructed and compared to existing modeling, revealing the field configuration and dynamics of our recurrent jet inducing geyser structure.

4.1 Solar Vector Magnetic Fields

Magnetic fields play a key role in the existence and variability of phenomena found on the Sun. Solar photospheric magnetic fields have been mapped for a considerable amount of time. To our knowledge, Hale [1908] first inferred the existence of photospheric magnetic fields using spectrograph observations. We quote the Hale [1908] conclusions as a parallel to our current observational capabilities.

“These results leave no doubt in my mind that the doublets and triplets in the sun-spot spectrum are actually due to a magnetic field... I hope it may become possible to investigate small spots, as well as large ones, and to resolve many of the doublets and triplets in their spectra”

Although Hale [1908] probably did not refer to what we now understand as small-scale, a thorough understanding of small-scale solar magnetism is still elusive. We can only hope, that the early 20th century optimism can be soon be rewarded. The importance of line of sight (LOS) photospheric magnetic field measurements, was exposed gradually, starting with the development of synoptic magnetic field observations. See the Babcock and Babcock [1952] works for the first systematic observations and Babcock [1959] who revealed solar polar magnetic field inversions, along multi-year timeframes, contributing to the knowledge of what we today know as the solar cycle. LOS magnetic field measurements improved in

the subsequent decades. Specialized instruments, e.g. the Haleakala Stokes Polarimeter [Mickey, 1985], which could recover vectorial magnetogram data were developed, greatly improving our understanding of magnetic field structures. These instruments were more or less manually operated, where just sporadic data are available.

Vector magnetic fields are the current generation magnetic field measurements. All discussed developments refer to photospheric magnetic fields. Higher atmosphere structures of the chromosphere or corona could only be reliably recovered indirectly, via forward modeling of the photospheric fields, in the form of extrapolations. Magnetic field extrapolations are described in section 4.3. Recently, a vast amount of work has been put into resolving issues that hinder a direct calculation of chromospheric magnetic fields, [see review; Wiegmann et al., 2014]. In the past, chromospheric magnetic fields estimations were inferred in the past as specially designed particular observations. A notable mention is the study of Metcalf et al. [1995] who estimated a very important lower limit for force-free conditions. Currently, a generalized solution of this topic is still out of reach.

The next logical step was, to obtain reliable vector magnetic observation pipelines. This was only a recent accomplishment, routine magnetic field imaging capabilities being important goals of the Hinode and SDO missions. The Hinode-SP [Tsuneta et al., 2008] provides the best spectral and imaging of magnetic fields at the sacrifice of temporal cadence. A standard Hinode-SP AR scan takes ~ 1 hour to complete. The available Hinode-SP AR11302 scan on the observation day (25 Sep. 2011) has a scanning datagap over our region of interest, hindering any analysis possibility. Only SDO-HMI data was available to incorporate in our Geyser study.

4.1.1 The SDO-HMI Instrumentation

The Helioseismic and Magnetic Imager [HMI; Scherrer et al., 2012] magnetogram data was utilized in order to recover the lower atmosphere features correspondent to the geyser emission site. The instrument is part of the SDO mission designed as complementary to the AIA EUV imager described in the previous chapters. The HMI imaging system uses two 4096×4096 pixel CCD cameras on different optical systems, obtaining a 0.5 pix^{-1} platescale resolution. The spatial resolution is $\sim 1''$. The instrument records sequences of polarization states in six wavelengths centered on the Fe I 6173.34\AA line. The final data products are created using a set of software modules, operating as analysis observations, commonly known as the JSOC pipeline.

The two optical systems are developed for different science goals. The ‘Doppler’ HMI camera recovers full-disk Doppler velocity, line-of-sight magnetic flux, and intensity continuum images with a data cadence of 45s. The ‘Vector’ magnetic field ensemble records spatially localized full vectorial maps every 135s. The integration time is not sufficient for accurate recovery of reliable signal. Thus, the JSOC pipeline integration times are thus set to 720s. An automated code detects and tracks newly emerged patches of active regions (HARP) providing near instant data. The HARP delimitations do not necessarily follow the NOAA AR classification.

We utilized the ‘best calibrated’ patch data. The product is referred to as definitive SHARP [Bobra et al., 2014]. This dataserie contains the most processed and best calibrated HMI vector data. SHARPs are computed after an active region completes its disk passage in order to ensure the best spatial extent and processing parameters are used. Detailed information on the HMI vector magnetic field products can be found in Hoeksema et al. [2014]. The Hoeksema et al. [2014] paper also presents an extensive overview of

assumptions, issues, and uncertainties that arise when creating the SDO-HMI vector maps. A full discussion on this topic would be outside our scope. The particular uncertainties correspondent to our observations are discussed.

4.1.2 Interpreting Vector Magnetic Field Observations

Investigations of solar magnetic manifestations of small-scale eruptive phenomena are rather scarce. This is due in part to the high uncertainties involved in interpreting solar magnetic fields. Also, the inherent instrumental and physical problems that govern magnetic data reconstruction do not ease the task. The general interpretation of vector magnetic fields is resulting from a series of convoluted processes. SDO-HMI is not an exception.

Firstly, a ‘good’ magnetically sensible spectroscopic emission line is required. SDO-HMI uses the Fe I 6173.34Å line. The vector HMI camera records a succession of polarization states around the emission line. Spectro-polarimetric interpretation is used to recover the Stokes linear and circular polarization profiles of the above mentioned ion. The instrument records the $I \pm V$, $I \pm Q$, and $I \pm U$, where I , Q , U , and V are the Stokes polarization states. The four profiles are transformed into raw magnetograms, assuming a Milne-Eddington (ME) model, using a specialized inversion method namely the Very Fast Inversion of the Stokes Vector [VFISV; Centeno et al., 2014] is a ME spectral line inversion code specifically designed for solar magnetic field reduction. The inversion is performed automatically as part of the JSOC procedure and is provided as a finite product. We are not aware of any benefits of altering this procedure and up to this point use the data as processed via the JSOC pipeline.

The ME inverted non-projected SHARP data (*hmi.sharp_720s*) provides three main products: The total field strength (B), the apparent inclination (γ) and the azimuth angle (ϕ). The inclination corresponds to SDO’s line of sight as a consequence of the fact that we are dealing with image based coordinates. Image coordinates can be misleading. The utilized HMI product pipeline corrects for distortion effects but does not do automatic remapping. In other words, each pixel, in time, corresponds to the same projected area on the CCD plane, but due to solar rotation, will correspond to a different projection with respect to the solar surface.

A vector transform remap, as sketched in fig. 4.1, is applied to the three vector components, in order to recover ‘true’ solar tangential magnetic field vectors. We start by separating the image projected components in transversal and longitudinal components as

$$B_l = B \cdot \cos(\gamma) \quad \text{and} \quad B_t = B \cdot \sin(\gamma). \quad (4.1)$$

The remapping can be achieved by assuming a set of image coordinates (B_x^i, B_y^i, B_z^i) where

$$B_x^i = -B_t \cdot \sin(\phi), \quad B_y^i = B_t \cdot \cos(\phi), \quad \text{and} \quad B_z^i = B_l. \quad (4.2)$$

We reproduced the Gary and Hagyard [1990] eqs. 1-2 and interpretation for an off-center coordinate transform. The magnetic field system of vectors along with the image coordinate vector are transformed into a heliographic-tangential system and projected on a new solar plane using

$$\begin{bmatrix} B_{xh}^h \\ B_{yh}^h \\ B_{zh}^h \end{bmatrix} = \begin{bmatrix} a_{11} & a_{12} & a_{13} \\ a_{21} & a_{22} & a_{23} \\ a_{31} & a_{32} & a_{33} \end{bmatrix} \begin{bmatrix} B_{xi}^i \\ B_{yi}^i \\ B_{zi}^i \end{bmatrix}, \quad \text{where} \quad \begin{bmatrix} xi \\ yi \end{bmatrix} = \begin{bmatrix} c_{11} & c_{12} \\ c_{21} & c_{22} \end{bmatrix} \begin{bmatrix} xh \\ yh \end{bmatrix}. \quad (4.3)$$

The a_{mn} and c_{mn} coefficients correspond to:

$$a_{11} = -\sin(B_0) \sin(P) \sin(L - L_0) + \cos(P) \cos(L - L_0).$$

$$a_{12} = +\sin(B_0) \cos(P) \sin(L - L_0) + \sin(P) \cos(L - L_0).$$

$$a_{13} = -\cos(B_0) \sin(L - L_0).$$

$$a_{21} = -\sin(B) \cdot [\sin(B_0) \sin(P) \cos(L - L_0) + \cos(P) \sin(L - L_0)] - \cos(B) \cos(B_0) \sin(P).$$

$$a_{22} = +\sin(B) \cdot [\sin(B_0) \cos(P) \cos(L - L_0) - \sin(P) \sin(L - L_0)] + \cos(B) \cos(B_0) \cos(P).$$

$$a_{23} = -\cos(B_0) \sin(B) \cos(L - L_0) + \cos(B) \sin(B_0).$$

$$a_{31} = +\cos(B) \cdot [\sin(B_0) \sin(P) \cos(L - L_0) + \cos(P) \sin(L - L_0)] - \sin(B) \cos(B_0) \sin(P).$$

$$a_{32} = -\cos(B) \cdot [\sin(B_0) \cos(P) \cos(L - L_0) - \sin(P) \sin(L - L_0)] + \sin(B) \cos(B_0) \cos(P).$$

$$a_{33} = +\cos(B_0) \cos(B) \cos(L - L_0) + \sin(B) \sin(B_0).$$

$$c_{11} = \cos(P) \cos(L_c - L_0) - \sin(P) \sin(B_0) \sin(L_c - L_0).$$

$$c_{12} = -\cos(P) \sin(B_c) \sin(L_c - L_0) - \sin(P) [\cos(B_0) \cos(B_c) + \sin(B_0) \sin(B_c) \cos(L_c - L_0)].$$

$$c_{21} = \sin(P) \cos(L_c - L_0) + \cos(P) \sin(B_0) \sin(L_c - L_0).$$

$$c_{22} = -\sin(P) \sin(B_c) \sin(L_c - L_0) + \cos(P) [\cos(B_0) \cos(B_c) + \sin(B_0) \sin(B_c) \cos(L_c - L_0)].$$

The B_0 and L_0 are the solar disk centre longitude and latitude coordinates and B_c and L_c the image center point. B and L represent the determined heliographic latitude and longitude of the discussed pixel, and P is the solar axial rotation angle. The resulting (B_x^h, B_y^h, B_z^h) vectors are computed, where each component is now mapped to a position in the heliographic plane.

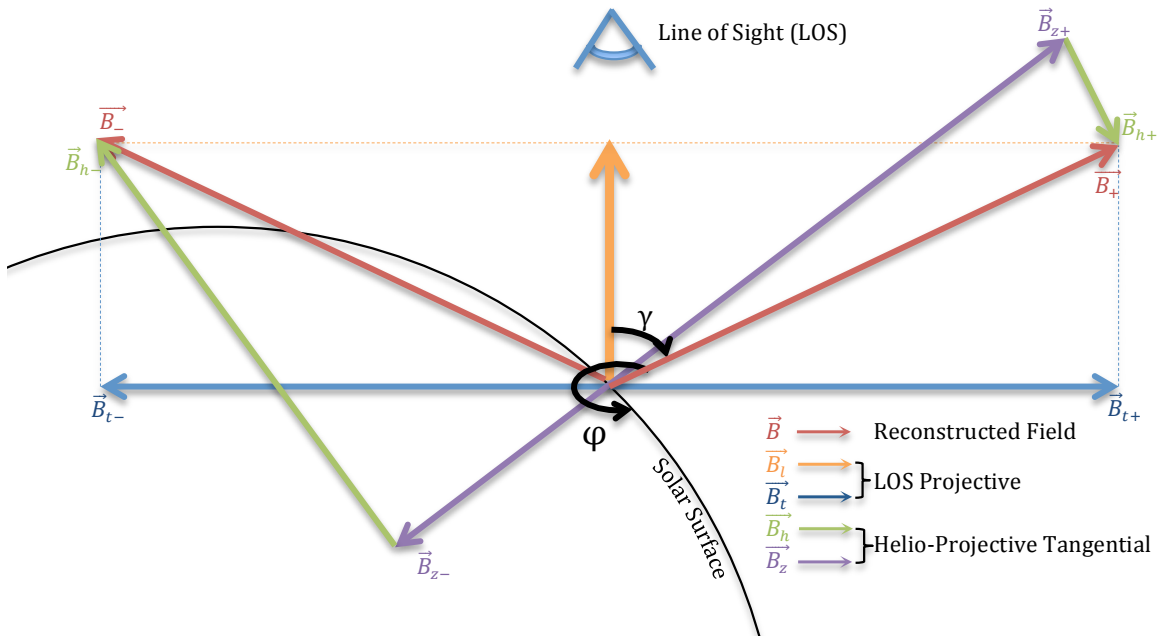


Figure 4.1: Line of sight projected (image) to solar-tangential (true) coordinate transform using the eq. (4.3) transformation matrices of Gary and Hagyard [1990]. The two possible vector component combinations that can reproduce the same scalar total field strength B are represented assuming the unresolved 180° ambiguous data. The 180° ambiguity does propagate when translating to the solar referential system.

One crucial issue exists in the HMI data processing pipeline. The VFISV inversion applied locally to each pixel does not address a 180° azimuth ambiguity present in the image projected B_t (transverse field) vector. If not resolved, the ambiguity will naturally translate along with the heliographic coordinate transform. We have treated this aspect separately in section 4.1.3. This secondary inversion is applied globally to the entire SHARP region. Although Milne-Eddington and ambiguity inversions are separate issues, assumptions resulted from the sequence of inversions are introduced in order to recover magnetic field information. A full discussion of vector magnetogram inversion limitations is outside our present scope but is discussed by Hoeksema et al. [2014, Sec. 7].

Once the heliographic field components are calculated, we investigate the particularities of our observation period. We are immediately faced with a geometrical concern. The solar disk position of the SHARP region on 25 Sep. 2011 was as a general reference, $x \sim [700'', 500'']$ and $y \sim [50'', 200'']$, significantly far from the disk center. The HMI maps are geometrically de-projected as mentioned above, but there is no ‘fix’ for a degraded quality of the initial Stokes profiles. In particular, the inclination angle measurement was noisy. This aspect will increase the noise altering the instrumental detection limit. Higher than standard uncertainties are expected. We note that line of sight magnetograms could not be used, at least in the first part of the observation day, since the LOS field was compromised by limb effects.

The AR11302 was one of the first to be subjected to the SHARP pipeline. We have checked the JSOC provided pixel confidence maps (*confid_map*) for the $25'' \times 25''$ penumbral region centered on the position of the photospheric geyser footpoints. At a quick glance, we report that most pixels behaved reasonably (code 0-1), for both quiet and eruption times. Few short-lived code 2-3 features could be detected, and only the occasional aberrant pixels were observed. Our main goal is the interpretation of small-scale fields of the geyser site. Even if discussing purely theoretically, penumbral fields are only of medium strength (250 - 700 G), being significant, but not very strong when compared with the quiet-sun background levels (~ 100 G). We thus investigated two statistical constraints searching for issues that could influence our particular observations.

Firstly, in order to understand the influence of solar position in evaluating systematic uncertainties, we computed the B_t background detection limits as our penumbral region is full of low-lying serpent or generally inclined canopy fields. We summed the first two hours of observation, 00:00UT to 02:00UT, in order to get an upper limit on the systematic noise. We computed the pixel-wise quiet-sun B_t distribution of background noise that manifest in close proximity to our geyser structure. The selected regions appeared to be void of any significant field. The distribution is presented in fig. 4.2 (left).

A mean noise threshold value of 130 G was found. Standard deviations of $\sigma_s = 41$ obtained by error propagation and $\sigma_G = 39$ resulting from the Gaussian fit were obtained. Scarce pixels with transversal field strengths between 250 G and 460 G were identified in the sampling region, but not represented in the plot. They were taken into account when computing the standard deviations.

As expected, the noise level is particularly high. Hanson et al. [2015] found noise values of 60 G in quiet sun patches neighboring an AR close to disk center. A confidence level of 6σ in B_t is usually utilized in order to recover meaningful signal. This is impractical in our case due to both the modest fields involved in jet eruptions and high background levels. We have relaxed our B_t detection limits to be accurate in the order of at least 3σ (~ 240 G).

Secondly, we computed the confidence map of the photospheric fields corresponding to our geyser structure (fig. 4.2, right). One frame, 01:24UT, close to the start of our

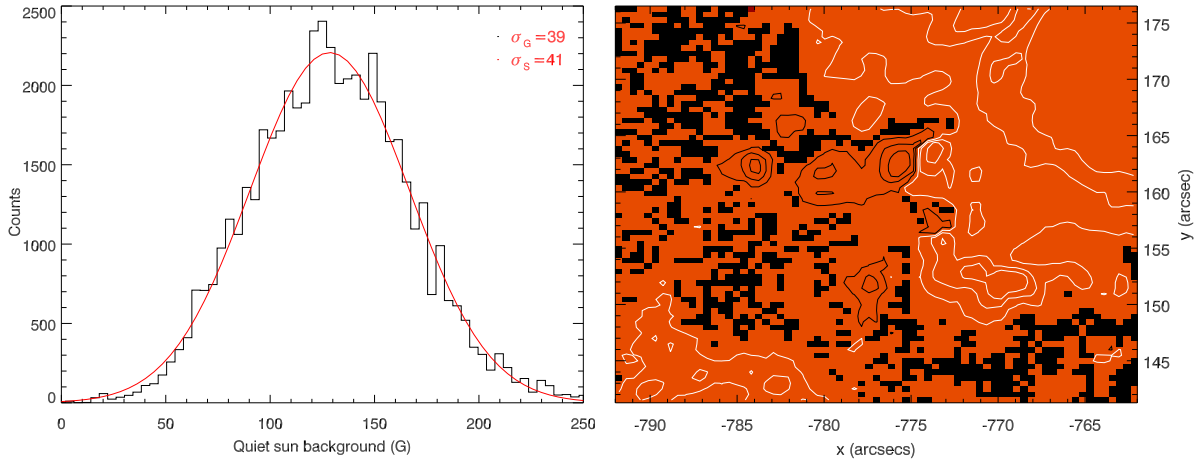


Figure 4.2: Estimation of magnetic field detection limits and the pixel uncertainties of SHARP region 892 (AR11302) for a two hour interval between 00:00UT and 02:00UT on 25.09.2011. We evaluate these uncertainties assuming that these are the higher limit of errors resulted from projection, as the AR is moving towards a disk central position. **Left Panel:** Histogram of the transversal fields (B_t) noise values close to the geyser region of interest. The purely statistical standard deviation σ_S along with the Gaussian fitted standard deviation σ_G are calculated. **Right Panel:** Example (01:24UT) of a confidence map for the photospheric geyser region. The relative uncertainty of the heliospheric vertical magnetic fields (B_z) is computed using the eq. (4.4) validation criterion. The contours represent fields of strength $[\pm 200 \text{ G}, \pm 500 \text{ G}, \pm 800 \text{ G}]$ of positive (white) and negative (black) polarity and the black patches represent uncertain areas.

observations was chosen with the intent to sample a measure of the highest magnetic uncertainties. We have checked confidence maps for multiple time instances finding similar results. The map represents the relative uncertainty of the heliospheric vertical magnetic fields (B_z), computed using an adapted version of the validation criterion employed by Hanson et al. [2015],

$$\frac{|B_z^2|}{|B_{z-err}^2|} > 1. \quad (4.4)$$

The base map is dual tone, where the red areas represent usable pixels and the black patches represent uncertain areas that are dominated by noise. We overplotted contours representing vertical fields of strength $[\pm 200 \text{ G}, \pm 500 \text{ G}, \pm 800 \text{ G}]$ of positive (white) and negative (black) polarity respectively.

The $\pm 10''$ area around $(X, Y) = (-780, 160)$ corresponds to the EUV geyser footpoint. It is shown that the grain-like fields, small dipole emergences, and the stronger pore present are not noise dominated. We have not utilized the standard SDO-HMI error maps. Instead, we followed standard error propagation when estimating uncertainties from regions close to the jet emitting site and correspondent to the custom disambiguation result.

Following standard error propagation and using the Goodman [1960] variance of products we assume the B , γ , and ϕ quantities as independent variables we can derive the error estimations corresponding to the image projected vectors B_x^i , B_y^i , and B_z^i as shown in eq. (4.5). The σ_{B_t} and σ_{B_l} estimations are obtained via histogram binning of quiet sun data (e.g. fig. 4.2, left) and σ_ϕ is presumed to be no larger than 5° . We further subject the obtained uncertainty maps to the same projection transform (eq. (4.3)) using the a_{mn} and c_{mn} coefficients used for the field measurements, obtaining uncertainties corresponding to the heliospheric B_x^h , B_y^h , and B_z^h vector components;

$$\begin{aligned}
B_{xi-err}^i &= \sqrt{\sin^2(\phi) \cdot \sigma_{B_t}^2 + B_t^2 \cos(\phi)^2 \sigma_\phi^2 + \sigma_{B_t}^2 \sigma_\phi^2 \cos(\phi)^2}, \\
B_{yi-err}^i &= \sqrt{\cos^2(\phi) \cdot \sigma_{B_t}^2 + B_t^2 \sin(\phi)^2 \sigma_\phi^2 + \sigma_{B_t}^2 \sigma_\phi^2 \sin(\phi)^2}, \\
B_{zi-err}^i &= \sigma_{B_t}.
\end{aligned} \tag{4.5}$$

Following the vertical field component (B_z^h), we tracked the uncertainties of the (above-noise) magnetic structures of our photospheric region of interest. The uncertainties varied on average from typical values of ± 90 G to ± 50 G during the 24 hours of observations as the region traveled towards disk centre. As can be observed, unsolvable effects still manifest as not all issues could be mitigated. Regardless of the meticulous employed, the retrieval of magnetic vectorial fields outside a disk central position can not be considered a precise procedure.

4.1.3 Custom Vector Magnetic Field Disambiguation

When analyzing the standard JSOC vector field products we noticed that, sporadically, small scale magnetic features manifested in a ‘physically unstable’ nature (see fig. 4.3). Sudden and short lived (usually one integration time) polarity jumps were noticed in areas that should have been quasi-stable magnetic structures. These effects also appeared along more unstable potential inversion lines, but our interest focused on the penumbral and satellite structures embedded the in quiet sun areas. The geyser region was affected by these manifestations. Thus, we assumed that the standard JSOC disambiguation product is insufficient in order to describe our data. Therefore, we computed a custom tailored solution to the 180° disambiguation problem.

The ambiguity manifests due to unresolvable issues in the atomic properties of magnetically sensitive emission lines. When recovering the four Stokes profiles via the VFISV inversion, an uncertainty in the derivation of the transverse field component appears [Harvey, 1969]. In practical terms, the problem translates into a ‘sign’ uncertainty, (180° ambiguity) in the azimuthal angle of the recovered photospheric magnetic fields. The issue, along with its propagation when converting coordinate systems is illustrated in fig. 4.1. Multiple solutions were developed to solve this issue [see review; Metcalf et al., 2006]. The implementation based on the AMBIG ME0 code [Leka et al., 2009] that employs the minimum energy ambiguity resolution method described by Metcalf [1994] is widely utilized. The JSOC pipeline uses the ME0 implementation of the ‘minimum energy’ algorithm in order to resolve the inherent 180° ambiguity.

At its core ME0 optimizes the functional

$$E = |\nabla \cdot B| + |J_z|, \tag{4.6}$$

where the ‘energy’ term E is subjected to a global minimization via the simulated annealing algorithm [Metropolis et al., 1953]. The field divergence $|\nabla \cdot B|$ gives a physically valid solution, while the vertical current $|J_z|$ provides smoothness to solutions in pixels where the field divergence is high. Metcalf [1994] described the algorithm as very robust when dealing with large sets of discrete data, as only two outcomes exist for each pixel. Leka et al. [2009] showed that the ME0 method is one of the best performing algorithms, in both temporal and accuracy scales, but pointed out that the convergence towards a solution in high noise pixels is problematic. Additional methods are implemented as part of ME0 for

Table 4.1: The stable AMBIG-ME0 disambiguation model parameters presented as a comparison in between the standard JSOC pipeline disambiguation and the custom implementation. The used parameters relate to: detection limits (atresh and btresh), the number of pixel flips at each iteration (neq), the weighting between the divergence and current terms in the minimization functional(lambda), and the simulated annealing initial start and cooling factor (tfac0 and tfactr).

setup	atresh	btresh	neq	lambda	tfac0	tfactr
JSOC Disambiguation	200	400	20	1	2.0	0.990
Custom Disambiguation	120	240	200	1	2.4	0.996

these situations. The JSOC pipeline uses the nearest neighbor acute angle method [Canfield et al., 1993] in areas of low and intermediate transversal field strengths [Hoeksema et al., 2014, Leka et al., 2009].

Our interest lies in obtaining the most accurate representation of the low and medium strength magnetic field areas. We paid particular attention to the manner in which the JSOC pipeline implements ME0, particularly to the acute angle method. The JSOC utilized ME0 parametrization scheme is designed to produce a fast and fully automatized disambiguation procedure. Also, the main SDO-HMI mission goals [Scherrer et al., 2012], favor a 180° ambiguity solution correspondent to large scale regions, as small scale fields are usually, and for good reason, considered untrustworthy.

In particular the HMI-SHARP region 892 (AR11302) has a low field threshold of 400 G. That translates into: all transversal magnetic fields with values of <400 G are not resolved via the minimum energy method, but are subjected to the nearest neighbor acute angle interpolation, inheriting the resolved azimuthal angle of a stronger flux. This aspect may have detrimental effects for the small scale area correspondent to our region. As discussed in section 4.1.2 we found the detection limit of the utilized SDO-HMI transversal fields to be ~ 130 G with a pure quiet sun standard deviation of $\sim \sigma = 40$, thus obtaining a minimally constrained 3σ detection limit of 240 G. The small-scale photospheric jet inducing fields have vertical B_z strengths of over $\pm 3\sigma$ levels with the notable exception of J7 which was corroborated to a $\sim 2\sigma$ detection, see section 4.2.

In order to accurately recover the small scale fields of interest and mitigate the 'polarity flip' issues discussed above, we computed a custom disambiguation for our geyser data using the AMBIG-ME0 code¹. We devised a stable custom parameter scheme which is suited to our goals. The setup is presented in table 4.1. The AMBIG runs are set to perform a full SHARP region minimization for the fields which are above the quiet sun detection limit of 120-130 G and subjected patches that are under the 3σ strength to nearest neighbor smoothing. The number of times each pixel can be visited at each annealing iteration was substantially increased in order to allow for a greater number of small patch flips. We have set a higher starting temperature (tfac0) and a significantly slower annealing (tfactr) conditions, as it creates a better chance of converging to the global minimum.

The AMBIG parameter configuration will not only influence the quality of the data but will also be meaningful when discussing the runtime. The JSOC pipeline is severely time constrained. As a consequence, the default parameters are not ideal, as they result from a mixture between execution time and recovery of larger scale AR structures. Our custom setup increases the run time of one AMBIG solution from the order of a few minutes (JSOC) to a couple of hours. Setting tfactr=0.999, generates a runtime of approximately 24 hours per image. We have observed that applying cooling rates >0.996 did not add any practical

¹ AMBIG-ME0 code obtained courtesy of K.D. Leka & G. Barnes

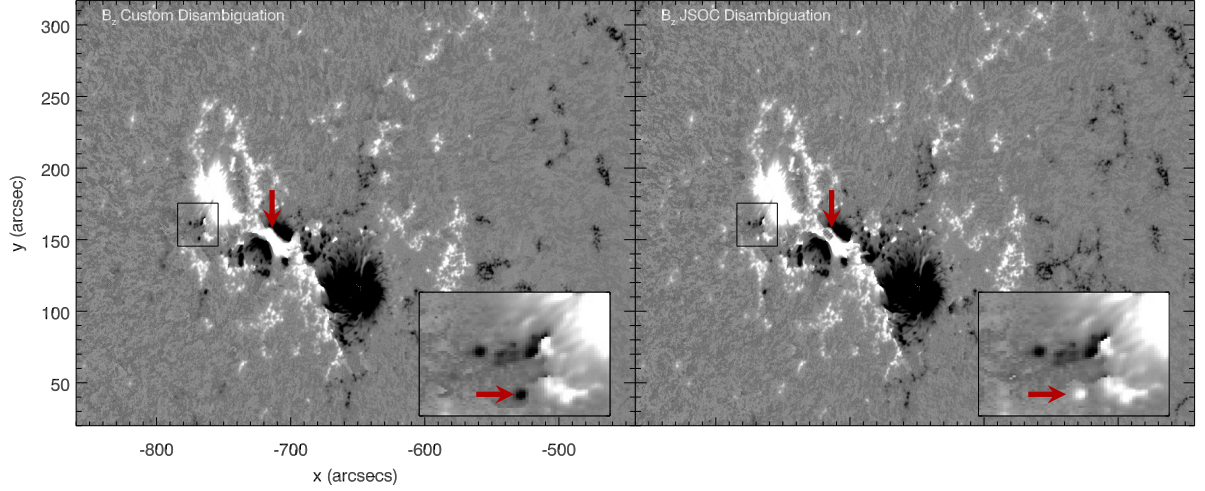


Figure 4.3: Comparison between the JSOC (right panel) and our Custom (left panel) disambiguation maps. The figure depicts the heliographic vertical B_z component, plotted in a ± 800 G range where the left-right differences manifest due to the azimuthal ϕ field component. A zoom-in of the boxed area representing the geyser region is included in the bottom-right corners of each plot. For example, when analyzing the temporal behavior of these features, it was observed that a southern pore experienced false polarity shifts in the standard SDO-HMI data products. The feature was stabilized to a true negative polarity for all its visible lifetime by the custom disambiguation. Also, ‘artifacts’ present in the geyser region (see red arrows) were mitigated by the slower annealing in our setup. In this instance (00:48UT), such ‘artifacts’ can be observed on the JSOC AR lightbridge at $(X, Y) = (-710'', 145'')$ and also in the zoomed-in area.

benefit, results being comparable to the $t_{\text{factr}}=0.996$ runs.

We tested the stability the disambiguation results by performing three individual attempts using different initial randomization seeds (iseed parameter) for each time instance. We verified, that at least in the geyser region, there were no discernible patches that behaved erratically. In general, no issues arouse for the fields above our 3σ detection limits, although fainter patches or individual problematic pixels showed problems. Additionally we checked that no non-physical ‘polarity flips’ occurred in any structures of interest during our observation. If found, problematic pixels were removed from any measurement. Also, the lambda factor representing the weighting factor between the divergence term and the vertical current density term was studied. We discovered that altering the parameter, even in a small way (e.g. 0.8-1.2) affected the multiple randomization runs of the disambiguations, generating less stable outputs.

All the azimuthal maps were subjected to the above described transformation. A comparative example is offered in fig. 4.3. The parameters were constrained using the noise uncertainties discussed in section 4.1.2, but were also affected by the relaxation of the standard detection limit constraints. Part of our recovered faint structures would be situated under a 6σ detection limit. It was found that at least for our particular region, the selected disambiguation parameter setup was stable.

4.2 Tracking Magnetic Moving Features at the Periphery of AR11302

When probing the photospheric magnetic fields of AR11302, it is observed that the underlying configuration plays a crucial role in continuously triggering the jets detected during 25 Sep. 2011. The location of all observed homologous jets is always associated with the south-eastern edge of the positive polarity of the main sunspot as shown in fig. 4.4. In order to understand why this region is so efficient in generating recurring jets, we investigated the photospheric rapid motions of observed magnetic polarities analogous to the detected EUV jets. SDO-HMI magnetograms often reveal moving magnetic features (MMFs) of modest sizes (~ 0.5 Mm). They carry flux of the same polarity as the active region, originate in its penumbra and stream almost radially outward with typical speeds in the order of $0.2\text{--}1 \text{ km s}^{-1}$ (See cancellation events in appendix C). Inflowing and opposite polarity MMFs are known to exist, although they are not detected for our region of interest. The interpretation of magnetic moving features provides insights into the lower atmosphere drivers that trigger the geyser structure to recurrently erupt.

4.2.1 Geyser Site Magnetic Ingredients

We discuss the magnetic configuration of the geyser structure. There exist a set of long lived vertical field structures that manifest in the region of interest. All data and recovered structures herein are obtained from vertical B_z heliographic fields that include the custom disambiguation of the azimuthal angle. If not mentioned otherwise, we describe the position of structures referential to the starting time of observations (00:00UT).

Moat: The eastern sunspot of AR11302 has a positive magnetic polarity and is surrounded by a highly dynamic moat, characterized by continuous magnetic flux emergences and cancellations. The moat region is continuously evolving during the surveyed 24 hours. The radially outward photospheric motion inside the moat is associated with the decay phase of the sunspot development.

Pores: The main pore ($\sim -900 \pm 80\text{G}$) which is linked to the jets generation initially appears at $(X, Y) \sim (-780'', 160'')$. A second pore is observed at about 10 Mm distance at $(X, Y) \sim (-775'', 150'')$ but is probably not involved in the jet eruptions.

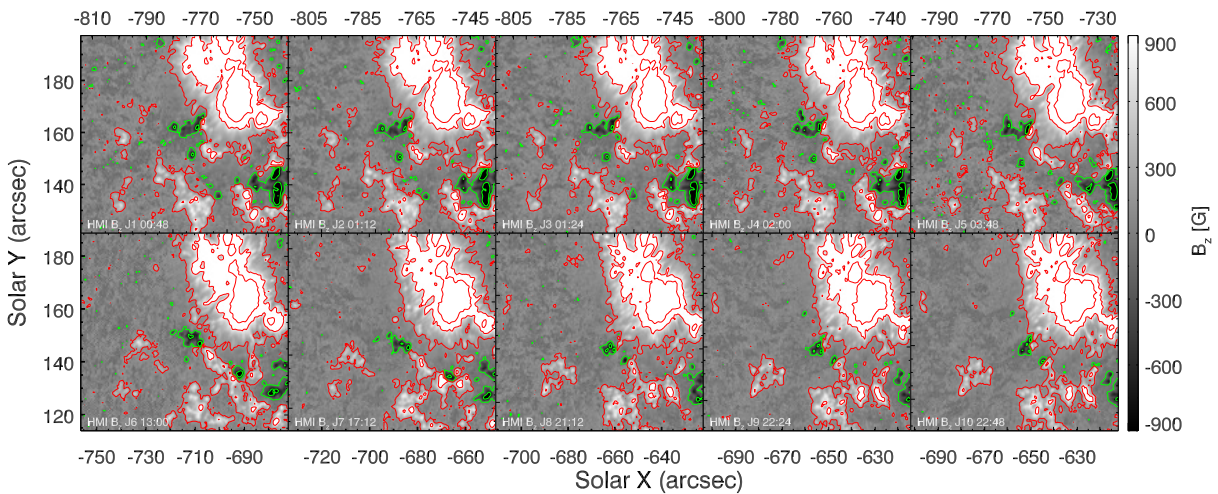


Figure 4.4: Magnetic configuration of the vertical component B_z of photospheric fields depicted prior to each individual jet eruption. Contours at $\pm 160\text{G}$, $\pm 800\text{G}$, $\pm 1500\text{G}$ levels, for positive (red) and negative (green) fluxes are shown in order to enhance visibility of small grains, emerging fields, and potential inversion lines related to jet activity.

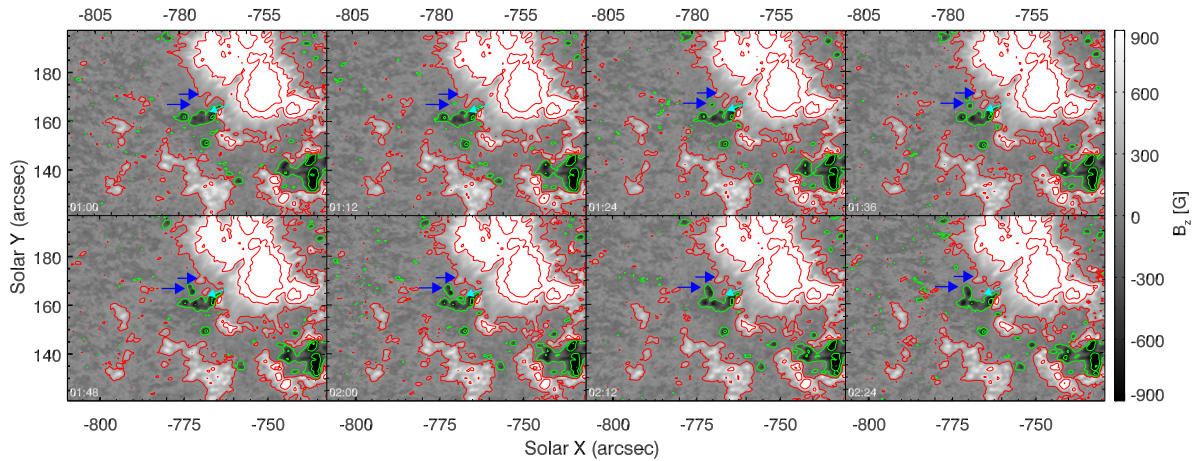


Figure 4.5: Timeseries of the vertical component B_z of photospheric fields in between 01:00UT and 02:24UT, covering the timespan of J2, J3, and J4 events. Contours at $\pm 160\text{G}$, $\pm 800\text{G}$, $\pm > 900\text{G}$ levels, for positive (red) and negative (green) fluxes are depicted. A region where a dipole flux emergence is developing during this period is shown by the two blue arrows that correspond to the emerging footpoints. The first vertical fields appear in close temporal and perfect spatial proximity with the J2-J3 events. The turquoise arrow is pointing to a region where a positive grain that is traveling outwards from the penumbra interacts with a small negative flux at the border of the pore, canceling out during a time frame in which the J4 event is seen erupting in the higher EUV atmosphere.

Dipole polarity and PIL: A notable structure is the sigmoidal polarity inversion line (PIL) present along dipole structure $((X, Y) \sim (-770'', 165''))$ of initial strength $\sim \pm 800 \pm 80\text{ G}$. The dipole tends to slowly drift southward over the observed 24 hours (fig. 4.4). This movement is much slower than the motion of the positive grain fluxes that are dragged around by the moat flow. During this time the PIL-dipole morphology is drastically changing. Regardless, the PIL is clearly distinguished all throughout the day.

Penumbra flux tubes: Above the highly dynamic moat, the hosting penumbra sustains a steady flux tube structure. Part of it is recognized as ‘open’ magnetic flux tubes that significantly contributes to the coronal connection of the underlying moat features. The magnetic canopy is also rooted in the penumbra of the sunspot. The magnetic flux tube rises and arches above the magnetic moat (fig. 4.8), then radially extending towards the outer heliosphere. The observed jet eruptions are guided along the direction of this structure.

Newly emergent magnetic fields: The locations of the flux emergence cases are co-spatial and co-temporal with the locations of the AIA-94Å hot filament observed during flaring. Additionally, penumbral grains with positive polarities are identified inside the penumbral moat. The positive grains migrate towards the edge of the penumbra, in the direction of the negative pore region eventually undergoing flux cancellation at the same location and time (relative to data cadence) with the SDO-AIA flaring. In both cases, the small scale polarities allow for efficient rising of low lying loops, that will interact with above penumbral canopy fields, releasing jet outflow to the high corona and heliosphere.

4.2.2 Jets Generated by Magnetic Grain Flux Cancellation

We study the photospheric magnetic field evolution leading to each jet eruption. Noticeable are a few bright positive polarity penumbral grains identified inside the moat penumbra, moving southward, with speeds on the order of $0.4 - 0.7 \pm 0.2\text{ km} \cdot \text{s}^{-1}$. The positive grains migrate towards the edge of the penumbra in the direction of the negative pore region identified as contributing towards generating coronal jets. The motion of these

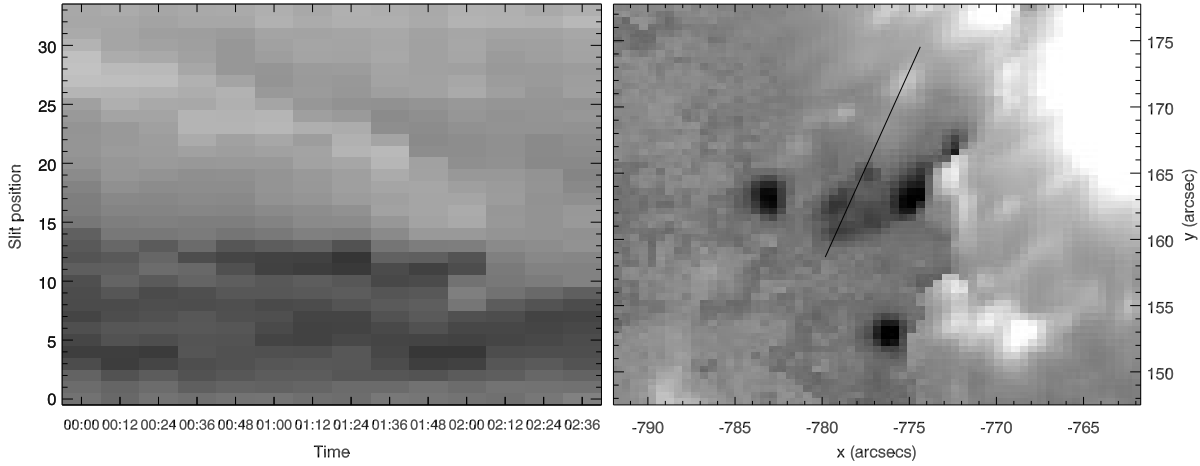


Figure 4.6: A slit based temporal tracking of photospheric grain magnetic moving features. **Left Panel:** Slit time-distance diagram tracking of B_z at the position of the slit included in the right image. The positive magnetic grain moves towards SE with a surface speed of $v_s = 0.6 \text{ km s}^{-1}$. The feature cancels with the negative pore group around the integration time of 02:12UT, while the SDO-AIA flaring starts at 02:14UT. **Right Panel:** Geyser location area as represented by the vertical field component B_z , plotted at 00:00UT. The slit is positioned along the direction of motion of the positive magnetic grain and is temporally tracked to account for solar rotation.

polarities allows for efficient rising of low lying loops, that inevitably will reconnect with the above sitting canopy. The magnetic cancellations of all correlated grain features occur during the 720s integration time of the SHARP data during which the jet bright-point flaring and eruptions were observed in the higher cadence EUV data.

We take as an example the J4 event. A timeseries depicting the moving grain feature up to the moment of it canceling with the pore is presented in fig. 4.5 (turquoise arrow). We use the B_z field component to track a positive polarity grain originating in the field penumbra at $(X, Y) = (-775'', 172'')$ in between 00:00UT to 03:00UT. For this we used an adaptation of the tracking slit that accounts for solar rotation employed in section 1.1.

The positive feature was moving outwards in the SE direction with an apparent speed of $v_s = 0.6 \text{ km s}^{-1}$. The positive grain of $\sim 530 \pm 80 \text{ G}$ strength cancels shortly after 02:12UT SDO-HMI frame with a similarly sized negative grain. The negative grain appears at position $(X, Y) = (-778'', 165'')$ and has vertical field strengths of $\sim -450 \pm 70 \text{ G}$ strength corresponding to the pore group. AIA-171Å flaring starts at approx 02:14UT and main jet is seen at 02:17. Both features dissipate completely. There was no other magnetic event occurring in or close 02:12UT.

The magnetic fields discussed in the context of J4 are above the detection limits. We approximated the strength of the fields as an average of at least two adjacent pixels that exhibited similar strengths in order to neglect erroneous signals. All cancellation events follow a similar scenario. They are described individually in appendix C. Four events, the J1, J4 (fig. 4.6), J6, and possibly the uncertain J7 are advocating in favor of the grain flux cancellation scenario. The J7 event resulted from the cancellation of a very faint flux under the 3σ detection limits and was marked as uncertain. Also, the grain appeared to cancel in the same integration time as the ADO-AIA flaring occurred. Although faint, the magnetic polarity (grain) was stable (no polarity flips) and could be tracked. Its estimated speed was around $v_s = 0.6 \text{ km s}^{-1}$ before cancellation. No other moving magnetic features could be correlated to this jet.

4.2.3 Jets Generated by Small Scale Flux Emergence

Analyzing the B_z vertical magnetic field, we identified new small scale emergent magnetic fields. A few particularities discern emerging flux events from magnetic cancellations due to advected grains. Usually, the emergent fields are longer lived, stationary, and jet eruptions are generated co-temporally to the first observations of the newly risen dipoles. In the case of subsequent short interval events, we could not distinguish changes in the emerging dipoles due to the data constraints.

To exemplify, we analyze here the photospheric motions associated to the J2 and J3 eruptions. Interestingly, the two jets are not a result of advected photospheric grains. Observing the geyser region in between 00:00UT to 03:00UT we initially tracked an elongated positive polarity feature originating in the field penumbra that was found to be the trigger of J1 around 00:48UT. The event is discussed in appendix C. Following that flux cancellation a newly emerged dipole developed starting at 01:12UT, at position $(X, Y) = (-780'', 167'')$. The newly emergent fields rise close to the same pore involved in producing J1 ($\sim 4''$). The emergence generated the recurring EUV long lasting flaring episodes represented in fig. 3.1. The AIA-171Å flaring starts at 01:11UT with a maximum at 01:13UT, when a jet is observed. A second event is recurring at 01:19UT with a jet erupting at 01:22UT.

For reference, we measured the dipole's strength after the jet events at 01:36UT and found magnetic values of -320 ± 75 G and 380 ± 80 G in the two newly formed footpoints. The newly emerged dipole will slowly interact with the pore. It was observed that the newly emerged magnetic fields have a tendency to cluster with pre-existing flux of the same polarity. The flux emergence is presented in fig. 4.5 (blue arrow).

The new magnetic dipole is co-spatial with the location of the AIA-94Å hot emission. For all jets, the EUV emission is described as an elongated ribbon tracing the PIL and warping towards the nearby pore. Additionally, some of the jets, namely J2, J3, J5, and curiously J6 involve a second flaring loop (double loop flaring) that brightens during their flaring phases. This loop overlaps almost parallel to the main flaring ribbon. The flaring morphology for J2, J3, and J6 was discussed and illustrated in section 3.3.1. As can be seen in appendix C, the discovery of the secondary flux emergence associated to these eruptions naturally explains the EUV double-loop flaring phenomena. J6 was associated to a single magnetic cancellation event, and no other potential magnetic feature trigger occurred in temporal proximity of the EUV eruption. We hypothesize that the eruption was impulsive enough to also destabilize the newer neighboring magnetic fields.

Six of the studied events (J2, J3, J5, J9, J10, and J8 (uncertain)) were linked to flux emergence occurrences. In the case of the J8 event the association was uncertain, as a very strong magnetic flux emerges at the edge of the PIL, after which it rapidly eroded. In the case of J9 and J10, a new smaller magnetic dipole emerged in very close proximity to the established pore. This explains the more constrained nature of the SDO-AIA flaring. We have assumed that this rising structure is the cause of both the J9 and J10 events, and probably even the O6 and O7 non-jet flaring events. Individual flare to magnetic field association for these events proved unsuitable inside our observational (temporal, spatial, and statistical) constraints. In general, we based our determinations on the temporal uniqueness of the emergence events, but supporting evidence was weak due to the temporal cadence constraints, thus rendering the determination qualitative. All flux emergence associated jet events are illustrated individually in appendix C.

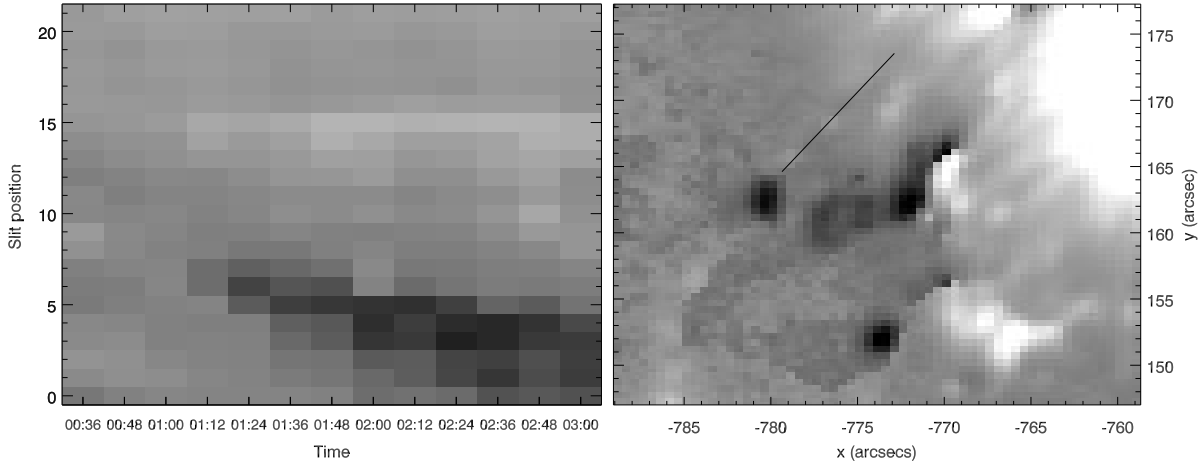


Figure 4.7: A slit based temporal tracking of photospheric small scale vertical flux emergence is presented. **Left Panel:** Slit time-distance diagram tracking the emergent dipole using the B_z magnetogram. The dipole emergence (01:12UT-01:24UT) is co-temporal with the J2 and J3 events where the SDO-AIA flaring starts at 01:13UT and 01:19UT. **Right Panel:** The vertical magnetic field component B_z at 00:36UT. The slit follows the direction of the future dipole emergence and it tracked in order to account for the solar rotation.

4.2.4 Non-Erupting Geyser Footpoint Events

We defined the non-eruptive flaring (O1-O7, see fig. 1.2) as the small flaring events recorded in EUV that did not generate detectable jet emission. We recovered photospheric magnetic features manifestations that likely trigger these events. In the EUV channels, all of these flares were significantly weaker than any of the main jet events. All non-eruptive events are also presented in appendix C.

A possible explanation is the lack of connections to the open fields of the above penumbral canopy structure. We attempt to deduce this via the same photospheric movements used to describe the jets eruption topology. The emergent dipole that triggered the J2 and J3 eruptions appears to have also been involved in producing some of the smaller flaring events (O1-O2) that did not generate jet emission. This time, we do not envision rising of flux-tube structures that interact with the pore or the canopy structure, but find that small advected grain features cancel with the dipole footpoints. The EUV flaring presents a much more localized manifestation, e.g. only the upper part of the structure manifests.

We stress that the associations discussed are of qualitative nature. We endeavored to produce magnetic field data products that are suitable for reasonable interpretation of small and intermediate flux fields and resolved stable patches of vertical fields. Not all of the non-eruptive flaring could be directly correlated to movements of photospheric fields. For example, a set of self similar EUV flaring is occurring for all five events that are grouped in the O6 and O7 sets. The features are correlated to a dipole emerging at a location, separated from the stronger dipole which we correlated to J9 and J10 events. We can not establish more than the general temporal agreement between this emergence and the very transient flaring present in the SDO-AIA filters. Also, the configuration envisioned the dipole to be separated from the PIL, thus possibly explaining the lack of coronal connectivity. In another case, the O3b event could not be associated to any magnetic moving or emerging features. Its magnetic topology is manifesting at even lower levels than our already relaxed disambiguation conditions. The magnetic moving feature correlation, distinctively the case for non-eruptive flaring, should be observed with skepticism as we are dealing with considerable data uncertainties and interpretation issues.

4.3 Geyser Structure Magnetic Field Extrapolations

When revealing the jets morphology, we need to directly relate the EUV observations and the lower lying photospheric magnetic fields. One requires to study the topology of the magnetic field at larger heights from the photosphere. This will provide significant input to our EUV and magnetic observational data and subsequently to the study of the geyser structure. Thus, to determine the above photospheric magnetic fields, a mathematical method was utilized. The model is based on constructing vertical magnetic field extensions from a source, usually the observed photospheric magnetic field. This is the so-called magnetic field extrapolation technique.

The base B_z vertical field magnetograms were obtained using the standard JSOC pipeline and transformed from an image to heliographic coordinate system, as discussed in section 4.1.2. The SDO-HMI data used in this form is subject to significant uncertainties in low and intermediate field magnetic flux. We removed the 180° ambiguity in the azimuthal angle. A full custom disambiguation (section 4.1.3) is applied to the data using the Minimum Energy Algorithm [Metcalf, 1994, Leka et al., 2009].

Extrapolating the magnetic field strength from photospheric observations can be achieved by assuming an analytical approximation constrained by boundary values. In the present case, we want to describe the magnetic field configuration in the solar atmosphere where the lower bound is represented by the photospheric SDO-HMI fields. The subsurface fields are implicitly ignored. Also, at the upper level, fields should vanish. An additional constraint is enforced, where the current can only run parallel to the magnetic field $j \times B = 0$. This is referred to as the ‘force-free’ condition. In this case, $\nabla \times B = \alpha B$ where α represents the force-free parameter.

There are two proposed solutions to the problem. The first employs Green’s functions [Chiu and Hilton, 1977], while the second uses fast Fourier transforms [Alissandrakis, 1981]. The fast Fourier transform solution is significantly faster, but requires a ‘padding’ (data needs to be placed centrally inside a wider array) in order to remove oscillatory aliasing patterns. It has been argued that the Green’s function solution can reproduce small-scale features better than the fast Fourier transform approach, although Alissandrakis [1981] showed that the analytical solutions are mathematically equivalent. A comparison of different techniques is presented by Neukirch [2005].

There exist an important number of physical assumptions and limitations inherent to any magnetic field extrapolation discussion. The corona above active region sites is considered to, at least in general, obey the force-free approximation [Metcalf et al., 1995, Wiegmann et al., 2014]. The key assumption of the force free modeling is its treatment of only the magnetic forces. For example, the gas pressure, and gravitational forces are not considered. The AR corona instinctively adheres to such an approximation, where the plasma β has typical values of $<10^{-2}$. Although extrapolated fields are traced back to their photospheric sources, magnetic field estimations can only be inferred at above transition region heights. On the other hand, the quiet-sun has been shown to not be in a good force-free approximation [Schrijver and van Ballegooijen, 2005].

Choosing how to address the force free parameter will influence the extrapolated field. The simplest approximation involves considering $\alpha=0$ thus recovering the potential (most relaxed) field configuration (PFF). In reality the α parameter is a function of the spatial location, in the same manner as B . The solution of such a system is non-trivial, and is called a non-linear force free field (NLFF). It has been shown that NLFF models not always accurately reproduce observed solar magnetic fields. See De Rosa et al. [2009] and references therein

for an in depth discussion. An intermediate solution is to consider a constant α across the desired volume, enabling a known [e.g. Alissandrakis, 1981] solution to the problem. The approach is referred to as a linear force free approximation (LFF). Naturally selecting a constant force-free parameter for an entire active region patch is problematic as α is a localized indicator of the ratio between the vertical current and magnetic fields.

A PFF or LFF extrapolation (NLFF is dependent on full vectorial measurements) formally requires only a photospheric line of sight (B_{los}) magnetogram measurement as input. Implicitly it was assumed that the region of interest is disk centered so that the B_{los} actually represents vertical fields. More recent revisions of the extrapolation model can also use longitudinal field components in order to better constrain the structures. With the coordinate transforms that were discussed in section 4.1.2, accurate extrapolation can be recovered for non disk-central active regions. Particularly, we have performed force free extrapolations in both Potential and linear approximations. The Alissandrakis [1981] approach was utilized on custom disambiguated SDO-HMI heliospheric vertical field magnetograms. We describe our implementation and assumptions subsequently.

4.3.1 A Potential Field Approximation

The base B_z vertical field magnetograms reveal the photosphere under the base of the jets to be highly dynamic. We have identified a moat region around the sunspot, where rapid flux emergences, moving magnetic penumbral grains, long lasting pores, and quasi-stable lasting dipole polarities are observed. These are described in section 4.2. Based on the added evidence, we hypothesize that a twisted microfilament interacts with these local flux elements and recurrently generates the ten detected jet eruptions.

We have showed throughout this work that the geyser site is connected to the ‘open’ heliosphere, though exceptions exist in the form of the smaller intensity O1-O7 events. We have confirmed that these events involve, at least in part, the magnetic features involved in releasing jets. These are explained (see appendix C) by:

- (i) Occurring at low heights that have no connection to the corona;
- (ii) Eruptions are not detected in EUV wavelengths;

The second interpretation of the non-eruptive events implies that the different reconnection events occurred at different heights. This assumption can not be tested with our current observations, or extrapolated magnetic fields due to resolution scale (~ 0.4 Mm in all three dimensions). This hypothesis supports the conclusions of the section 4.2 MMF analysis, where no unique self-recurring process could be set as the ‘generator’ of the recurrent jet eruptions.

The potential field extrapolation model,

$$B(r) = \nabla \phi(r), \quad j = \frac{1}{4\pi}(\nabla \times \nabla \phi) = 0, \quad j \times B = 0, \quad (4.7)$$

can be used to investigate the general topological configuration of the geyser site. Figure 4.8 reveals the extension of AR11302 canopy fields that sit above the geyser. The vertical size of the extrapolation domain was set to 37.5 Mm. We estimated the geyser’s flaring site to manifest at a heights of maximum 2.3 Mm. This result suggests that the geyser is located at smaller than previously quoted heights, e.g. Cairns et al. [2018] who placed the source at 5-10 Mm. The estimation is based on the height above our region of interest at which

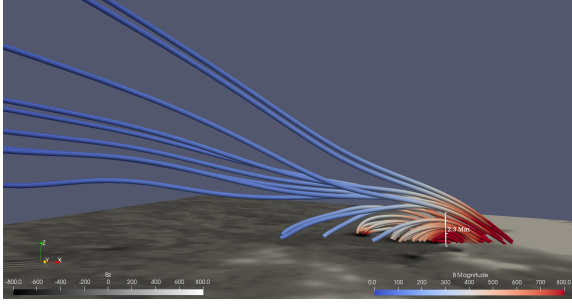


Figure 4.8: Model of the coronal magnetic field extrapolated under the force-free potential field assumption (see eq. (4.7)). Base layer represents the vertical B_z component of the magnetic field, scaled in the $[-800 \text{ G}, 800 \text{ G}]$ interval and computed at 01:24UT on 25 September 2011. In potential conditions, the magnetic canopy becomes ‘open’ to the heliosphere at heights above 2.3 Mm.

the extrapolated fields do not connect back to the photosphere (bottom boundary), but exit through the lateral or upper boundaries of the computational domain. We mention that the SE direction to where our eruptions are directed is a quiet sun area and no close active region follows.

In the horizontal plane, the EUV flaring structures are best seen during the J6 eruption (13:08UT) observed in the AIA-94Å filter and are spatially correlated with the photospheric HMI-SHARP B_z magnetograms. The horizontal projected length of these filaments are of $\sim 6.5 \pm 1.4 \text{ Mm}$ (upper), and $\sim 3.6 \pm 1.4 \text{ Mm}$ (lower) as seen at photospheric level by the HMI B_z magnetograms. Length of magnetic flaring loops in AIA-94Å (figs. 1.1 and 3.2) are $\sim 5.5 \pm 1.4 \text{ Mm}$ (upper) and $\sim 3.0 \pm 1.4 \text{ Mm}$ (lower). The length of the low lying potential extrapolated fluxtubes are found to be in the order of $\sim 7 \text{ Mm}$ (upper), and $\sim 4.5 \text{ Mm}$ (lower) respectively. These estimations were used as input when calculating the geyser structure’s cross-sectional area and volume needed to obtain the EUV DEM (section 3.3.1) and X-Ray energy estimations (section 3.4). We consider these three estimations to be in sufficient agreement considering the difference in scale height, the high projection angle correspondent to the EUV measurement, and the multiple transformations that are applied to the B_z magnetograms.

We attributed the 2.3 Mm heights to correspond to a region between the high-chromosphere and low corona. More accurate determinations are impossible as the solar atmospheric envelopes are dependent on the local conditions. For example, the chromosphere is revealed in hydrostatic numerical experiments (e.g. Fontenla et al. [2011] models, fig. i.2) to be at heights lower than 2 Mm. On the observational side, the chromospheric structures have been seen extending to heights of $\sim 4 \text{ Mm}$ above the photospheric limb in non-polar regions [Johannesson and Zirin, 1996]. The geyser DEM estimations presented in section 3.3.1 also characterize the plasma to be at chromospheric to transition region characteristics. Furthermore, section 2.2 calculates the time travel of reconnection generated electron beams from a chromospheric density region, finding it to match observations. The topology revealed by potential fields is interpreted by us as an upper limit on the height as the structures are in the most relaxed state. It is safe to assume that the site is indeed rooted in the ‘low solar atmosphere’.

4.3.2 A Non-Idealized Geyser Interpretation

Due to the limitation of the idealized potential force-free field assumption ($j=0$), the resulting extrapolation (see for example fig. 4.8) is unable to offer any insight into the configuration of presumed twisted fluxtubes that may be part of the geyser structure. A linear force free field extrapolation,

$$j = \frac{1}{4\pi}(\nabla \times B), \quad j \times B = 0, \quad (\nabla \times B) \times B = 0, \quad \nabla \times B = \alpha B, \quad \alpha = \text{const.}, \quad (4.8)$$

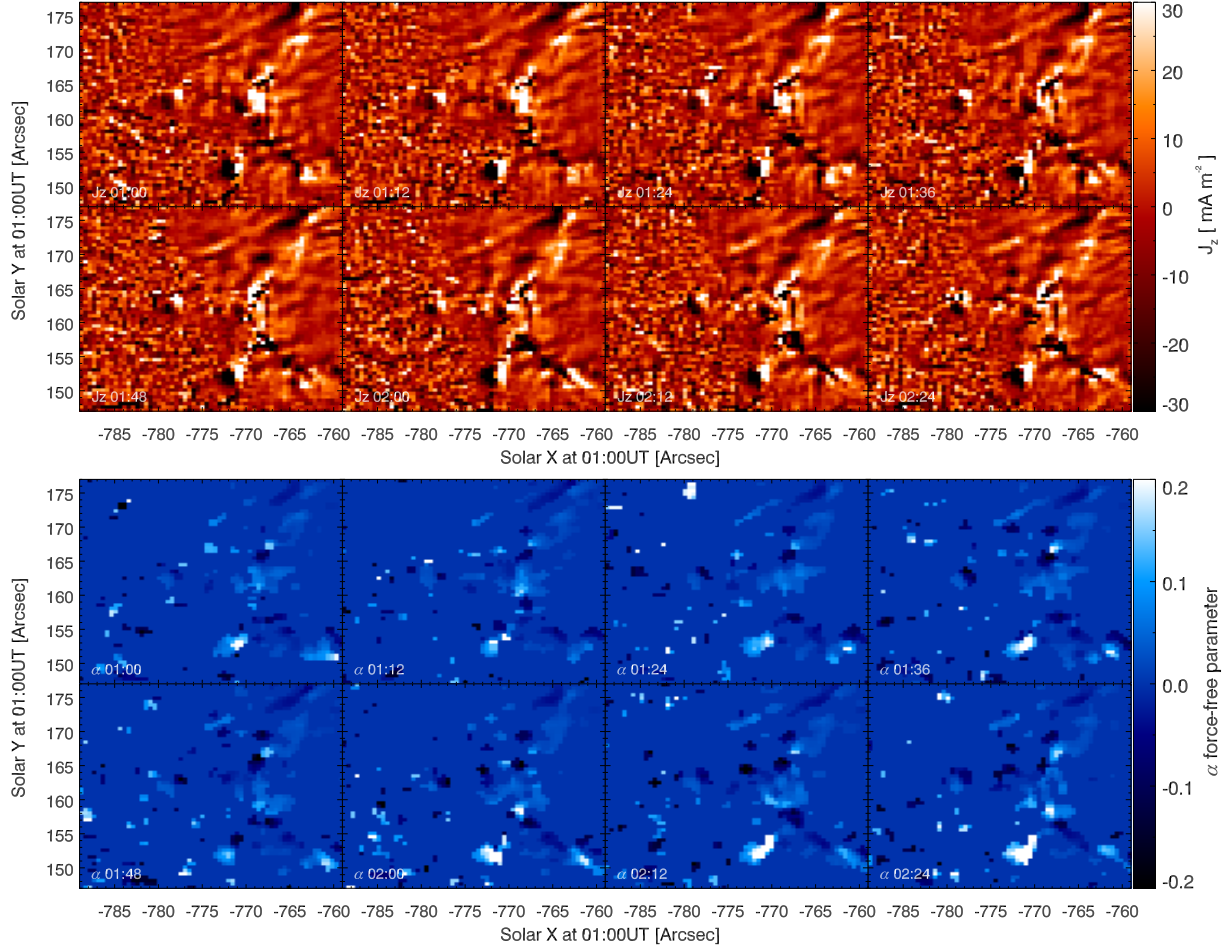


Figure 4.9: A timeseries 01:00UT - 02:24UT of geyser non-potential electrical current and force-free parameters that are derived from the HMI-SHARP observations. The heliospheric vertical currents J_z are presented in **Upper Panel**. The force-free α parameter is mapped in the **Bottom Panel**. The two maps are calculated utilizing the eq. (4.9) formulations. The structure positions are tracked in time. We have fixed the heliospheric coordinates corresponding to the 01:00UT frame for clear location reference. The $(X, Y) = (-770'', 152'')$ structure is not part of the geyser footpoint which is rooted between $(X_1 : X_2, Y_1 : Y_2) = (-780'' : -765'', 162'' : 175'')$. See fig. 3.2 (upper and middle panels) which depict the analogous EUV imaging during flaring peaks.

along with vertical current (j_z) and helicity/force free parameter (α) are derived from the HMI-SHARP magnetograms using the

$$j_z = \frac{dB_y}{dx} - \frac{dB_x}{dy} \quad \text{and} \quad \alpha = \frac{j_z}{B_z} \quad (4.9)$$

formulations.

The vertical current J_z is obtained from a set of spatial gradients of the horizontal fields. Our HMI magnetic field data is discretized in the form of pixels. This adds a difficulty in addressing the dB_y/dx and dB_x/dy terms. These are treated numerically as finite differences between two adjacent pixels. This leads to the mapping of a current map pixel as being centered at the corner of four initial HMI B_z pixels. We have thus shifted the fig. 4.9 J_z maps in order to realign them with the B_z fields. The force-free α parameter represents the ratio between induced vertical currents flowing parallel ($j \times B = 0$) to the vertical magnetic fields. The α parameter is also interpreted as a measured of the magnetic field shear and twist effects. The potential state of a magnetic field is characterized by $\alpha = 0$ where the

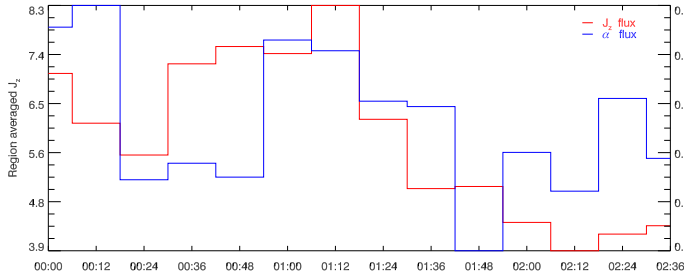


Figure 4.10: Timeseries evolution of the vertical current J_z and the force-free α parameter. The parameters are averaged over a $4'' \times 5''$ area centered at position: $(X, Y) \sim (-770'', 165'')$, between 01:00UT and 02:36UT. The location corresponds to the photospheric footpoints of the discussed PIL.

field has no torsion embedded.

Following the section 4.2 discussion on the geyser's magnetic ingredients we map a short observational timeseries of the J_z and α parameters in order to discuss the yet undisclosed nature of the PIL structure and the main pore. We have chosen an identical period (01:00UT to 02:24UT) to the section 4.2 B_z timeseries. The observation time corresponds to the J2-J4 events, where the first two were attributed to a small dipole emergence, while the J4 event was attributed to a grain cancellation event. The geyser footpoint is situated around $(X_1 : X_2, Y_1 : Y_2) = (-780'' : -765'', 162'' : 175'')$. The analogous EUV imaging during the J2 and J3 flaring peaks are presented in fig. 3.2 (upper and middle panels). A visual inspection is sufficient to correlate the SDO-AIA flaring loops with their magnetic footpoints.

We now address the small scale potential inversion line around a sigmoidal dipole at approximate position $(X, Y) \sim (-770'', 165'')$. We have treated this ingredient as an important indicator that a twisted microfilament may be rooted in this region. Its long time quasi-stable behavior (fig. 4.4) initially reinforced this assumption. The fig. 4.9 (upper panel) J_z portraits that significant vertical current is being eroded at the PIL between 01:12UT and 01:24UT which correspond to the J2 and J3 flaring.

We also observe a current patch at position $(X, Y) = (-774'', 171'')$ that corresponds to the position of the newly emergent dipole which was found to be the cause of the J2-J3 events. Curiously, we can observe the vertical current feature at least one 12 min integration time (01:00UT) before it started to manifest in the magnetic field map (01:12UT, fig. 4.7). The fig. 4.9 (lower panel) α map depicts a similar behavior (as the two measurements are related) which can interpret a substantial helicity release near the PIL site.

Also noteworthy is the mention of vertical current concentrations in the 02:12UT frame at location $(X, Y) = (-773'', 165'')$ correspondent to the location of the grain cancellation event (fig. 4.6) that was found to be the cause of J4. The PIL structure is evolving concomitantly with the flaring of J4, but we can not safely assess whether this is due to the jet eruption. J4 is less energetic than the J2 and J3 events.

A timeseries of the vertical current J_z and the force-free α parameter is presented in fig. 4.10. The two parameters are averaged inside $4'' \times 5''$ region that is centered at position: $(X, Y) \sim (-770'', 165'')$ and corresponds to the photospheric location of the PIL. The 12 minute cadence inherent to HMI vector magnetogram observations limits our capability to associate changes of the two parameters to individual jet eruptions. Regardless, we can observe that a significant amount of vertical current is dissipated before the 01:36UT integration time, three consecutive jet eruptions (J1-J3) are manifesting in the previous half-hour, when the J_z was increasing. A second positive slope behavior is observed between 02:12UT-02:36UT during which the J4 eruption occurred.

In fig. 4.10 we did not utilize the absolute values for neither the J_z or α . The plot shows a constant imbalance in favor of the positive fluxes in both cases. This is particularly important when discussing α as an always positive flux can be interpreted as a counter-clockwise axial rotation if we take into account standard magnetic field flow conventions. This is indeed

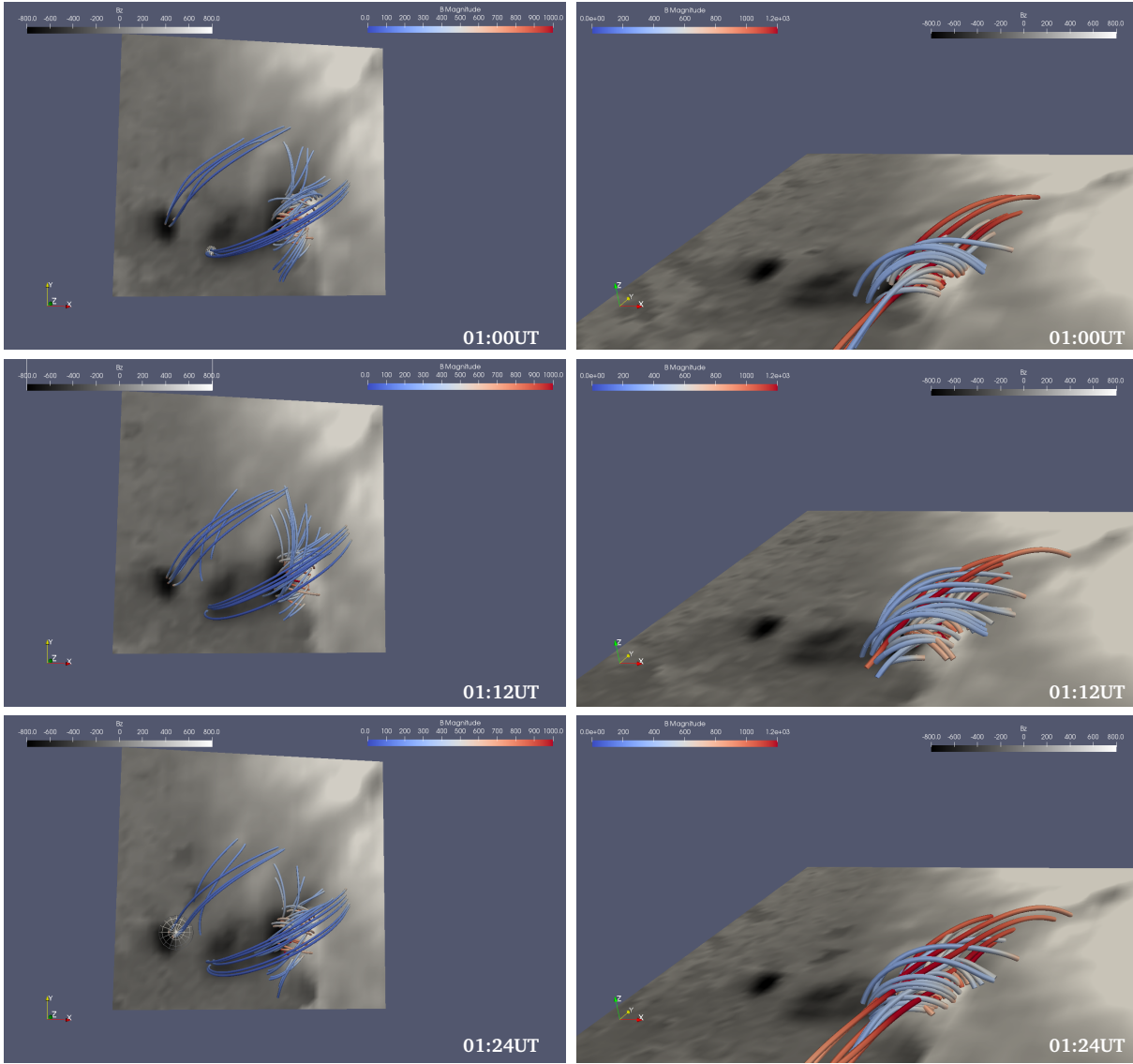


Figure 4.11: Linear field extrapolations that reproduce the observational features of the AR11302 geyser. The base layer represents the vertical magnetic field B_z plotted in ± 800 G range. The panels reproduce HMI observing times of 01:00UT, 01:12UT and 01:24UT during which the J2 and J3 eruptions occurred. The view direction is sketched in the lower right corner of each plot. **Left Panel:** Top view of the reconstructed components using unique α parameter configurations for each substructure. This illustration appears compatible to the observed EUV flaring (fig. 3.2). **Right Panel:** Side view of the PIL linearly extrapolated using a combination of α values ($\pm 0.03 < \alpha < 0.16$) as revealed by the fig. 4.9.

the direction of axial rotation (untwisting motions, see fig. 1.4) of our recurrent jets, that was discussed previously (section 1.1).

Based on co-aligning both EUV and magnetic data, we have assumed that the $(X, Y) = (-770'', 152'')$ structure (second pore discussed in section 4.2) is not part of the geyser footpoint due to its distance from the geyser and, more importantly, because it has not flared coincidental with any jet. The structure is seen to manifest strongly in the α parameter map.

We have used the results from the fig. 4.9 (lower panel) α maps to get a rough estimate of the twisting inherent in the geyser structure. The B_z topological analysis showed that there are multiple sub-components of this structure. We have thus decided to create several linear extrapolations in order to recover the desired twisting parameter. As discussed above, in a linear field extrapolation, the α parameter is set to a constant value over the entire integration domain. In our case, each individual geyser component has its own distinct α

setting, as recovered from the HMI-SHARP magnetograms. We can model several linear extrapolated fields and over-plot the respective components, each with own characteristic α force-free approximation. For each component, we have taken an average across small kernels of a few pixels diameter in order to mitigate potential spikes. We have only addressed pixels that were deemed measurable as discussed in section 4.1.2.

We have obtained linear extrapolated fluxtubes for a short series of three consecutive frames (01:00UT-01:24UT), during which the J2 and J3 jets erupt. Figure 4.11 presents the resulting extrapolated magnetic structures. The upper panel presents the fluxtubes spanned by the main pore, and the sigmoidal PIL. This superposition of reconstructed structures appears analogous to the observed EUV flaring (fig. 3.2) of the geyser structure. The newly emerging dipole which was identified to be the trigger of the two events can be observed in the 01:12 and 01:24 frames.

In fig. 4.11 (bottom) we zoom-in on the sigmoidal PIL region. Initially, at 01:00UT, we observe two types fields. In lower areas, the extrapolated fluxtubes are almost horizontal, where the polarities are being pulled apart. This effect creates the sigmoidal pattern seen in the B_z observations. As the color scheme reveals, these are very strong, and sheared low fields. On top of these (>1 Mm) sit a second set of fluxtubes. These connect over the potential inversion line forming a twisted braid-like structure. We then plot extrapolated fields in the next two timesteps, using identical sources for integrating the fluxtubes. In the 01:12UT frame we observe a general relaxation of the twisted braid loops. The trend is continuing in the 01:24UT frame, where even the lower sheared loops appear to slowly rise. The integration times of the two frames is corresponding to the J2 and J3 Events. We here see a general relaxation of embedded helicity, as an effect of the jet eruptions.

The information on the α force-free parameter can be utilized to probe into the details of the reconnective processes. The J_z and α maps, corroborate our hypothesis which attributes the PIL structure as a source of helicity. The superposed linear field extrapolations showed that the PIL structure sheds its stored helicity during jet eruptions (see timeseries, fig. 4.10). The extrapolations gave us significant information on the topology of the geyser region, but these are still limited as the winding is assumed constant along each individual geyser component in our particular case.

4.4 Discussion

We report the discovery of 10 successive coronal jets that are erupting from a unique magnetic structure, rooted at the south-eastern penumbral boundary of AR11302. The observations cover a period of 24 hours. The jets all share the spatial origin and were apparently linked to a common eruptive mechanism. They exhibit a homologous behavior where the recurrent jets are following the same propagation direction, have globally comparable morphological features, and recur at the same location with similar but not identical morphological features. The magnetic configuration/structure that enables these jet phenomena is analyzed and named ‘coronal geyser’ due to the many similarities with its earth counterpart.

During jet eruptions the reconnected plasma follows the pre-existing magnetic fields along the ‘open’ canopy fields that are all rooted in a photospheric penumbral region close to where the geyser structure is also anchored. The photosphere is in continuous development, with a initial twisted filament located at the edge of the penumbra, where its footprints are constantly moving (fig. 4.4).

We have shown throughout this work that a microfilament eruption scenario is supported given the observational evidence from the EUV, radio, and magnetic field data. The magnetic topological layout revealed the presence of significantly twisted magnetic fields that released helicity during the jet eruption (section 4.3). This magnetic configuration is analogous to larger helical CME's and supports the erupting mechanism proposed by Sterling et al. [2015]. The microfilament eruption scenario requires that multiple short-lived (<30 s) and fast reconnection events occur in order to constitute an observed eruptive blowout jet. Moore et al. [2010] present a qualitative sketch of a blow-out jet eruption.

The SDO-AIA jets exhibited multiple observed EUV erupting strands that we interpret as a multiple short succession of flaring events. When examining the geyser site during the J2, J3 and J6 eruptions, we notice that detailed EUV footpoint flaring peaks presented in fig. 3.1 support our assumption. The observed EUV jet's threaded morphologies are compatible with an eruptive filamentary structure. A subset of jets (J2, J3, J5, and J6) were highly dynamic and exhibited multiple Type-III bursts manifesting due to electron beams generated co-temporally with the multiple SDO-AIA EUV flaring peaks. This aspect represents additional evidence that multiple individual reconnection events are occurring in very short timescales. In a series of papers, [Sterling et al., 2015, Panesar et al., 2016, Sterling et al., 2016, 2017] the authors study blowout jets which they attributed to microfilament eruptions. Our DEMs of short and fast flaring events along with the Type-III radio bursts episodes indirectly support the microfilament eruption supposition and theory.

Sterling et al. [2016] proposed magnetic cancellation across a neutral line to be the main process that drives jet eruptions. This is analogous to the now common large scale flare scenaria. Panesar et al. [2016] further analyzed a set of very energetic recurrent jets that are tied to CMEs. All jets originated from the same base-arched structure, which the authors identified as a microfilament footpoint. In a series of papers, Sterling et al. [2016, 2017] analyzed sets of recurring AR jets and discussed potential trigger and emission mechanisms, concluding that magnetic flux cancellation should be considered as a fundamental process for AR jet production. On the other hand, Sakaue et al. [2017, 2018] presented a case study where flux emergence plays a significant role in producing an AR jet. Our magnetic moving feature topological correlation described in section 4.2 and detailed in appendix C showed that both flux emergence and flux cancellation play a crucial role in producing the recurrent jets. This is valid at least in the case of our studied geyser structure. The two possible scenaria were attributed to jets in an almost even ratio. No scenario has been found to dominate. This result is particularly intriguing as we initially expected one singular process to be the cause of recurrent (homologous) jets that result from the same reconnection site.

We have shown that a stochastic combination of penumbral moving features and small dipole emergence are at least involved in producing jets. Due to the limited SDO-HMI temporal cadence of 12 min, we can not safely assess whether the magnetic features are a result or a cause of the jet's eruptions. More trustworthy are the small grains that could be tracked for intervals in the order of hours before canceling with the geyser structure. Alternatively, flux emergence events were seen first manifesting in the 12 min integration time of HMI that also covered the EUV eruptions. The possibility that magnetic features are an effect and not a cause can not be discounted via our current observations and will be further studied.

To this extent, we consider possible jet triggering scenarios. The observational interpretation of a microfilament eruption translates to a 'store and release' process [Cheung and Isobe, 2014] involving multiple stages:

- (i) Energy is deposited in the site;
- (ii) The site is destabilized;
- (iii) The stored energy is released, usually in the form of eruptions;

In our particular case, we hypothesize that the photospheric features are the destabilizing factor for at least jets that resulted via flux cancellation, and that helical energy is transported to the site (particularly in the PIL region) via flux emergence. In the absence of grain destabilization, an additional factor must be included. The literature jet numerical experiments are generally based on flux-emergence-like scenaria [Moreno-Insertis and Galsgaard, 2013, Fang et al., 2014, Lee et al., 2015] or are claimed to be independent with regards to the trigger mechanism [Wyper et al., 2018]. Helicity was introduced via the emergence of braided or sheared structures (filaments from an observational point of view). The helical structures evolved towards instabilities, generating synthetic jets.

The Moreno-Insertis and Galsgaard [2013] and Wyper et al. [2018] experiments independently reported that kink (and also torus) instabilities are formed. Kink-like configurations have been proposed as triggers for jet eruptions. Kink-induced jets have been proposed by Shibata and Uchida [1986] as the ‘sweeping-magnetic-twist mechanism’. The study proposed that the transfer of stored shear (twist) from a closed structure to open field lines would drive a helical jet as the sheared energy transfers to a traveling nonlinear Alfvénic wave. Shibata and Uchida [1986] discussed their results in terms of solar observations and hypothesized at the time that the fieldline shear must be embedded in a small filamentary structure.

In a general case, laboratory studies [Moser and Bellan, 2012] have shown that astrophysical jets may be triggered by a cascade of instabilities. An MHD kink mode destabilizes a helically twisted bundle of plasma leading in turn to a Rayleigh-Taylor reconnective instability. In solar conditions, it has been hypothesized [Leka et al., 2005] that small kink unstable patches may be found in or around active regions. The amount of twist that is required to trigger a kink instability is still a matter of debate. Analyzing large scale flaring loops Leamon et al. [2003] found that ‘twisted coronal loops are unstable to the MHD kink mode only if their total twist exceeds a critical value . . . not less than $T \sim 2\pi$ ’. We note that this assumption is idealized. In solar scenaria the threshold is slightly higher ($T < 2.5\pi$) in the presence of additional stabilizing forces (gravity, non force-free conditions, etc.). The Leka et al. [2005] and Leamon et al. [2003] conclusions suggested that although active regions are not generally kink unstable, but smaller concentrations and patches might be susceptible to the instability. Could our geyser, and in particular the braided fluxtubes above the PIL that are revealed via the linear extrapolations (see fig. 4.11, bottom panel) be susceptible to a kink instability?

We probe the stored helical energy that is released in the form of the untwisting motions. We can approximate a twist factor,

$$T = l \cdot q = \frac{\pi d}{2} \cdot \frac{\alpha}{2}, \quad (4.10)$$

to be the product of a winding rate q of a fluxtube of semi-circular length l that sits above two photospheric footpoints. The winding rate is approximated to $2q = \alpha$ following Leka et al. [2005] and Leka and Skumanich [1999] estimations. The T factor is normalized with respect to one rotation and presented as $T/2\pi$.

In EUV observations [Guo et al., 2013, Schmieder et al., 2013, Hong et al., 2013], the jet eruptions show a strand morphology, with many of these strands undergoing untwisting

motions while propagating along the guiding ‘open’ field lines as we also described (see section 4.3) in our particular case. EUV helical movements do not necessarily depend on a blowout eruption type or on a kink instability. These untwisting motions have been associated in the standard jet eruption scenario with newly emerging flux that is released by an interchange reconnection with an open field structure as described by Canfield et al. [1996] and Pariat et al. [2009]. Such a scheme assumes ideal conditions and can occur without the need to include twisted filaments like the ones described as being part of the geyser structure. We disregard this scenario, due to our collected evidence we interpret our jet observations using the hypothesis involving microfilament eruption.

We compute the untwisting motion analyzed by Hong et al. [2013] to be $T/2\pi \sim 0.8$ from the fit performed on an untwisting strand as it moves along the jet axis. This is indeed very close to the theoretical stability limit. Our SDO-AIA results show unwinding movements of $T/2\pi \sim 1$, hinting that the eruptions might be linked to kink instabilities.

We have utilized the maps of the force-free α parameter discussed in fig. 4.9 in order to compute the winding that may be embedded near the PIL location, close to the J2, J3 and J4 eruptions. We assume the width of the fluxtube to be in the order of 1 Mm and we integrate the α measurement over a respective area, and over a length of 3 Mm. We obtain a $T/2\pi$ approximately 0.6 at 01:00UT, increasing up to 0.85 at 01:12UT then decreasing until 0.5 at 01:48UT. The pattern is analogous to the averaged α parameter plotted in fig. 4.10. Our geyser did not produce any jet event that could be attributed to a destabilization resulting from a kink unstable PIL patch, although in the cases of J2, J3, J5, and j6, the winding was approaching the critical threshold.

These estimations lead to a non trivial interpretation. The high winding present at the PIL location puts the geyser close to being kink unstable, although the theoretical threshold does not appear to be met. This implies that our found magnetic features produce a destabilizing effect when interacting with the geyser generating the high, but not critically twisted jets. On the other hand, results from the EUV observations (section 1.1) show that jets appear to be twisted above the kink instability threshold. We speculate possible explanations for this apparent disagreement:

- (i) There exists the possibility that the PIL region is not the only supplier of helicity (although it is dominant). The other geyser ingredients may each contribute to a total untwist, as seen in the EUV observations;
- (ii) If the reconnection angles are not acute, snapping of the newly formed field-lines might occur. In EUV observations, the effect could blend with the released twist, explaining our observations;
- (iii) The low detectability of the geyser’s magnetic fields, and the non disk-central position of the structure which substantially degraded the HMI detection levels lead to poorly constrained estimations of the J_z and α quantities. These may be detrimental to an accurate portrayal;

The SDO-HMI observations provided extremely useful validations for the hypotheses pursued herein, although the data was shown to be unreliable for a series of important questions. Low noise and fast cadence spectro-polarimetric magnetic field measurements of a geyser’s topology in both the photosphere and chromosphere will be able to confirm, or invalidate, our current findings. The commencement of DKIST operations will prove invaluable to this goal. As hopefully shown throughout this work, an analysis of the physics and morphology of small-scale solar phenomena will provide, by comparison, crucial information to the understanding of the large scale eruptive events.

Outlook

This work focused on broadening our understanding of both the physics and morphological characteristics that describe energetically modest solar eruptions. A set of recurrent coronal jets was analyzed by bringing together a substantial amount of independent observations, each addressing a piece of the puzzle. We illustrated a quasi-stable magnetic region rooted in the low solar atmosphere, that was highly prolific in generating recurrent jets. Its unique characteristics were analyzed. We then showed that this ‘geyser structure’ is not a unique occurrence, since several similar sites were found to be manifesting at the penumbral peripheries of different active regions.

The Coronal Geysers are long-lived small-scale penumbral active region structures that have an open field coronal connectivity, are prolific generators of recurrent jet eruptions, sources of particle acceleration and radio bursts, and are classified from an energetic point of view as impulsive microflare sites. The geyser structures have roots in complex magnetic topologies, are subject to helicity conservation, and can contain filamentary structures. The coronal geyser nomenclature aims to be a first step towards a pursuit of a wider sample automated survey of active region jets.

As solar small-scale events exhibit a high morphological and energetic variability, we believe that the assumed theoretical physical mechanisms can only be scrutinized in the solar environment by utilizing significant datasets. Only by employing statistically valuable studies, we can gather meaningful coronal context data. The study of small-scale solar flares should become an intrinsic topic of solar research due to the advances in instrumentation that lead to higher quality observations.

Jet morphological parameters were extracted via multiwavelength and timeseries analysis using a set of spectroscopic filter images. A meticulous slit-jaw analysis revealed evidence for substantial helical energy release as part of the jet eruptions. Signs of torsional Alfvénic waves are observed to propagate along the newly reconnected fieldlines. We aim to concentrate on these observations in the future, with the hope of characterizing the torsional waves, and in turn gain more information on the elusive nature of the reconnection giving rise to the jet eruptions.

We propose the geyser structures as coronal sources of Type-III radio bursts that are detected propagating into the interplanetary space. We have shown via cross-interpretation of multiple types of data that the geyser sites generated bona-fide microflares, do indeed fit in the standard flare model, and are energetic enough to accelerate particle beams. A condition for Type-III radio bursts to manifest is to have the right physical conditions to allow for inter-connections of the low reconnection site to the above coronal fields. This is generally implied, but we also have demonstrated that a coronal connection for small-flaring sites should not be taken for granted. We compiled a statistically relevant dataset of geyser sites and their associated jet eruptions. The non-thermal bursts and thermal EUV manifestations were correlated both observationally and by modeling of the travel of interplanetary electron beams.

This demonstrated that the geyser flaring sites are the interplanetary Type-III burst sites of particle acceleration.

The accuracy of the EUV-burst correlation is limited by the instrumental capabilities and constraints in the analytic solution. Radio observations of the highest quality are a must. New physics may be brought to light by sampling radio emission in the higher frequency range at high cadence. Our future work will focus on closing the gap between higher frequency radio imaging at the source locations and the interplanetary electron beams. We aim to probe into the particularities of the Sun's small reconnection events. As seen, today's observational and theoretical results on electron beam generation and propagation show that although a general phenomenological understanding holds true, a unifying mechanism remains elusive. We are currently preparing a proposal for correlated DKIST [Tritschler et al., 2016] remote sensing data and in-situ plasma measurements using the Parker Solar Probe. Further input on particle acceleration, transport and escape into the inner heliosphere in the context of Sun-Earth interconnections is a key aspect that can be extended to more general astrophysics applications.

We have shown herein, hopefully to a sufficient degree of confidence, that our geyser and its jet eruptions, and recurrent jet inducing sites in general, exhibit high temperature emission at substantial emission measures. This is analogous to standard flares. Additionally, the magnetic field configuration prior to the jets plays a crucial role in the energetics of jet events.

We have found a peculiar partition between kinetic and heating parameters by studying the energetics of jet eruption. The thermal/enthalpic energy flux is found to be a couple of times stronger than the bulk kinetic acceleration. If we describe the jet flaring in terms of the classical 2D reconnection models, we expect the kinetic term to dominate by orders of magnitude. This result suggests that much more detailed theory is required in order to describe jet eruption mechanics.

We revealed the heliospheric travel of electron beams and jet ejecta along open fluxtubes. The physical parameter and energy constraints provide valuable information for modeling solar wind parameters. We speculate that although very energetic, active region jets lack the ubiquity that their polar counterparts exhibit, limiting their potential influence on heliospheric energetics and dynamics. Even so, a generic geyser ejecta may be tracked out to in-situ particle flux detectors as WIND and ACE. Such an analysis may answer important questions regarding the anisotropy of the heliospheric solar wind flux.

We used RHESSI observations to analyze high energy electrons accelerated co-temporally with jets. When compared to typical microflare pictures where jet emission is not always detected, the geyser site's flaring episodes appear to be impulsive. The analysis of the footpoint flaring revealed that there exist distinct source morphology between soft and hard X-ray emission, showing yet again that non-thermal processes are involved in small-scale jet eruptions. We have found that the X-ray energy release is quite substantial and is compatible with the EUV computed energetics. The geyser induced microflares are heated to temperatures above the EUV emission limits, again exhibiting an analogous manifestation to standard flares.

Furthermore, the geyser microflares are analyzed via RHESSI spectral fitting of the microflare site. We found that a combination of thermal and non-thermal emission models are needed in order to interpret the data. This result interpretation reveals that downwards particle acceleration is occurring during the geyser's jet-inducing microflare events. Non-thermal emission models cannot fit the X-ray spectra outside the peak flaring times. Micro-class jet-inducing reconnection is thus brought closer to the standard flare model. RHESSI is one of the most successful solar missions to date, massively helping us advance our knowledge of flare energetics and particle acceleration for the last two decades. As it approaches the end of its life, a new mission focused on high energy solar spectroscopy and imaging is highly desired. An increase in energy resolution along with lower instrumental noise, will help settle the main problems of small-scale flaring properties.

Evidence from the EUV, radio, and magnetic field data discussed in this thesis revealed that a microfilament eruption scenario is supported by the observations. The magnetic topological layout revealed the presence of significantly twisted magnetic fields that release helicity during the jet eruptions. This magnetic configuration is analogous to larger helical CME's. The EUV jets exhibited multiple erupting strands that we interpret as multiple short succession flaring events, which is a requirement of a filament eruption scenario. A subset of jets were highly dynamic and exhibited multiple Type-III bursts manifesting due to electron beams generated co-temporally with the multiple SDO-AIA EUV flaring peaks. This aspect represents additional evidence that multiple individual reconnection events are occurring on very short timescales.

The quasi periodic pulsation-like behavior of the jet-inducing microflares is intriguing as these phenomena are not very well understood. The energetics at the level of microflares can help to better understand the mechanics of large scale flaring. Quasi periodic pulsations have also been associated with stellar flares. X-ray analysis of the intricate reconnective processes is a highly desired capability in the context of resolving stellar phenomena using solar observations. For this purpose, we aim to explore possible opportunities of NuSTAR high-energy observations.

At least in the case of the AR11302 geyser site, we find that the recurrent jets are not the result of a series of self-similar reconnection events. We have shown that a chaotic combination of penumbral magnetic moving features and small dipole emergences are all involved in producing the observed jets. The two competing mechanisms (flux cancellation vs. flux emergence) were found to be distributed almost evenly among eruptions. This is a striking finding, as a unique site appeared to be subjected to very similar reconnective events over a long period of observations, while it kept its quasi-stable demeanor.

Coronal plasma spectroscopy reveals that torsional untwisting waves (kink) may be generated and can propagate along the jet plasma. The torsional forces along magnetic flux tubes are highlighted and a comparison made between pre-eruptive and post-eruptive states. Our geyser did not appear to produce any jet that could be attributed to a destabilization resulting from a kink unstable potential inversion line patch, although in some cases, the winding was approaching the critical threshold. The low quality of the data may play an important negative role in this determination. To this extent, an

analytical parameter study on the conditions under which a kink instability can be considered a jet generating process is a natural (planned) extension of our work.

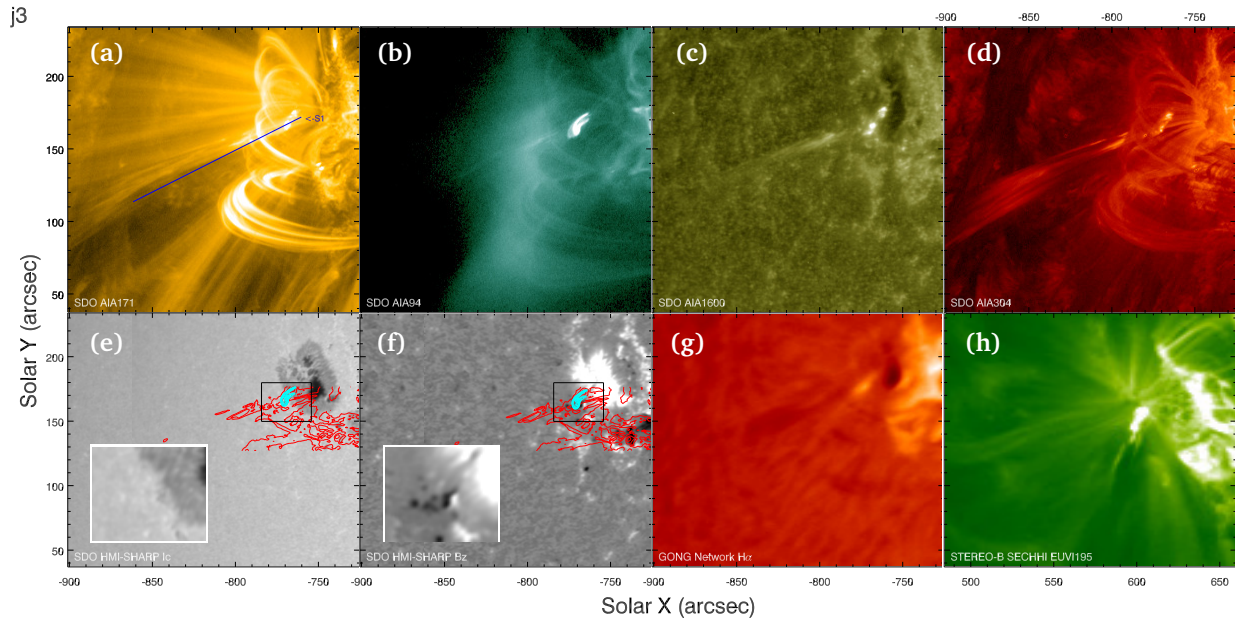
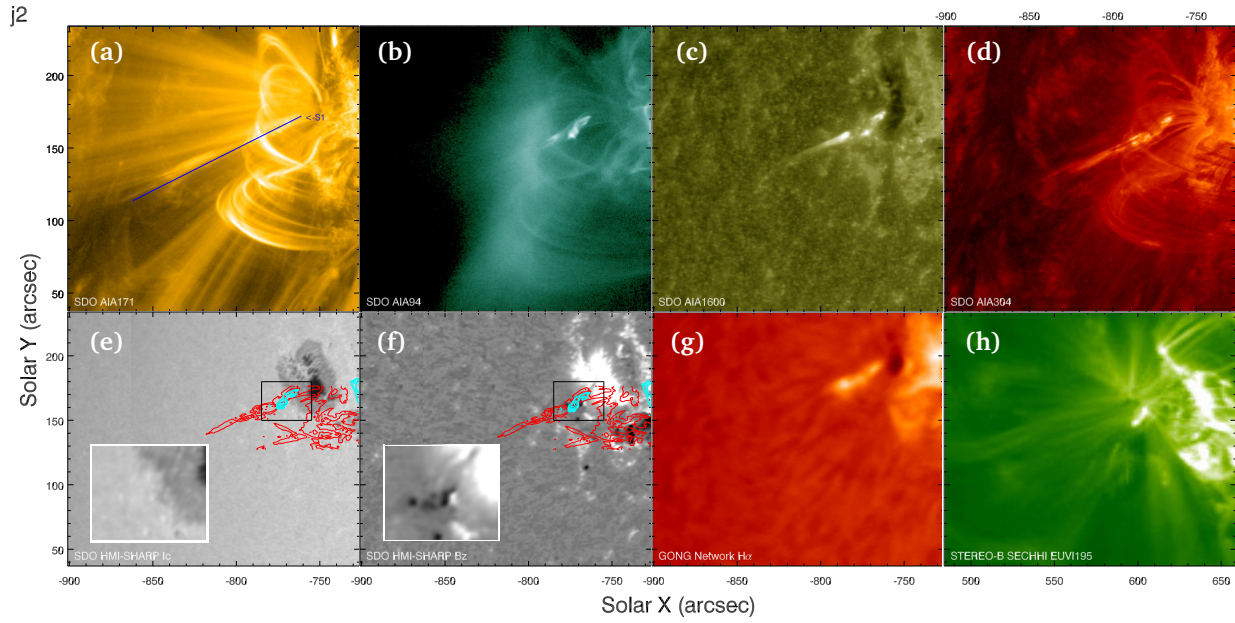
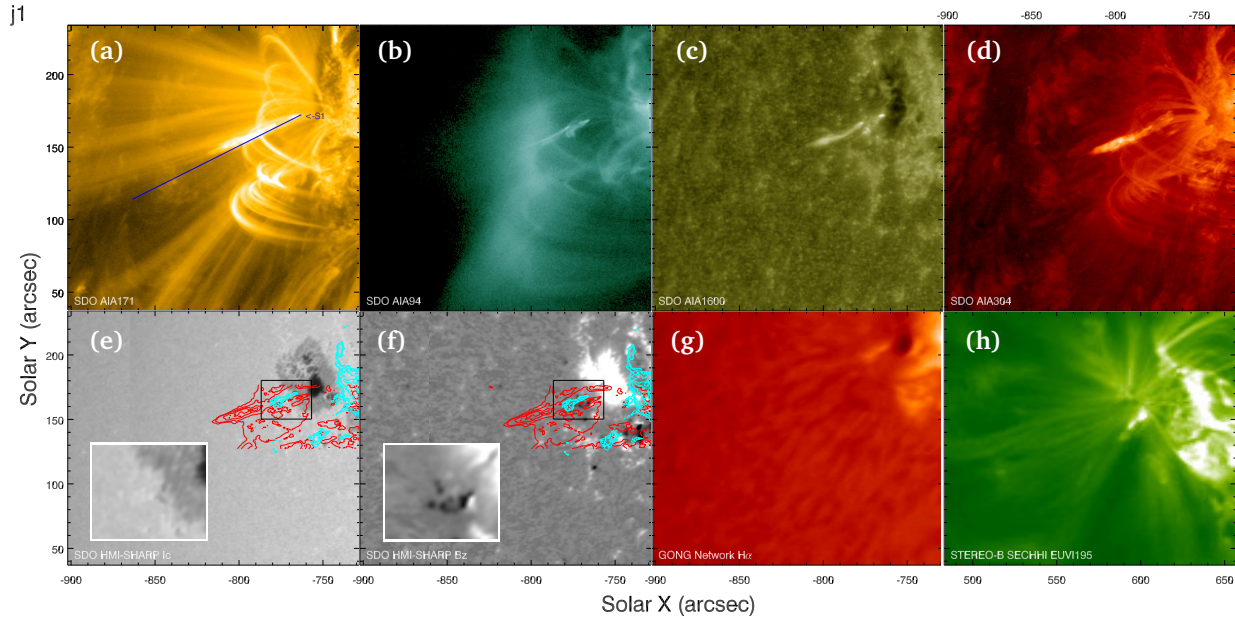
As emphasized throughout this thesis, the current generation of instruments is not designed for small-scale structures. We endeavored to manually finely tune the available data in order to reach our conclusions. Even then, results are significantly affected by instrumental limitations. Low noise and fast cadence spectro-polarimetric magnetic field measurements capable of revealing a geyser's topology, in both the photosphere and chromosphere, will be able to confirm or invalidate our current topological and kink instability findings. We are preparing DKIST proposals in order to further pursue this goal.

It is a great time, and a great honor, to be part of the exciting field of observational solar research. This week, in August 2018, the Parker Solar Probe [Fox et al., 2016] was launched and started its 'hot' journey towards the Sun's inner corona. The scientific output will be outstanding! DKIST, the most ambitious ground based solar telescope will commence operations in the following months, probing the low solar atmosphere with unprecedented detail. As we have hoped to have shown, the study of the physics of small-scale solar phenomena will provide, by comparison, crucial information towards understanding the large scale eruptive events which influence our life-sustaining heliosphere. I am grateful to have been able to contemplate the awe of discovery...

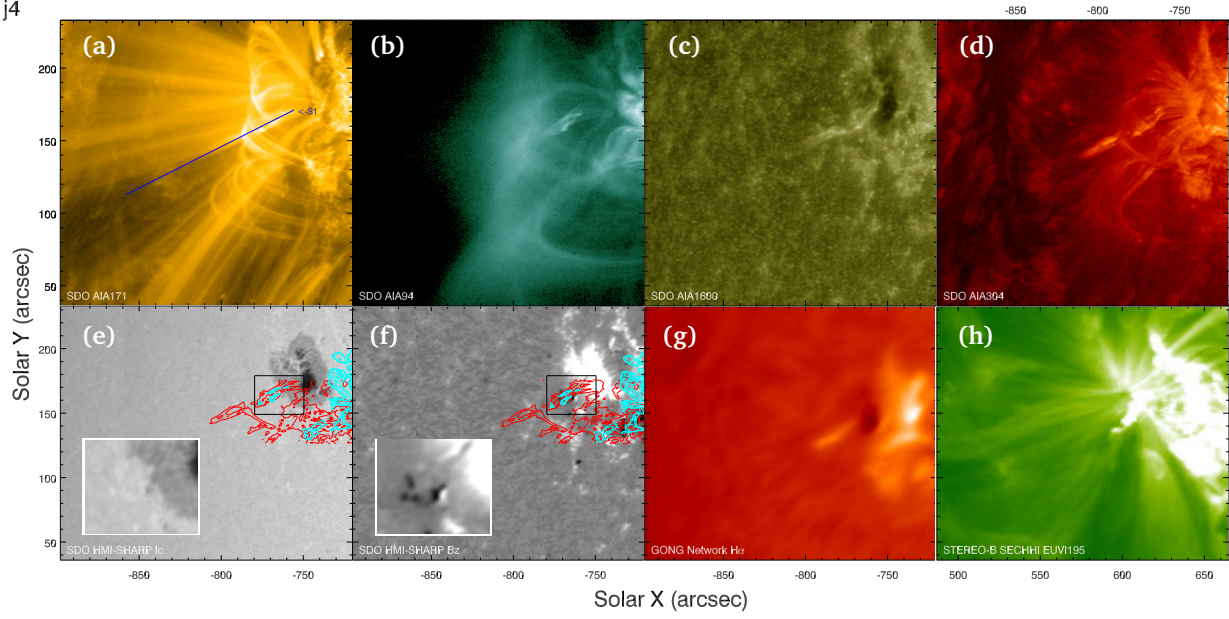
Appendix A

The multiwavelength view of the AR11302 geyser site jets

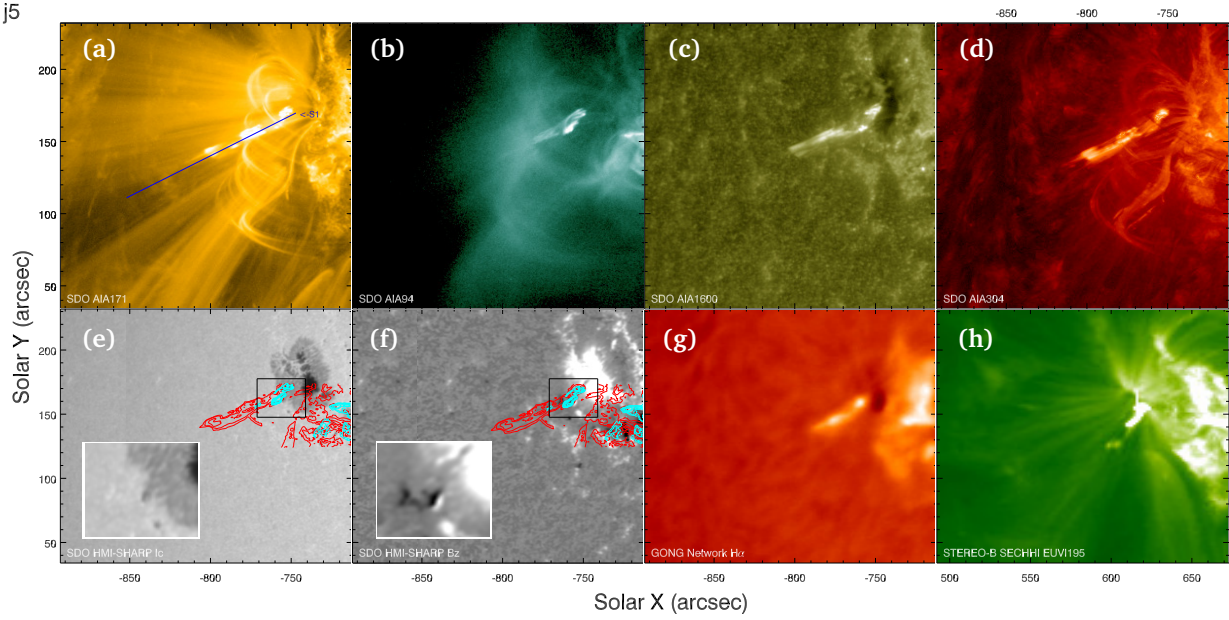
Geyser coronal jets J1 to J10 detected on 25.09.2011 at the south-eastern periphery of AR11302 are visualized in a multiwavelength arrangement of complementary observations. The figure sub-panels represent different correlated manifestations of jet eruptions: (a) AIA-171Å ($T_{main} \sim 0.8 - 1MK$) and the location of the timeseries slit; (b) AIA-94Å ($T_{main} \sim 5 - 8MK$); (c) AIA-1600Å ($T_{main} \sim 0.4MK + continuum$); (d) AIA-304Å ($T_{main} \sim 0.5MK$) and timeseries region (B1); (e) SDO HMI intensity continuum with added AIA-304Å (red) and AIA-94Å (blue) contours, (f) HMI vertical B_z magnetogram with added AIA-304Å (red) and AIA-94Å (blue) contours; (g) BBSO H α ; (h) STEREO-B EUVI-195Å ($T_{main} \sim 1 - 2MK$) different viewpoint observation. Filtergram temperatures are provided for comparison and are of qualitative nature. A full differential emission measure analysis is required in order to recover plasma physical temperatures. A emission measure estimation is available in chapter 3.



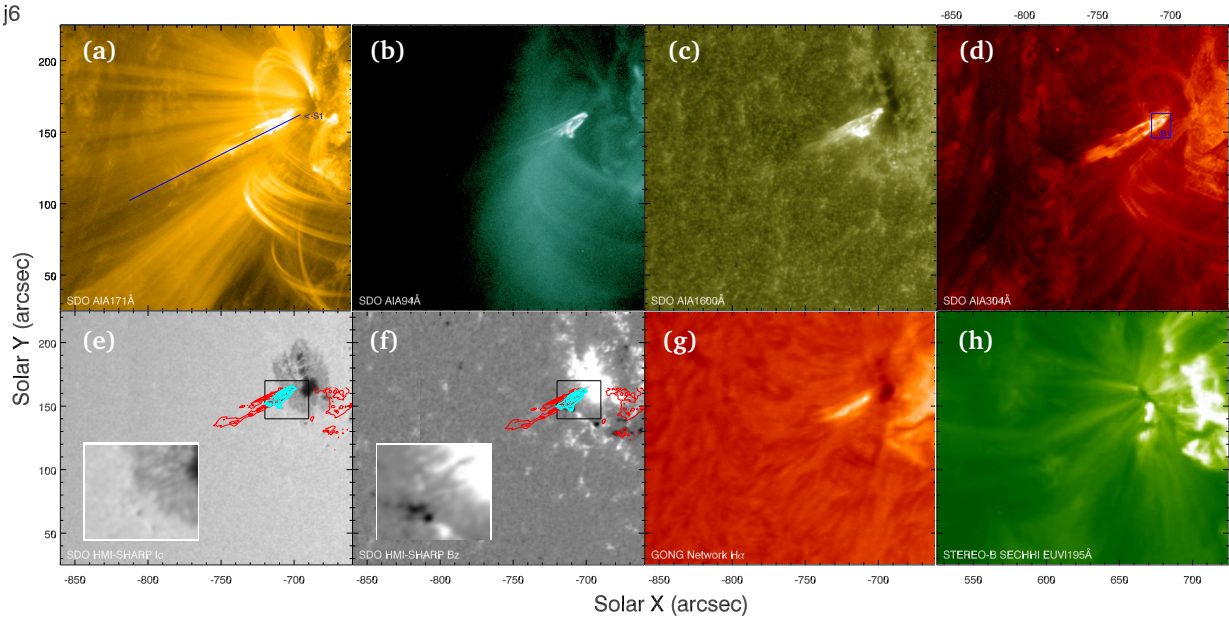
j4

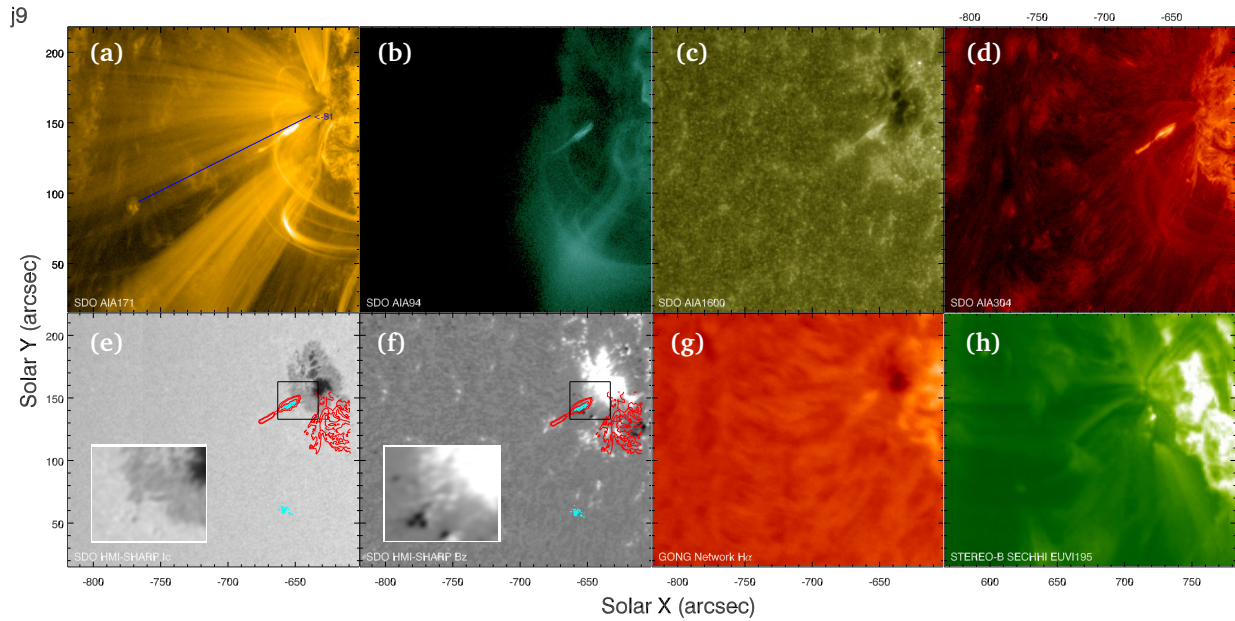
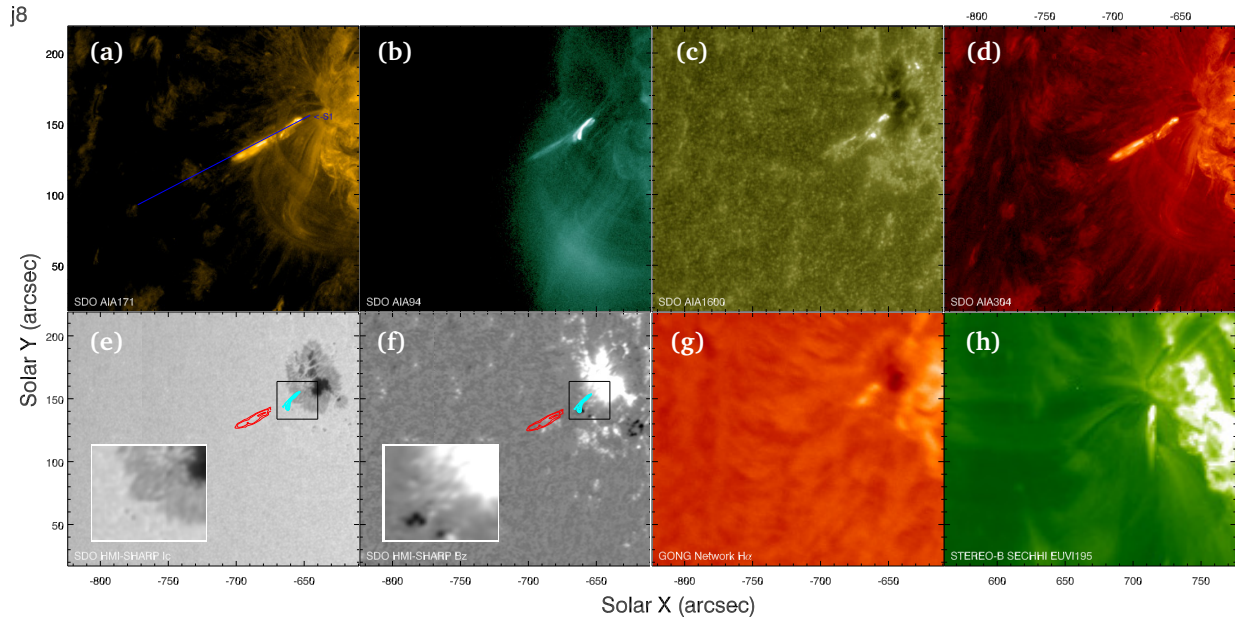
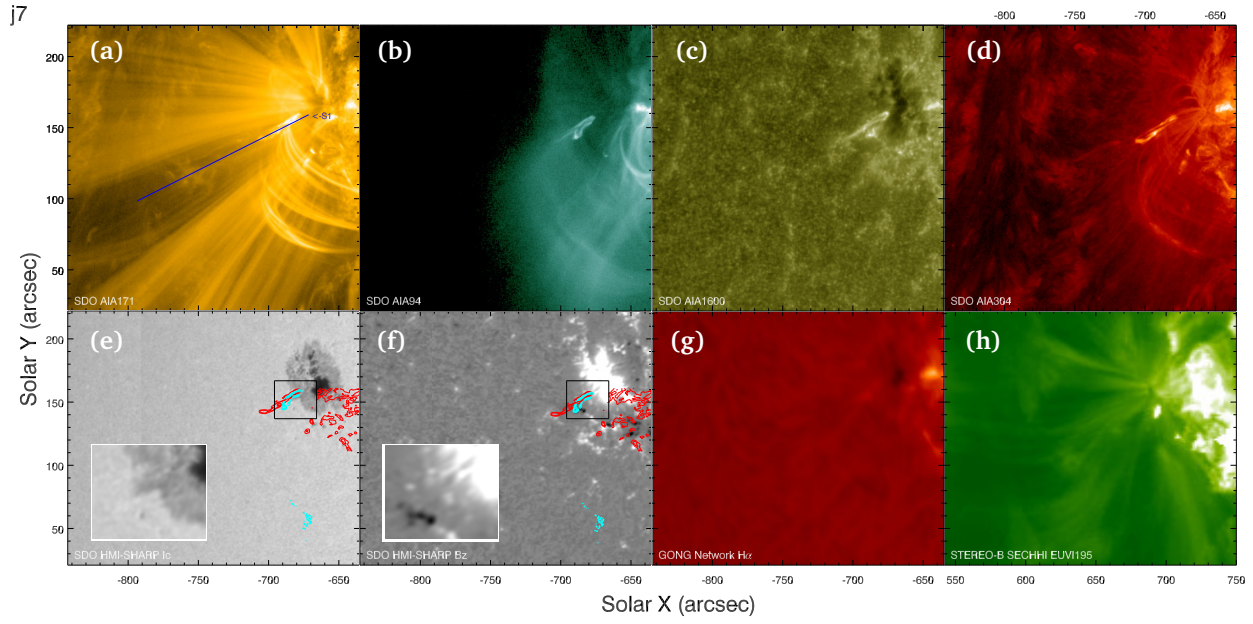


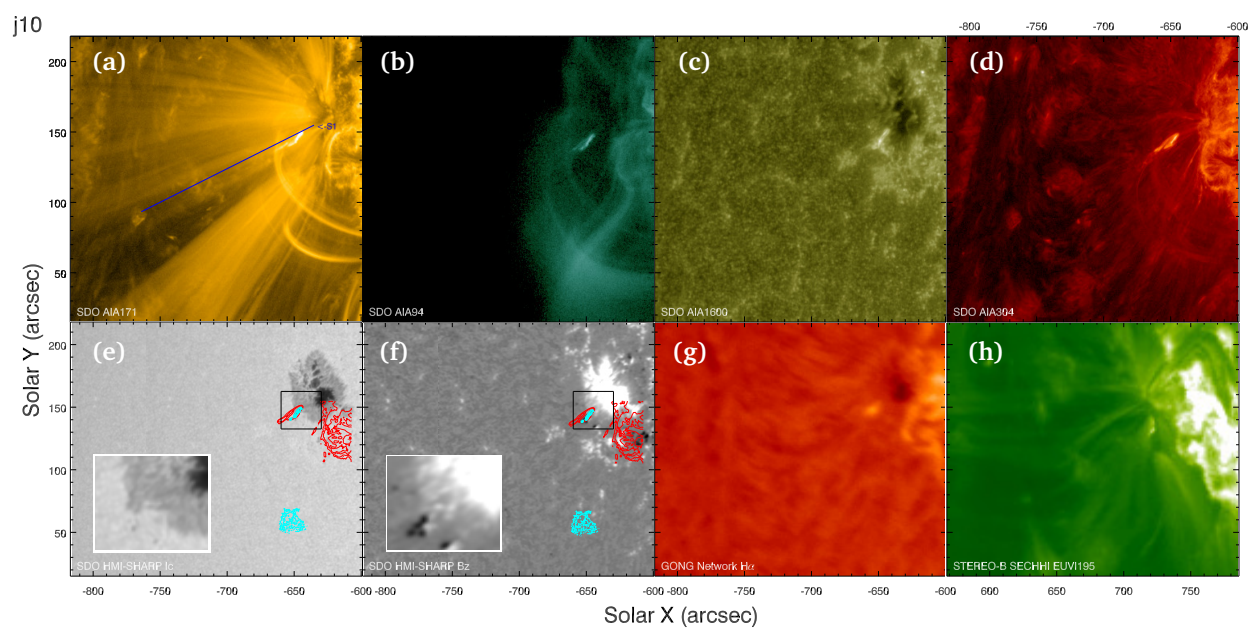
j5



j6



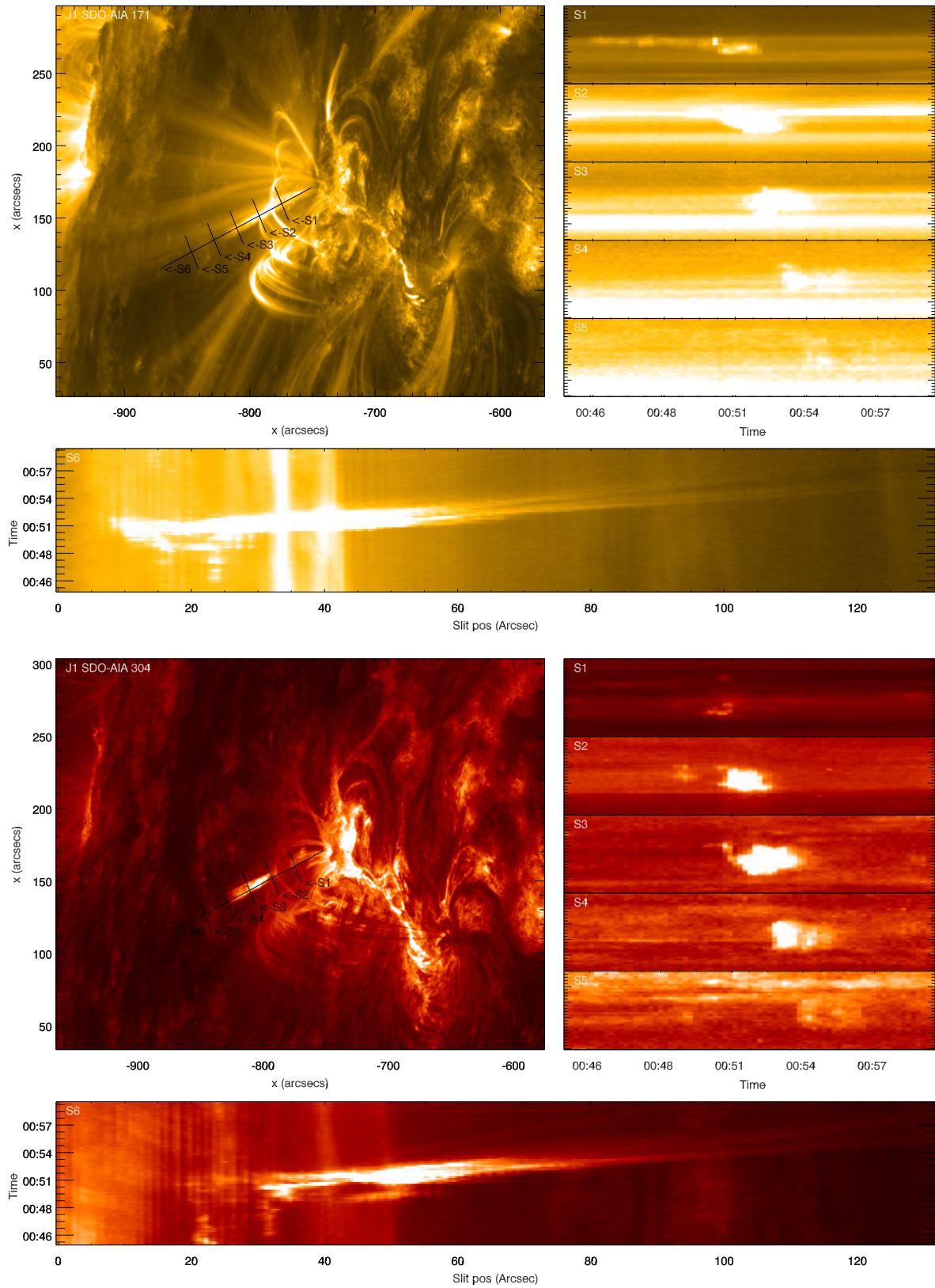


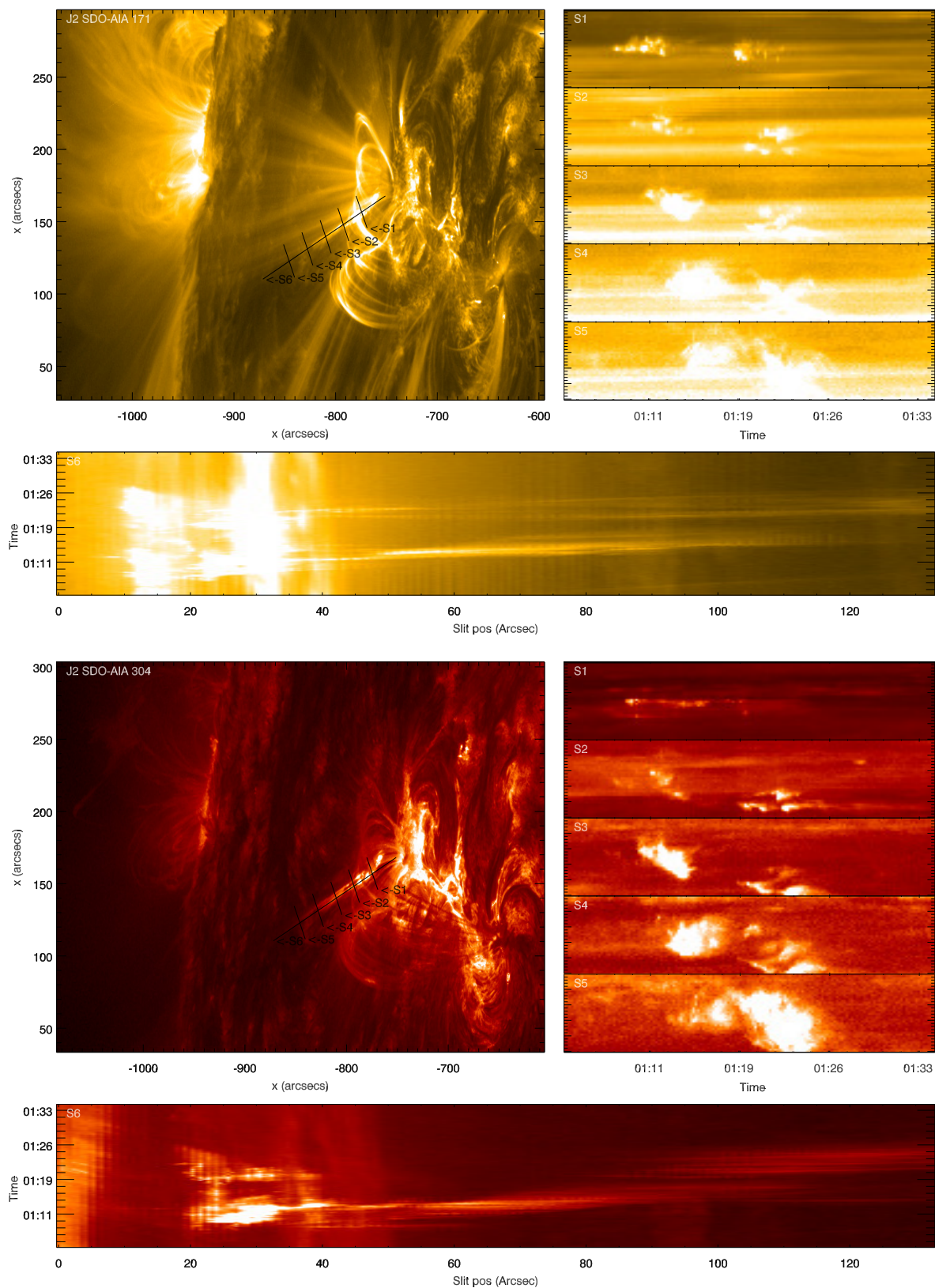


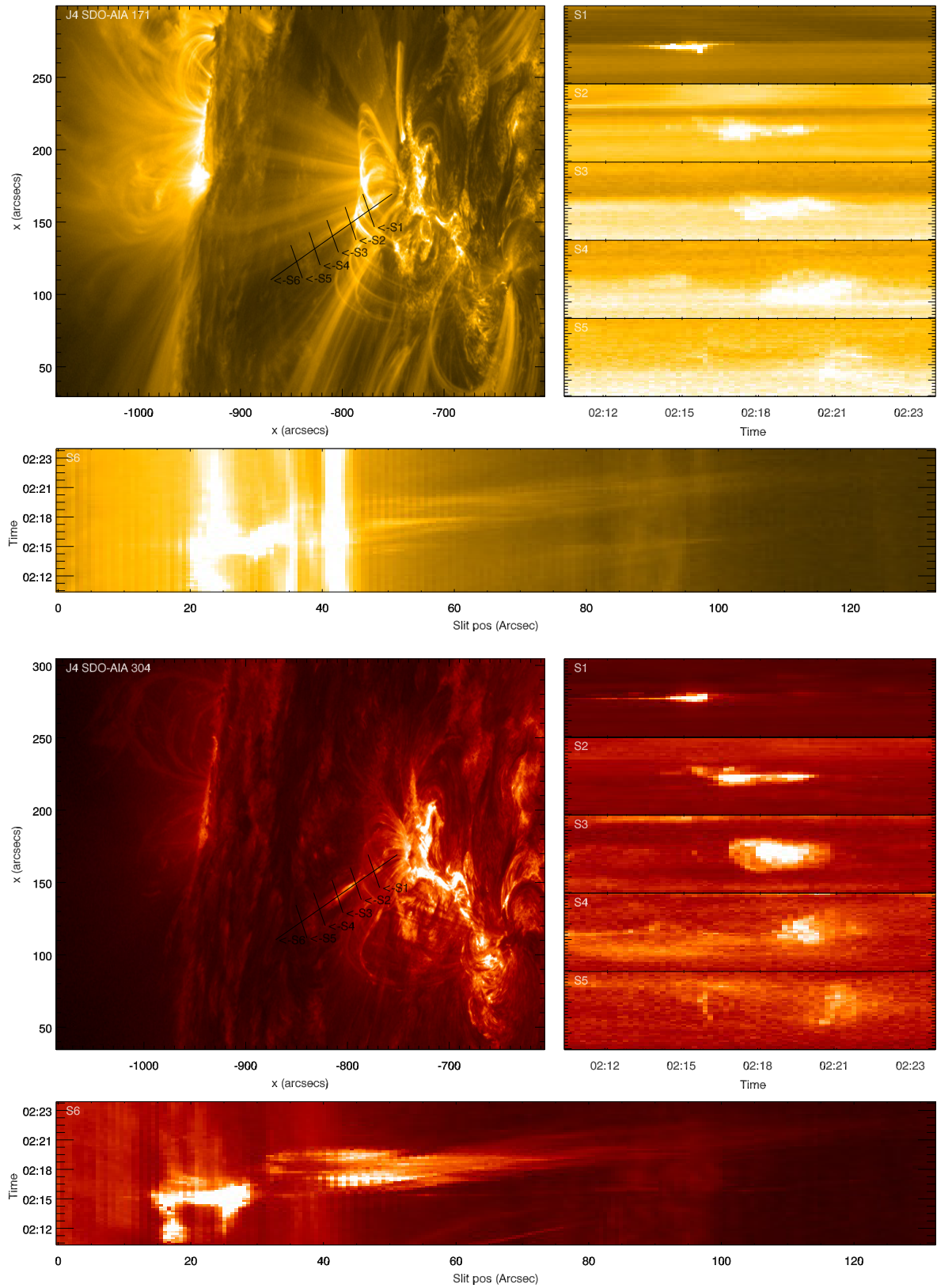
Appendix B

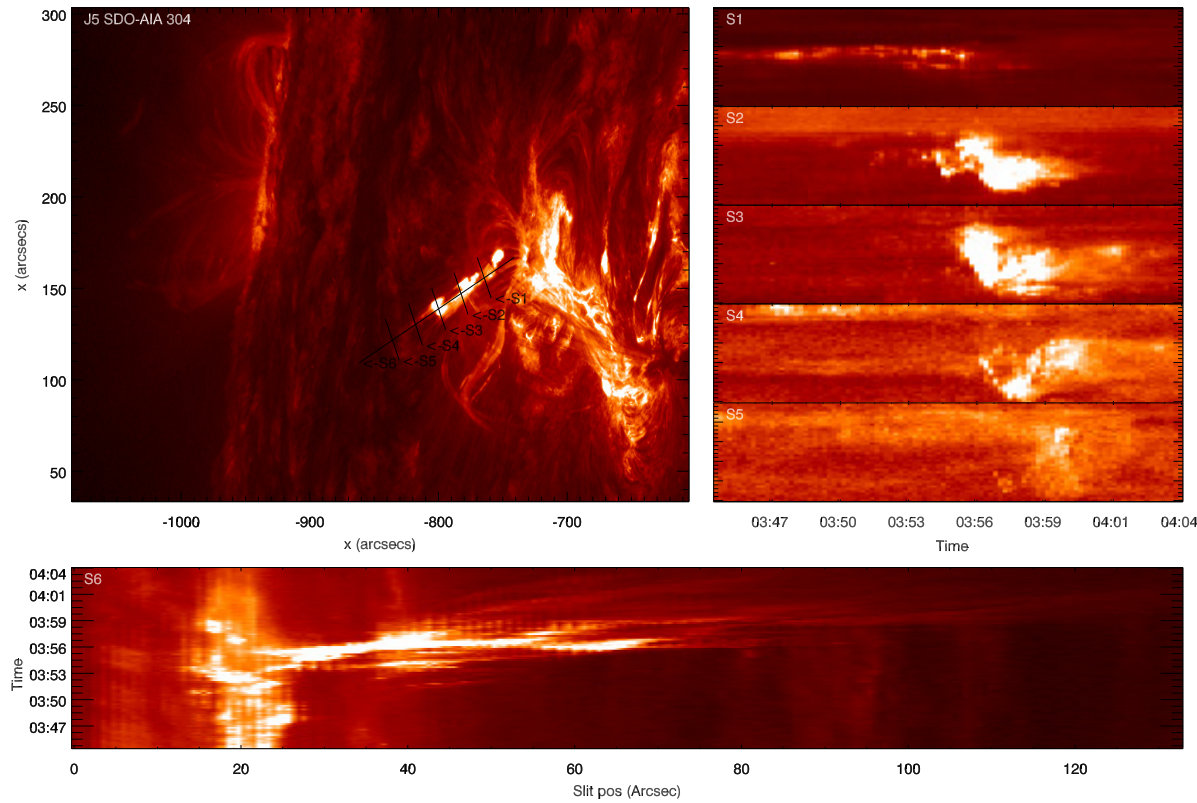
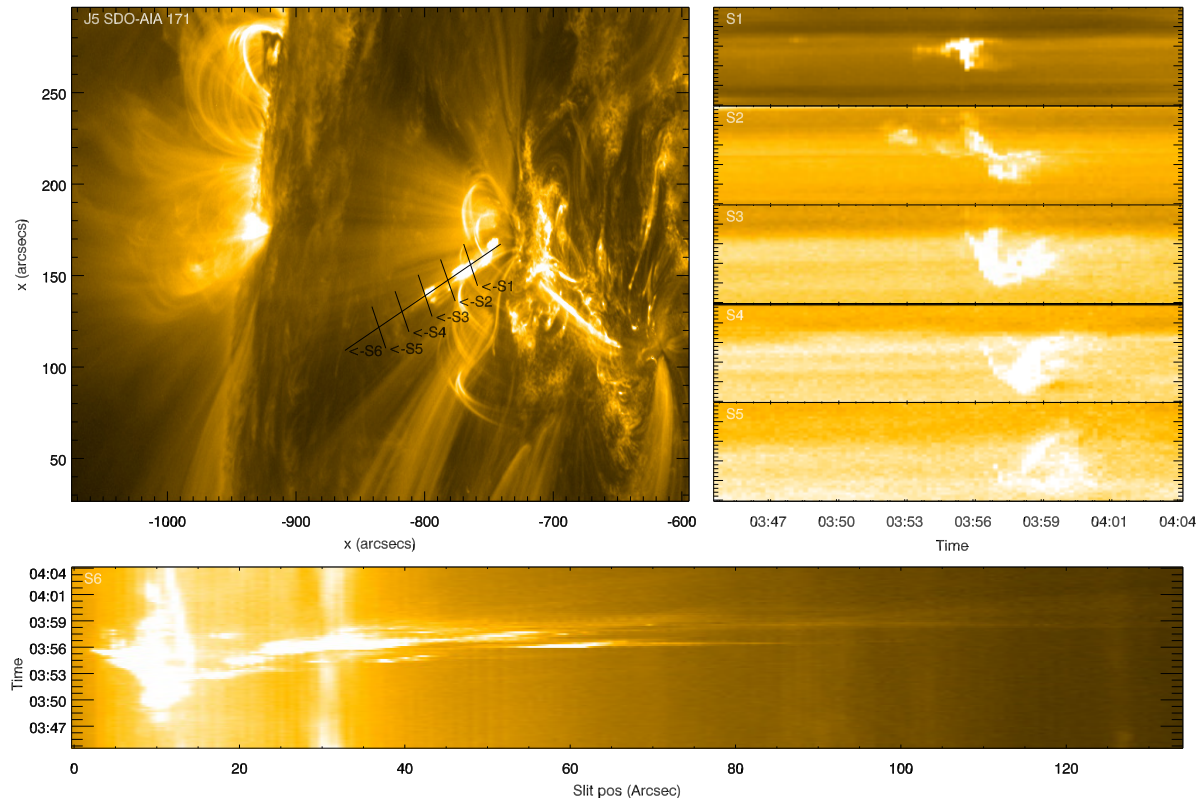
The AR11302 geyser jets slit-jaw perspective

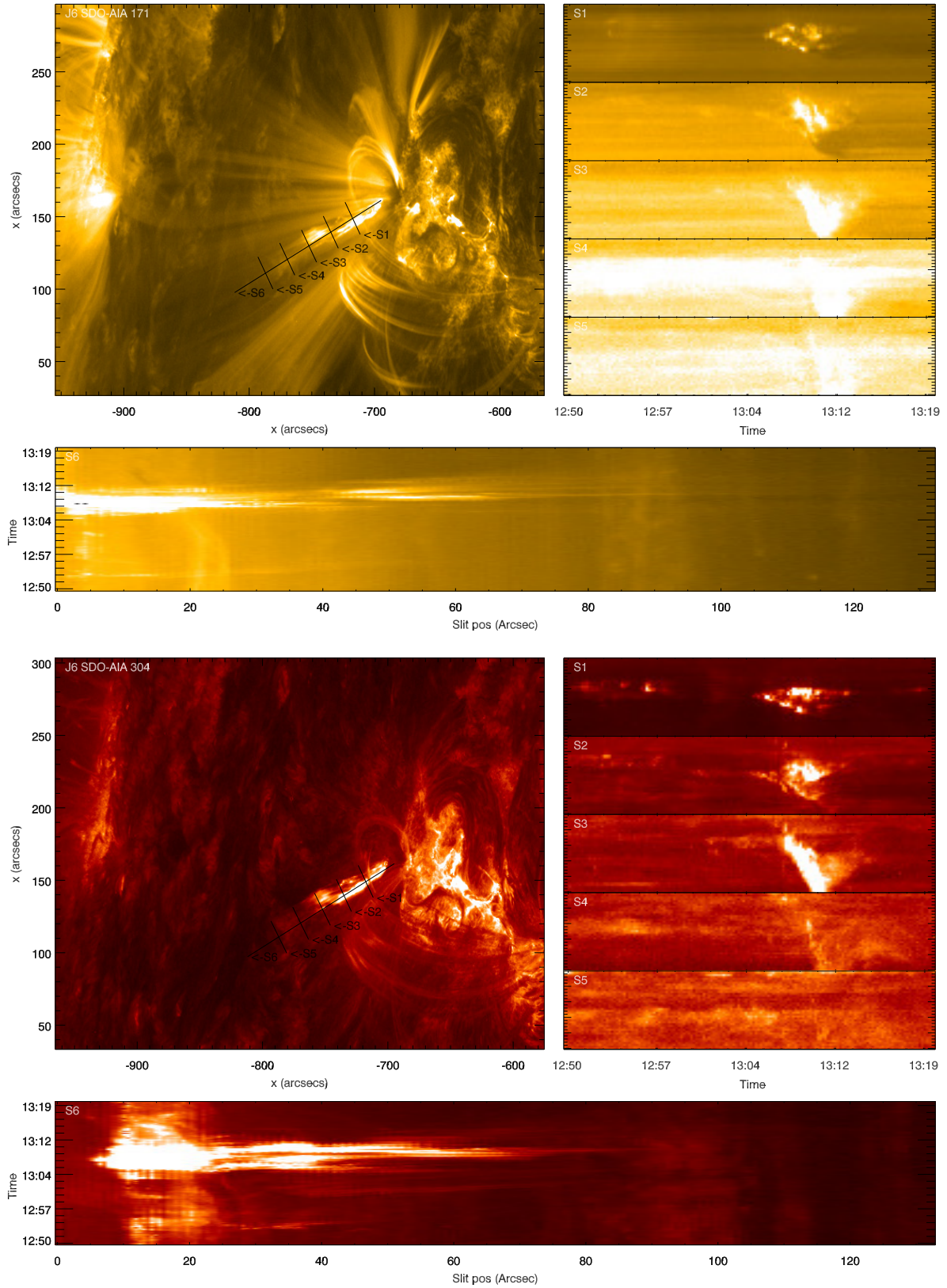
A slit based visualisation of the Geyser coronal jets J1 to J10 eruptions is presented. The jet eruptions were detected on 25.09.2011 at the southern periphery of AR11302. A slit system comprising of one narrow parallel (S6) slit along with five narrow perpendicular slits (S1 to S5) were fitted over the AIA-171Å and AIA-304Å filtergrams. S6 is traced along the jet axis and covers both the outflow and the footpoint flaring. The S1-S5 slits are traced perpendicular to the jets eruptions direction where S1 is close to the geyser site, crossing the lower footpoint. Individual jet outflow speed and basic morphology was deduced from analysing the slit system. Most events exhibit helical untwisting motions as they propagate. This aspect can be observed in the S6 slit where the individual strands are seen unravelling, but also in the S2-S5 slits where discernible arrival times were detected.

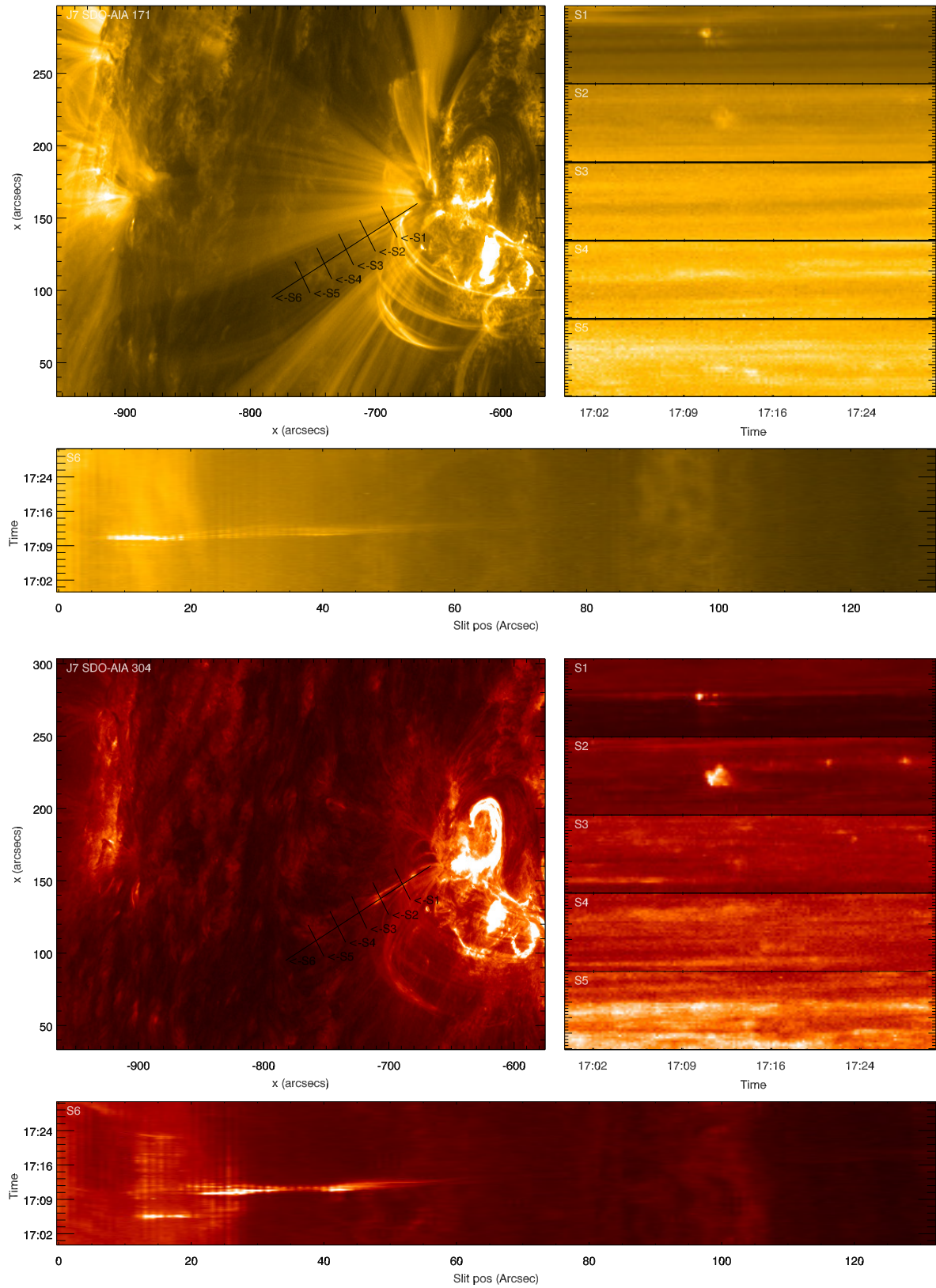


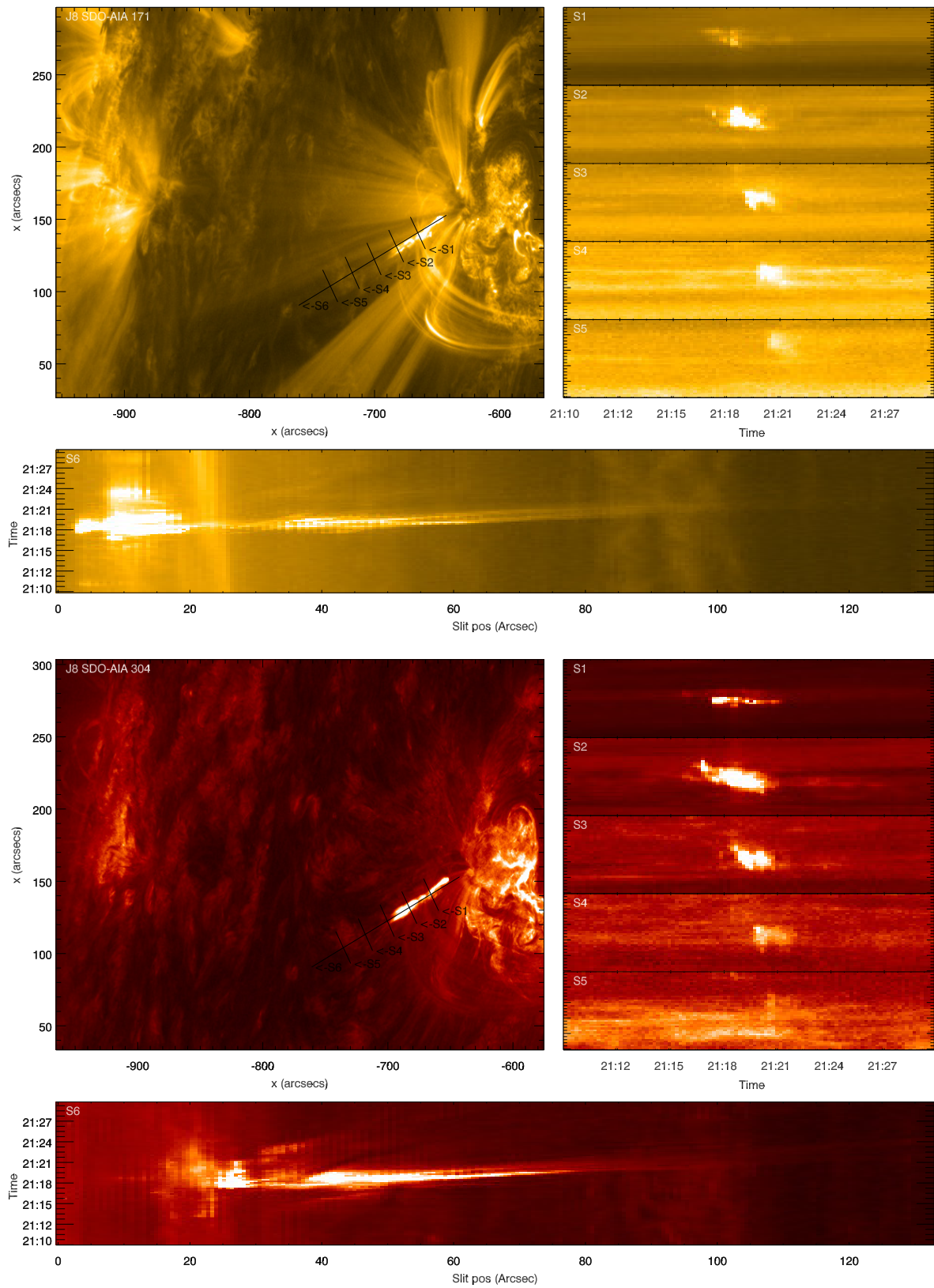


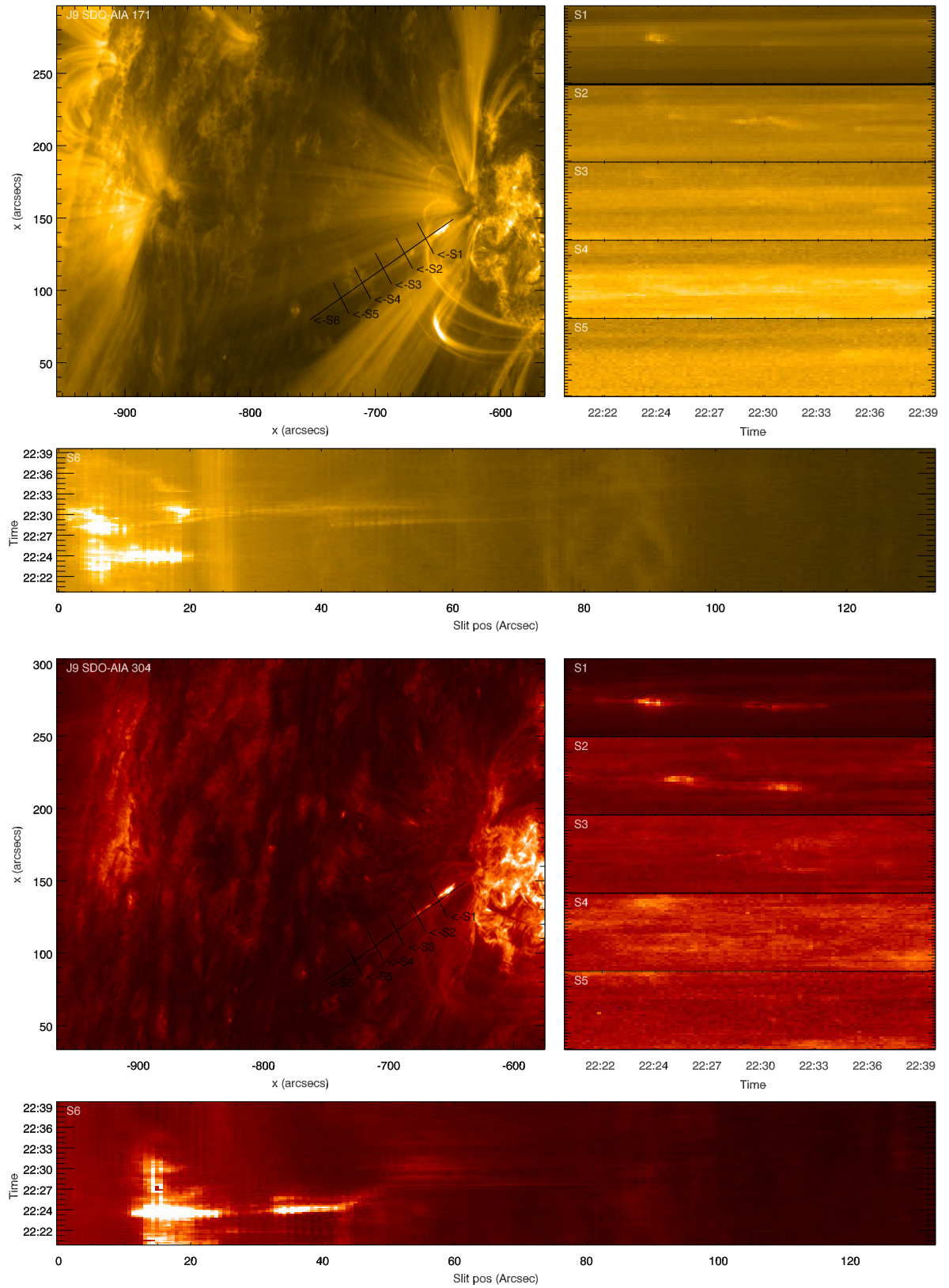


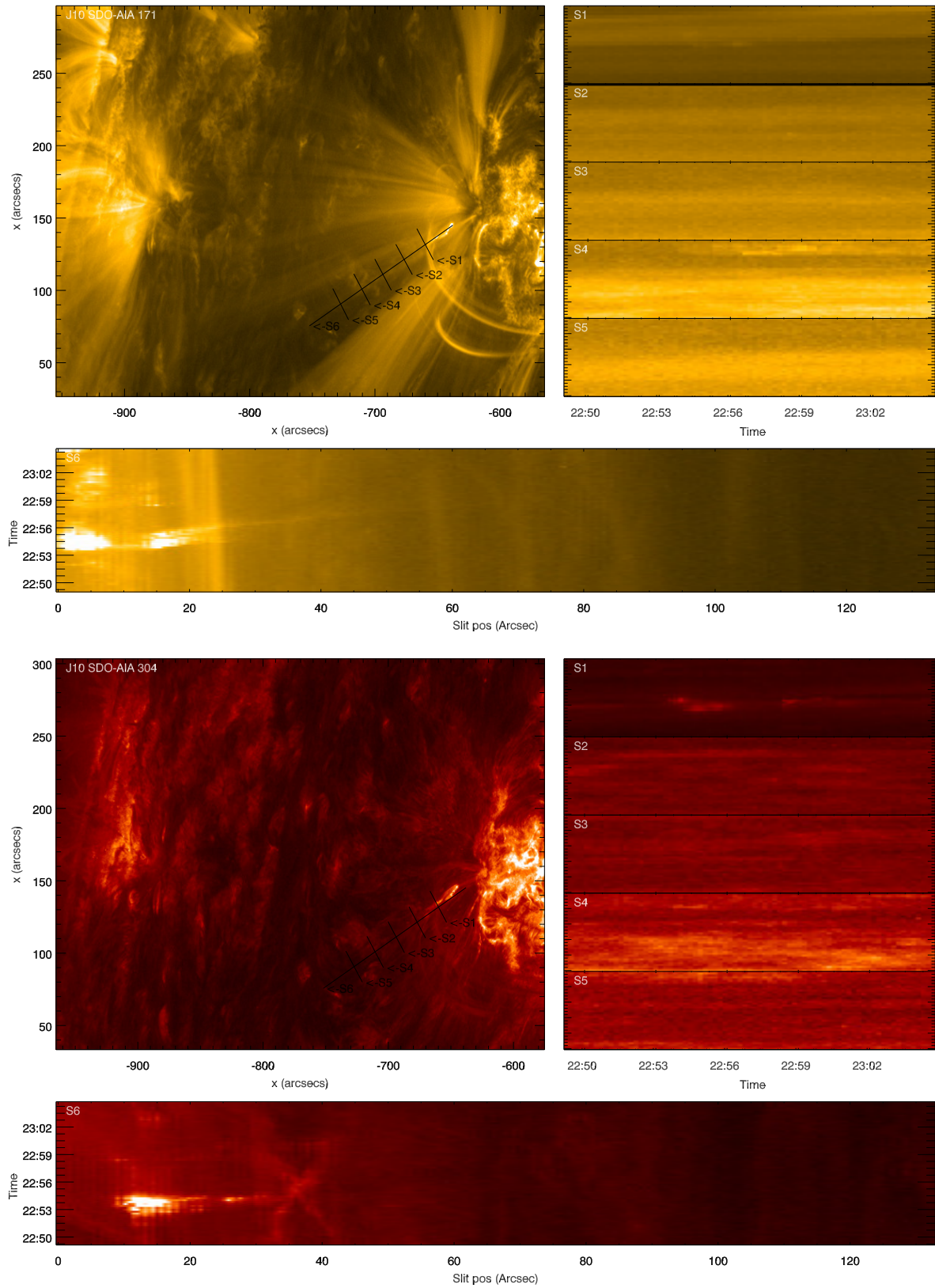












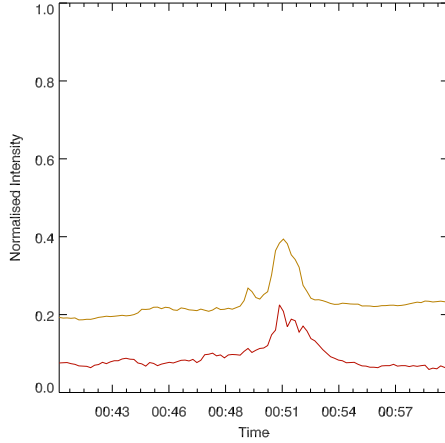
Appendix C

Magnetic moving features interacting with the AR11302 site

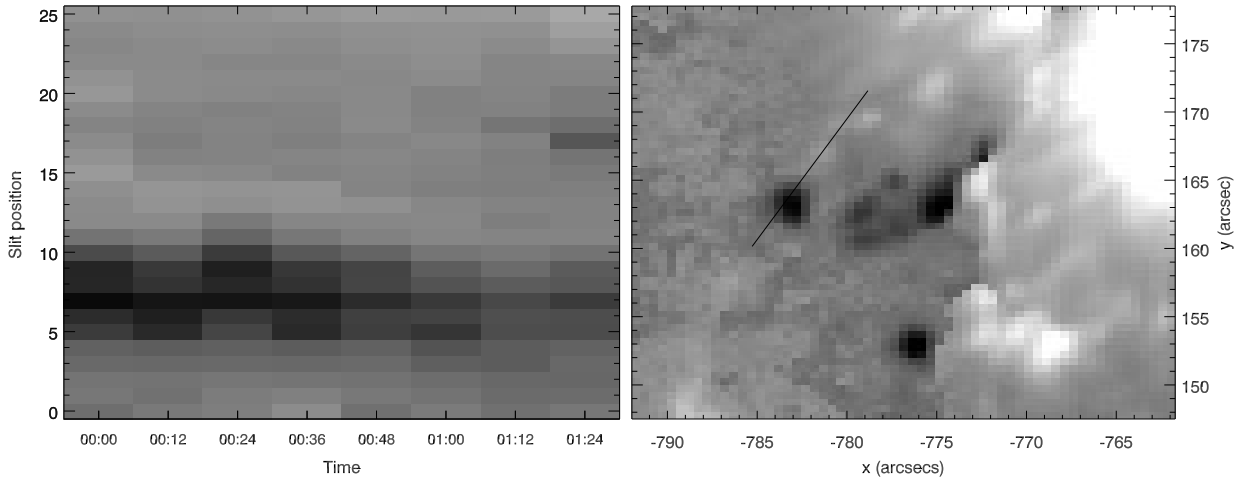
The section presents the magnetic moving features that potentially influence the geyser site jets detected on 25.09.2011 at the south-eastern periphery of AR11302. The smaller intensity flaring O1-O7 could also be correlated to photospheric movements. These transient fluxes were cautiously interpreted as being the trigger of the jet eruptions and smaller flaring events. The events were identified via SDO-AIA flux timeseries (fig. 1.2) analysis. Short temporal cuts of AIA-171Å (yellow) and AIA-304Å (red) normalized intensity timeseries are provided as reference. The moving fluxes are detected in vectorial magnetograms representing the heliocentric vertical field component B_z . Both flux emergence and flux cancellation situations were observed. The different jets are shown to not be self-similar or self recurring, but a product of chaotic flux drifts that interact with the quasi stable geyser footpoint (microfilament).

MMF Cancellation Events

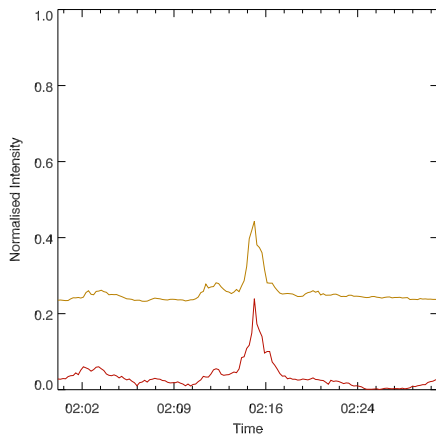
The J1 event



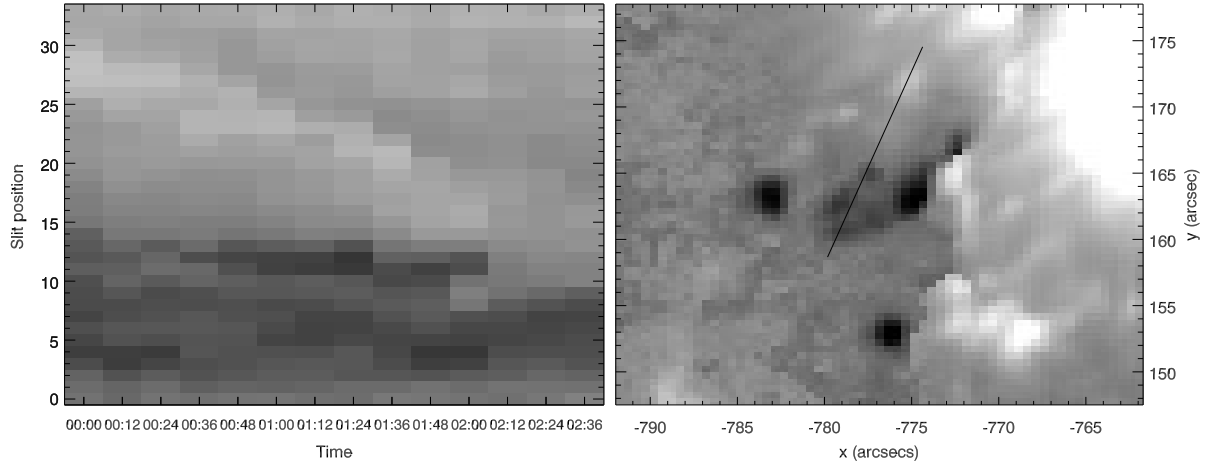
We track between 00:00UT-01:24UT a set of elongated positive polarity features of 238 ± 71 G and 361 ± 75 G originating in the field penumbra $(X, Y) = (-781'', 166'')$. The features are moving outwards in the SE direction with an approximate surface speed $v_s = 0.4 \text{ km s}^{-1}$. The flux cancels with the negative pore of -955 ± 84 G during the 12 minutes integration time of the 00:48UT frame. AIA-171Å flaring starts at approx 00:49UT and the main jet is seen at 00:51UT corresponding with the two patches that interact with the pore consecutively.



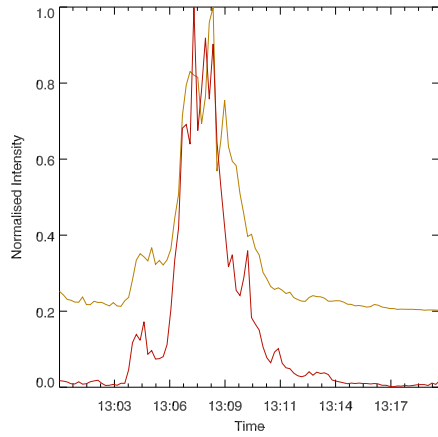
The J4 event



We track a positive polarity grain originating in the field penumbra $(X, Y) = (-775'', 172'')$ from 00:00UT to 03:00UT. The feature is moving outwards in the SE direction with $v_s = 0.6 \text{ km s}^{-1}$. The positive grain of 535 ± 79 G cancels after 02:12UT with a similarly sized negative grain, $(X, Y) = (-778'', 165'')$, of -458 ± 69 G strength corresponding to the pore group. AIA-171Å flaring starts at approx 02:14UT and the main jet is seen at 02:17. Both features dissipate completely.

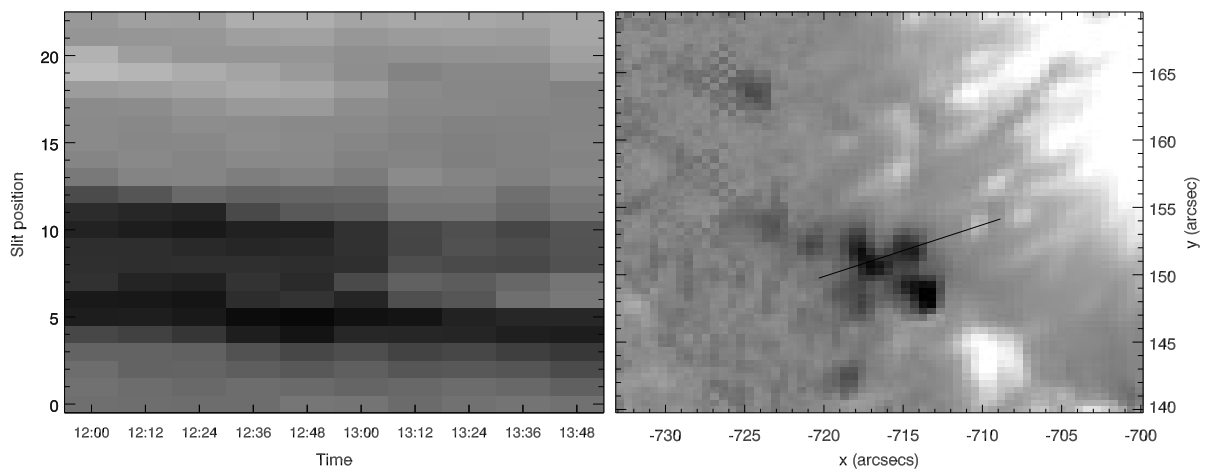


The J6 event

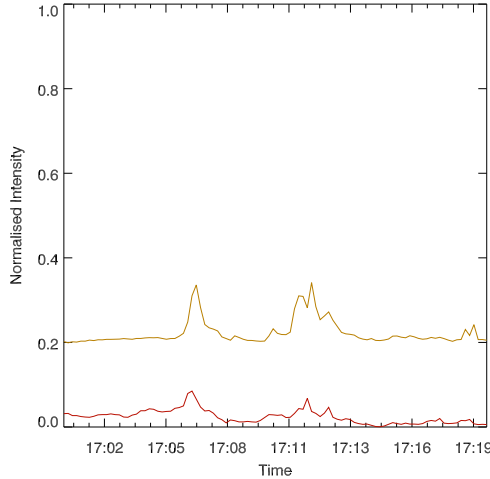


We track a positive penumbral feature drifting towards the pore group from 12:00UT to 13:48UT. The feature appears at $(X, Y) = (-711'', 154'')$ at 12:12UT, and has a $v_s = 0.5 \text{ km s}^{-1}$. The positive feature ($333 \pm 60 \text{ G}$) completely cancels with a negative grain of initial ($-322 \pm 56 \text{ G}$) during the 13:00UT integration time. The SDO-AIA flaring is complex and can be separated into three categories. The first flaring occurs between 12:50UT and 12:57UT does not generate a jet (O3a).

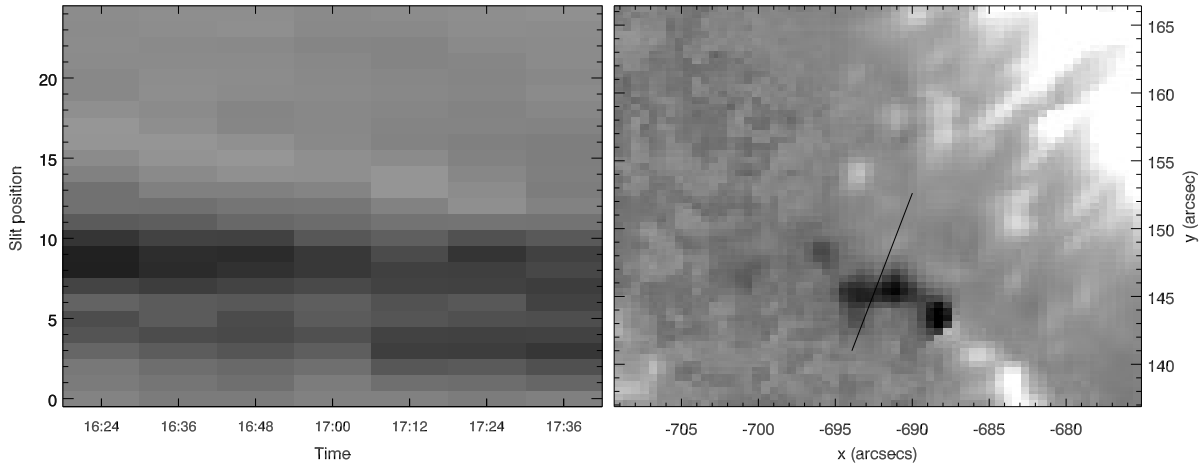
Main J6 flaring occurs in between 13:04UT and 13:11UT. Both AIA channels show 3 distinct flaring peaks. They can not be resolved via MMF approach. Last flaring episode (O3b) occurs at 13:24UT, and is not accompanied by any jet eruption. The O3 events will be discussed separately.



The J7 event (uncertain)

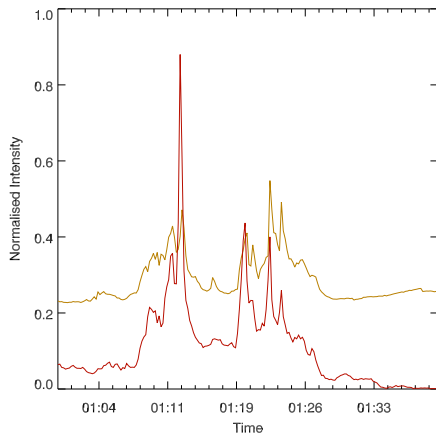


A series of short lived self similar reconnection events including one jet are observed. Analyzing the time from 16:24UT to 17:36UT we identify a modest positive grain feature of uncertain 161 ± 58 G strength ($< 3\sigma$) that is moving with a speed of $v_s = 0.5 \text{ km s}^{-1}$ towards the now coagulated negative pore (-518 ± 52 G). The feature is observed at $(X, Y) = (-691'', 149'')$ very close to the negative pore group and slowly erodes between the 17:00UT-17:24UT frames. We hypothesize that this slow dissipation is the trigger of all reconnection events as seen in the SDO-AIA channels.



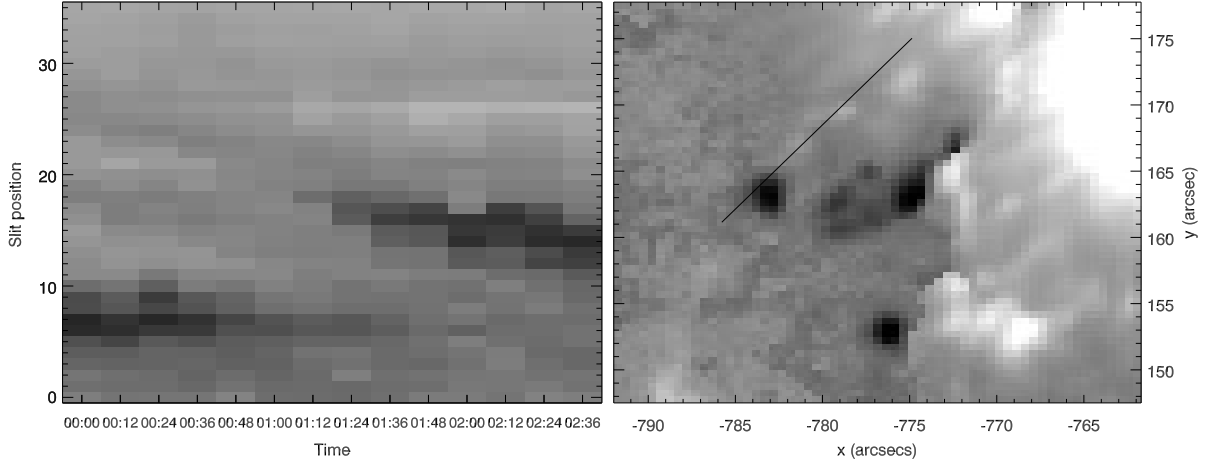
MMF Flux Emergence Events

The J2 and J3 events

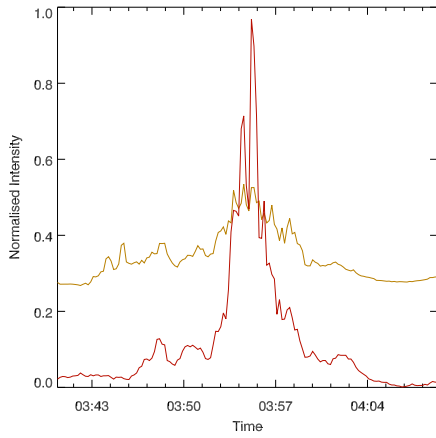


Observing between 00:00UT to 03:00UT, we initially track an elongated positive polarity feature originating in the field penumbra that is involved in generating J1. This flux cancels and is replaced by a newly emerged dipole starting with the 01:12UT frame, at position $(X, Y) = (-780'', 167'')$. The J2 and J3 fields do not appear related to the main pore. This possibly generated the recurring long lasting and flaring episodes represented in the EUV plot. The AIA-171Å flaring starts at 01:11UT with a maximum at 01:13UT, when a jet is observed. A second event is occurring at 01:19UT with a jet starting to erupt at 01:22UT.

The newly emerged dipole is afterwards slowly drifting towards the pore with $v_s = 0.4 \text{ km s}^{-1}$. For reference, we measured the dipole's strength after the jet events at 01:36UT and found -321 ± 75 G and 378 ± 76 G fields in the two footpoints.

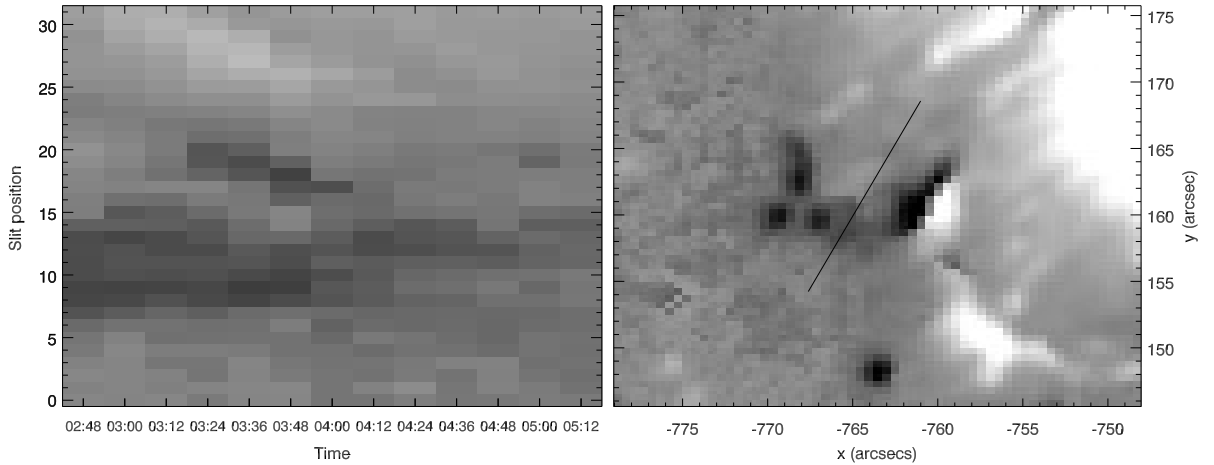


The J5 event

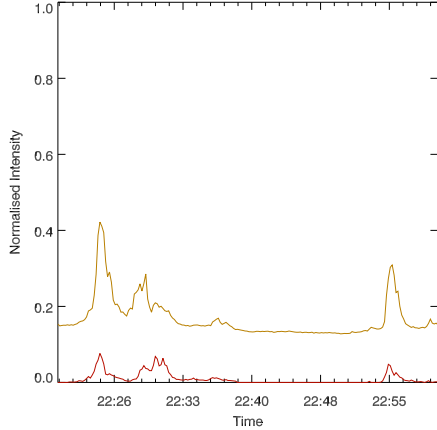


Using frames from 02:48UT to 05:12UT we track an emerging dipole feature originating in the field penumbra and moving outwards in the same SE direction. The positive footpoint (348 ± 76 G) appears at $(X, Y) = (-758'', 168'')$ at 03:12UT and the negative footpoint (-291 ± 39 G) emerges at $(X, Y) = (-761'', 163'')$ at 03:24UT. The newly emerged positive footpoint of the dipole is slowly drifting towards the pore group with a speed of $v_s = 0.6 \text{ km s}^{-1}$. The field strength was measured at 03:36UT, prior to the J5 event as the dipole dissipated during the eruption.

The SDO-AIA eruption is long lived and depicting multiple flare peaks. The AIA-171Å eruption occurs between 03:52UT and 03:59UT with multiple small peaks but no apparent maximum while the AIA-304Å is shorter lasting but noticeably stronger.

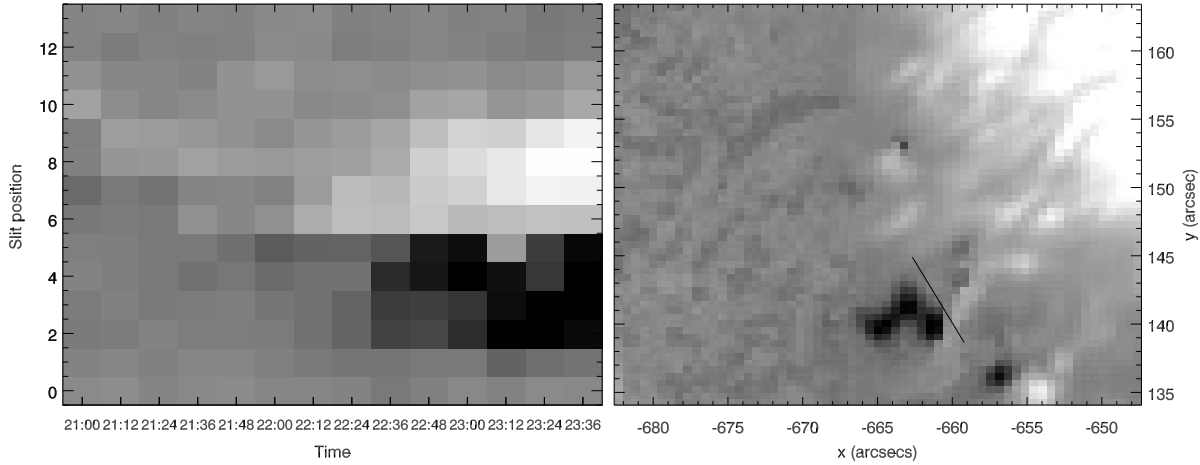


The J9 and J10 events

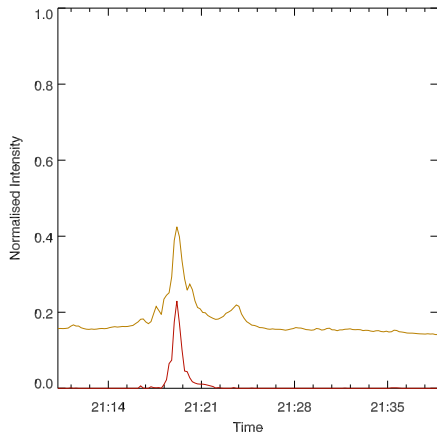


We recover an emerging flux that is rising in close proximity to the pore. The slit region was observed between the 21:00UT and 23:36UT frames. The emerging feature appears at $(X, Y) = (-661'', 142'')$ at 22:24UT. We have assumed that this rising structure is the cause of both the J9 and J10 events, and maybe even the O6 and O7 smaller flaring events. The data does not permit a clear association with the exception of J9 which is co-temporal with the first observations of the emerging dipole.

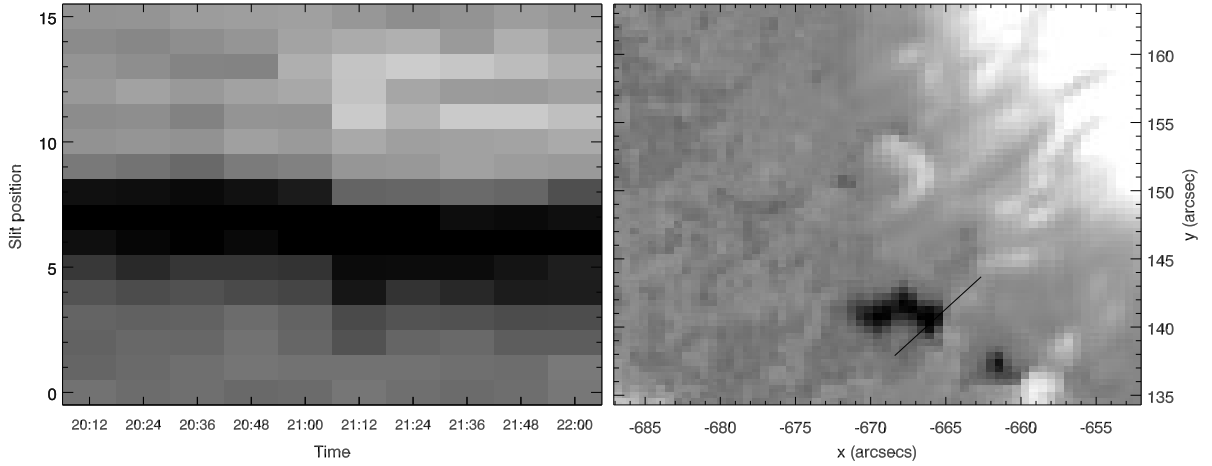
The SDO-AIA flaring is subdivided into three events. J9 has associated flaring peaking in two distinct events at 22:24UT and 22:28UT. The third flaring at 22:55UT is associated to the J10 jet. For reference, we measured the dipole's field at 23:00UT after the two jets erupted. We found strengths of -339 ± 56 G and 448 ± 53 G respectively.



The J8 event (uncertain)

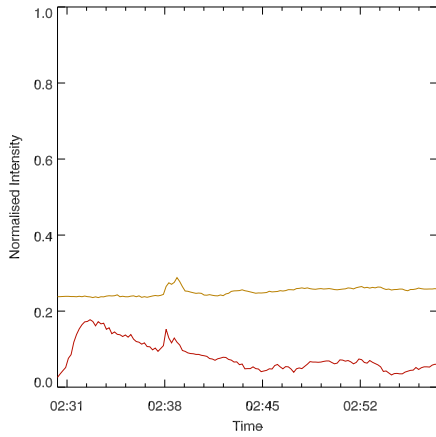


Using frames from 20:12:UT to 22:00UT we initially track an outer region of the pore of strength -277 ± 63 G, observing an emerging positive polarity at 21:12UT of strength 645 ± 69 G that is observed along the slit. The feature appears at $(X, Y) = (-664'', 143'')$ and is very rapidly eroded in the next integration time (21:24UT). Afterwards it slowly decays without exhibiting any EUV signatures. SDO-AIA depicts one flaring and jet event at 21:19UT.



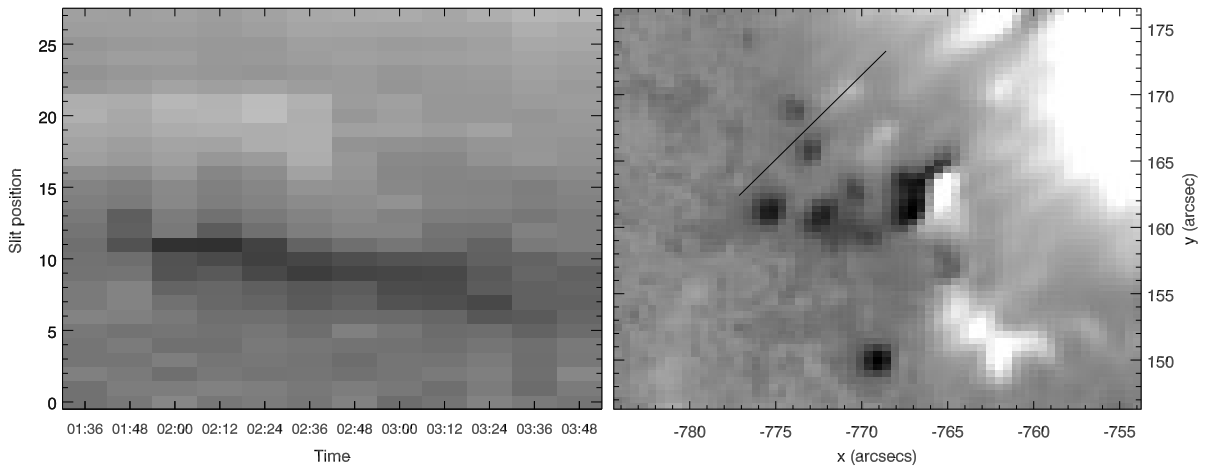
Other MMF related to the Geyser region. No jets recorded

The O1 event

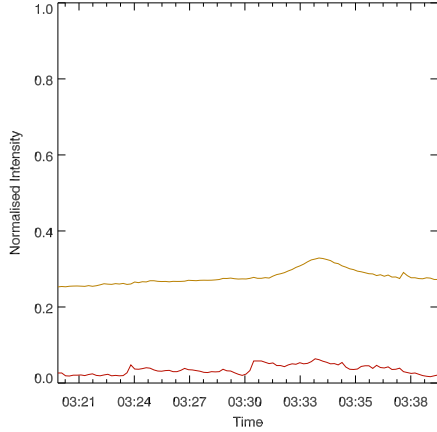


A MMF development in conjuncture with the flaring associated with the 02:27UT M4.4 flare from AR11302 is presented. A rapid increase at 02:29UT then a steady decrease is observed in the AIA-304Å signal as result of downflows following the M4.4 flare. AIA-171Å counts are not affected. The second peak occurs at 02:38UT and is related to the geyser loops (O1). It appears as the flaring event also occurs due to photospheric motions. We track the region close to the dipole emergence related to jets J2 and J3 at position $(X, Y) = (-772'', 169'')$ at 01:36UT.

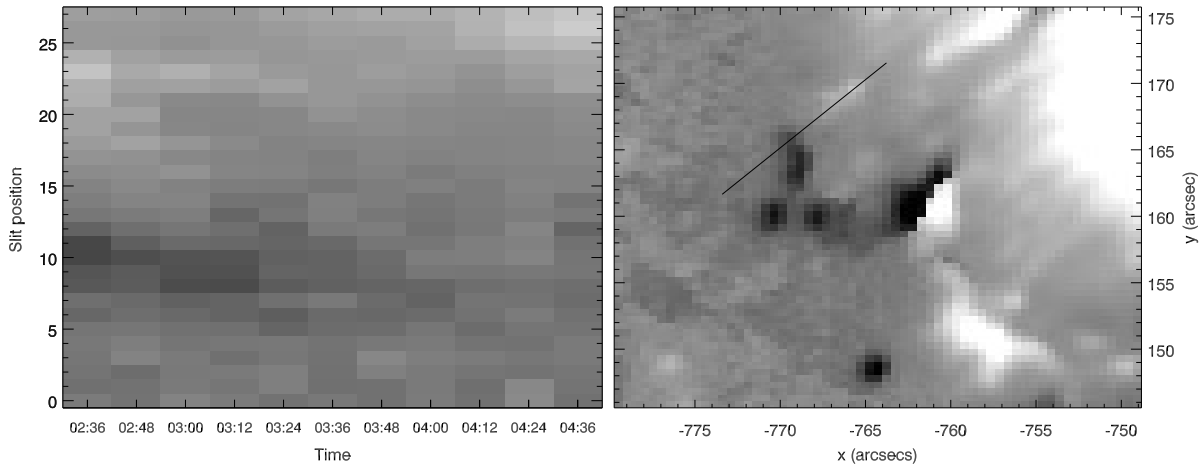
A positive feature (474 ± 75 G) cancels out with its negative counterpart during the 02:36UT instance. The SDO-AIA response is modest. The flaring spike manifested at 02:38UT and no jet could be detected. This event involved the dipole emerged at 01:12UT and does not appear directly related to the pore. We can not safely address if this is indeed a failed jet or was indistinguishable to SDO-AIA due to its modest manifestation. A comparison of the localized flaring between O1 and J4 leads us to favor the first case.



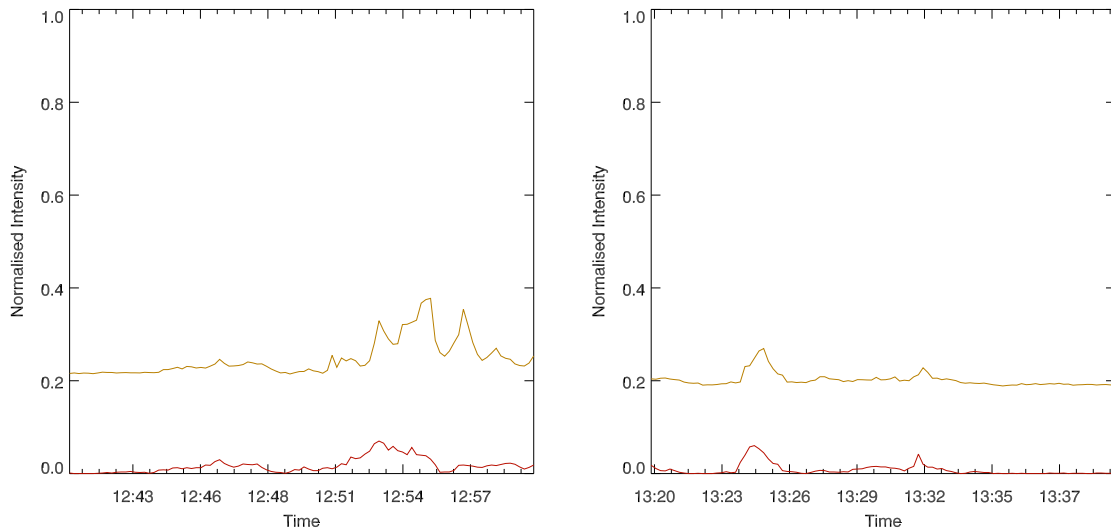
The O2 event



Using frames from 02:36UT to 05:12UT we track a second positive polarity feature (204 ± 72 G) originating from the dipole emergence related to jets J2 and J3 at position $(X, Y) = (-766'', 169'')$ that appears to cancel out with a negative flux (-232 ± 69 G) at 03:24UT. The loops are separated when this happens. Both positive and negative fluxes dissipate in the 03:36UT integrating time. Faint flaring is present in the AIA-171Å channel at 03:34UT.

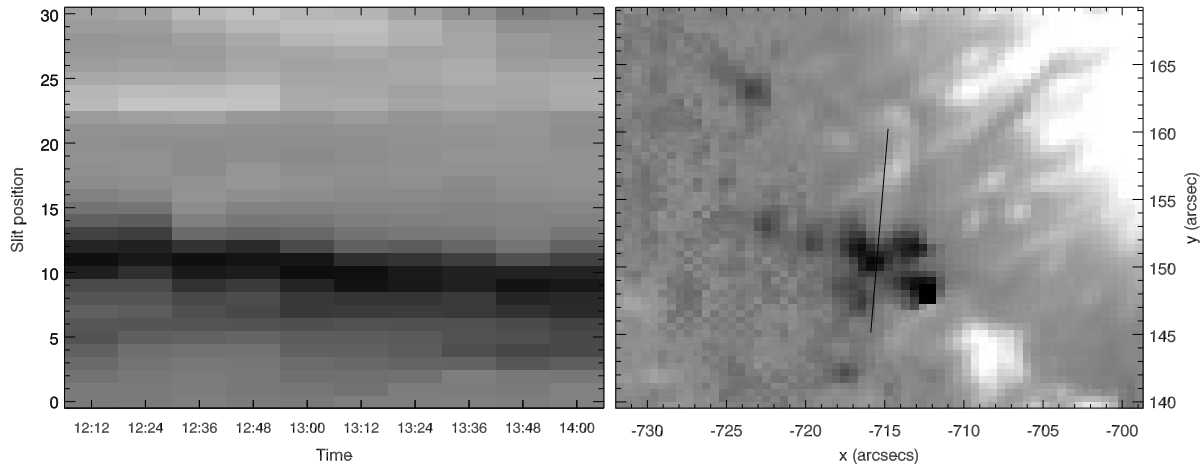


The O3a and O3b events

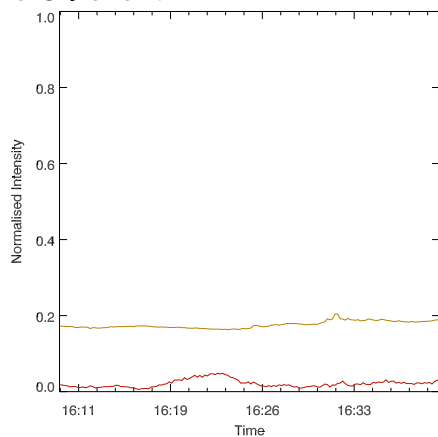


The O3 is viewed as a set of pre and post jet flaring occurring in succession: O3a between 12:50UT and 12:57UT, the main flaring of J6, and a second flaring burst at 13:24UT. The two O3 events do not generate full blown jets, though plasma "strands" are seen rising during O3a. We did not consider these jets, as they were too close to detection limits. They seem to connect at least in part to the "open" flux tubes. In the case of O3a, we track a stationary positive polarity feature (331 ± 64 G) originating at position $(X, Y) = (-716'', 155'')$ during

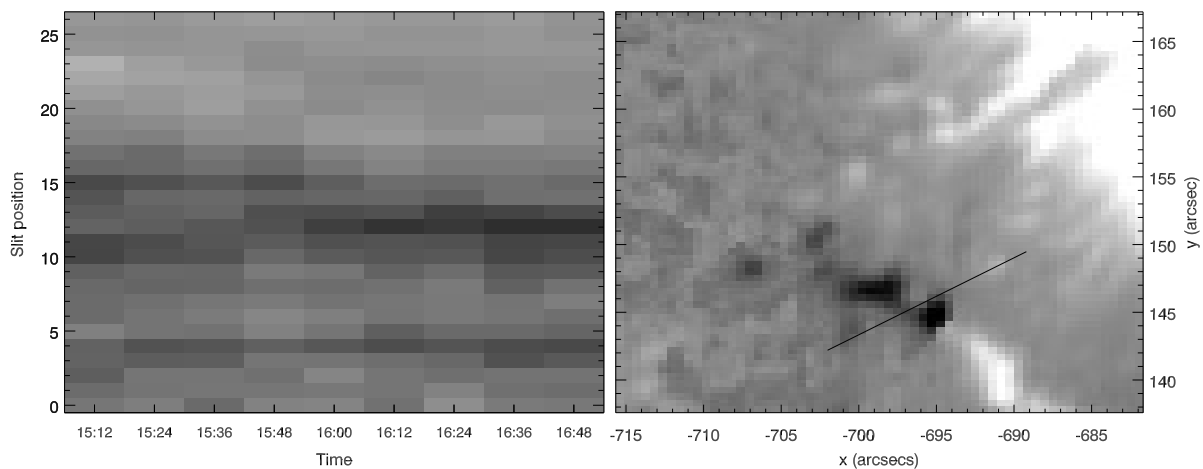
12:12UT-14:00UT. The feature keeps its close proximity to the pore group until is dissipated before the 13:00UT frame. The SDO-AIA signal is "bursty" between 12:50UT and 12:57UT. We could not detect any discernible moving features or flux emergence corresponding to the O3b event. We speculate that the small-scale flaring is a secondary result of the arrangement that triggered the J6 eruption.



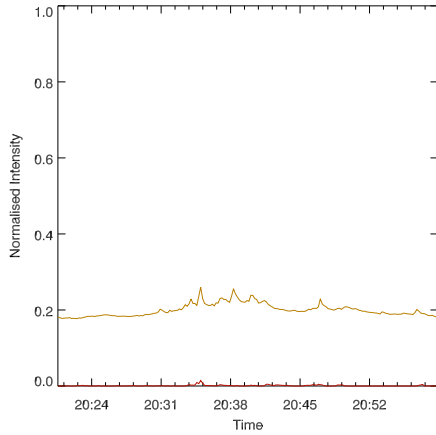
The O4 event



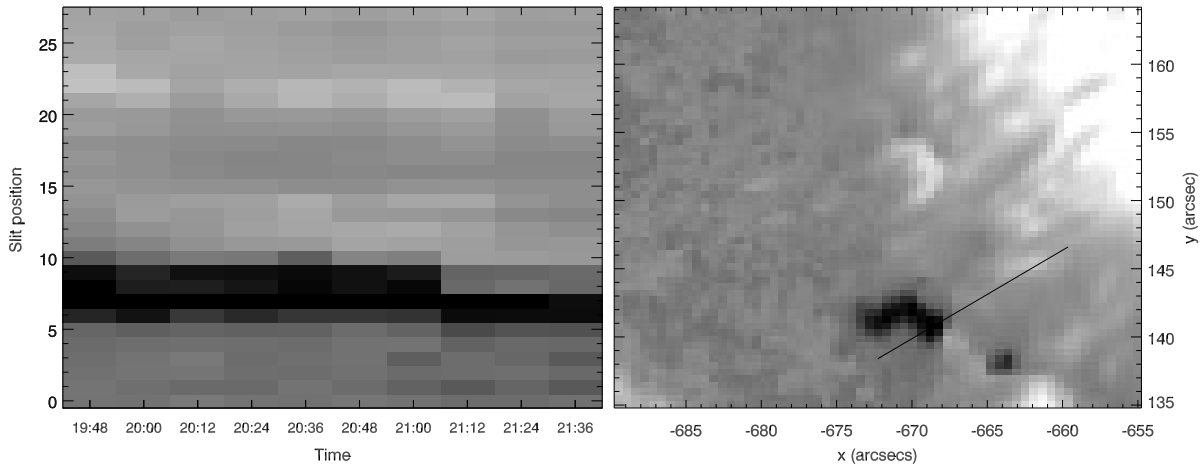
Using frames from 15:12UT to 16:48UT we track a grain positive polarity feature of 236 ± 56 G strength, originating at position $(X, Y) = (-691'', 148'')$ at 15:12UT. This feature is very faint but correlates to the flaring emission recorded by SDO-AIA. Its movement speed is $v_s = 0.6 \text{ km s}^{-1}$. This flux cancels with the now coagulated pore during the integration times of the 16:24UT-16:36UT frames. The AIA-304Å signal is not perturbed. A flaring spike can be observed just in the AIA-171Å intensity, at 16:32UT.



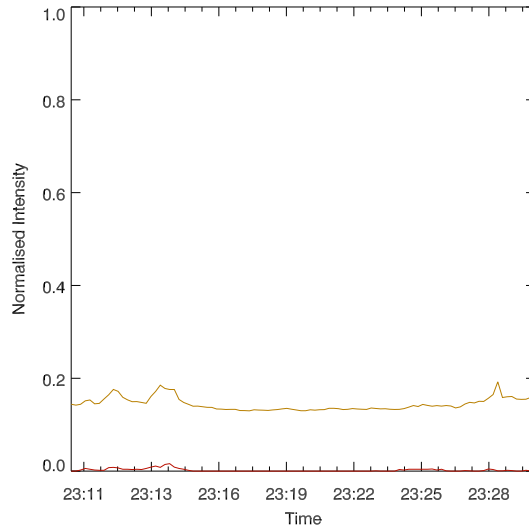
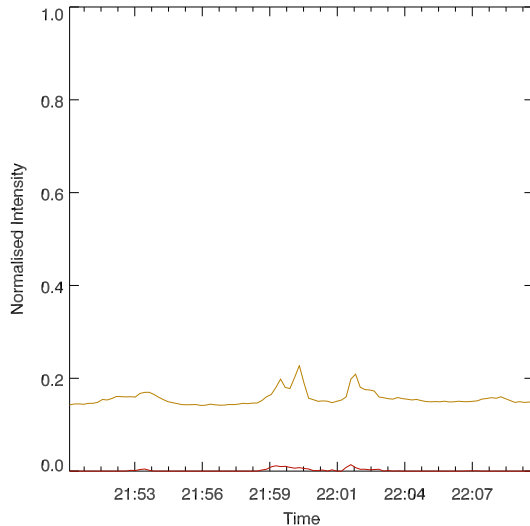
Then O5 event



We track a (possibly emerging?) positive polarity feature originating at position $(X,Y) = (-668'', 144'')$ between 19:48UT and 21:36UT. This feature suddenly appears near the negative pore group and slowly erodes up to 21:12UT frame. This feature is different than the emerging polarity correspondent to J8, being separated by about $4''$ - $5''$. There is no direct correlation to the four flaring events recorded by SDO-AIA between 20:34UT-20:47UT. Also, this flux is completely dissipated later in the 21:12UT frame, coincidental to the J8 event. We speculate that the J8 eruption also helped cancel this grain.

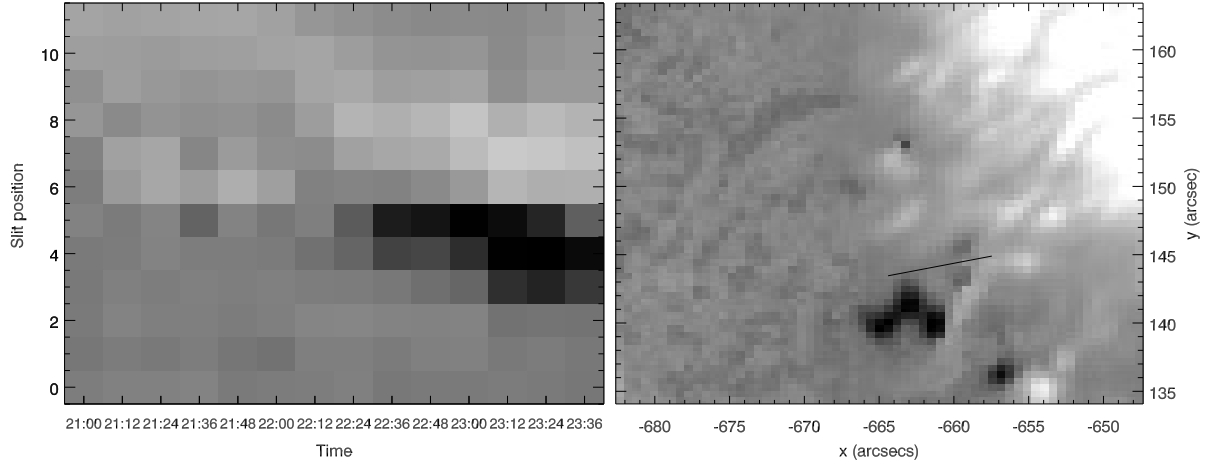


The O6 and O7 events



Using frames from 21:00UT to 23:36UT we track ubiquitous grain manifestation occurring in close proximity to the pore group. A set of self similar flaring is occurring for all five peaks that are grouped in the O6 and O7 sets. The features manifest at position $(X,Y) = (-663'', 145'')$ being spatially separated from the identified source of the J9 and J10 events. A small positive grain (147 ± 63 G) emerged around 21:12UT and

dissipated before 22:12UT possibly accounting for the SDO-AIA flaring events between 21:57UT-22:04UT (O6). The feature is replaced by a new dipole (-338 ± 56 G and 384 ± 64 G respectively) emerging at the location, separated from the stronger dipole which we correlated to J9 and J10. We can not establish more than the general temporal agreement between this emergence and the very transient flaring present in the SDO-AIA filters at 23:11UT, 23:13UT, and 23:28UT.



Acknowledgements

A chapter ends and a new story starts. I would most certainly not be today in the position of writing these thoughts if wandering alone through life. Wiser people, which reached a form of immortality, have said that their fortune is a result of standing on the shoulders of giants. I often ponder on the implications. Are there ‘giants’ that help guide the existence and day to day life of us, the normal mortals? Mithrandir found that it is the small everyday deeds of ordinary folk that keep ‘the darkness’ at bay. Small acts of kindness and love. An extraordinary amount of exceptional people have contributed more or less knowingly to my journey.

How did my journey through science all start? By the effort and dedication of truly gifted teachers whom I now see as the ‘roadsigns’ that led me on this long path. Constantina Marin, Daniela Oprescu, and Cristina Dămăcuș deserve ovations for their dedication and pursuit of their vocation, educating young adults. Additionally, Doina Călugăru and Dr. Mircea Rusu have my greatest thanks and gratitude for guiding me down this path.

To Dr. Alessandro Bemporad and Dr. Marilena Mierlă: My first steps into research occurred under your splendid guidance. True role models, I remain forever grateful to your generous supervision and mentoring during my early years. Dr. Elena Moise and Dr. Ilia Roussev deserve praise for always keeping tabs on me and for their guidance. Georgeta Mariș-Muntean and Dr. Ovidiu Teșileanu deserve a place on this list. Warm thoughts go to my good friend who was always there, Dr. Diana Ionescu! Additional thanks for pushing me to relocate to Australia and arranging my initial contact with Monash.

My PhD supervisors, Dr. Alina Donea and Prof. Paul Cally have special place in my enumeration. Two extraordinary people doing a fantastic job at Monash. They impart their knowledge and expertise, offered guidance when needed, showed me how to teach and more importantly, how to understand mathematics and physics. Their influence was fundamental in completing this work. I thank Alina for being much more than a supervisor, a kind and true friend who always endeavored to do her best by me, always going beyond what a formal relationship would require.

Dr. Phil Judge, a physicist, and one of the best! I regard him as my additional supervisor. Always going for the truth hidden under the veil of ‘doing things fast’. His view centred on always describing the physics underlying the observations hopefully has imprinted on me, and was influential in my postgraduate research. His sincere comments greatly improved the quality of this thesis. His mentoring was critical for my development.

I also recognize the very productive discussions and training that took place at CORA/NWRA and would like to thank Dr. K.D Leka and Dr. Graham Barnes for the guidance and support offered. Dr. Charles Lindsey deserves special praise for his generosity, his unending kindness, and lessons imparted.

Cheers to the fantastic support team at Monash. I thank Linda Mayer and Karen Hogeboom for all their support, help, and for putting up with me. I am truly grateful to Gertrude Nayak for all her kindness, and for the official and personal support rendered. John Chan... I have not ever seen a person quite

like him. A fantastic job, done by a genuinely compassionate human. I have not seen someone so dedicated, not just at his job, but to help postgrads reach their goal. Although not formally, his shadow influence got me to this point! Written words are insufficient to describe this person. Thank you John, for everything!

I am grateful to Dr. Felicity Holmes, a true mind healer, for managing to help me course through these last months and climb out of ‘the pit’. I thank my parents Mircea and Eliza Paraschiv for their unwavering absolute confidence in me. Nothing is possible without this!

Speaking of pits, one needs a ladder to climb out. My Ladder consisted in ordinary deeds from extraordinary people. For an orderly yet chaotic organization we will split this set into random shuffled sub-lists based on arbitrary chosen references and mean comments. We shuffle ‘the romanians’: Daniel Coman for inspiring good table manners, Adrian Panait for ‘cinste’, Măriuca Călin for not being able to do maths, and lastly (in a randomly defined set!) Dana Tălpeanu for being stubborn. ‘The Monash BBQ club’: Sarah ‘~45 dresses’ Jabbari, Jens Grimm for proving that businessmen have a soul, and the Best Darcy. The ‘mate’ pack: Damien Przybylski, bike junkie, and Calum ‘I’ll finish soon’ Robertson. On a serious note, thank you guys!

One saves the best things for last, right? Daniela Lăcătuș for always being there, besides me. One of the smartest persons I’ve ever met, my first and foremost support, partner to good and bad times, completing my core. You are precious to me. I couldn’t have done it without you!

The ‘Giants’ are everywhere, in all sizes shapes and experiences. One just needs to open his eyes. I am thankful and humbled to have discovered so many!

Special thanks go to HAO/NCAR and NWRA institutes in Colorado for providing the support enabling me to pursue my research interests during the two visits to Boulder undertaken during my postgraduate study.

I acknowledge the outstanding support from the School of Mathematical Sciences, Monash University. This research was supported by an Australian Government Research Training Program (RTP) Scholarship.

Raw data and calibration instructions are obtained courtesy of NASA/SDO-AIA, SDO-HMI, Hinode, STEREO-EUVI and STEREO-SWAVES, WIND-WAVES, IRIS, and RHESSI science teams. I welcome and appreciate the open data policy of the SDO, IRIS, WIND and STEREO missions.

List of Figures

- i.1 Schematic depiction of the observational features of the solar atmosphere. The principal solar atmospheric layers, the Photosphere, Chromosphere, Transition Region, and Corona are illustrated along with their associated main plasma temperatures and solar atmospheric structures. 3
- i.2 Solar atmospheric density and temperature distributions plotted against radial heliospheric height. The main heliospheric layers are: The Photosphere(1); Chromosphere(2); Transition Region(3); Corona and inner heliosphere(4). A very sharp increase in temperature can be observed manifesting in the very narrow (~ 500 km) Transition Region. This manifestation constitutes the coronal heating problem. The graphs correspond to an enhanced network atmosphere, e.g. above a small scale pore, obtained via the Fontenla et al. [2011] models, using chromospheric (Model Index 1003) and coronal (Model Index 1013) boundary values. 5
- i.3 Running-difference map of the emission measure recovered via the Hannah and Kontar [2012] regularized inversion. The emission is integrated across the $\log(T_e) = [5.70, 7.14]$ portraying a coronal jet eruption (13:08UT), associated to the AR11302 recurrent jet ‘geyser-like’ site. Multiple such sites were discovered in the literature, see table 2.1). Simultaneous ‘strand’ eruption components are observed along the jet’s body. 8
- i.4 Model of the coronal magnetic field extrapolated under the force-free potential field assumption (see eq. (4.7)). Base layer represents the vertical B_z component of the magnetic field, scaled in the $[-1000 \text{ G}, 1000 \text{ G}]$ interval and computed at 01:36UT on 25 September 2011. Two low lying loops are conspicuous under a penumbral canopy field of the active region, that is extending to the outer heliosphere. 10
- 1.1 Coronal jets (**Upper panel:** J6, 13:09UT 25.09.2011, **Bottom panel:** J2, 01:13:09UT 25.09.2011) as revealed by multiple observations. The individual multiwavelength portrayals of all J1 to J10 jets are presented in appendix A. The figure sub-panels represent different correlated manifestations of jet activity: (a) SDO AIA-171Å ($T \sim 0.8 - 1 \text{ MK}$) and timeseries tracked slit (S1) position; (b) AIA-94Å ($T \sim 5 - 8 \text{ MK}$); (c) AIA-1600Å ($T \sim 0.4 \text{ MK} + \text{continuum}$); (d) AIA-304Å ($T \sim 0.5 \text{ MK}$) and timeseries tracked region (B1) position; (e) SDO HMI intensity continuum with added AIA-304Å (red) and AIA-94Å (blue) contours, (f) HMI SHARP (active region patch) vertical B_z magnetogram with added AIA-304Å (red) and AIA-94Å (blue) contours; (g) BBSO H α ; (h) STEREO-B EUVI-195Å ($T \sim 1 - 2 \text{ MK}$) different viewpoint observation. Filtergram temperatures are provided here for comparison and are only approximate. A full DEM analysis is required in order to recover plasma physical temperatures. An emission measure estimation is available in chapter 3. 14
- 1.2 Geyser structure full-day region tracking: **Upper panel:** S1 slit (fig. 1.1 a) based tracking along the jet eruptions direction as applied to the AIA-171Å data. **Bottom panel:** The B1 (fig. 1.1 d) $13'' \times 17''$ region centered around the Geyser flaring footpoint (jet bright-point) using SDO’s AIA-171Å, AIA-304Å, and STEREO-B EUVI-195Å filters. Two datagaps are present in the AIA series at 06:03-07:12 and 21:00-21:02, and in the STEREO-B series at 19:00-19:10. Individual jet events are labeled J1-J10 and other peculiar geyser flaring, that do not exhibit any distinguishable jet emission are labeled O1-O7. Major AR11302 flaring events that can potentially interact with the B1 integrating region are illustrated. 16

1.3	The Geyser coronal jet J5 eruption is interpreted via a slit-jaw method. A slit system comprising six slits was developed and utilized. A narrow parallel slit (S6) together with five, also narrow, perpendicular slits (S1 to S5) were calculated manually and fitted over the AIA-171Å (upper panel) and AIA-94Å (bottom panel) filtergrams (AIA-304Å in appendix B). The S6 slit is traced along the jet's axis and is stretched to depict both the jet's erupting outflow and the footpoint flaring. The S1-S5 evenly spaced slits are positioned perpendicular to the jet's outflow direction. The S1 slit is close to the geyser site, crossing over the lower flaring footpoint. All jets outflow speeds and eruption morphologies presented in table 1.1 were deduced from analyzing the plasma traversing the slit system. The individual slit based determinations of all J1 to J10 jets are presented in appendix B.	19
1.4	The geyser coronal jet J5 subjected to a slit based feature tracking procedure. Upper Panel: A perpendicular narrow slit is temporally tracking the movement of one of the jet's leading edge strands. Bottom Panel: The selected strand propagation in time as revealed by the AIA-171Å and AIA-304Å filtergrams. A clear helical movement of $\sim 2\pi$ is observed before the jet dissipated in the fluxtube.	21
1.5	Intensity data from the SDO-AIA instrument on the SDO spacecraft are shown as a function of heliographic solar X and solar Y coordinates. The field of view spans part of active region 11890 on 2013 November 9 th . The data highlight the chromospheric and coronal environment surrounding the flare ribbon under examination. Upper/lower panels show data prior to/during ribbon brightening, respectively. In SDO-AIA data, the ribbon is seen most clearly in the 304 Å band (predominantly He II), and marginally in the 1600Å band (a mix of transition region lines and chromospheric continuum emission). Our study is originally prompted by the absence of 'moss' emission in AIA-171Å overlying the ribbon, which is outlined by the two white lines. Typical moss emission is seen all around the ribbon in the bright patches of network plage emission, for example at $(X, Y) = (170, 190)$, associated with strong LOS magnetic fields. (see fig. 1.7).	24
1.6	Intensity data are shown for active region 11890 on 2013 November 9th, corresponding to two modest flaring events associated to ribbon D. Upper panels show the weaker 12:07 flare ribbon analysed by Testa et al. [2014]. Lower panels show the stronger flaring peaking at 12:15. All panels have been co-aligned by eye to approximately 0''.3. The solar coordinates are referred to the coordinate system specified in the headers. Only a 30'' × 35'' field of view is shown, to highlight the precise position of the flare ribbon traced in all panels except for the slit-jaw IRIS panels.	25
1.7	Magnetic data are shown for active region 11890, before, during, and after the two flares at 12:07 (ribbon extent traced with a white line) and 12:15 (black line) shown in fig. 1.6. Each row shows longitudinal, tangential fields, un-dissambiguated field azimuth, and the continuum intensity. The upper panels show the Hinode scan obtained before the flares, the middle panels show HMI data closest to the flaring events, and the lower panels show Hinode data from the next complete scan some six hours later. Six hours is a considerable fraction of the lifetimes of supergranules, so surface field evolution has occurred between the two Hinode scans.	26
2.1	Schematic illustration of observational jet eruption features along with the associated upwards and downwards electron beams. The upwards beam propagation into the heliosphere is characterized using the observational properties of generated Type-III radio bursts. The cartoon is consistent with the widely accepted flare scenario based on magnetic reconnection, referred to as the CSHKP[Carmichael, 1964, Sturrock, 1966, Hirayama, 1974, Kopp and Pneuman, 1976] standard flare model that now also includes potential particle acceleration mechanisms [see review; Shibata and Magara, 2011].	32
2.2	Dynamic spectra of the solar radio emission as viewed from the STEREO-B SWAVES, STEREO-A SWAVES, and WIND WAVES perspectives. The relative satellite positions are shown in the upper right corner. The E (earth) position corresponds to the position of WIND and SDO. The active region appears on the western side of STEREO-B's visible disk and were detected by EUVI's SWAVES instrument. The jet events were temporally positively correlated with both the WIND and STEREO-B data, although a fraction of the jets were missed by WIND. The site was not visible from the STEREO-A viewpoint. Plots are reproduced from the NASA-GSFC swaves service. 34	

2.3	Temporal tracking of the regions centered on the studied geyser structures using SDO's AIA-171Å(yellow), AIA-304Å(red), STEREO-B SWAVES (blue), STEREO-A SWAVES (pink) and WIND WAVES (green) data. The individual jets are labelled incrementally for each referenced dataset. The x-axis (time) is not normalised across the datasets. The temporal range for each site is arbitrarily set to be analogous to the original studies. Uncorrelated events labels along with very faint or expected events which we could identify are marked (red). Uncertain events are also highlighted (purple). The radio data is slightly moved up on the y-axis in order to increase plot readability. Additional information on the six datasets can be found in Table 2.1.	36
2.4	Observational and analytical interpretation of the recorded time delay between the SDO-AIA microflaring jet onset events and the correlated interplanetary Type-III radio bursts. Left Panel: Time delay between the peak/onset SDO-AIA171Å flaring of the Geyser structure versus the associated subsequent Type-III bursts. The distribution is Gaussian fitted with its peak corresponding to the 72 s delay and a $\sigma = 27$ uncertainty. Events ≤ 24 s and ≥ 120 s are marked as uncertain in fig. 2.3. Right Panel: Type-III Burst drift parameters as depicted from a number density viewpoint (black) and first harmonic frequency (red) as a function of the radial distance from the chromosphere via eq. (2.6) or eq. (2.7). Units are normed solar radii. The 16 MHz or $7.93 \cdot 10^5 \text{ cm}^{-3}$ start corresponds to a heliospheric height of $2.73 R_{\odot}$ and the low boundary 3 MHz or $2.87 \cdot 10^4 \text{ cm}^{-3}$ signal corresponds to radial distance of $8.10 R_{\odot}$.	40
3.1	Total Intensity timeseries of the six utilized SDO-AIA filters, temporally centered around the three eruptions. Pixel intensity was averaged inside the individual footpoint borders, illustrated by the contour of the AIA-131Å sub-panel of fig. 3.2. The upper panel corresponds to the temporally close J2 and J3 events while the bottom panel corresponds to the J6 jet event.	54
3.2	Observational features of the footpoint structures during the main phase corresponding to the J2, J3, and J6 events. The Coronal Geyser is revealed in each SDO filtergram, DEM inversion, and peak temperature maps around maximum flaring times: 01:13:00UT for J2 (Upper), 01:19:00UT for J3 (Middle), and 13:08:24UT for J6 (Bottom) respectively. Each of the depicted AIA filters exhibits a unique morphology, where the AIA-131Å and AIA-94Å filters are the closest to resembling the DEM emission maps. The contours correspondent to the AIA-131Å sub-panels represent the distinct borders of the observed flaring footpoints, at peak emission time and corresponding to each event. The total EM maps are plotted inside the $[5 \cdot 10^{27}, 5 \cdot 10^{28}]$ interval and the A2013 T_e map is plotted inside the $\log T_e = [5.7, 7.0]$ K interval	56
3.3	SDO-AIA A2013 χ^2 inversion uncertainty distributions inside the selected jet emitting region. Upper Panel: Histograms of χ^2 fit goodness for quiet (background) conditions as compared to peak flaring time. Bottom Panel: Histograms of the temperature widths σ_{T_e} comparing quiet sun and peak flaring conditions. The distributions are comprised from the individual fitting results of the pixels corresponding to the footpoint area and across the temporal domain corresponding to flaring and quiet sun conditions. The H2012 χ^2 results exhibit an analogous behavior.	58
3.4	SDO-AIA EM results corresponding to the three analyzed flaring events of the geyser footpoints recovered via the three alternative inversion approaches. Values are averaged across the footpoint areas. Upper Panel: Total average emission measure over the dominant $T_e \pm \sigma_{T_e}$ range for A2013, and across the $\log T_e \sim [5.7, 7.3]$ temperature space recovered from the H2012 and C2015 inversion methods. A general agreement occurs between the different approaches, though small systematic differences can be seen manifesting. Bottom Panel: Temporally averaged emission measure plotted against the electron T_e bins for the selected temporal subsets of quiet and flaring plasma conditions via H2012 and C2015 inversions. The different events exhibit their unique emission temperature distributions.	59
3.5	Timeseries set depicting the A2013, H2012, and C2015 inversions of the main jet emission in selected regions. Both the region averaged EM and A2013 T_e estimations are depicted for the two datasets containing the three events. The plotted temperature range is constrained in order to depict the co-temporal variation of the two quantities, although the absolute temperature variations are modest. No T_e averages have been provided for the C2015 and H2012 inversions as no unique temperature was found at one timeframe.	62
3.6	The J2, J3, and J6 EM profiles across the temperature space as derived from the H2012 and C2015 inversions. Erupting material is plotted against the quieter background selected for each individual event. Data was re-binned in the same intervals in order to better compare the EM profiles.	63

3.7	The H2012 inversion emission measure maps correspondent to the erupting jets material and unique geyser footpoint presented for the J2 (upper), J3 (middle), and J6 (bottom) events. The EM profiles are mapped across the selected T_e bins of approximately 0.3 in logarithmic size revealing different strands (spires) manifesting in different temperature ranges and spatial locations in all three cases.	64
3.8	The C2015 inversion emission measure maps correspondent to the erupting jets material and unique geyser footpoint presented for the J2 (upper), J3 (middle), and J6 (bottom) events. The EM profiles are mapped across the selected T_e bins revealing different strands (spires) manifesting in different temperature ranges and spatial locations in all three cases.	65
3.9	RHESSI X-Ray emission over-plotted on three of the jet eruptions (the J2-01:13UT, J3-01:19UT, and J6-13:08UT events). Contours represent the soft (magenta) 6 – 12 KeV and hard (black) 12 – 25 KeV energy channels. The contours represent the normalized [0.3, 0.5, 0.7, 0.9] levels. The EM maps were recovered via the C2015 method, and depict the onset times of the jet eruptions which are closest to maximum peaks in the RHESSI flux data.	68
3.10	RHESSI X-Ray emission spectrum correspondent to the J2, J3, and J6 jet eruptions. Left Panels: Timeseries plots of the total X-Ray count rates for the 6 – 12 KeV, 12 – 25 KeV, and 25 – 50 KeV channels. Right Panels: Thermal and non-thermal plasma emission models fitted on the spectral distribution in the 1 KeV to 250 KeV range. No discernible emission could be recovered in the 25–50 KeV and higher channels. We focus on the results at energies < 30 KeV. The spectra was averaged over short timescales correspondent to peaks in the photon flux timeseries of the 12 – 25 KeV band.	70
4.1	Line of sight projected (image) to solar-tangential (true) coordinate transform using the eq. (4.3) transformation matrices of Gary and Hagyard [1990]. The two possible vector component combinations that can reproduce the same scalar total field strength B are represented assuming the unresolved 180° ambiguous data. The 180° ambiguity does propagate when translating to the solar referential system.	84
4.2	Estimation of magnetic field detection limits and the pixel uncertainties of SHARP region 892 (AR11302) for a two hour interval between 00:00UT and 02:00UT on 25.09.2011. We evaluate these uncertainties assuming that these are the higher limit of errors resulted from projection, as the AR is moving towards a disk central position. Left Panel: Histogram of the transversal fields (B_t) noise values close to the geyser region of interest. The purely statistical standard deviation σ_s along with the Gaussian fitted standard deviation σ_G are calculated. Right Panel: Example (01:24UT) of a confidence map for the photospheric geyser region. The relative uncertainty of the heliospheric vertical magnetic fields (B_z) is computed using the eq. (4.4) validation criterion. The contours represent fields of strength [± 200 G, ± 500 G, ± 800 G] of positive (white) and negative (black) polarity and the black patches represent uncertain areas.	86
4.3	Comparison between the JSOC (right panel) and our Custom (left panel) disambiguation maps. The figure depicts the heliographic vertical B_z component, plotted in a ± 800 G range where the left-right differences manifest due to the azimuthal ϕ field component. A zoom-in of the boxed area representing the geyser region is included in the bottom-right corners of each plot. For example, when analyzing the temporal behavior of these features, it was observed that a southern pore experienced false polarity shifts in the standard SDO-HMI data products. The feature was stabilized to a true negative polarity for all its visible lifetime by the custom disambiguation. Also, ‘artifacts’ present in the geyser region (see red arrows) were mitigated by the slower annealing in our setup. In this instance (00:48UT), such ‘artifacts’ can be observed on the JSOC AR lightbridge at $(X, Y) = (-710'', 145'')$ and also in the zoomed-in area.	89
4.4	Magnetic configuration of the vertical component B_z of photospheric fields depicted prior to each individual jet eruption. Contours at ± 160 G, ± 800 G, ± 1500 G levels, for positive(red) and negative(green) fluxes are shown in order to enhance visibility of small grains, emerging fields, and potential inversion lines related to jet activity.	90

4.5	Timeseries of of the vertical component B_z of photospheric fields in between 01:00UT and 02:24UT, covering the timespan of J2, J3, and J4 events. Contours at $\pm 160G$, $\pm 800G$, $\pm > 900G$ levels, for positive (red) and negative (green) fluxes are depicted. A region where a dipole flux emergence is developing during this period is shown by the two blue arrows that correspond to the emerging footpoints. The first vertical fields appear in close temporal and perfect spatial proximity with the J2-J3 events. The turquoise arrow is pointing to a region where a positive grain that is traveling outwards from the penumbra interacts with a small negative flux at the border of the pore, canceling out during a time frame in which the J4 event is seen erupting in the higher EUV atmosphere.	91
4.6	A slit based temporal tracking of photospheric grain magnetic moving features. Left Panel: Slit time-distance diagram tracking of B_z at the position of the slit included in the right image. The positive magnetic grain moves towards SE with a surface speed of $v_s = 0.6 \text{ km s}^{-1}$. The feature cancels with the negative pore group around the integration time of 02:12UT, while the SDO-AIA flaring starts at 02:14UT. Right Panel: Geyser location area as represented by the vertical field component B_z , plotted at 00:00UT. The slit is positioned along the direction of motion of the positive magnetic grain and is temporally tracked to account for solar rotation. .	92
4.7	A slit based temporal tracking of photospheric small scale vertical flux emergence is presented. Left Panel: Slit time-distance diagram tracking the emergent dipole using the B_z magnetogram. The dipole emergence (01:12UT-01:24UT) is co-temporal with the J2 and J3 events where the SDO-AIA flaring starts at 01:13UT and 01:19UT. Right Panel: The vertical magnetic field component B_z at 00:36UT. The slit follows the direction of the future dipole emergence and it tracked in order to account for the solar rotation.	94
4.8	Model of the coronal magnetic field extrapolated under the force-free potential field assumption (see eq. (4.7)). Base layer represents the vertical B_z component of the magnetic field, scaled in the $[-800 \text{ G}, 800 \text{ G}]$ interval and computed at 01:24UT on 25 September 2011. In potential conditions, the magnetic canopy becomes ‘open’ to the heliosphere at heights above 2.3 Mm. . .	97
4.9	A timeseries 01:00UT - 02:24UT of geyser non-potential electrical current and force-free parameters that are derived from the HMI-SHARP observations. The heliospheric vertical currents J_z are presented in Upper Panel . The force-free α parameter is mapped in the Bottom Panel . The two maps are calculated utilizing the eq. (4.9) formulations. The structure positions are tracked in time. We have fixed the heliospheric coordinates corresponding to the 01:00UT frame for clear location reference. The $(X, Y) = (-770'', 152'')$ structure is not part of the geyser footpoint which is rooted between $(X_1 : X_2, Y_1 : Y_2) = (-780'' : -765'', 162'' : 175'')$. See fig. 3.2 (upper and middle panels) which depict the analogous EUV imaging during flaring peaks.	98
4.10	Timeseries evolution of the vertical current J_z and the force-free α parameter. The parameters are averaged over a $4'' \times 5''$ area centered at position: $(X, Y) \sim (-770'', 165'')$, between 01:00UT and 02:36UT. The location corresponds to the photospheric footpoints of the discussed PIL.	99
4.11	Linear field extrapolations that reproduce the observational features of the AR11302 geyser. The base layer represents the vertical magnetic field B_z plotted in $\pm 800 \text{ G}$ range. The panels reproduce HMI observing times of 01:00UT, 01:12UT and 01:24UT during which the J2 and J3 eruptions occurred. The view direction is sketched in the lower right corner of each plot. Left Panel: Top view of the reconstructed components using unique α parameter configurations for each substructure. This illustration appears compatible to the observed EUV flaring (fig. 3.2). Right Panel: Side view of the PIL linearly extrapolated using a combination of α values ($\pm 0.03 < \alpha < 0.16$) as revealed by the fig. 4.9.	100

List of Tables

1.1	Basic morphological estimates of the observed geyser jets. Individual jet scale lengths and outflow propagation speeds are derived from the slit-jaw analysis of the SDO AIA-304Å and AIA-171Å filtergrams. The eruptions are assumed to be perpendicular to the line of sight. The length of the jets was estimated as the maximum outward extent of the jet spire during the eruptive phase. The estimated flow speed is projected along the line of sight, thus it is assumed to be an underestimate of the natural outflow speed. The n/a positions denote events for which the respective measurement could not be applied.	22
2.1	Jet datasets collected from different literature studies. Radio data sources are STEREO-A (S-A), STEREO-B (S-B), and Wind (W). The detected jets column lists the events that were observed by the corresponding studies. All correlated events were checked for statistical relevance against background radio counts. Not all events described in the G4 and G6 datasets could be distinctively separated from the SDO-AIA background. The established temporal correlations are described in section 2.2. Uncertain events are listed inside brackets. The three data sources occupy unique positions for each dataset, enabling both positive (1) and negative (2) correlations to be discussed via individual source position.	38
3.1	J2, J3, and J6 footpoint plasma density [$n_e \cdot 10^{11} \text{ cm}^{-3}$] for all possible SDO-AIA filter pair combinations derived via the filter ratio formulations described in section 3.2.2. The determinations are performed for the two distinct emitting temperature regimes of $\log T_e \sim 7.0$ and $\log T_e \sim 6.3$. The method proved invalid as the filter ratio results are inconsistent across the SDO-AIA filtergram ratios.	57
3.2	Jet and Geyser footpoint morphological parameters as derived from the SDO AIA-304Å, SDO AIA-171Å, SDO AIA-94Å, and AIA-131Å filters. The plasma physical and energetic parameters are derived via the Aschwanden [2013], Hannah and Kontar [2012] and Cheung et al. [2015a] inversion approaches, taking into account the morphological parameters, geometrical approximations, and the particular assumptions and limitations of the models.	66
4.1	The stable AMBIG-ME0 disambiguation model parameters presented as a comparison in between the standard JSOC pipeline disambiguation and the custom implementation. The used parameters relate to: detection limits (atresh and btresh), the number of pixel flips at each iteration (neq), the weighting between the divergence and current terms in the minimization functional(lambda), and the simulated annealing initial start and cooling factor (tfac0 and tfactr).	88

Bibliography

- C. E. Alissandrakis. On the computation of constant alpha force-free magnetic field. *Astron. Astrophys.*, 100: 197–200, July 1981.
- L. S. Anderson and R. G. Athay. Model solar chromosphere with prescribed heating. *Astrophys. J.*, 346: 1010–1018, November 1989. doi: 10.1086/168083.
- V. Archontis and A. W. Hood. A Numerical Model of Standard to Blowout Jets. *Astrophys. J. lett.*, 769:L21, June 2013. doi: 10.1088/2041-8205/769/2/L21.
- V. Archontis, K. Tsinganos, and C. Gontikakis. Recurrent solar jets in active regions. *Astron. Astrophys.*, 512: L2, March 2010. doi: 10.1051/0004-6361/200913752.
- M. J. Aschwanden. *Physics of the Solar Corona. An Introduction with Problems and Solutions (2nd edition)*. Pour la Science, December 2005.
- M. J. Aschwanden. A Nonlinear Force-Free Magnetic Field Approximation Suitable for Fast Forward-Fitting to Coronal Loops. I. Theory. *Solar Phys.*, 287:323–344, October 2013. doi: 10.1007/s11207-012-0069-7.
- M. J. Aschwanden and P. Boerner. Solar Corona Loop Studies with the Atmospheric Imaging Assembly. I. Cross-sectional Temperature Structure. *Astrophys. J.*, 732:81, May 2011. doi: 10.1088/0004-637X/732/2/81.
- M. J. Aschwanden, P. Boerner, C. J. Schrijver, and A. Malanushenko. Automated Temperature and Emission Measure Analysis of Coronal Loops and Active Regions Observed with the Atmospheric Imaging Assembly on the Solar Dynamics Observatory (SDO/AIA). *Solar Phys.*, 283:5–30, March 2013. doi: 10.1007/s11207-011-9876-5.
- M. J. Aschwanden, P. Boerner, A. Caspi, J. M. McTiernan, D. Ryan, and H. Warren. Benchmark Test of Differential Emission Measure Codes and Multi-thermal Energies in Solar Active Regions. *Solar Phys.*, 290: 2733–2763, October 2015. doi: 10.1007/s11207-015-0790-0.
- H. D. Babcock. The Sun's Polar Magnetic Field. *Astrophys. J.*, 130:364, September 1959. doi: 10.1086/146726.
- H. W. Babcock and H. D. Babcock. Mapping the Magnetic Fields of the Sun. *Pub. Astron. Soc. Pac.*, 64:282, December 1952. doi: 10.1086/126495.
- T. E. Berger, M. G. Löfdahl, R. A. Shine, and A. M. Title. Measurements of Solar Magnetic Element Dispersal. *Astrophys. J.*, 506:439–449, October 1998. doi: 10.1086/306228.
- L. Bharti, S. K. Solanki, and J. Hirzberger. Lambda-shaped jets from a penumbral intrusion into a sunspot umbra: a possibility for magnetic reconnection. *Astron. Astrophys.*, 597:A127, January 2017. doi: 10.1051/0004-6361/201629656.
- A. Bhattacharjee, Y.-M. Huang, H. Yang, and B. Rogers. Fast reconnection in high-Lundquist-number plasmas due to the plasmoid Instability. *Physics of Plasmas*, 16(11):112102, November 2009. doi: 10.1063/1.3264103.
- M. G. Bobra, X. Sun, J. T. Hoeksema, M. Turmon, Y. Liu, K. Hayashi, G. Barnes, and K. D. Leka. The helioseismic and magnetic imager (hmi) vector magnetic field pipeline: Sharps – space-weather hmi active region patches. *Solar Physics*, 289(9):3549–3578, Sep 2014. doi: 10.1007/s11207-014-0529-3. URL <https://doi.org/10.1007/s11207-014-0529-3>.
- J.-L. Bougeret, M. L. Kaiser, P. J. Kellogg, R. Manning, K. Goetz, S. J. Monson, N. Monge, L. Friel, C. A. Meetre, C. Perche, L. Sitruk, and S. Hoang. Waves: The Radio and Plasma Wave Investigation on the Wind Spacecraft. *Space Sci. Rev.*, 71:231–263, February 1995. doi: 10.1007/BF00751331.
- J. L. Bougeret, K. Goetz, M. L. Kaiser, S. D. Bale, P. J. Kellogg, M. Maksimovic, N. Monge, S. J. Monson, P. L. Astier, S. Davy, M. Dekkali, J. J. Hinze, R. E. Manning, E. Aguilar-Rodriguez, X. Bonnin, C. Briand, I. H. Cairns, C. A. Cattell, B. Cecconi, J. Eastwood, R. E. Ergun, J. Fainberg, S. Hoang, K. E. J. Huttunen, S. Krucker, A. Lecacheux, R. J. MacDowall, W. Macher, A. Mangeney, C. A. Meetre, X. Moussas, Q. N. Nguyen, T. H. Oswald, M. Pulupa, M. J. Reiner, P. A. Robinson, H. Rucker, C. Salem, O. Santolik, J. M. Silvis, R. Ullrich, P. Zarka, and I. Zouganelis. S/WAVES: The Radio and Plasma Wave Investigation on the STEREO Mission. *Space Sci. Rev.*, 136:487–528, April 2008. doi: 10.1007/s11214-007-9298-8.

- J. C. Brown. The Deduction of Energy Spectra of Non-Thermal Electrons in Flares from the Observed Dynamic Spectra of Hard X-Ray Bursts. *Solar Phys.*, 18:489–502, July 1971. doi: 10.1007/BF00149070.
- G. E. Brueckner, R. A. Howard, M. J. Koomen, C. M. Korendyke, D. J. Michels, J. D. Moses, D. G. Socker, K. P. Dere, P. L. Lamy, A. Llebaria, M. V. Bout, R. Schwenn, G. M. Simnett, D. K. Bedford, and C. J. Eyles. The Large Angle Spectroscopic Coronagraph (LASCO). *Solar Phys.*, 162:357–402, December 1995. doi: 10.1007/BF00733434.
- I. H. Cairns, V. V. Lobzin, A. Donea, S. J. Tingay, P. I. McCauley, D. Oberoi, R. T. Duffin, M. J. Reiner, N. Hurley-Walker, N. A. Kudryavtseva, D. B. Melrose, J. C. Harding, G. Bernardi, J. D. Bowman, R. J. Cappallo, B. E. Corey, A. Deshpande, D. Emrich, R. Goeke, B. J. Hazelton, M. Johnston-Hollitt, D. L. Kaplan, J. C. Kasper, E. Kratzenberg, C. J. Lonsdale, M. J. Lynch, S. R. McWhirter, D. A. Mitchell, M. F. Morales, E. Morgan, S. M. Ord, T. Prabu, A. Roshii, N. Udaya Shankar, K. S. Srivani, R. Subrahmanyam, R. B. Wayth, M. Waterson, R. L. Webster, A. R. Whitney, A. Williams, and C. L. Williams. Low altitude solar magnetic reconnection, type iii solar radio bursts, and x-ray emissions. *Scientific Reports*, 8(1):1676, 2018. doi: 10.1038/s41598-018-19195-3. URL <https://doi.org/10.1038/s41598-018-19195-3>.
- P. S. Cally. Alfvén waves in the structured solar corona. *Mon. Not. Roy. Astron. Soc.*, 466:413–424, April 2017. doi: 10.1093/mnras/stw3215.
- E. J. Candes and T. Tao. Near-optimal signal recovery from random projections: Universal encoding strategies? *IEEE Transactions on Information Theory*, 52(12):5406–5425, Dec 2006. ISSN 0018-9448. doi: 10.1109/TIT.2006.885507.
- Emmanuel Candes and Terence Tao. The dantzig selector: Statistical estimation when p is much larger than n. *Ann. Statist.*, 35(6):2313–2351, 12 2007. doi: 10.1214/009053606000001523. URL <https://doi.org/10.1214/009053606000001523>.
- R. C. Canfield, J.-F. de La Beaujardiere, Y. Fan, K. D. Leka, A. N. McClymont, T. R. Metcalf, D. L. Mickey, J.-P. Wuelser, and B. W. Lites. The morphology of flare phenomena, magnetic fields, and electric currents in active regions. I - Introduction and methods. *Astrophys. J.*, 411:362–369, July 1993. doi: 10.1086/172836.
- R. C. Canfield, K. P. Reardon, K. D. Leka, K. Shibata, T. Yokoyama, and M. Shimojo. H α Surges and X-Ray Jets in AR 7260. *Astrophys. J.*, 464:1016, June 1996. doi: 10.1086/177389.
- H. Carmichael. A Process for Flares. *NASA Special Publication*, 50:451, 1964.
- G. Cauzzi, K. P. Reardon, H. Uitenbroek, F. Cavallini, A. Falchi, R. Falciani, K. Janssen, T. Rimmele, A. Vecchio, and F. Wöger. The solar chromosphere at high resolution with IBIS. I. New insights from the Ca II 854.2 nm line. *Astron. Astrophys.*, 480:515–526, March 2008. doi: 10.1051/0004-6361/20078642.
- R. Centeno, J. Schou, K. Hayashi, A. Norton, J. T. Hoeksema, Y. Liu, K. D. Leka, and G. Barnes. The Helioseismic and Magnetic Imager (HMI) Vector Magnetic Field Pipeline: Optimization of the Spectral Line Inversion Code. *Solar Phys.*, 289:3531–3547, September 2014. doi: 10.1007/s11207-014-0497-7.
- J. Chae, J. Qiu, H. Wang, and P. R. Goode. Extreme-Ultraviolet Jets and H α Surges in Solar Microflares. *Astrophys. J. Lett.*, 513:L75–L78, March 1999. doi: 10.1086/311910.
- R. Chandra, G. R. Gupta, S. Mulay, and D. Tripathi. Sunspot waves and triggering of homologous active region jets. *Mon. Not. Roy. Astron. Soc.*, 446:3741–3748, February 2015. doi: 10.1093/mnras/stu2305.
- K. Chandrashekar, A. Bemporad, D. Banerjee, G. R. Gupta, and L. Teriaca. Characteristics of polar coronal hole jets. *Astron. Astrophys.*, 561:A104, January 2014. doi: 10.1051/0004-6361/201321213.
- H.-D. Chen, J. Zhang, and S.-L. Ma. The kinematics of an untwisting solar jet in a polar coronal hole observed by SDO/AIA. *Research in Astronomy and Astrophysics*, 12:573–583, May 2012. doi: 10.1088/1674-4527/12/5/009.
- J. Chen, J. Su, Z. Yin, T. G. Priya, H. Zhang, J. Liu, H. Xu, and S. Yu. Recurrent Solar Jets Induced by a Satellite Spot and Moving Magnetic Features. *Astrophys. J.*, 815:71, December 2015. doi: 10.1088/0004-637X/815/1/71.
- M. C. M. Cheung and H. Isobe. Flux Emergence (Theory). *Living Reviews in Solar Physics*, 11:3, July 2014. doi: 10.12942/lrsp-2014-3.
- M. C. M. Cheung, P. Boerner, C. J. Schrijver, P. Testa, F. Chen, H. Peter, and A. Malanushenko. Thermal Diagnostics with the Atmospheric Imaging Assembly on board the Solar Dynamics Observatory: A Validated Method for Differential Emission Measure Inversions. *Astrophys. J.*, 807:143, July 2015a. doi: 10.1088/0004-637X/807/2/143.
- M. C. M. Cheung, B. De Pontieu, T. D. Tarbell, Y. Fu, H. Tian, P. Testa, K. K. Reeves, J. Martínez-Sykora, P. Boerner, J. P. Wülser, J. Lemen, A. M. Title, N. Hurlburt, L. Kleint, C. Kankelborg, S. Jaeggli, L. Golub, S. McKillop, S. Saar, M. Carlsson, and V. Hansteen. Homologous Helical Jets: Observations By IRIS, SDO, and Hinode and Magnetic Modeling With Data-Driven Simulations. *Astrophys. J.*, 801:83, March 2015b. doi: 10.1088/0004-637X/801/2/83.
- C. Chifor, H. Isobe, H. E. Mason, I. G. Hannah, P. R. Young, G. Del Zanna, S. Krucker, K. Ichimoto,

- Y. Katsukawa, and T. Yokoyama. Magnetic flux cancellation associated with a recurring solar jet observed with Hinode, RHESSI, and STEREO/EUVI. *Astron. Astrophys.*, 491:279–288, November 2008a. doi: 10.1051/0004-6361:200810265.
- C. Chifor, P. R. Young, H. Isobe, H. E. Mason, D. Tripathi, H. Hara, and T. Yokoyama. An active region jet observed with Hinode. *Astron. Astrophys.*, 481:L57–L60, April 2008b. doi: 10.1051/0004-6361:20079081.
- Y. T. Chiu and H. H. Hilton. Exact Green's function method of solar force-free magnetic-field computations with constant alpha. I - Theory and basic test cases. *Astrophys. J.*, 212:873–885, March 1977. doi: 10.1086/155111.
- J. W. Cirtain, L. Golub, L. Lundquist, A. van Ballegooijen, A. Savcheva, M. Shimojo, E. DeLuca, S. Tsuneta, T. Sakao, K. Reeves, M. Weber, R. Kano, N. Narukage, and K. Shibasaki. Evidence for Alfvén Waves in Solar X-ray Jets. *Science*, 318:1580–, December 2007. doi: 10.1126/science.1147050.
- William G. Cochran. The χ^2 test of goodness of fit. *Ann. Math. Statist.*, 23(3):315–345, 09 1952. doi: 10.1214/aoms/1177729380. URL <http://dx.doi.org/10.1214/aoms/1177729380>.
- L. Comisso and A. Bhattacharjee. On the value of the reconnection rate. *Journal of Plasma Physics*, 82(6): 595820601, December 2016. doi: 10.1017/S002237781600101X.
- I. J. D. Craig. The use of a-priori information in the derivation of temperature structures from X-ray spectra. *Astron. Astrophys.*, 61:575–590, November 1977.
- I. J. D. Craig and J. C. Brown. *Inverse problems in astronomy: A guide to inversion strategies for remotely sensed data*. Adam Hilger, Ltd., 1986.
- Steven R. Cranmer, Sarah E. Gibson, and Pete Riley. Origins of the Ambient Solar Wind: Implications for Space Weather. *Space Sci. Rev.*, 212:1345–1384, November 2017. doi: 10.1007/s11214-017-0416-y.
- C. de Jager, M. E. Bruner, and C. J. Crannel. Energetics of the impulsive phase. In *Energetic Phenomena on the Sun, NASA Conf. Pub. 2439, ed. M. R. Kundu B. E. Woodgate (Greenbelt, MD NASA)*, 5.5, page 422, 1986. URL <https://ntrs.nasa.gov/archive/nasa/casi.ntrs.nasa.gov/19870009895.pdf>.
- B. De Pontieu, S. W. McIntosh, M. Carlsson, V. H. Hansteen, T. D. Tarbell, C. J. Schrijver, A. M. Title, R. A. Shine, S. Tsuneta, Y. Katsukawa, K. Ichimoto, Y. Suematsu, T. Shimizu, and S. Nagata. Chromospheric Alfvénic Waves Strong Enough to Power the Solar Wind. *Science*, 318:1574, December 2007. doi: 10.1126/science.1151747.
- B. De Pontieu, S. W. McIntosh, M. Carlsson, V. H. Hansteen, T. D. Tarbell, P. Boerner, J. Martinez-Sykora, C. J. Schrijver, and A. M. Title. The Origins of Hot Plasma in the Solar Corona. *Science*, 331:55–, January 2011. doi: 10.1126/science.1197738.
- B. De Pontieu, L. Rouppe van der Voort, S. W. McIntosh, T. M. D. Pereira, M. Carlsson, V. Hansteen, H. Skogsrud, J. Lemen, A. Title, P. Boerner, N. Hurlburt, T. D. Tarbell, J. P. Wuelser, E. E. De Luca, L. Golub, S. McKillop, K. Reeves, S. Saar, P. Testa, H. Tian, C. Kankelborg, S. Jaeggli, L. Kleint, and J. Martinez-Sykora. On the prevalence of small-scale twist in the solar chromosphere and transition region. *Science*, 346:1255732, October 2014. doi: 10.1126/science.1255732.
- M. L. De Rosa, C. J. Schrijver, G. Barnes, K. D. Leka, B. W. Lites, M. J. Aschwanden, T. Amari, A. Canou, J. M. McTiernan, S. Régnier, J. K. Thalmann, G. Valori, M. S. Wheatland, T. Wiegmann, M. C. M. Cheung, P. A. Conlon, M. Fuhrmann, B. Inhester, and T. Tadesse. A Critical Assessment of Nonlinear Force-Free Field Modeling of the Solar Corona for Active Region 10953. *Astrophys. J.*, 696:1780–1791, May 2009. doi: 10.1088/0004-637X/696/2/1780.
- G. Del Zanna. The multi-thermal emission in solar active regions. *Astron. Astrophys.*, 558:A73, October 2013. doi: 10.1051/0004-6361/201321653.
- G. Del Zanna, K. P. Dere, P. R. Young, E. Landi, and H. E. Mason. CHIANTI - An atomic database for emission lines. Version 8. *Astron. Astrophys.*, 582:A56, October 2015. doi: 10.1051/0004-6361/201526827.
- J.-P. Delaboudinière, G. E. Artzner, J. Brunaud, A. H. Gabriel, J. F. Hochedez, F. Millier, X. Y. Song, B. Au, K. P. Dere, R. A. Howard, R. Kreplin, D. J. Michels, J. D. Moses, J. M. Defise, C. Jamar, P. Rochus, J. P. Chauvineau, J. P. Marioge, R. C. Catura, J. R. Lemen, L. Shing, R. A. Stern, J. B. Gurman, W. M. Neupert, A. Maucherat, F. Clette, P. Cugnon, and E. L. van Dessel. EIT: Extreme-Ultraviolet Imaging Telescope for the SOHO Mission. *Solar Phys.*, 162:291–312, December 1995. doi: 10.1007/BF00733432.
- B. R. Dennis and R. L. Pernak. Hard X-Ray Flare Source Sizes Measured with the Ramaty High Energy Solar Spectroscopic Imager. *Astrophys. J.*, 698:2131–2143, June 2009. doi: 10.1088/0004-637X/698/2/2131.
- K. P. Dere, J.-D. F. Bartoe, and G. E. Brueckner. Chromospheric jets - Possible extreme-ultraviolet observations of spicules. *Astrophys. J. lett.*, 267:L65–L68, April 1983. doi: 10.1086/184004.
- V. Domingo, B. Fleck, and A. I. Poland. The SOHO Mission: an Overview. *Solar Phys.*, 162:1–37, December 1995. doi: 10.1007/BF00733425.
- A. C. Donea and I. J. Cairns. Private communication. , 2013.
- B. Edlén and P. Swings. Term Analysis of the Third Spectrum of Iron (Fe III). *Astrophys. J.*, 95:532, May 1942.

- doi: 10.1086/144421.
- B. Edlén and F. Tyrén. Atomic Energy States of an Unusual Type. *Nature*, 143:940–941, June 1939. doi: 10.1038/143940a0.
- F. Fang, Y. Fan, and S. W. McIntosh. Rotating Solar Jets in Simulations of Flux Emergence with Thermal Conduction. *Astrophys. J. lett.*, 789:L19, July 2014. doi: 10.1088/2041-8205/789/1/L19.
- L. Fletcher, B. R. Dennis, H. S. Hudson, S. Krucker, K. Phillips, A. Veronig, M. Battaglia, L. Bone, A. Caspi, Q. Chen, P. Gallagher, P. T. Grigis, H. Ji, W. Liu, R. O. Milligan, and M. Temmer. An Observational Overview of Solar Flares. *Space Sci. Rev.*, 159:19–106, September 2011. doi: 10.1007/s11214-010-9701-8.
- J. M. Fontenla, J. Harder, W. Livingston, M. Snow, and T. Woods. High-resolution solar spectral irradiance from extreme ultraviolet to far infrared. *Journal of Geophysical Research: Atmospheres*, 116 (D20), 2011. doi: 10.1029/2011JD016032. URL <https://agupubs.onlinelibrary.wiley.com/doi/abs/10.1029/2011JD016032>.
- J. K. Fotheringham. A solution of ancient eclipses of the sun. *Mon. Not. Roy. Astron. Soc.*, 81:104–126, December 1920.
- N. J. Fox, M. C. Velli, S. D. Bale, R. Decker, A. Driesman, R. A. Howard, J. C. Kasper, J. Kinnison, M. Kusterer, D. Lario, M. K. Lockwood, D. J. McComas, N. E. Raouafi, and A. Szabo. The solar probe plus mission: Humanity’s first visit to our star. *Space Science Reviews*, 204(1):7–48, Dec 2016. ISSN 1572-9672. doi: 10.1007/s11214-015-0211-6. URL <https://doi.org/10.1007/s11214-015-0211-6>.
- G. A. Gary and M. J. Hagyard. Transformation of vector magnetograms and the problems associated with the effects of perspective and the azimuthal ambiguity. *Solar Phys.*, 126:21–36, March 1990. doi: 10.1007/BF00158295.
- T. Gold and F. Hoyle. On the origin of solar flares. *Mon. Not. Roy. Astron. Soc.*, 120:89, 1960. doi: 10.1093/mnras/120.2.89.
- L. Golub and J. M. Pasachoff. *The Solar Corona*. Cambridge University Press, 2009, October 2009.
- L. Golub, E. Deluca, G. Austin, J. Bookbinder, D. Caldwell, P. Cheimets, J. Cirtain, M. Cosmo, P. Reid, A. Sette, M. Weber, T. Sakao, R. Kano, K. Shibasaki, H. Hara, S. Tsuneta, K. Kumagai, T. Tamura, M. Shimojo, J. McCracken, J. Carpenter, H. Haight, R. Siler, E. Wright, J. Tucker, H. Rutledge, M. Barbera, G. Peres, and S. Varisco. The X-Ray Telescope (XRT) for the Hinode Mission. *Solar Phys.*, 243:63–86, June 2007. doi: 10.1007/s11207-007-0182-1.
- Leo A. Goodman. On the exact variance of products. *Journal of the American Statistical Association*, 55(292): 708–713, 1960. doi: 10.1080/01621459.1960.10483369. URL <https://www.tandfonline.com/doi/abs/10.1080/01621459.1960.10483369>.
- W. Grotian. Ergebnisse der Potsdamer Expedition zur Beobachtung der Sonnenfinsternis am 9. Mai 1929 in Takengon (Nordsumatra). 8. Mitteilung. Über den Intensitätsverlauf und das Intensitätsverhältnis der Koronalinien. Mit 12 Abbildungen. *Zeitschrift für Astrophysik*, 7:26, 1933.
- Y. Guo, P. Démoulin, B. Schmieder, M. D. Ding, S. Vargas Domínguez, and Y. Liu. Recurrent coronal jets induced by repetitively accumulated electric currents. *Astron. Astrophys.*, 555:A19, July 2013. doi: 10.1051/0004-6361/201321229.
- G. E. Hale. On the Probable Existence of a Magnetic Field in Sun-Spots. *Astrophys. J.*, 28:315, November 1908. doi: 10.1086/141602.
- Yoichiro Hanaoka, Ryuichi Hasuo, Tsukasa Hirose, Akiko C. Ikeda, Tsutomu Ishibashi, Norihiro Manago, Yukio Masuda, Sakuhiro Morita, Jun Nakazawa, Osamu Ohgoe, Yoshiaki Sakai, Kazuhiro Sasaki, Koichi Takahashi, and Toshiyuki Toi. Solar Coronal Jets Extending to High Altitudes Observed during the 2017 August 21 Total Eclipse. *Astrophys. J.*, 860:142, June 2018. doi: 10.3847/1538-4357/aac49b.
- I. G. Hannah and E. P. Kontar. Differential emission measures from the regularized inversion of Hinode and SDO data. *Astron. Astrophys.*, 539:A146, March 2012. doi: 10.1051/0004-6361/201117576.
- I. G. Hannah, S. Christe, S. Krucker, G. J. Hurford, H. S. Hudson, and R. P. Lin. RHESSI Microflare Statistics. II. X-Ray Imaging, Spectroscopy, and Energy Distributions. *Astrophys. J.*, 677:704–718, April 2008. doi: 10.1086/529012.
- W. J. Hanneman and K. K. Reeves. Thermal Structure of Current Sheets and Supra-arcade Downflows in the Solar Corona. *Astrophys. J.*, 786:95, May 2014. doi: 10.1088/0004-637X/786/2/95.
- P C Hansen. Numerical tools for analysis and solution of fredholm integral equations of the first kind. *Inverse Problems*, 8(6):849–872, December 1992. ISSN 0266-5611.
- C. S. Hanson, A. C. Donea, and K. D. Leka. Enhanced Acoustic Emission in Relation to the Acoustic Halo Surrounding Active Region 11429. *Solar Phys.*, 290:2171–2187, August 2015. doi: 10.1007/s11207-015-0743-7.
- V. Hansteen, B. De Pontieu, M. Carlsson, J. Lemen, A. Title, P. Boerner, N. Hurlburt, T. D. Tarbell, J. P. Wuelser, T. M. D. Pereira, E. E. De Luca, L. Golub, S. McKillop, K. Reeves, S. Saar, P. Testa, H. Tian, C. Kankelborg,

- S. Jaeggli, L. Kleint, and J. Martínez-Sykora. The unresolved fine structure resolved: IRIS observations of the solar transition region. *Science*, 346:1255757, October 2014. doi: 10.1126/science.1255757.
- F. A. Harrison, W. W. Craig, F. E. Christensen, C. J. Hailey, W. W. Zhang, S. E. Boggs, D. Stern, W. R. Cook, K. Forster, P. Giommi, B. W. Grefenstette, Y. Kim, T. Kitaguchi, J. E. Koglin, K. K. Madsen, P. H. Mao, H. Miyasaka, K. Mori, M. Perri, M. J. Pivovarov, S. Puccetti, V. R. Rana, N. J. Westergaard, J. Willis, A. Zoglauer, H. An, M. Bachetti, N. M. Barrière, E. C. Bellm, V. Bhalerao, N. F. Brejnholt, F. Fuerst, C. C. Liebe, C. B. Markwardt, M. Nynka, J. K. Vogel, D. J. Walton, D. R. Wik, D. M. Alexander, L. R. Cominsky, A. E. Hornschemeier, A. Hornstrup, V. M. Kaspi, G. M. Madejski, G. Matt, S. Molendi, D. M. Smith, J. A. Tomsick, M. Ajello, D. R. Ballantyne, M. Baloković, D. Barret, F. E. Bauer, R. D. Blandford, W. N. Brandt, L. W. Brenneman, J. Chiang, D. Chakrabarty, J. Chenevez, A. Comastri, F. Dufour, M. Elvis, A. C. Fabian, D. Farrah, C. L. Fryer, E. V. Gotthelf, J. E. Grindlay, D. J. Helfand, R. Krivonos, D. L. Meier, J. M. Miller, L. Natalucci, P. Ogle, E. O. Ofek, A. Ptak, S. P. Reynolds, J. R. Rigby, G. Tagliaferri, S. E. Thorsett, E. Treister, and C. M. Urry. The Nuclear Spectroscopic Telescope Array (NuSTAR) High-energy X-Ray Mission. *Astrophys. J.*, 770:103, June 2013. doi: 10.1088/0004-637X/770/2/103.
- J. W. Harvey. *Magnetic Fields Associated with Solar Active-Region Prominences*. PhD thesis, National Solar Observatory <EMAIL>jharvey@nso.edu</EMAIL>, June 1969.
- L. A. Hayes, P. T. Gallagher, B. R. Dennis, J. Ireland, A. R. Inglis, and D. F. Ryan. Quasi-periodic Pulsations during the Impulsive and Decay phases of an X-class Flare. *Astrophys. J. Lett.*, 827:L30, August 2016. doi: 10.3847/2041-8205/827/2/L30.
- E. Hiei and T. Hirayama. Observation of the Outer Layer of the Sun at the Total Solar Eclipse of 12 November 1966. *Pub. Astron. Soc. Japan*, 22:545, 1970.
- T. Hirayama. Theoretical Model of Flares and Prominences. I: Evaporating Flare Model. *Solar Phys.*, 34:323–338, February 1974. doi: 10.1007/BF00153671.
- J. T. Hoeksema, Y. Liu, K. Hayashi, X. Sun, J. Schou, S. Couvidat, A. Norton, M. Bobra, R. Centeno, K. D. Leka, G. Barnes, and M. Turmon. The Helioseismic and Magnetic Imager (HMI) Vector Magnetic Field Pipeline: Overview and Performance. *Solar Phys.*, 289:3483–3530, September 2014. doi: 10.1007/s11207-014-0516-8.
- J.-C. Hong, Y.-C. Jiang, J.-Y. Yang, R.-S. Zheng, Y. Bi, H.-D. Li, B. Yang, and D. Yang. Twist in a polar blowout jet. *Research in Astronomy and Astrophysics*, 13:253–258, March 2013. doi: 10.1088/1674-4527/13/3/001.
- R. A. Howard, J. D. Moses, A. Vourlidas, J. S. Newmark, D. G. Socker, S. P. Plunkett, C. M. Korendyke, J. W. Cook, A. Hurley, J. M. Davila, W. T. Thompson, O. C. St Cyr, E. Mentzell, K. Mehalick, J. R. Lemen, J. P. Wuelser, D. W. Duncan, T. D. Tarbell, C. J. Wolfson, A. Moore, R. A. Harrison, N. R. Waltham, J. Lang, C. J. Davis, C. J. Eyles, H. Mapson-Menard, G. M. Simnett, J. P. Halain, J. M. Defise, E. Mazy, P. Rochus, R. Mercier, M. F. Ravet, F. Delmotte, F. Auchere, J. P. Delaboudiniere, V. Bothmer, W. Deutsch, D. Wang, N. Rich, S. Cooper, V. Stephens, G. Maahs, R. Baugh, D. McMullin, and T. Carter. Sun Earth Connection Coronal and Heliospheric Investigation (SECCHI). *Space Sci. Rev.*, 136:67–115, April 2008. doi: 10.1007/s11214-008-9341-4.
- G. J. Hurford, E. J. Schmahl, R. A. Schwartz, A. J. Conway, M. J. Aschwanden, A. Csillaghy, B. R. Dennis, C. Johns-Krull, S. Krucker, R. P. Lin, J. McTiernan, T. R. Metcalf, J. Sato, and D. M. Smith. The RHESSI Imaging Concept. *Solar Phys.*, 210:61–86, November 2002. doi: 10.1023/A:1022436213688.
- A. R. Inglis and S. Christe. Investigating the Differential Emission Measure and Energetics of Microflares with Combined SDO/AIA and RHESSI observations. *Astrophys. J.*, 789:116, July 2014. doi: 10.1088/0004-637X/789/2/116.
- D. E. Innes, R. H. Cameron, and S. K. Solanki. EUV jets, type III radio bursts and sunspot waves investigated using SDO/AIA observations. *Astron. Astrophys.*, 531:L13, July 2011. doi: 10.1051/0004-6361/201117255.
- Y. C. Jiang, H. D. Chen, K. J. Li, Y. D. Shen, and L. H. Yang. The H α surges and EUV jets from magnetic flux emergences and cancellations. *Astron. Astrophys.*, 469:331–337, July 2007. doi: 10.1051/0004-6361:20053954.
- A. Johannesson and H. Zirin. The Pole-Equator Variation of Solar Chromospheric Height. *Astrophys. J.*, 471:510, November 1996. doi: 10.1086/177987.
- P. G. Judge. On Spectroscopic Filling Factors and the Solar Transition Region. *Astrophys. J.*, 531:585–590, March 2000. doi: 10.1086/308458.
- P. G. Judge, V. Hubeny, and J. C. Brown. Fundamental Limitations of Emission-Line Spectra as Diagnostics of Plasma Temperature and Density Structure. *Astrophys. J.*, 475:275–290, January 1997. doi: 10.1086/303511.
- P. G. Judge, V. Hansteen, Ø. Wikstøl, K. Wilhelm, U. Schühle, and T. Moran. Evidence in Support of the “Nanoflare” Picture of Coronal Heating from SUMER Data. *Astrophys. J.*, 502:981–996, August 1998. doi:

10.1086/305915.

- P. G. Judge, L. Kleint, and A. Sainz Dalda. On Helium 1083 nm Line Polarization during the Impulsive Phase of an X1 Flare. *Astrophys. J.*, 814:100, December 2015. doi: 10.1088/0004-637X/814/2/100.
- P. G. Judge, A. Paraschiv, D. Lacatus, A. Donea, and C. Lindsey. Are All Flare Ribbons Simply Connected to the Corona? *Astrophys. J.*, 838:138, April 2017. doi: 10.3847/1538-4357/aa656c.
- M. L. Kaiser, T. A. Kucera, J. M. Davila, O. C. St. Cyr, M. Guhathakurta, and E. Christian. The STEREO Mission: An Introduction. *Space Sci. Rev.*, 136:5–16, April 2008. doi: 10.1007/s11214-007-9277-0.
- Y.-H. Kim, Y.-J. Moon, Y.-D. Park, T. Sakurai, J. Chae, K. S. Cho, and S.-C. Bong. Small-Scale X-Ray/EUV Jets Seen in Hinode XRT and TRACE. *Pub. Astron. Soc. Japan*, 59:763, November 2007.
- A. S. Kirichenko and S. A. Bogachev. Plasma Heating in Solar Microflares: Statistics and Analysis. *Astrophys. J.*, 840:45, May 2017. doi: 10.3847/1538-4357/aa6c2b.
- J. L. Kohl, L. D. Gardner, L. Strachan, and D. M. Hassler. Ultraviolet spectroscopy of the extended solar corona during the SPARTAN 201 mission. *Space Sci. Rev.*, 70:253–261, October 1994. doi: 10.1007/BF00777876.
- E. P. Kontar, M. Piana, A. M. Massone, A. G. Emslie, and J. C. Brown. Generalized Regularization Techniques with Constraints for the Analysis of Solar Bremsstrahlung X-ray Spectra. *Solar Phys.*, 225:293–309, December 2004. doi: 10.1007/s11207-004-4140-x.
- R. A. Kopp and G. W. Pneuman. Magnetic reconnection in the corona and the loop prominence phenomenon. *Solar Phys.*, 50:85–98, October 1976. doi: 10.1007/BF00206193.
- T. Kosugi, K. Matsuzaki, T. Sakao, T. Shimizu, Y. Sone, S. Tachikawa, T. Hashimoto, K. Minesugi, A. Ohnishi, T. Yamada, S. Tsuneta, H. Hara, K. Ichimoto, Y. Suematsu, M. Shimojo, T. Watanabe, S. Shimada, J. M. Davis, L. D. Hill, J. K. Owens, A. M. Title, J. L. Culhane, L. K. Harra, G. A. Doschek, and L. Golub. The Hinode (Solar-B) Mission: An Overview. *Solar Phys.*, 243:3–17, June 2007. doi: 10.1007/s11207-007-9014-6.
- S. Koutchmy. Coronal physics from eclipse observations. *Advances in Space Research*, 14, April 1994. doi: 10.1016/0273-1177(94)90156-2.
- S. Krucker, E. P. Kontar, S. Christe, L. Glesener, and R. P. Lin. Electron Acceleration Associated with Solar Jets. *Astrophys. J.*, 742:82, December 2011. doi: 10.1088/0004-637X/742/2/82.
- M. R. Kundu, J. P. Raulin, N. Nitta, H. S. Hudson, M. Shimojo, K. Shibata, and A. Raoult. Detection of Nonthermal Radio Emission from Coronal X-Ray Jets. *Astrophys. J. Lett.*, 447:L135, July 1995. doi: 10.1086/309567.
- R. J. Leamon, R. C. Canfield, Z. Blehm, and A. A. Pevtsov. What Is the Role of the Kink Instability in Solar Coronal Eruptions? *Astrophys. J. Lett.*, 596:L255–L258, October 2003. doi: 10.1086/379530.
- E. J. Lee, V. Archontis, and A. W. Hood. Helical Blowout Jets in the Sun: Untwisting and Propagation of Waves. *Astrophys. J. Lett.*, 798:L10, January 2015. doi: 10.1088/2041-8205/798/1/L10.
- K. D. Leka and A. Skumanich. On the value of ‘ α AR’ from vector magnetograph data - I. Methods and Caveats. *Solar Phys.*, 188:3–19, August 1999. doi: 10.1023/A:1005108632671.
- K. D. Leka, Y. Fan, and G. Barnes. On the Availability of Sufficient Twist in Solar Active Regions to Trigger the Kink Instability. *Astrophys. J.*, 626:1091–1095, June 2005. doi: 10.1086/430203.
- K. D. Leka, G. Barnes, A. D. Crouch, T. R. Metcalf, G. A. Gary, J. Jing, and Y. Liu. Resolving the 180° Ambiguity in Solar Vector Magnetic Field Data: Evaluating the Effects of Noise, Spatial Resolution, and Method Assumptions. *Solar Phys.*, 260:83–108, November 2009. doi: 10.1007/s11207-009-9440-8.
- J. R. Lemen, A. M. Title, D. J. Akin, P. F. Boerner, C. Chou, J. F. Drake, D. W. Duncan, C. G. Edwards, F. M. Friedlaender, G. F. Heyman, N. E. Hurlburt, N. L. Katz, G. D. Kushner, M. Levay, R. W. Lindgren, D. P. Mathur, E. L. McFeaters, S. Mitchell, R. A. Rehse, C. J. Schrijver, L. A. Springer, R. A. Stern, T. D. Tarbell, J.-P. Wuelser, C. J. Wolfson, C. Yanari, J. A. Bookbinder, P. N. Cheimets, D. Caldwell, E. E. Deluca, R. Gates, L. Golub, S. Park, W. A. Podgorski, R. I. Bush, P. H. Scherrer, M. A. Gummin, P. Smith, G. Auker, P. Jerram, P. Pool, R. Soufli, D. L. Windt, S. Beardsley, M. Clapp, J. Lang, and N. Waltham. The Atmospheric Imaging Assembly (AIA) on the Solar Dynamics Observatory (SDO). *Solar Phys.*, 275:17–40, January 2012. doi: 10.1007/s11207-011-9776-8.
- X. Li, S. Yang, H. Chen, T. Li, and J. Zhang. Trigger of a Blowout Jet in a Solar Coronal Mass Ejection Associated with a Flare. *Astrophys. J. Lett.*, 814:L13, November 2015. doi: 10.1088/2041-8205/814/1/L13.
- R. P. Lin, B. R. Dennis, G. J. Hurford, D. M. Smith, A. Zehnder, P. R. Harvey, D. W. Curtis, D. Pankow, P. Turin, M. Bester, A. Csillaghy, M. Lewis, N. Madden, H. F. van Beek, M. Appleby, T. Raudorf, J. McTiernan, R. Ramaty, E. Schmahl, R. Schwartz, S. Krucker, R. Abiad, T. Quinn, P. Berg, M. Hashii, R. Sterling, R. Jackson, R. Pratt, R. D. Campbell, D. Malone, D. Landis, C. P. Barrington-Leigh, S. Slassi-Sennou, C. Cork, D. Clark, D. Amato, L. Orwig, R. Boyle, I. S. Banks, K. Shirey, A. K. Tolbert, D. Zarro, F. Snow, K. Thomsen, R. Henneke, A. McHedlishvili, P. Ming, M. Fivian, J. Jordan, R. Wanner, J. Crubb, J. Preble, M. Matraga, A. Benz, H. Hudson, R. C. Canfield, G. D. Holman, C. Crannell, T. Kosugi, A. G. Emslie, N. Vilmer, J. C. Brown, C. Johns-Krull, M. Aschwanden, T. Metcalf, and A. Conway. The Reuven Ramaty High-Energy Solar

- Spectroscopic Imager (RHESSI). *Solar Phys.*, 210:3–32, November 2002. doi: 10.1023/A:1022428818870.
- R. Lionello, T. Török, V. S. Titov, J. E. Leake, Z. Mikić, J. A. Linker, and M. G. Linton. The Contribution of Coronal Jets to the Solar Wind. *Astrophys. J.*, 831:L2, November 2016. doi: 10.3847/2041-8205/831/1/L2.
- J. Liu, Y. Wang, R. Erdélyi, R. Liu, S. W. McIntosh, T. Gou, J. Chen, K. Liu, L. Liu, and Z. Pan. On the Magnetic and Energy Characteristics of Recurrent Homologous Jets from An Emerging Flux. *Astrophys. J.*, 833:150, December 2016. doi: 10.3847/1538-4357/833/2/150.
- B. Lyot and R. K. Marshall. The Study of the Solar Corona without an Eclipse. *J. Roy. Astron. Soc. Canada*, 27:225, August 1933.
- G. Mann, F. Jansen, R. J. MacDowall, M. L. Kaiser, and R. G. Stone. A heliospheric density model and type III radio bursts. *Astron. Astrophys.*, 348:614–620, August 1999.
- P. I. McCauley, I. H. Cairns, J. Morgan, S. E. Gibson, J. C. Harding, C. Lonsdale, and D. Oberoi. Type III Solar Radio Burst Source Region Splitting Due to a Quasi-Separatrix Layer. *ArXiv e-prints*, November 2017.
- D. H. Menzel. A study of the flash spectrum. In *Publications of the American Astronomical Society*, volume 6 of *Publications of the American Astronomical Society*, page 145, 1931.
- T. R. Metcalf. Resolving the 180-degree ambiguity in vector magnetic field measurements: The ‘minimum’ energy solution. *Solar Phys.*, 155:235–242, December 1994. doi: 10.1007/BF00680593.
- T. R. Metcalf, L. Jiao, A. N. McClymont, R. C. Canfield, and H. Uitenbroek. Is the solar chromospheric magnetic field force-free? *Astrophys. J.*, 439:474–481, January 1995. doi: 10.1086/175188.
- T. R. Metcalf, H. S. Hudson, T. Kosugi, R. C. Puetter, and R. K. Pina. Pixon-based Multiresolution Image Reconstruction for Yohkoh’s Hard X-Ray Telescope. *Astrophys. J.*, 466:585, July 1996. doi: 10.1086/177533.
- T. R. Metcalf, K. D. Leka, G. Barnes, B. W. Lites, M. K. Georgoulis, A. A. Pevtsov, K. S. Balasubramaniam, G. A. Gary, J. Jing, J. Li, Y. Liu, H. N. Wang, V. Abramenko, V. Yurchyshyn, and Y.-J. Moon. An Overview of Existing Algorithms for Resolving the 180 Ambiguity in Vector Magnetic Fields: Quantitative Tests with Synthetic Data. *Solar Phys.*, 237:267–296, September 2006. doi: 10.1007/s11207-006-0170-x.
- N. Metropolis, A. W. Rosenbluth, M. N. Rosenbluth, A. H. Teller, and E. Teller. Equation of State Calculations by Fast Computing Machines. *J. Chem. Phys.*, 21:1087–1092, June 1953. doi: 10.1063/1.1699114.
- D. L. Mickey. The Haleakala Stokes polarimeter. *Solar Phys.*, 97:223–238, June 1985. doi: 10.1007/BF00165987.
- R. L. Moore, J. W. Cirtain, A. C. Sterling, and D. A. Falconer. Dichotomy of Solar Coronal Jets: Standard Jets and Blowout Jets. *Astrophys. J.*, 720:757–770, September 2010. doi: 10.1088/0004-637X/720/1/757.
- R. L. Moore, A. C. Sterling, J. W. Cirtain, and D. A. Falconer. Solar X-ray Jets, Type-II Spicules, Granule-size Emerging Bipoles, and the Genesis of the Heliosphere. *Astrophys. J. lett.*, 731:L18, April 2011. doi: 10.1088/2041-8205/731/1/L18.
- R. L. Moore, A. C. Sterling, D. A. Falconer, and D. Robe. The Cool Component and the Dichotomy, Lateral Expansion, and Axial Rotation of Solar X-Ray Jets. *Astrophys. J.*, 769:134, June 2013. doi: 10.1088/0004-637X/769/2/134.
- F. Moreno-Insertis and K. Galsgaard. Plasma Jets and Eruptions in Solar Coronal Holes: A Three-dimensional Flux Emergence Experiment. *Astrophys. J.*, 771:20, July 2013. doi: 10.1088/0004-637X/771/1/20.
- F. Moreno-Insertis, K. Galsgaard, and I. Ugarte-Urra. Jets in Coronal Holes: Hinode Observations and Three-dimensional Computer Modeling. *Astrophys. J. lett.*, 673:L211–L214, February 2008. doi: 10.1086/527560.
- A. L. Moser and P. M. Bellan. Magnetic reconnection from a multiscale instability cascade. *Nature*, 482:379–381, February 2012. doi: 10.1038/nature10827.
- S. M. Mulay, D. Tripathi, G. Del Zanna, and H. Mason. Multiwavelength study of 20 jets that emanate from the periphery of active regions. *Astron. Astrophys.*, 589:A79, May 2016. doi: 10.1051/0004-6361/201527473.
- S. M. Mulay, G. D. Zanna, and H. Mason. Temperature and density structure of a recurring active region jet. *Astron. Astrophys.*, 598:A11, February 2017a. doi: 10.1051/0004-6361/201628796.
- S. M. Mulay, G. D. Zanna, and H. Mason. Cool and hot emission in a recurring active region jet. *Astron. Astrophys.*, 606:A4, September 2017b. doi: 10.1051/0004-6361/201730429.
- V. M. Nakariakov and V. F. Melnikov. Quasi-Periodic Pulsations in Solar Flares. *Space Sci. Rev.*, 149:119–151, December 2009. doi: 10.1007/s11214-009-9536-3.
- V. M. Nakariakov and E. Verwichte. Coronal Waves and Oscillations. *Living Reviews in Solar Physics*, 2:3, May 2005. doi: 10.12942/lrsp-2005-3.
- V. M. Nakariakov, S. Anfinogentov, A. A. Storozhenko, E. A. Kurochkin, V. M. Bogod, I. N. Sharykin, and T. I. Kaltman. Quasi-periodic pulsations in a solar microflare. *The Astrophysical Journal*, 859(2):154, 2018. URL <http://stacks.iop.org/0004-637X/859/i=2/a=154>.

- Marcia Neugebauer. Evidence for polar x-ray jets as sources of microstream peaks in the solar wind. *The Astrophysical Journal*, 750(1):50, 2012. URL <http://stacks.iop.org/0004-637X/750/i=1/a=50>.
- T. Neukirch. Magnetic Field Extrapolation. In D. E. Innes, A. Lagg, and S. A. Solanki, editors, *Chromospheric and Coronal Magnetic Fields*, volume 596 of *ESA Special Publication*, page 12.1, November 2005.
- R. R. Newton. *Ancient astronomical observations and the accelerations of the earth and moon*. Baltimore: J.Hopkins Press, 1970.
- N. Nishizuka, M. Shimizu, T. Nakamura, K. Otsuji, T. J. Okamoto, Y. Katsukawa, and K. Shibata. Giant Chromospheric Anemone Jet Observed with Hinode and Comparison with Magnetohydrodynamic Simulations: Evidence of Propagating Alfvén Waves and Magnetic Reconnection. *Astrophys. J. lett.*, 683: L83, August 2008. doi: 10.1086/591445.
- N. Nishizuka, A. Asai, H. Takasaki, H. Kurokawa, and K. Shibata. The Power-Law Distribution of Flare Kernels and Fractal Current Sheets in a Solar Flare. *Astrophys. J. lett.*, 694:L74–L78, March 2009. doi: 10.1088/0004-637X/694/1/L74.
- G. Nisticò, V. Bothmer, S. Patsourakos, and G. Zimbardo. Characteristics of EUV Coronal Jets Observed with STEREO/SECCHI. *Solar Phys.*, 259:87–108, October 2009. doi: 10.1007/s11207-009-9424-8.
- G. Nisticò, S. Patsourakos, V. Bothmer, and G. Zimbardo. Determination of temperature maps of EUV coronal hole jets. *Advances in Space Research*, 48:1490–1498, November 2011. doi: 10.1016/j.asr.2011.07.003.
- D. Nóbrega-Siverio, F. Moreno-Insertis, and J. Martínez-Sykora. The Cool Surge Following Flux Emergence in a Radiation-MHD Experiment. *Astrophys. J.*, 822:18, May 2016. doi: 10.3847/0004-637X/822/1/18.
- Y. Ogawara, T. Takano, T. Kato, T. Kosugi, S. Tsuneta, T. Watanabe, I. Kondo, and Y. Uchida. The SOLAR-A Mission - An Overview. *Solar Phys.*, 136:1–16, November 1991. doi: 10.1007/BF00151692.
- N. K. Panesar, A. C. Sterling, and R. L. Moore. Homologous Jet-driven Coronal Mass Ejections from Solar Active Region 12192. *Astrophys. J. lett.*, 822:L23, May 2016. doi: 10.3847/2041-8205/822/2/L23.
- A. R. Paraschiv, D. A. Lacatus, T. Badescu, M. G. Lupu, S. Simon, S. G. Sandu, M. Mierla, and M. V. Rusu. Study of Coronal Jets During Solar Minimum Based on STEREO/SECCHI Observations. *Solar Phys.*, 264: 365–375, July 2010. doi: 10.1007/s11207-010-9584-6.
- A. R. Paraschiv, A. Bemporad, and A. C. Sterling. Physical properties of solar polar jets. A statistical study with Hinode XRT data. *Astron. Astrophys.*, 579:A96, July 2015. doi: 10.1051/0004-6361/201525671.
- A. R. Paraschiv, A. C. Donea, and C. Lindsey. in preparation. , 2018.
- E. Pariat, S. K. Antiochos, and C. R. DeVore. A Model for Solar Polar Jets. *Astrophys. J.*, 691:61–74, January 2009. doi: 10.1088/0004-637X/691/1/61.
- E. Pariat, S. K. Antiochos, and C. R. DeVore. Three-dimensional Modeling of Quasi-homologous Solar Jets. *Astrophys. J.*, 714:1762–1778, May 2010. doi: 10.1088/0004-637X/714/2/1762.
- E. Pariat, K. Dalmasse, C. R. DeVore, S. K. Antiochos, and J. T. Karpen. Model for straight and helical solar jets. I. Parametric studies of the magnetic field geometry. *Astron. Astrophys.*, 573:A130, January 2015. doi: 10.1051/0004-6361/201424209.
- E. Pariat, K. Dalmasse, C. R. DeVore, S. K. Antiochos, and J. T. Karpen. A model for straight and helical solar jets. II. Parametric study of the plasma beta. *Astron. Astrophys.*, 596:A36, November 2016. doi: 10.1051/0004-6361/201629109.
- E. N. Parker. Newtonian development of the dynamical properties of ionized gases of low density. *Phys. Rev.*, 107:924–933, Aug 1957. doi: 10.1103/PhysRev.107.924. URL <https://link.aps.org/doi/10.1103/PhysRev.107.924>.
- E. N. Parker. Dynamics of the Interplanetary Gas and Magnetic Fields. *Astrophys. J.*, 128:664, November 1958. doi: 10.1086/146579.
- C. E. Parnell and I. De Moortel. A contemporary view of coronal heating. *Philosophical Transactions of the Royal Society of London Series A*, 370:3217–3240, July 2012. doi: 10.1098/rsta.2012.0113.
- Karl Pearson. X. on the criterion that a given system of deviations from the probable in the case of a correlated system of variables is such that it can be reasonably supposed to have arisen from random sampling. *Philosophical Magazine*, 50(302):157–175, 1900. doi: 10.1080/14786440009463897. URL <http://dx.doi.org/10.1080/14786440009463897>.
- W. D. Pesnell, B. J. Thompson, and P. C. Chamberlin. The Solar Dynamics Observatory (SDO). *Solar Phys.*, 275:3–15, January 2012. doi: 10.1007/s11207-011-9841-3.
- H. E. Petschek. Magnetic Field Annihilation. *NASA Special Publication*, 50:425, 1964.
- S. Pucci, G. Poletto, A. C. Sterling, and M. Romoli. Physical Parameters of Standard and Blowout Jets. *Astrophys. J.*, 776:16, October 2013. doi: 10.1088/0004-637X/776/1/16.
- N.-E. Raouafi and G. Stenborg. Role of Transients in the Sustainability of Solar Coronal Plumes. *Astrophys. J.*, 787:118, June 2014. doi: 10.1088/0004-637X/787/2/118.
- N.-E. Raouafi, G. J. D. Petrie, A. A. Norton, C. J. Henney, and S. K. Solanki. Evidence for Polar Jets as Precursors

- of Polar Plume Formation. *Astrophys. J. lett.*, 682:L137–L140, August 2008. doi: 10.1086/591125.
- N. E. Raouafi, S. Patsourakos, E. Pariat, P. R. Young, A. C. Sterling, A. Savcheva, M. Shimojo, F. Moreno-Insertis, C. R. DeVore, V. Archontis, T. Török, H. Mason, W. Curdt, K. Meyer, K. Dalmasse, and Y. Matsui. Solar Coronal Jets: Observations, Theory, and Modeling. *Space Sci. Rev.*, 201:1–53, November 2016. doi: 10.1007/s11214-016-0260-5.
- Fabio Reale. Coronal loops: Observations and modeling of confined plasma. *Living Reviews in Solar Physics*, 11(1):4, Jul 2014. ISSN 1614-4961. doi: 10.12942/lrsp-2014-4. URL <https://doi.org/10.12942/lrsp-2014-4>.
- H. A. S. Reid and H. Ratcliffe. A review of solar type III radio bursts. *Research in Astronomy and Astrophysics*, 14:773–804, July 2014. doi: 10.1088/1674-4527/14/7/003.
- D. M. Rust, D. F. Webb, and W. MacCombie. Do surges heat the corona. *Solar Phys.*, 54:53–56, September 1977. doi: 10.1007/BF00146424.
- V. M. Sadykov, A. G. Kosovichev, I. N. Sharykin, I. V. Zimovets, and S. Vargas Dominguez. Relationship Between Chromospheric Evaporation and Magnetic Field Topology in an M-Class Solar Flare. *Astrophys. J.*, 828:4, September 2016. doi: 10.3847/0004-637X/828/1/4.
- T. Sakaue, A. Tei, A. Asai, S. Ueno, K. Ichimoto, and K. Shibata. Observational study on the fine structure and dynamics of a solar jet. I. Energy build-up process around a satellite spot. *Pub. Astron. Soc. Japan*, 69:80, October 2017. doi: 10.1093/pasj/psx071.
- T. Sakaue, A. Tei, A. Asai, S. Ueno, K. Ichimoto, and K. Shibata. Observational study on the fine structure and dynamics of a solar jet. II. Energy release process revealed by spectral analysis. *Pub. Astron. Soc. Japan*, January 2018. doi: 10.1093/pasj/psx133.
- N. Sako, M. Shimojo, T. Watanabe, and T. Sekii. A Statistical Study of Coronal Active Events in the North Polar Region. *Astrophys. J.*, 775:22, September 2013. doi: 10.1088/0004-637X/775/1/22.
- Susmita Sarkar, Samit Paul, and Raicharan Denra. Bump-on-tail instability in space plasmas. *Physics of Plasmas*, 22(10):102109, 2015. doi: 10.1063/1.4933041. URL <https://doi.org/10.1063/1.4933041>.
- A. Savcheva, J. Cirtain, E. E. Deluca, L. L. Lundquist, L. Golub, M. Weber, M. Shimojo, K. Shibasaki, T. Sakao, N. Narukage, S. Tsuneta, and R. Kano. A Study of Polar Jet Parameters Based on Hinode XRT Observations. *Pub. Astron. Soc. Japan*, 59:771, November 2007.
- P. H. Scherrer, J. Schou, R. I. Bush, A. G. Kosovichev, R. S. Bogart, J. T. Hoeksema, Y. Liu, T. L. Duvall, J. Zhao, A. M. Title, C. J. Schrijver, T. D. Tarbell, and S. Tomczyk. The Helioseismic and Magnetic Imager (HMI) Investigation for the Solar Dynamics Observatory (SDO). *Solar Phys.*, 275:207–227, January 2012. doi: 10.1007/s11207-011-9834-2.
- E. J. Schmahl, R. L. Pernak, G. J. Hurford, J. Lee, and S. Bong. Analysis of RHESSI Flares Using aRadio Astronomical Technique. *Solar Phys.*, 240:241–252, February 2007. doi: 10.1007/s11207-007-0263-1.
- J. T. Schmelz, M. Asgari-Targhi, G. M. Christian, R. S. Dhaliwal, and S. Pathak. Hot Plasma from Solar Active Region Cores: a Test of AC and DC Coronal Heating Models? *Astrophys. J.*, 806:232, June 2015. doi: 10.1088/0004-637X/806/2/232.
- B. Schmieder, Y. Guo, F. Moreno-Insertis, G. Aulanier, L. Yelles Chaouche, N. Nishizuka, L. K. Harra, J. K. Thalmann, S. Vargas Dominguez, and Y. Liu. Twisting solar coronal jet launched at the boundary of an active region. *Astron. Astrophys.*, 559:A1, November 2013. doi: 10.1051/0004-6361/201322181.
- C. J. Schrijver and A. A. van Ballegoijen. Is the Quiet-Sun Corona a Quasi-steady, Force-free Environment? *Astrophys. J.*, 630:552–560, September 2005. doi: 10.1086/431754.
- N. R. Sheeley, Jr., J. D. Bohlin, G. E. Brueckner, J. D. Purcell, V. E. Scherrer, and R. Tousey. The reconnection of magnetic field lines in the solar corona. *Astrophys. J. lett.*, 196:L129–L131, March 1975. doi: 10.1086/181761.
- K. Shibata and T. Magara. Solar Flares: Magnetohydrodynamic Processes. *Living Reviews in Solar Physics*, 8:6, December 2011. doi: 10.12942/lrsp-2011-6.
- K. Shibata and Y. Uchida. Sweeping-magnetic-twist mechanism for the acceleration of jets in the solar atmosphere. *Solar Phys.*, 103:299–310, February 1986. doi: 10.1007/BF00147831.
- M. Shimojo and K. Shibata. Physical Parameters of Solar X-Ray Jets. *Astrophys. J.*, 542:1100–1108, October 2000. doi: 10.1086/317024.
- M. Shimojo, S. Hashimoto, K. Shibata, T. Hirayama, H. S. Hudson, and L. W. Acton. Statistical Study of Solar X-Ray Jets Observed with the YOHKOH Soft X-Ray Telescope. *Pub. Astron. Soc. Japan*, 48:123–136, February 1996.
- O. C. St. Cyr, R. A. Howard, G. M. Simnett, J. B. Gurman, S. P. Plunkett, N. R. Sheeley, R. Schwenn, M. J. Koomen, G. E. Brueckner, D. J. Michels, M. Andrews, D. A. Biesecker, J. Cook, K. P. Dere, R. Duffin, E. Einfalt, C. M. Korendyke, P. L. Lamy, D. Lewis, A. Llebaria, M. Lyons, J. D. Moses, N. E. Moulton, J. Newmark, S. E. Paswaters, B. Podlipnik, N. Rich, K. M. Schenk, D. G. Socker, S. T. Stezelberger, S. J. Tappin, B. Thompson, and D. Wang. White-Light Coronal Mass Ejections: A New Perspective from LASCO. In A. Wilson, editor,

- Correlated Phenomena at the Sun, in the Heliosphere and in Geospace*, volume 415 of *ESA Special Publication*, page 103, December 1997.
- A. C. Sterling, R. L. Moore, D. A. Falconer, and M. Adams. Small-scale filament eruptions as the driver of X-ray jets in solar coronal holes. *Nature*, 523:437–440, July 2015. doi: 10.1038/nature14556.
- A. C. Sterling, R. L. Moore, D. A. Falconer, N. K. Panesar, S. Akiyama, S. Yashiro, and N. Gopalswamy. Minifilament Eruptions that Drive Coronal Jets in a Solar Active Region. *Astrophys. J.*, 821:100, April 2016. doi: 10.3847/0004-637X/821/2/100.
- A. C. Sterling, R. L. Moore, D. A. Falconer, N. K. Panesar, and F. Martinez. Solar Active Region Coronal Jets. II. Triggering and Evolution of Violent Jets. *Astrophys. J.*, 844:28, July 2017. doi: 10.3847/1538-4357/aa7945.
- P. A. Sturrock. Model of the High-Energy Phase of Solar Flares. *Nature*, 211:695–697, August 1966. doi: 10.1038/211695a0.
- Y. Su, A. M. Veronig, I. G. Hannah, M. C. M. Cheung, B. R. Dennis, G. D. Holman, W. Gan, and Y. Li. Determination of Differential Emission Measure from Solar Extreme Ultraviolet Images. *Astrophys. J. lett.*, 856:L17, March 2018. doi: 10.3847/2041-8213/aab436.
- R. Susino, D. Spadaro, A. C. Lanzafame, and A. F. Lanza. Properties of multistranded, impulsively heated hydrodynamic loop models. *Astron. Astrophys.*, 552:A17, April 2013. doi: 10.1051/0004-6361/201116542.
- P. A. Sweet. The Neutral Point Theory of Solar Flares. In B. Lehnert, editor, *Electromagnetic Phenomena in Cosmical Physics*, volume 6 of *IAU Symposium*, page 123, 1958.
- P. Testa, F. Reale, E. Landi, E. E. DeLuca, and V. Kashyap. Temperature Distribution of a Non-flaring Active Region from Simultaneous Hinode XRT and EIS Observations. *Astrophys. J.*, 728:30, February 2011. doi: 10.1088/0004-637X/728/1/30.
- P. Testa, B. De Pontieu, J. Allred, M. Carlsson, F. Reale, A. Daw, V. Hansteen, J. Martinez-Sykora, W. Liu, E. E. DeLuca, L. Golub, S. McKillop, K. Reeves, S. Saar, H. Tian, J. Lemen, A. Title, P. Boerner, N. Hurlburt, T. D. Tarbell, J. P. Wuelser, L. Kleint, C. Kankelborg, and S. Jaeggli. Evidence of nonthermal particles in coronal loops heated impulsively by nanoflares. *Science*, 346:1255724, October 2014. doi: 10.1126/science.1255724.
- W. T. Thompson, J. M. Davila, R. R. Fisher, L. E. Orwig, J. E. Mentzell, S. E. Hetherington, R. J. Derro, R. E. Federline, D. C. Clark, P. T. C. Chen, J. L. Tveekrem, A. J. Martino, J. Novello, R. P. Wesenberg, O. C. StCyr, N. L. Reginald, R. A. Howard, K. I. Mehalick, M. J. Hersh, M. D. Newman, D. L. Thomas, G. L. Card, and D. F. Elmore. COR1 inner coronagraph for STEREO-SECCHI. In S. L. Keil and S. V. Avakyan, editors, *Innovative Telescopes and Instrumentation for Solar Astrophysics*, volume 4853 of *Society of Photo-Optical Instrumentation Engineers (SPIE) Conference Series*, pages 1–11, February 2003.
- H. Tian, E. E. DeLuca, S. R. Cranmer, B. De Pontieu, H. Peter, J. Martínez-Sykora, L. Golub, S. McKillop, K. K. Reeves, M. P. Miralles, P. McCauley, S. Saar, P. Testa, M. Weber, N. Murphy, J. Lemen, A. Title, P. Boerner, N. Hurlburt, T. D. Tarbell, J. P. Wuelser, L. Kleint, C. Kankelborg, S. Jaeggli, M. Carlsson, V. Hansteen, and S. W. McIntosh. Prevalence of small-scale jets from the networks of the solar transition region and chromosphere. *Science*, 346(27):1255711, October 2014. doi: 10.1126/science.1255711.
- Hui Tian, Vasyl Yurchyshyn, Hardi Peter, Sami K. Solanki, Peter R. Young, Lei Ni, Wenda Cao, Kaifan Ji, Yingjie Zhu, Jingwen Zhang, Tanmoy Samanta, Yongliang Song, Jiansen He, Linghua Wang, and Yajie Chen. Frequently occurring reconnection jets from sunspot light bridges. *The Astrophysical Journal*, 854(2):92, 2018.
- S. J. Tingay, R. Goeke, J. D. Bowman, D. Emrich, S. M. Ord, D. A. Mitchell, M. F. Morales, T. Booler, B. Crosse, R. B. Wayth, and et al. The murchison widefield array: The square kilometre array precursor at low radio frequencies. *Publications of the Astronomical Society of Australia*, 30:e007, 2013. doi: 10.1017/pasa.2012.007.
- S. Tomczyk, S. W. McIntosh, S. L. Keil, P. G. Judge, T. Schad, D. H. Seeley, and J. Edmondson. Alfvén Waves in the Solar Corona. *Science*, 317:1192–, August 2007. doi: 10.1126/science.1143304.
- T. Török, R. Lionello, V. S. Titov, J. E. Leake, Z. Mikić, J. A. Linker, and M. G. Linton. Modeling Jets in the Corona and Solar Wind. In *Coimbra Solar Physics Meeting: Ground-based Solar Observations in the Space Instrumentation Era*, volume 504, page 185, April 2016.
- A. Tritschler, T. R. Rimmele, S. Berukoff, R. Casini, J. R. Kuhn, H. Lin, M. P. Rast, J. P. McMullin, W. Schmidt, F. Wöger, and DKIST Team. Daniel K. Inouye Solar Telescope: High-resolution observing of the dynamic Sun. *Astronomische Nachrichten*, 337:1064, November 2016. doi: 10.1002/asna.201612434.
- S. Tsuneta, L. Acton, M. Bruner, J. Lemen, W. Brown, R. Carvalho, R. Catura, S. Freeland, B. Jurcevich, M. Morrison, Y. Ogawara, T. Hirayama, and J. Owens. The Soft X-ray Telescope for the SOLAR-A Mission. *Solar Phys.*, 136:37–67, November 1991. doi: 10.1007/BF00151694.

- S. Tsuneta, K. Ichimoto, Y. Katsukawa, S. Nagata, M. Otsubo, T. Shimizu, Y. Suematsu, M. Nakagiri, M. Noguchi, T. Tarbell, A. Title, R. Shine, W. Rosenberg, C. Hoffmann, B. Jurcevich, G. Kushner, M. Levay, B. Lites, D. Elmore, T. Matsushita, N. Kawaguchi, H. Saito, I. Mikami, L. D. Hill, and J. K. Owens. The Solar Optical Telescope for the Hinode Mission: An Overview. *Solar Phys.*, 249:167–196, June 2008. doi: 10.1007/s11207-008-9174-z.
- J. E. Vernazza, E. H. Avrett, and R. Loeser. Structure of the solar chromosphere. III - Models of the EUV brightness components of the quiet-sun. *Astrophys. J. Supp.*, 45:635–725, April 1981. doi: 10.1086/190731.
- Y.-M. Wang, N. R. Sheeley, Jr., D. G. Socker, R. A. Howard, G. E. Brueckner, D. J. Michels, D. Moses, O. C. St. Cyr, A. Llebaria, and J.-P. Delaboudinière. Observations of Correlated White-Light and Extreme-Ultraviolet Jets from Polar Coronal Holes. *Astrophys. J.*, 508:899–907, December 1998. doi: 10.1086/306450.
- H. P. Warren. A Solar Minimum Irradiance Spectrum for Wavelengths below 1200 Å. *Astrophys. J. Supp.*, 157:147–173, March 2005. doi: 10.1086/427171.
- H. P. Warren, A. R. Winebarger, and D. H. Brooks. A Systematic Survey of High-temperature Emission in Solar Active Regions. *Astrophys. J.*, 759:141, November 2012. doi: 10.1088/0004-637X/759/2/141.
- Thomas Wiegmann, Julia K. Thalmann, and Sami K. Solanki. The magnetic field in the solar atmosphere. *The Astronomy and Astrophysics Review*, 22(1):78, Nov 2014. ISSN 1432-0754. doi: 10.1007/s00159-014-0078-7. URL <https://doi.org/10.1007/s00159-014-0078-7>.
- P. J. Wright, I. G. Hannah, B. W. Grefenstette, L. Glesener, S. Krucker, H. S. Hudson, D. M. Smith, A. J. Marsh, S. M. White, and M. Kuhar. Microflare Heating of a Solar Active Region Observed with NuSTAR, Hinode/XRT, and SDO/AIA. *Astrophys. J.*, 844:132, August 2017. doi: 10.3847/1538-4357/aa7a59.
- J.-P. Wuelser, J. R. Lemen, T. D. Tarbell, C. J. Wolfson, J. C. Cannon, B. A. Carpenter, D. W. Duncan, G. S. Gradwohl, S. B. Meyer, A. S. Moore, R. L. Navarro, J. D. Pearson, G. R. Rossi, L. A. Springer, R. A. Howard, J. D. Moses, J. S. Newmark, J.-P. Delaboudinière, G. E. Artzner, F. Auchere, M. Bougnet, P. Bouyries, F. Bridou, J.-Y. Clotaire, G. Colas, F. Delmotte, A. Jerome, M. Lamare, R. Mercier, M. Mullot, M.-F. Ravet, X. Song, V. Bothmer, and W. Deutsch. EUVI: the STEREO-SECCHI extreme ultraviolet imager. In S. Fineschi and M. A. Gummin, editors, *Telescopes and Instrumentation for Solar Astrophysics*, volume 5171 of *Society of Photo-Optical Instrumentation Engineers (SPIE) Conference Series*, pages 111–122, February 2004. doi: 10.1117/12.506877.
- P. F. Wyper, C. R. DeVore, and S. K. Antiochos. A Breakout Model for Solar Coronal Jets with Filaments. *Astrophys. J.*, 852:98, January 2018. doi: 10.3847/1538-4357/aa9ffc.
- P. R. Young and K. Muglach. Solar Dynamics Observatory and Hinode Observations of a Blowout Jet in a Coronal Hole. *Solar Phys.*, February 2014. doi: 10.1007/s11207-014-0484-z.
- P. R. Young, G. Del Zanna, H. E. Mason, K. P. Dere, E. Landi, M. Landini, G. A. Doschek, C. M. Brown, L. Culhane, L. K. Harra, T. Watanabe, and H. Hara. EUV Emission Lines and Diagnostics Observed with Hinode/EIS. *Pub. Astron. Soc. Japan*, 59:S857–S864, November 2007. doi: 10.1093/pasj/59.sp3.S857.
- H. Yu-kun, X. Zhi, X. Zhi-ke, Y. Xiao-li, S. Yuan-deng, W. Ning, and L. Jun. Recurrent Jets Occurred Nearby Active Region NOAA 11931. *Chinese Astronomy and Astrophysics*, 40:504–523, October 2016. doi: 10.1016/j.chinastron.2016.10.003.

